Contribution to the development of numerical methods for the investigation of phase change processes of compressible non-ideal fluids

From the Faculty of Engineering, Department of Mechanical and Process Engineering
of

University of Duisburg Essen

for obtaining the academic degree

of

Doctor of Engineering

Dr.-Ing.

accepted dissertation

by

Katharina Tegethoff
from
Duisburg

Examiners: Univ.-Prof. Dr.-Ing. Dieter Brillert
Univ.-Prof. Dr.-Ing. Romuald Skoda

Day of oral examination: 7 June 2024

DOI: 10.17185/duepublico/82536
URN: urn:nbn:de:hbz:465-20241024-131248-6

English translation by the author of the dissertation originally published in German in June 2024: "Beitrag zur Entwicklung numerischer Verfahren für die Untersuchung von Phasenwechselvorgängen kompressibler nicht-idealer Fluide", the original German version is available at: https://doi.org/10.17185/duepublico/82080

The English translation was published in **October 2024.**

Acknowledgement

Obtaining a doctoral degree has been a significant life goal for me since the age of fourteen, and writing this thesis has brought it within reach. This achievement would have been inconceivable without the support of many companions. It is therefore a matter of great personal importance to begin this dissertation with a heartfelt expression of thanks.

I would like to express my gratitude to Professor Brillert, my PhD supervisor and first examiner for both this dissertation and, previously, my Master's thesis. In the darkest moments, when I felt I could go no further, you were always by my side, trying to guide me towards the light. You also facilitated my time at the Whittle Laboratory in Cambridge immediately after my defence.

I extend my gratitude to my second examiner, Professor Skoda, for your deep interest in my dissertation topic. Your written feedback and our personal exchange were invaluable in helping me to categorise and critically assess my own work.

Three professors have had a profound influence on my academic journey up to my time as a PhD student, and I would like to take this opportunity to thank them:
Professor Nagarajah, you believed in me and my abilities from the early stages of my academic journey, beginning with my bachelor's degree, and really encouraged me to pursue my goals. I am deeply grateful to you for that. Professor Panglisch, you have been, and continue to be, a great role model for me, both professionally and personally. I have always admired the way you explain complex matters without losing your personal touch. Professor Bathen, I cannot thank you enough for the time you invested in me and the completely selfless and honest advice you provided. In my experience, people like you are rare in your position.

Special thanks go to my colleagues at the German Aerospace Center in Cologne. Thanks to you, Edmund, Jens, Christian, Graham, Simon, Georg, and Jan, my work on TRACE was possible in the first place. You always made me feel welcome and supported me with help and advice in every conceivable situation. This was by no means taken for granted and means a great deal to me.

Dominik and Alex, working with you as research assistants made my time at the chair unforgettable. Also the students with whom I later worked as a research associate also provided countless wonderful moments. Thank you, Johanna, Carolina, Jana, Olli, and Aaron, for your emotional support.

I am particularly proud of my small army of thesis students: Yipeng, Hamed, Basel, Wael, Ayoub, Ilyas, Jannis, Carolina, Olga, Alicja, Mücahit, Alex, Massimiliano, and Isaac. It was an honour to accompany you on your journey towards your Bachelor's or Master's degree.

I would like to thank my former colleagues Rebecca, Tina, Jingjing, Alex, Ihab, and Tobi for the time we spent together as a team on the first floor. You were an important support to me in daily life. Detlev and Ben, even though I was always just a „simulant“ to you two, I could always rely on your backing in the lab. I am very grateful for that. Thank you, Silke, Jenny, and Bastian, for the insignificant and significant conversations, the listening, and the countless words of encouragement.

Stefan, thank you for comforting me in difficult times and for the little guardian I found on my desk one morning, who has been there ever since when I've felt all alone.
Flo, even though you were rarely in our shared office because you were working on your test rig in Ruhrort, I really enjoyed our time together and the laughs we shared. Thank you for your light-heartedness.
Haikun, thank you for all the conversations and discussions that began with „a small question about thermodynamics“ and for your big heart, which I only discovered rather late.

I would like to thank my current colleagues Nick, Till, and Lloyd, aka Laserman, for their unwavering belief that I would succeed. Thank you, Nick, for literally finding me on the floor of my office early in the morning and always searching for alternatives for me. Till, thank you for your trust and the long conversations we had about everything under the sun. Lloyd, thank you for every single round of 5D chess.

I would especially like to thank Sebastian, my Master's thesis supervisor, sparring partner against will, equal in stubbornness, and favourite colleague, for all the wonderful moments and opportunities for growth, both professionally and personally. Despite all the deep valleys we had to go through together or alone, you will always remain a very special person to me.

My heartfelt thanks go to my proofreaders, Dr Dohmen, Christian, and Jens, for every comment and idea, and for the great dedication with which they supported me. Mr Dohmen, thank you for always being someone I could trust and for giving me the feeling that I was good enough, even in moments of failure. Christian, thank you for your time, your humour, and the way you treated me as an equal. Jens, thank you so much for always being there for me and standing behind me unconditionally, even though we rarely saw each other in person.

A huge thank you to you, Carmen: Without you, I would not have made it through the last year of my time as a PhD student. Thanks to you, I was quickly able to laugh about things that had cost me many tears and sleepless nights. You were also someone I could always turn to in times of need.

Mum, thank you for your care and boundless support at any time of the day or night. Thank you for not letting me give up. Thank you for your honest opinions, your unwavering conviction, and your ability to listen to my often repetitive problems over and over again. Thank you for all this and so much more!

Abstract

Numerical methods are an integral part of the design process of modern turbomachinery and contribute to a significant increase in time and resource efficiency. Numerous methods used for this purpose are based on the assumption of a calorically perfect gas, which enables a suitable approximation of the real fluid properties in the context of conventional working media such as air. In utilising alternative energy sources, such processes are becoming increasingly relevant for which the choice of working medium can be tailored to the application. The fluids used due to their special thermophysical properties can only be described inadequately by the model of the calorically perfect gas and are therefore classified as non-ideal. Since it is often impossible to take this non-ideality or possible phase change phenomena into account using established numerical methods, a design of related turbomachinery first requires the development of suitable methods. The approach for calculating numerical flux terms presented in this work contributes to that and can be applied to single-phase and two-phase flows of non-ideal fluids. In addition to high numerical robustness against discontinuities, it is characterised in particular by its applicability to arbitrary equations of state. Various modelling approaches can be used to describe the dispersed phase formed during a phase change in different degrees of detail. Thus, the droplet size distribution can be modelled as either monodispersed or polydispersed, whereby, in the latter case, it is described through its statistical moments. Furthermore, the developed method enables the consideration of velocity differences between the phases, which lays the foundation for a detailed investigation of the movement of the dispersed phase in the flow field. By tabulating the thermophysical quantities, it is also possible to achieve an increase in calculation time efficiency that is relevant in the context of the design process. The associated loss in terms of accuracy of description is minimised by using a Taylor series approach for interpolation. A verification and validation based on a representative selection of test cases demonstrates the applicability of the developed method to single-phase and two-phase flows of compressible non-ideal fluids of different molecular complexity. In particular, the phase change based on homogeneous non-equilibrium condensation is described in high agreement with results of experimental investigations.

Declaration

The present document is an English translation of a doctoral thesis, which was previously published in German:

Katharina Tegethoff. 'Beitrag zur Entwicklung numerischer Verfahren für die Untersuchung von Phasenwechselvorgängen kompressibler nicht-idealer Fluide'. University of Duisburg Essen. (June 2024). DOI 10.17185/duepublico/82080

Partial results of the present work have already been published or accepted for publication in:

Katharina Tegethoff, Sebastian Schuster und Dieter Brillert. 'Numerical simulation of real gas one-component two-phase flow using a Roe-based scheme'. In Journal: *Computers & Fluids* 245 (2022), No. 105560. DOI 10.1016/j.compfluid.2022.105560.

Katharina Tegethoff, Carolina Borges de Almeida, Sebastian Schuster and Dieter Brillert. 'Numerical method for investigating non-ideal flow demonstrated on a centrifugal compressor operating near the critical point of CO_2'. In: Proceedings of the ASME Turbo Expo 2024: Turbo Expo: Power for Land, Sea and Air, Volume 11: Supercritical CO_2. (June 2024). DOI 10.1115/GT2024-124068

Contents

List of Figures

List of Tables

Symbols and Abbreviations

Latin Symbols

Symbol	Unit	Description
A	m^2	flow area
A_C	-	model parameters of the Cunningham correction
A_s	m^2	surface of a spherical droplet
A^*	m^2	narrowest cross section
$\boldsymbol{A}(\boldsymbol{U})$	-	Jacobian matrix
a	m/s	speed of sound
a, b	-	van der Waals coefficients
C	-	number of components in a system
C_C	-	correction factor according to Cunningham
C_D	-	dimensionless drag coefficient
$C_{D,SN}$	-	dimensionless drag coefficient according to Schiller and Naumann
CFL	-	metric according to Courant, Friedrichs and Lewy
c_p	J/(kg·K)	specific isobaric heat capacity
c_v	J/(kg·K)	specific isochoric heat capacity
dV	m^3	infinitesimal control volume
E	J/kg	total specific inner energy
$\boldsymbol{E}$	-	matrix of right eigenvectors
e	J/kg	specific inner energy
F	-	number of degrees of freedom in a system
F_D	N	aerodynamic drag force
$\boldsymbol{F}, \boldsymbol{G}, \boldsymbol{H}$	-	flux vector
$\boldsymbol{F}_c$	-	convective part of the flux vector
$\boldsymbol{F}_v$	-	viscous part of the flux vector
f	J/kg	specific Helmholtz energy
$f(r)$	-	number density function of the droplet radii
f_x, f_y, f_z	$\mathrm{m/s}^2$	cartesian components of body forces
$G(r)$	m/s	growth rate
Gr	-	Grüneisen parameter
g	J/kg	specific Gibbs energy
H	J/kg	total specific enthalpy
h	J/kg	specific enthalpy
h_v	J/kg	specific enthalpy of vapourisation
$\boldsymbol{I}$	-	unit matrix
$\bar{J}$	1/(kg·s)	mass-related nucleation rate

J	$1/(\mathrm{m}^3 \cdot \mathrm{s})$	nucleation rate
J_0	$1/(\mathrm{m}^3 \cdot \mathrm{s})$	pre-exponential factor of nucleation rate
Kn	-	Knudsen number
L	m	length
$\bar{l}$	m	mean free path length
M	kg/mol	molar mass
Ma	-	Mach number
$\boldsymbol{M}$	-	vector of the dispersed phase in Lagrangian frame of reference
m	kg	mass
$\dot{m}$	kg/s	mass flow
N	-	number of active degrees of freedom
N_T	1/kg	number of droplets per unit mass of the mixture
n	-	number of droplets
n_A	-	number of queries
n_G	-	number of equations to solve
n_T	-	table dimension
n_V	-	number of grid cells
n_s	rpm	rotational speed
n_x, n_y, n_z	-	components of the normal vector
P	-	number of phases in a system
Pr	-	Prandtl number
p	Pa	static pressure
$\dot{p}$	1/s	expansion rate
p_s	Pa	saturation vapour pressure
$\boldsymbol{Q}$	-	source term vector
$\boldsymbol{Q}_L$	-	source term vector in Lagrangian frame of reference
q	-	symbolic quantity of Roe averaging
q_c	-	condensation coefficient
$\dot{q}_r$	J/(kg·s)	heat flow due to radiation
R_s	J/(kg·K)	specific gas constant
$\boldsymbol{R}$	-	right eigenvector
Re	-	Reynolds number
$ResL1$	-	L1 norm of the residual
r	m	radius
r_{20}	m	surface-averaged radius
r_{32}	m	Sauter radius
r_{crit}	m	critical radius
r_G	-	refinement factor of the spatial grid

r_T	-	refinement factor of the table
S	-	supersaturation
St	-	Stokes number
s	J/(kg·K)	specific entropy
T	K	static temperature
T_s	K	saturation temperature
t	s	time
$\boldsymbol{U}$	-	conservation vector
$\boldsymbol{u}$	m/s	unit vector of velocity
u, v, w	m/s	cartesian components of velocity
v	m^3/kg	specific volume
$\boldsymbol{v}$	m/s	vector of velocity
V	m^3	volume
V_V	-	cell volume
x	-	vapour quality
x, y, z	-	cartesian coordinates
y	-	wetness fraction
$y_{Nucleation}$	-	proportion of nucleation to wetness fraction
y_{Growth}	-	proportion of growth to wetness fraction
y^+	-	dimensionless wall distance
Z	-	compressibility factor
z	-	symbolic thermophysical quantity

Greek symbols

Symbol	Unit	Description
α, β, ν	-	empirical parameters according to Young
α	J/(m^2·s·K)	heat transfer coefficient
α_{crit}	J/(m^2·s·K)	heat transfer coefficient for a nucleus with r_{crit}
$\tilde{\alpha}$	-	wave strength
α_p	1/K	thermal isobaric expansion coefficient
Γ	-	fundamental derivative of gas dynamics
Δ	-	set of derivative terms for interpolation
ΔG	J	difference in Gibbs energy
ΔG_{crit}	J	energy barrier for nucleation
ΔG_s	J	surface portion of Gibbs energy
ΔG_v	J	volume portion of Gibbs energy
$\Delta\kappa$	-	Difference between isentropic pressure-volume exponent and ratio of specific heat capacities
ΔT	K	subcooling

Δt	-	dimensionless time step
Δx	-	dimensionless grid point spacing
δ	-	dimensionless density
δ^*	-	parameters of the entropy condition
δ_∞^c	-	dimensionless reciprocal of $c_{v,\infty}$
$\varepsilon_1, \varepsilon_2, \varepsilon_3, \varepsilon_4, \varepsilon_5$	-	auxiliary parameters for formulating Jacobi matrices
θ_G	-	order of convergence of the spatial grid
θ_T	-	order of convergence of the table
η	Pa·s	dynamic viscosity
κ	-	isentropic exponent of the perfect gas
κ_{pv}	-	isentropic pressure-volume exponent
κ_{pT}	-	isentropic pressure-temperature exponent
κ_T	1/Pa	isothermal compressibility
$\mathbf{\Lambda}$	-	diagonal matrix of eigenvalues
Λ_N	1/s	proportion of nucleation to mass transfer
Λ_G	1/s	proportion of droplet growth to mass transfer
λ	-	eigenvalue
λ_g	J/(m·s·K)	thermal conductivity
μ	J/mol	chemical potential
μ_k	-	moments of the droplet radius distribution
π	-	pressure ratio
ρ	kg/m^3	density
σ	-	parameter of molecular complexity by Invernizzi
σ_{lg}	N/m	surface tension
τ	-	dimensionless temperature
τ_{ij}	-	shear stress
Φ	-	dimensionless Helmholtz energy
ϕ	-	non-isothermal correction factor
ϕ_0	-	pre-factor of the non-isothermal correction factor
φ	-	volume fraction of a phase
χ	-	mean error of evaluation based on tables
ω	1/s	angular velocity

Indices und Superscripts

Symbol	Description
$1, 2, 4$	levels of refinement for discretisation errors
c	critical state
d	index of differential equation
δ	partial derivative by dimensionless density

EOS	equation of state
eq	state of equilibrium
g	quantity of gas phase
i	group of droplets of same size
in	quantity at inlet
int	quantity at phase boundary
j	spacial discretisation
L	left state of a Riemann problem
l	quantity of liquid phase
m	quantity of two-phase mixture
max	maximum
out	quantity at outlet
p	isobaric change of state
R	right state of a Riemann problem
RE	Richardson extrapolation
r	reduced quantity
s	isentropic change of state
s,l	saturation state of the liquid phase
s,g	saturation state of the gas phase
$trip$	quantity at triple point
T	isothermal change of state
t	total quantity
tab	evaluation using tables
v	isochoric change of state
x,y,z	cartesian spatial directions
τ	partial derivative by dimensionless temperature
Φ	Helmholtz based
∞	quantity evaluated for $v \to \infty$
$\perp$	orthogonal

0	ideal part
$iter$	iterative routine
k	order of statistical moments
n	temporal discretisation
r	real part
$*$	correction to meet the entropy condition

Mathematical Operators und Constants

Symbol		Description
d		exact differential
Δ		difference
δ		unspecific partial differential
∂		partial differential
$\mathscr{F}$		symbolic function
$\tilde{}$		Roe averaging
T		transposition
∞		infinity

k_b	$\mathrm{m^2 \cdot kg/\left(s^2 \cdot K\right)}$	Boltzmann constant
N_A	1/mol	Avogadro constant
R	J/(mol·K)	universal gas constant
π		ratio of a circle's circumference to its diameter

Abbreviations

Symbol	Description
AIAA	**A**merican **I**nstitute of **A**eronautics and **A**stronautics
CDV	**C**onverging **D**iverging **V**erification
CFD	**C**omputational **F**luid **D**ynamics
DLR	German Aerospace Center
DNS	**D**irect **N**umerical **S**imulation
E-E	**E**ulerian-**E**ulerian frame of reference
E-L	**E**ulerian-**L**agrangian frame of reference
EPGIRoe	**E**xplicit **P**hase **G**eneralised **I**deal **Roe**
GIRoe	**G**eneralised **I**deal **Roe**
HLL	**H**arten **L**ax van **L**eer
IAPWS	**I**nternational **A**ssociation for the **P**roperties of **W**ater and **S**team
IWSMP	**I**nternational **W**et **S**team **M**odelling **P**roject
LES	**L**arge **E**ddy **S**imulation
M	**M**ixture based
Mono	**Mono**dispersed
MUSCL	**M**onotonic **U**pstream-centered **S**cheme for **C**onservation **L**aws
NASA	**N**ational **A**eronautics and **S**pace **A**dministration
NICFD	**N**on-**I**deal **C**ompressible **F**luid **D**ynamics

NIST	**N**ational **I**nstitute of **S**tandards and **T**echnology
ORC	**O**rganic **R**ankine **C**ycle
P	**P**hase based
PGIRoe	**P**hase **G**eneralised **I**deal **Roe**
Poly	**Poly**dispersed
RANS	**R**eynolds **A**veraged **N**avier **S**tokes
S	**S**lip
sCO_2	**s**upercritical **CO_2**
SST	**S**hear **S**tress **T**ransport
TRACE	**T**urbomachinery **R**esearch **A**erodynamic **C**omputational **E**nvironment

1 Introduction

While experimental and theoretical fluid dynamics findings can be traced back to the time of Hellenistic Greece, the first application of numerical methods to investigate flow phenomena can only be proven based on anecdotal evidence. According to this, Lewis Fry Richardson [121] devised a method for numerical weather forecasting at the beginning of the 20th century. To calculate a weather forecast for a period of eight hours, he spent six weeks of his time and failed in the end. His observation of a very high computational effort prompted him to design a potential solution. This describes a collection of 64,000 people, each equipped with a mechanical calculator, which he calls a *forecast factory*. To coordinate the calculation process, Richardson envisaged a person visible to all, who would use coloured light signals and telegraphic communication techniques. Even the grumpiest user of today's computer-aided fluid dynamics (CFD), who sits alone in front of his computer and can achieve a converged solution for most problems within minutes or hours, will at least smile internally at this thought. In the next moment, he will probably realise the analogy to the high-performance computers available to us nowadays. The human computers are replaced by processor cores and the coordinator equipped with tools is replaced by a system for process parallelisation. Even before the first high-performance computers were designed, researchers were already working on developing computer-aided methods. Contemporary military conflicts and exploring our planet's vast expanses were a particular driving force. With this in mind, NASA employees in Los Alamos developed numerous methods for the numerical description of currents in the 1960s. The rapidly advancing technical development of computers made it possible to establish commercial CFD methods in relevant branches of industry, such as the turbomachinery sector, as from the early 1980s. In the context of the design and optimisation of modern turbomachinery, numerical solution methods have now become indispensable. However, their application to fluid flows, characterised by a deviation of their thermophysical properties from the model of the perfect gas, remains a challenge. The areas of investigation summarised under the field of *Non-Ideal Compressible Fluid Dynamics* (NICFD) include single-phase flows of non-ideal fluids as well as two-phase flows. In classic steam turbine applications, condensation effects in the low-pressure stages pose particular challenges for numerical modelling. Due to the increasing interest in the utilisation of alternative energy sources, organic fluids and carbon dioxide in a supercritical state (sCO_2) are also becoming the focus of numerical investigations. For such fluids, which are to be modelled as non-ideal, large gradients of thermophysical quantities can be observed both in the context of phase change processes and for changes of state in the vicinity of the critical point. Therefore, the CFD methods for calculating corresponding flows must ensure a high modelling accuracy of the state quantities with simultaneous robustness against large gradients in the flow field. The present work aims to contribute to the development of such numerical methods. The focus is on describing the phase change processes of compressible non-ideal fluids. To make the approaches presented in this work accessible to the scientific community and industrial applications, the derived schemes are implemented in the *Turbomachinery Research Aerodynamic Computational Environment* (TRACE). It is a CFD solver developed by the German Aerospace Centre (DLR). Since TRACE uses an implicit method for the temporal integration of the system of equations, the methods presented in this thesis for determining the convective flux terms are also validated using a three-dimensional method implemented by the author using an explicit temporal integration approach.

The present work is structured as follows:
The **State of the Art** is documented with a focus on the fields relevant to this work and motivates the research question. The relevance of the investigation of compressible non-ideal fluids is demonstrated based on their areas of application. Different numerical methods for describing single-phase and two-phase flows are compared and their suitability for describing phase change processes is categorised.
The **Thermodynamic Description of Compressible Non-Ideal Fluids** introduces the thermodynamics concepts relevant to this work. For this purpose, a distinction is first made between thermodynamic state areas and their characteristics. To make these accessible to a mathematical description, various types of equations of state are presented. The classification of a fluid as compressible and non-ideal is based on a selection of suitable parameters. Before the special properties of the working media investigated in this thesis are highlighted, the models used to describe the phase change are detailed.
Subsequently, the **Numerical Modelling** of the systems of equations to be solved to investigate single-phase and two-phase flows of compressible non-ideal fluids is outlined. The mathematical derivation of an extension of the Roe scheme for the application to the calculation of single-phase and two-phase flows of different complexity represents the main contribution of the present work and is introduced for a compact presentation in one dimension. The way of implementing the resulting schemes in the flow solver TRACE, as well as methods for the evaluation of numerical solutions, are presented.
The results obtained in the course of a **Application of the Model to Various Validation Cases** of single-phase and two-phase flows are discussed. A numerical investigation of the expansion of CO_2 and the organic fluid MDM in Laval nozzles is followed by an analysis of the compression of CO_2 in a supercritical state using the geometry of a sCO_2 compressor. The condensation of steam and CO_2 in Laval nozzles serves to validate the models implemented to describe the phase change process. The numerical investigation of a turbine cascade with steam flowing through it is used to investigate the interactions between the liquid and gaseous phases in detail.
Summary and Outlook serve to categorise the knowledge gained from the present work and point out possible aspects for further investigations.
The **Appendix** contains a tabular list of the thermophysical model equations used and an analysis of their evaluation in the two-phase region as well as the equations and matrices for an implementation of the presented method for calculating convective flux terms in three dimensions.

2 State of the Art

This thesis aims to contribute to the development of numerical methods for the investigation of phase change processes of compressible non-ideal fluids. To achieve this, a combination of the concepts and findings of thermophysics, fluid dynamics, and numerical mathematics is necessary. Firstly, the areas of application and special properties of compressible non-ideal working fluids in the context of turbomachinery must be considered. The methods required for the numerical investigation of such fluids need to enable the description of single-phase and two-phase flows. An overview of the state of the art represented by the relevant technical literature is used to select approaches to be pursued in subsequent sections. The investigation of phase change processes imposes special requirements on the selected numerical method, which are discussed for the specification of the objective.

2.1 Areas of Application for Compressible Non-Ideal Working Media

Thermal energy conversion into mechanical or electrical energy has historically been achieved using cycles powered by conventional working media such as steam or air. Usually, the combustion of a fossil fuel serves as the heat source. The utilisation of other heat sources is significantly limited by a lack of flexibility with regard to changes in operating conditions. In addition to attempts to overcome these limitations by adapting existing processes, approaches that develop technologies tailored to the respective process boundary conditions appear particularly promising. The possibility of choosing the working medium represents an additional degree of freedom for the latter. Due to their specific thermophysical properties, compressible non-ideal working media can be found in many of these applications. In addition to their relevance for compression processes in left-hand circuits of refrigeration and heat pump technology, their potential is also evident in the context of right-hand Rankine circuits. The working media used for these *Organic Rankine Cycles* (ORC) are organic compounds or mixtures. The advantage of organic fluids is largely based on the possibility of chemically producing an optimal working medium for the application in question. Due to their low thermal resistance, they are mostly used near low-temperature heat sources. In addition to the utilisation of industrial waste heat, the areas of application of ORC cycles also include biomass [119], solar thermal [47] and geothermal power plants [46]. When specifying the optimum fluid properties, operating conditions in terms of prevailing temperature levels and power requirements can be considered.

Carbon dioxide in a supercritical state is another working fluid that is characterised by its non-ideality of thermodynamic states. The idea of using this fluid in a Brayton cycle goes back to the work of Angelino [5]. The liquid-like fluid properties of carbon dioxide near its critical point make it possible to reduce the power required for compression. Unlike in the case of ORC applications, sCO_2 cycles are found in particular in the environment of high-temperature heat sources such as heat removal in nuclear power plants [39], industrial waste heat utilisation [95] and the conversion of concentrated solar energy [108].

The spread of cycles whose working media can be classified as non-ideal is significantly hindered by a lack of experience in the design of their components and a deficit of experimental evidence. In this respect, the design of turbomachinery is of particular relevance due to its influence on cycle efficiency, as demonstrated by Colonna et al. [32] and Allison et al. [2]. The extent to which it is possible to adapt the design guidelines established for conventional media to organic fluids and CO_2 in a supercritical state cannot yet be conclusively clarified due to the fluid properties that deviate greatly from the model of the perfect gas. To be able to investigate these questions in more detail, numerical methods for describing flows of non-ideal fluids are required in addition to experimental approaches. Applying numerical methods enables a time- and cost-efficient design of turbomachinery and is, therefore, a necessary criterion for establishing associated energy conversion processes. Numerical investigations of expansion and compression processes of compressible non-ideal fluids are, therefore, the focus of numerous current publications.

The non-ideality of organic media in the vicinity of the dew line and the critical point, as documented by Thompson and Lambrakis [147] for example, is taken by Romei et al. [126] as an opportunity for comprehensive numerical investigations of the expansion process in this region of state. They consider the supersonic flow through a turbine cascade with the organic fluid hexamethyldisiloxane. In contrast to subcritical states, the flow characteristics for supercritical inlet states deviate strongly from those of ideal gas dynamics. The authors conclude that established design rules for ORC turbines are applicable for inlet conditions below the critical point and that further investigation is required for expansions of supercritical states. The increase in Mach number above an oblique shock in flows of non-ideal molecularly complex fluids described by Gori et al. represents such a deviation of the flow characteristics from ideal gas dynamics. For the design of turbines, the underestimation or overestimation of flow losses due to deviating flow characteristics is of particular importance. Tosto et al. [151] carry out numerical investigations of an axial turbine cascade for the media CO_2 and hexamethyldisiloxane. They observe a dependence of the deviations of the flow characteristics on the molecular complexity and the non-ideality of the fluid. They can also correlate the flow losses that occur with the fluid properties and, as a result, the occurrence of shock waves and wake vortices in the area of the blade's trailing edge.

The compression of carbon dioxide in a supercritical state poses three particular challenges for numerical design. Close to the critical point, the thermophysical quantities exhibit considerable gradients, which require a high degree of accuracy in describing the state. Furthermore, no clear separation of liquid and gaseous states can be made above the critical point. The continuous second-order phase transition takes place along the Widom line, which is surrounded by areas of large gradients. Finally, a drop into the two-phase region and the formation of a second phase can occur within the vane passage of the compressor. Pečnik et al. [116] and Rinaldi et al. [122] demonstrate these special features of the flow of CO_2 in a supercritical state within a radial compressor using numerical investigations. The geometry considered is the compressor of the experimental sCO_2 cycle of the *Sandia National Laboratories* [168]. Numerous other authors (see, for example, [3, 132]) carry out detailed studies using this geometry and show limitations in the form of a poor convergence of the methods they use and a high computing time requirement for evaluating the thermophysical quantities. Baltadjiev et al. [15] investigate the influence of the non-ideality of the fluid as well as condensation on the leading edge of the blade on the performance parameters of the compressor. For the operating point they investigated, the authors conclude that the ratio of the time required for droplet formation and the residence time of the droplets in the flow is too small to induce a relevant influence of condensation on the operation of the compressor. The need for numerically stable and computationally efficient methods for the description of compressible non-ideal single-phase and two-phase flows is thus clearly demonstrated by the above investigations.

2.2 Numerical Methods for the Description of Single- and Two-Phase Flows

The mathematical description of a flow is based on the conservation laws of mass, momentum, and energy. To be able to describe the flow phenomena occurring in turbomachinery as comprehensively as possible using numerical methods, the flow is usually modelled as viscous and compressible. The resulting system of equations is characterised by partial nonlinear differential equations. These equations are also known as Navier-Stokes equations.

To solve them numerically, the way in which turbulent fluctuations in the flow field are taken into account is of particular importance. In a direct numerical simulation (DNS) of a flow, the turbulent fluctuations in space and time are fully resolved. Due to the very fine spatial and temporal resolution of the flow quantities, this requires a high accuracy of the physical representation and results in a very high demand for computing resources. *Large eddy* simulations (LES) reduce the required computing capacity by applying a spatial filter to the Navier-Stokes equations. This results in a complete resolution of larger vortex structures, while smaller vortices are only described approximately using fine structure models. The prioritisation of large-scale over small-scale components in the course of the LES leads to a reduction in description accuracy compared to the DNS. A temporal or Reynolds averaging of the Navier-Stokes equations (RANS) represents a further simplification. The turbulent fluctuations are considered as part of the viscous flux terms using additional terms described by so-called turbulence models. For numerous turbomachinery applications, the solution of the RANS equations provides a sufficiently accurate description while requiring significantly less computing time. Since the focus of the present work is on the advancement of a method for the calculation of convective flux terms of the Navier-Stokes equations, a limitation to the RANS equation system appears to be sufficient.

Using a system of hyperbolic partial differential equations such as the RANS equations, an initial value problem can be formulated as a Riemann problem. This is defined using a finite volume approach for two neighbouring spatially discrete volumes. The work of Godunov [56] forms the starting point for the development of approaches for solving such initial value problems, whereby the flux across the volume boundaries is an essential target variable. A large number of authors deal with the formulation of approximate solution methods. A comparative selection of these can be found in van Leer et al. [90]. The methods differ significantly in their ability to represent the wave types that characterise the Riemann problem. The approach of Lax and Friedrich [87] does not contain any information about the wave structure of the Riemann problem. It is consequently only insufficiently suitable for the description of shock waves, contact discontinuities, and expansion fans. The Riemann solver, according to Harten, Lax, and van Leer (HLL) [70], the methods of *flux vector splitting* (cf. exemplary [88]) and the approach according to Rusanov [128] are each able to capture specific wave types with high accuracy. In contrast, a complete representation of the wave structure can be achieved with the approaches according to Osher [110], Roe [124] or further developments of the HLL approach (cf. [149, 43]).

Compared to other methods, the Roe formulation is characterised by a very high accuracy in the resolution of discontinuities. This is due, in particular, to the absence of additional numerical damping terms. Therefore, it is preferred to describe complex flow fields with large gradients of flow quantities. Peery and Imlay [112] document the occurrence of the so-called *carbuncle phenomenon* for the Roe scheme, which describes numerical instabilities in the vicinity of a shock under hypersonic conditions. The flux calculation scheme developed by Roe violates the entropy condition and consequently allows unphysical solutions. However, this can be corrected by an appropriate limitation involving a modification of the eigenstructure [69]. The restriction of Roe's approach to the model of the perfect gas caused by its derivation poses a further challenge. The linearised system of equations is no longer uniquely determined when considering an equation of state of a non-ideal fluid. As a result, the formulation of the pressure partial derivatives contained in the Jacobi matrix and the resulting definition of the Roe-averaged state are of central importance.

Grossman and Walters [58] retain the relationships derived under the assumption of a perfect gas. The influence of modelling the gas as non-ideal is limited to determining an equivalent ratio of specific heat capacities as a function of density and internal energy. Glaister [55], Vinokur [155] and Liou et al. [93], on the other hand, concentrate on an exact determination of the partial derivatives of the pressure. However, this means that the derivation and, thus, the resulting expressions depend on the type of equation of state. Mottura et al. [103] provide an overview of such adaptations of the Roe scheme for different equations of state. According to Abgrall [1], the number of Roe-averaged state quantities required increases with increasing complexity of the equation of state. The robustness of the method adapted for non-ideal fluids also decreases compared to the original formulation due to the need to solve complex non-linear equations. To counter this, Cinella [27] proposes a series of specific simplifications concerning the averaging of the quantities. This work is also based on an extension of the Roe scheme that attempts to minimise the complexity of the formulation while retaining the accuracy and robustness of the original approach. The approach referred to below as *Generalised Ideal Roe* (GIRoe) [142] can be applied to equations of state of any complexity. Its special feature is the evaluation of the Roe-averaged speed of sound based on the selected equation of state.

The methods presented so far for calculating the convective flux terms are limited to single-phase flows. In the case of two-phase flows, the definition of the convective flux is directly related to the type of phase modelling and the selected frame of reference of the dispersed phase. If the conservation equations are formulated separately for each phase using an Eulerian frame of reference, there is at least a doubling of the equations to be solved. In the approach also known as the *two-fluid* model, the interaction of phases and, in particular, phase changes are taken into account by corresponding source terms. Increasing the level of detail of the modelling by considering different droplet sizes and a fluid-specific equation of state has a strong influence on the complexity of the Jacobian matrix. As Ndjinga et al. [107] show, a numerical diagonalisation of the matrix using conventional methods is no longer possible. Simplifying the Jacobian matrix for a specific equation of state can meet this challenge [73]. However, the system of equations remains highly complex, and its applicability is limited to just one working medium.

Another option for modelling the two-phase system is to use a mixing approach, which is particularly common for flows with low wetness fractions. If the dispersed phase is described in a Lagrangian frame of reference, it is possible to subdivide the numerical solution procedure into conservation and transport equations. The methods for determining the convective flux for single-phase flows can be applied to the system of conservation equations. The quantities characterising the liquid phase are determined either using source terms [50] or by coupling a separate system of equations [53]. In both cases, no adaptation of the flux calculation scheme is necessary, which preserves the robustness of the single-phase method. A description of the dispersed phase in an Eulerian frame of reference also increases the number of equations to be solved when applying the mixing approach. At the same time, however, considering velocity differences between the phases and parallelisation of the calculation method is simplified. By modelling the droplet size distribution using statistical moments as proposed by Hill [72] for the formation of a liquid dispersed phase, the number of additional equations can be significantly reduced compared to a discrete droplet size distribution. Irrespective of this, however, there is a need to adapt the method for determining the convective flux terms. Halama et al. [67] formulate such an adaptation for a thermally perfect gas, while Zhu et al. [175] strive for an adaptation that is independent of the equation of state. In both cases, the complete system of equations is taken into account. Analogous to the challenges discussed in the context of *two-fluid* models, this prevents the application of equations of state of high complexity. For a perfect gas, Mei and Guha [98] present a simplification of the system of equations. Only the differential equation of the wetness fraction remains in the main equation system, while the remaining three differential equations of the moments are solved separately. The coupling of the two systems can be ensured by the wetness fraction.

The extensions of Roe schemes documented in the literature for application to two-phase flows of non-ideal fluids are significantly limited by two criteria. These are the restriction to describing the dispersed phase in a Lagrangian frame of reference and a conflict of objectives between the lowest possible complexity of the system of equations and the simultaneous use of highly complex equations of state. Therefore, this thesis aims to present an approach that can be applied to both Eulerian and Lagrangian frames of reference and minimises the formulation's complexity, irrespective of the equation of state selected. Here, the accuracy and robustness of the method are significantly influenced by the numerical implications of the occurrence of phase change processes.

2.3 Special Requirements for Numerical Schemes in the Context of Phase Change Processes

When solving the Riemann problem described above, the thermodynamic states in two spatially neighbouring volumes are considered. If there are large local gradients near their interface, special requirements arise for the solution method. For substantial spatial and temporal differences in the conservation quantities of the flow, numerical oscillations may occur during the iterative solution, which jeopardise convergence and, thus, stability. In addition to approaches to avoid or attenuate such oscillations using so-called *limiter*, which limit the maximum permissible change, the approach chosen to determine the convective flux terms itself also influences the method's stability. In the case of single-phase flows of non-ideal fluids, large gradients are found in the flow field, especially for changes of state in the immediate vicinity of the critical point as well as the dew line as well as in the vicinity of discontinuities such as shock fronts.

Phase change processes from the gaseous to the liquid phase are often initiated in turbomachinery by spontaneous homogeneous nucleation. A liquid dispersed phase is formed in a very short time interval. Due to the differences in the thermophysical properties of liquid and gaseous media, this mechanism also leads to locally large gradients. The spatial extent of their occurrence is referred to as a condensation front. Its propagation speed is directly dependent on the speed of sound, which, according to Guha [62], is not uniquely defined for a two-phase flow in the absence of thermodynamic equilibrium. Since the speed of sound plays a central role in solving the Riemann problem, its modelling is particularly important.

To model the phase change process as accurately as possible concerning the condensation front, the flux calculation scheme must be robust against numerical oscillations analogous to discontinuities in single-phase flows. On the other hand, it must allow a description of the state quantities and, in particular, the speed of sound of the non-ideal fluid for both phases with high accuracy. Due to the specific suitability of the approach according to Roe for the description of shocks and the extension of this approach for arbitrary non-ideal fluids in terms of the GIRoe scheme, the present work aims at a further numerical generalisation with regard to the modelling of phase change processes of varying complexity.

3 Thermodynamic Description of Compressible Non-Ideal Fluids

To be able to describe the thermodynamic properties of compressible non-ideal fluids, it is first necessary to introduce basic terms and concepts. For this purpose, except for the representations used in Chapter 3.5, only fluid-unspecific representations are shown. As the working media analysed in this work are all pure substances, the occurrence of chemical reactions can be negated. However, intermolecular interactions can occur between the molecules of a pure substance. The strength of the forces causing these interactions is central to the definition of the term *fluid*. In the case of a solid, the forces prevailing between the molecules are so strong that they arrange themselves in a spatial grid and thus assume an almost stationary position. Between the molecules of a liquid, on the other hand, there are significantly lower forces that allow relative movement while maintaining the relative distance to the next molecule. The relative distance between two gas molecules is even variable due to very small intermolecular interactions. A fluid is a substance whose intermolecular interactions enable a relative movement of the molecules. As a result, liquid and gaseous substances can be summarised under the term fluids. Solids form the complement of fluids [71].

In addition to the microscopic approach used in the above definition, a macroscopic description of fluids is also possible. In this case, a defined volume is considered rather than a specific number of molecules as before. The choice of the size of this volume is limited by a lower and an upper threshold case. If the volume is chosen too small, the observed properties of the fluid are subject to statistical fluctuations due to molecular movements across the volume limits. If the volume is too large, on the other hand, spatial changes in fluid properties are no longer adequately resolved. Continuum theory postulates a homogeneous distribution of fluid properties within the volume for a volume whose size is chosen so that it just exceeds the lower limiting case. This volume thus forms the smallest possible macroscopic representation of the fluid and can also be described as an infinitesimal fluid element. Each physical volume in space can be interpreted accordingly Figure 1 as a finite set of fluid elements, whereby the properties of the fluid can be determined for any point in space. [83]

If the boundaries of a thermodynamic system are chosen so that they exactly enclose a fluid element, the thermodynamic properties of the fluid can be quantified using physical quantities. The system is in a well-defined thermodynamic state if this state can be described unambiguously at any time by an independent set of variables [10]. Such variables are then also referred to as state quantities, whereby a distinction can be made between extensive and intensive quantities. Intensive state quantities are characterised by the fact that their values

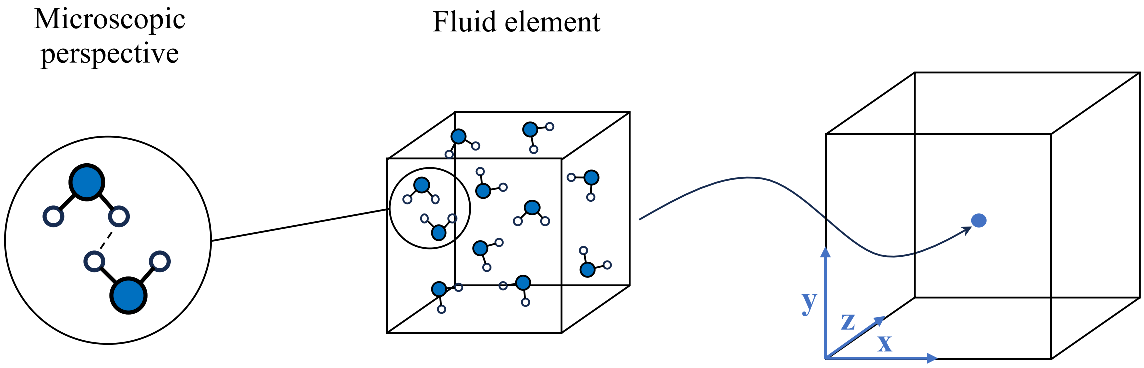

Figure 1: Different perspectives on the concept of a fluid

are independent of the size of the homogeneous system. The two best-known representatives of intensive state quantities are the pressure p and the temperature T. [139]

As a fluid element always has a homogeneous distribution of fluid properties by definition, it can also be classified as a phase, according to Gibbs [51]. If there is more than one phase within the system boundaries, the system is described as heterogeneous due to the abrupt changes in thermodynamic properties at the phase boundaries. Three criteria must be met for the phases of such a heterogeneous system to be in thermodynamic equilibrium. Therefore, the two phases have the same temperature and are in thermal equilibrium. In addition, there is mechanical equilibrium between the phases in that the pressure of the phases is the same. Finally, the chemical potentials μ of the two phases are the same, so a material equilibrium prevails. [10]

For a system that is in such a thermodynamic equilibrium, Gibbs [51] derives an equation to determine the degrees of freedom of the system:

$$F = C + 2 - P \tag{3.1}$$

The degree of freedom of the system F is determined by the number of components in the system C and the number of phases present P. This work considers only single-component systems so that C takes the value one. This results in a degree of freedom of two for single-phase systems, while two-phase systems only have a degree of freedom of one.

The degree of freedom can be interpreted using the phase diagram in Figure 2. First, however, the characteristic points and lines of the phase diagram should be briefly explained. Figure 2 shows a plot of the reduced pressure p_r against the reduced temperature T_r for an exemplary single-component system. The three phases, solid, liquid, and gaseous, in which the fluid can exist, are shown as surfaces. The boundary curves between the phases represent the respective phase equilibria at which coexistence of the two neighbouring phases is possible. The melting curve separates the solid from the liquid phase, while the sublimation curve separates the solid from the gaseous phase. The vapour pressure curve separates the liquid phase from the gaseous phase and is therefore the most relevant for the investigation of fluids.

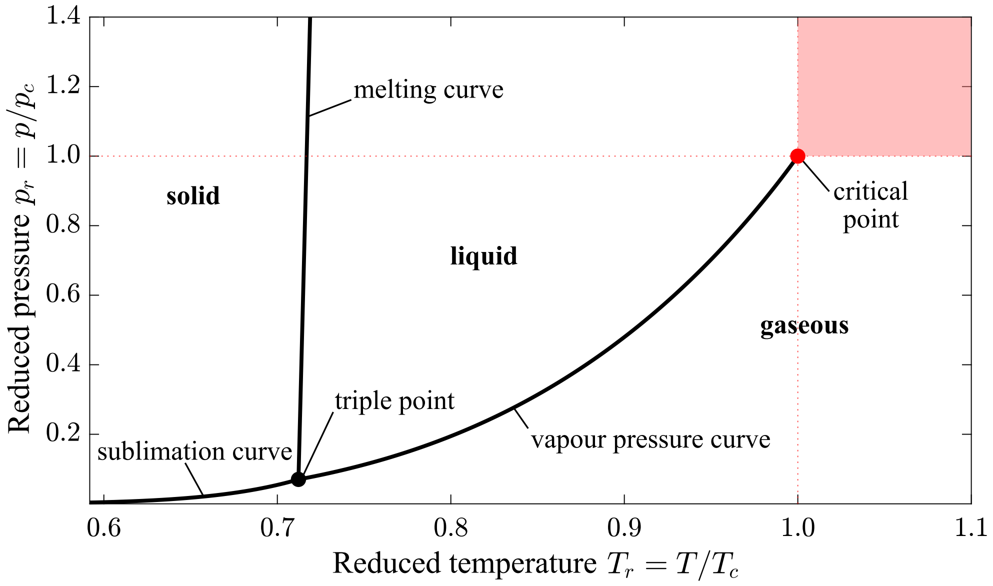

Figure 2: Phase diagram of a pure substance in reduced representation

Its beginning is defined by the triple point at which all three phases are in thermodynamic equilibrium. The end of the vapour pressure curve is marked by the critical point, whose state quantities are indicated by the letter c. Thermodynamic states with a reduced pressure and a reduced temperature greater than one are referred to as supercritical. As explained in detail in the next section, they cannot be definitively assigned to either the liquid or gaseous phase due to the lack of a defined phase boundary. [174]

If a single-phase system is considered, both the pressure and the temperature can be varied independently within the limits enclosing this phase. This corresponds to the degree of freedom of two previously determined using Equation 3.1. If, on the other hand, a heterogeneous system consisting of two different phases is considered, a thermodynamic equilibrium only exists between the two phases if the state of the system lies on the curve separating the phases. As this boundary curve forms a relationship between pressure and temperature, only one of the two intensive state quantities can be freely selected, which results in a degree of freedom of one. If a state is reached that is no longer on the boundary curve, a coexistence of the two phases is no longer possible. There is then a phase transition to the phase in which the system's current state lies.

3.1 Thermodynamic Ranges of State and Their Characteristics

In order to define the thermodynamic state of a single-phase system, an extensive quantity is required in addition to two intensive state quantities. This quantity, which is often represented by the mass m or the volume V, only describes the system's spatial size. If the system volume is divided by its mass, this results in a further intensive state quantity, the specific volume v. The reciprocal of the specific volume is known as the density ρ. As two independent intensive state quantities define the intensive state of a single-phase system, there must be a mathematical relationship between the pressure, the temperature, and the specific volume:

$$T = \mathscr{F}(v, p) \tag{3.2}$$

Equation 3.2 defines the temperature as a function of pressure and specific volume and is therefore referred to as the thermal equation of state. The variables contained in it are also called thermal state quantities. In Figure 3, this relationship is shown by means of a p-v diagram. Three selected isotherms visualise the temperature. In addition to the critical isotherm ($T_r = 1$), the curve of a subcritical and a supercritical isotherm is shown. The boundary between the liquid and gaseous phases does not take the form of a line but that of a surface, also known as a two-phase region. Within the two-phase region, assuming thermodynamic equilibrium for the mixture of liquid and gaseous phase, there is a clear relationship between pressure and temperature, which is already known from the vapour pressure curve in Figure 2. The boiling line delimits the two-phase region towards the liquid phase, while the dew line forms the boundary to the gaseous phase. The liquid phase near the boiling line is also referred to as subcooled liquid, the gaseous phase in the vicinity of the dew line as superheated vapour. The point at which the boiling line and the tau line meet is the critical point. The isotherm of the reduced temperature of one consequently runs through this point. Suppose the pressure of a system in a gaseous state is raised along a subcritical isotherm ($T_r < 1$). In that case, the system enters the two-phase region when the vapour pressure is reached, forming a liquid phase. The physical processes that characterise this phase transition are described in detail in Chapter 3.4. It should be noted that a further change

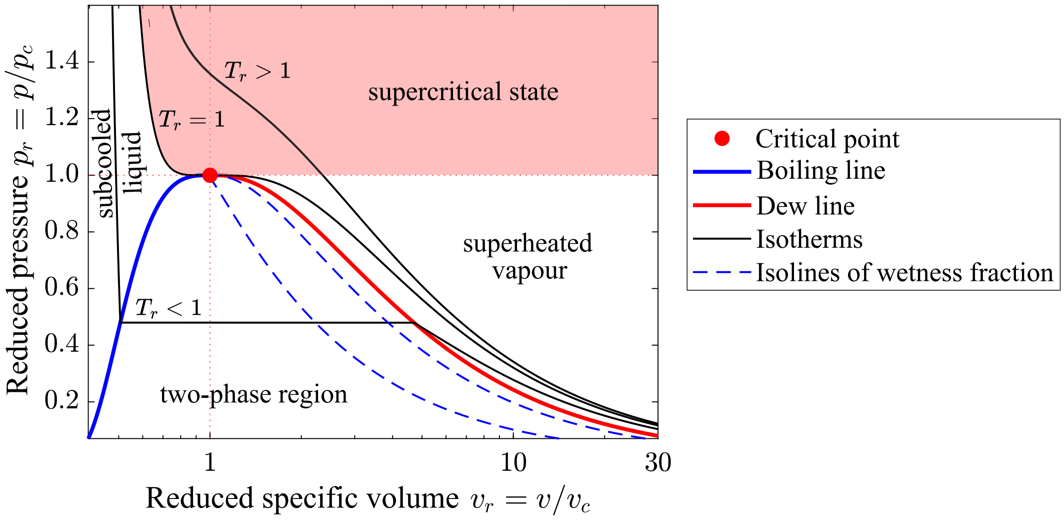

Figure 3: Ranges of state of a fluid in a reduced *p*-*v* diagram

in pressure cannot achieve the crossing of the two-phase region along the isotherms. Since pressure and temperature are not independent in the two-phase region, an additional quantity must be used to define the state. Besides the specific volume, the vapour quality x or its reciprocal value the wetness fraction y is often used for this purpose. Therefore, exemplary isolines of the wetness fraction are also shown in Figure 3. An increase in pressure within the system along a supercritical isotherm ($T_r > 1$), on the other hand, does not lead to an entry into the two-phase region. When the critical pressure is exceeded, the system reaches a state known as supercritical. Besides describing the system using thermal state quantities, caloric state quantities can also be used for this purpose. These are variables that represent the energy contained in the system. A link between a caloric quantity and two thermal state quantities is known as a caloric equation of state:

$$e = \mathscr{F}(v,T) \tag{3.3}$$

The specific energy e of the system can be formulated in this way using the specific volume and the temperature. A differentiation of Equation 3.3 yields:

$$de = \left(\frac{\partial e}{\partial T}\right)_v dT + \left(\frac{\partial e}{\partial v}\right)_T dv \tag{3.4}$$

The exact differential is divided into two terms, each containing a differential coefficient. Assuming a change of state at constant volume, the second term in Equation 3.4 is omitted. The remaining differential coefficient is also referred to as the specific isochoric heat capacity c_v and is another quantity characterising the state of the system:

$$c_v = \left(\frac{\partial e}{\partial T}\right)_v \tag{3.5}$$

In addition to the specific internal energy, the specific enthalpy h is also one of the caloric state quantities. It results from the addition of the specific energy and the product of pressure and specific volume:

$$h = e + pv = \mathscr{F}(p,T) \tag{3.6}$$

Enthalpy can also be described by means of a caloric equation of state as a function of two thermal state quantities. A differentiation analogous to Equation 3.4 leads to the definition of another state quantity, the specific isobaric heat capacity c_p:

$$c_p = \left(\frac{\partial h}{\partial T}\right)_p \tag{3.7}$$

The second law of thermodynamics introduces the concept of entropy to assess the reversibility of changes of state. The specific entropy s is a state quantity often considered separately from the classical thermal and caloric state quantities. If the entropy is formulated as a function of two thermal state quantities, this relationship is referred to as an entropy equation of state:

$$s = \mathscr{F}(p,T) \tag{3.8}$$

To fully describe the thermodynamic properties of a system, a set of thermal, caloric and entropy equations of state can be used. According to Gibbs, an equation that combines the three types of equations of state in a single formulation is known as a fundamental equation:

$$e = \mathscr{F}(s,v) \tag{3.9}$$

Two other fundamental equations, which are at the centre of the following considerations, can be derived by applying a Legendre transformation [9] to Equation 3.9:

$$f = \mathscr{F}(v,T) = e - Ts \tag{3.10}$$

$$g = \mathscr{F}(p,T) = h - Ts \tag{3.11}$$

Here, f denotes the specific Helmholtz energy, while g defines the specific Gibbs energy. The chemical potential introduced in the context of the definition of thermodynamic equilibrium is identical to the molar Gibbs energy in the case of a single-component system. Therefore, the classification of phase transitions according to Ehrenfest can be formulated in the present case using the differentials of the Gibbs energy [81]. Following Ehrenfest [42], a first-order phase transition is present if a discontinuity is formed for one of the first partial derivatives of the Gibbs energy at the phase boundary. According to Table 1, the first-order derivatives of the Gibbs energy can be expressed by the specific volume and the entropy.

In Figure 3, such a discontinuity of the specific volume is recognisable in the form of the subcritical isotherms ($T_r < 1$) running vertically in the two-phase region. Therefore, the order of the phase transition between the gaseous and the liquid phase along the vapour pressure curve is one. According to Ehrenfest's classification, a second-order phase transition is present if the first-order derivatives do not show any discontinuity but the second-order derivatives do. A second-order phase transition can thus be identified according to Table 1 on the basis of a

Table 1: First and second order derivatives of the specific Gibbs energy

First order	$\left(\frac{\partial g}{\partial p}\right)_T = \mathbf{v}$		$\left(\frac{\partial g}{\partial T}\right)_p = -\mathbf{s}$
Second order	$\left(\frac{\partial^2 g}{\partial p^2}\right)_T = -v\kappa_\mathbf{T}$	$\left(\frac{\partial^2 g}{\partial T^2}\right)_p = -\frac{\mathbf{c_p}}{T}$	$\left(\frac{\partial^2 g}{\partial p \partial T}\right) = v\alpha_\mathbf{p}$

discontinuity in the specific isobaric heat capacity, the isothermal compressibility κ_T or the thermal isobaric expansion coefficient α_p. According to Ansermet and Brechet [6], such a discontinuity exists at the critical point. The description of the supercritical state with regard to the phases present thus requires detailed consideration.

Supercritical range of state

In the supercritical range of state, it is no longer possible to distinguish between the liquid and gaseous phases due to the lack of a first-order phase transition. However, both experimental (see [109], [133]) and theoretical (see [45], [23]) investigations show that liquid-like and gas-like states can be distinguished in this range. According to Banuti et al. [16], the approaches to distinguishing states in the literature can be divided into microscopic and macroscopic descriptions.

The methodology for analysing the types of states at the microscopic level is based on molecular motion. As already mentioned in the definition of the term fluid, there are stronger intermolecular interactions between the molecules of a liquid phase than in the gas phase. As a result, gas molecules move along a straight trajectory until they collide with another gas molecule. The movement of the molecules in the liquid phase, on the other hand, is dominated by the stronger intermolecular forces. This results in a diffusive movement similar to the movement of gas molecules and an oscillatory behaviour similar to that of solids [28]. An increase in temperature or a decrease in pressure leads to a decrease in the relaxation time, which is a parameter for describing the characteristics of these oscillations [23]. If the relaxation time approaches its minimum, the oscillatory component of the molecular motion is eliminated. The state points, which are characterised by a minimum of the relaxation time, offer a possibility to define the so-called Frenkel line [28]. In addition to this formulation, there are also approaches that describe the points of the Frenkel line using a relationship between the isochoric heat capacity of an atom and the Boltzmann constant k_b [24]. However, according to Pipich and Schwahn [117], different definitions and methods for determining the defining quantities also result in different curves of the Frenkel line. Irrespective of this, the Frenkel line allows fluid states to be classified even at a great distance from the critical point due to its definition for arbitrarily high pressures and temperatures.

For the description of supercritical states near the critical point, which are particularly relevant for this work, however, macroscopic approaches are mainly used. These investigate the pressure and temperature dependence of the formation of molecular clusters based on density fluctuations. According to Widom [166], the spontaneous density fluctuation can be used to describe the size of the clusters using a so-called correlation length. The local density fluctuates as a function of time around a certain mean value. The set of points in which the local density corresponds to this mean value at a certain point in time forms the basis of a geometric definition of the correlation length [127]. The second derivatives of the Gibbs energy form thermodynamic response functions of this correlation length. The link between the response functions and the subdivision of the supercritical range of states into liquid-like and gas-like states can be made using Figure 4.

In the left part of the figure, the reduced pressure is plotted against the reduced temperature for a region surrounding the critical point. The critical point marks the end of the vapour pressure curve and, thus, the section for which a distinction between the states is to be investigated using the response functions. If, as an example, a reduced pressure of $p_r = 1.2$

is selected, the first and second derivatives of the Gibbs energy can be determined along the reduced temperature. A plot of the quantities related to their respective maximum value occurring in the definition range over the reduced temperature can be found on the right-hand side of Figure 4. The curves of the first derivatives normalised in this way are shown in black on the left-hand ordinate, while the curves of the second derivatives are visualised in red on the right-hand ordinate. The curves of the specific volume and the specific entropy show no discontinuity in the temperature interval shown. This confirms the absence of a first-order phase transition in the supercritical state range. The second-order derivatives also show no discontinuity so that no second-order phase transition can be assumed. However, a maximum can be recognised for all three curves at a value of the reduced temperature of approximately $T_r = 1.03$. Determining these maxima for further values of the reduced pressure and plotting the resulting pairs of values in a pressure-temperature diagram leads to the so-called Widom lines [171]. Two Widom lines are shown in the left part of Figure 4.
The lower of the two curves represents the maxima of the specific isobaric heat capacity evaluated for different temperatures at constant pressure. If the maxima of the specific isobaric heat capacity are analysed for different pressures at constant temperature, a different shape of the Widom line results. As Brazhkin et al. [25] show, the curves also differ depending on the selected response function. The deviation between the Widom lines increases with the distance to the critical point. This also becomes clear for the two curves shown. Up to the point of intersection with the isobars selected as an example, the two Widom lines show a very similar shape but diverge as the distance from the critical point increases. Also, the response functions for arbitrarily high pressures and temperatures do not necessarily show corresponding maxima. The Widom lines are therefore not suitable for differentiating between the states at a large distance from the critical point, but provide sufficient information in the range shown. Consequently, the Widom line of the specific isobaric heat capacity is analysed at constant pressure for the further investigations in this work to subdivide the supercritical state region. The liquid-like states are labelled as liquid, and the gas-like states as gaseous, for clear naming, as illustrated in Figure 4.

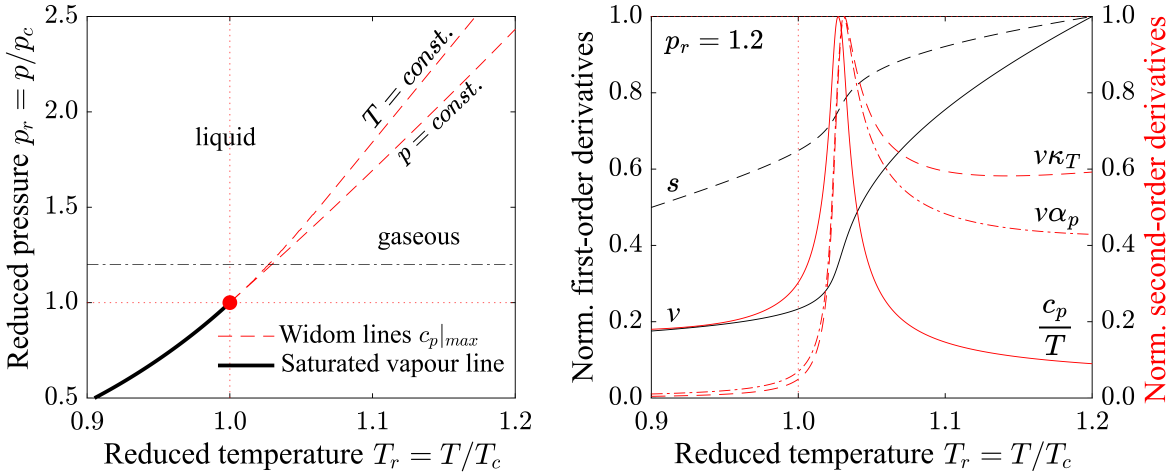

Figure 4: Subdivision of the supercritical range of states into liquid and gaseous (left) and curves of the derivatives of the Gibbs energy for a reduced pressure of $p_r = 1.2$ (right)

The states of the system considered so far are all characterised by the existence of a stable thermodynamic equilibrium. The term stable characterises a state of equilibrium that returns to its original state following a disturbance. On the other hand, an unstable thermodynamic equilibrium exists when a disturbance of the system leads to a permanent change in the state. Two influencing factors play a unique role in distinguishing between stable and unstable equilibrium states. Firstly, the extent of the disturbance must be assumed to be relatively small, as otherwise, all real equilibrium states could be classified as unstable. Secondly, the time scale on the basis of which the system behaviour is observed must be selected according to a time scale characteristic of the system. If an equilibrium state is only stable for very small perturbations and time scales, it is referred to as metastable. Since metastable states are particularly present in the context of phase change processes, a detailed consideration of the metastable range of states is necessary for further explanations.

Metastable range of state

According to Gibbs [51], a stable thermodynamic equilibrium exists when the system is in a state of maximum entropy. Such a global maximum of entropy is equivalent to a global minimum of Gibbs energy [38]. Equilibrium states in which there is a local minimum of Gibbs energy are referred to as metastable. If a small and very short-lasting disturbance occurs in such a system, the system returns to its original metastable state [10]. However, if the perturbation is more significant or lasts longer, the system returns to a stable thermodynamic state. Mathematically, the existence of a minimum of a function is defined by a necessary and a sufficient criterion:

$$\begin{aligned} \delta g\big|_{p,T} &= 0 && \text{Necessary criterion} \\ \delta^2 g\big|_{p,T} &> 0 && \text{Sufficient criterion} \end{aligned} \tag{3.12}$$

The sufficient criterion can also be formulated as follows using Table 1:

$$\delta^2 g\big|_{p,T} = \left(\frac{\partial^2 g}{\partial p^2}\right)_T = -v\kappa_T = \left(\frac{\partial v}{\partial p}\right)_T = -\left(\frac{\partial p}{\partial v}\right)_T > 0 \qquad \Leftrightarrow \qquad \left(\frac{\partial p}{\partial v}\right)_T < 0 \tag{3.13}$$

A state of stable or metastable equilibrium of a phase thus exists if the pressure decreases with increasing specific volume along an isotherm. A graphical interpretation of this definition can be made using Figure 5. The sufficient criterion from Equation 3.13 is fulfilled for all liquid and gaseous state points along the isotherm shown. Beyond the two-phase region, only stable states are found. It should be noted that the isotherm is extrapolated into the two-phase region to illustrate the validity of the stability criterion for metastable states beyond the boiling or dew line. The black dashed lines can thus be physically interpreted as spontaneous changes of state on a very short time scale. This corresponds to the definition of the metastable state according to Skripov [134], which assumes a crossing of the vapour pressure curve without the onset of a phase change. As soon as the partial differential from Equation 3.13 reaches a value of zero, an unstable state is present, which is exclusively theoretical due to the endeavour of every system to reach a stable equilibrium state.

The resulting criterion for distinguishing between metastable and unstable states can also be formulated based on isothermal compressibility:

$$\delta^2 g\big|_{p,T} = \left(\frac{\partial^2 g}{\partial p^2}\right)_T = -v\kappa_T = 0 \qquad \Leftrightarrow \qquad \kappa_T = 0 \tag{3.14}$$

The line connecting all state points that fulfil this criterion is referred to as spinodal or spinodal limit. There is one such limit for the liquid phase and one for the gaseous phase. The state region of the metastable liquid phase can be identified in Figure 5 as the blue area between the boiling line and the spinodal limit of the liquid phase. Similarly, the metastable gas phase can be found in red between the dew line and the spinodal limit of the gas phase. The area within the two-phase region that lies beyond the boundaries of the metastable state regions is called the unstable region [30]. In this region, the separate existence of one of the two phases is impossible, even for a short time.

It can be observed that the boundaries of the metastable state regions approach the boundaries of the two-phase region with increasing pressure. At the critical point, the spinodal limits of the liquid and gas phases meet the boiling and dew line. In the immediate vicinity of the critical point, the extent of the metastable state regions thus tends towards zero.

In the supercritical range, the fluid states can be divided into liquid and gaseous according to the definition of the Widom line given above. However, the existence of a spinodal limit according to Equation 3.14 beyond the critical point can neither be found in the right part of Figure 4 nor in the literature (cf. [23]). Also, the strictly monotonically decreasing course of the supercritical isotherm in Figure 3 does not indicate a violation of the criterion from Equation 3.12, so that the supercritical range of states can be assumed to be thermodynamically stable.

All state quantities introduced so far in this subchapter can be uniquely defined, taking into account the respective phases present in the entire range of states of the fluids. This does not apply to the state quantity of the speed of sound, so its definition requires a detailed description.

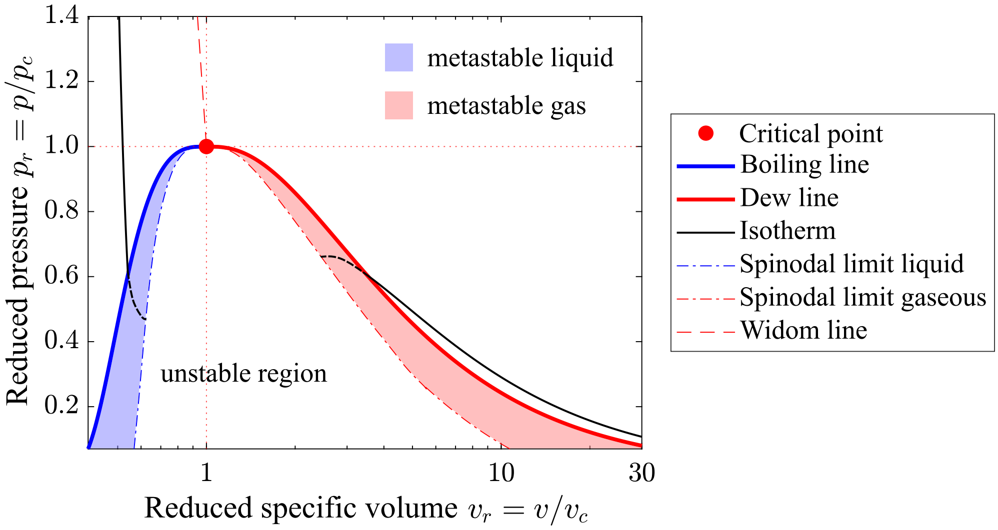

Figure 5: Distinction between meta and unstable states in a reduced *p*-*v* diagram

Definition of speed of sound

The speed of sound a describes the speed of propagation of a sound wave in a medium. According to Baehr and Kabelac [10], a sound wave is a periodic longitudinal pressure and density fluctuation of small amplitude. Similar to the consideration of metastable states, the speed of sound relates to a disturbance occurring in the system. It is assumed that two properties characterise this disturbance. Firstly, the magnitude of the pressure fluctuation is much smaller than the value of the equilibrium pressure of the system, so that the disturbance has a sufficiently small amplitude. Secondly, the short-term change in state caused by the fluctuation should be reversible. A wave characterised in this way propagates in the fluid through the collision of moving molecules. Intermolecular interactions between the molecules subsequently have a strong influence on the speed of sound [49]. Due to the postulated reversibility, the propagation of the disturbance in the fluid can be modelled as an isentropic process. Under this assumption, the thermodynamic state of the system and the sound wave itself are not influenced by the propagation. The speed of propagation of a sound wave modelled in this way defines the isentropic speed of sound:

$$a = \sqrt{\left(\frac{\partial p}{\partial \rho}\right)_s} \tag{3.15}$$

Based on this formulation as a function of two independent intensive quantities, the association of the speed of sound with the thermodynamic state quantities becomes obvious. An evaluation of the expression in Equation 3.15 is initially conceivable for any fluid state. However, suppose a second phase is formed, as is possible for states within the two-phase region. In that case, the above modelling of wave propagation is not necessarily sufficient due to the system's heterogeneity. As according to Radovskii [120], the propagation of the sound wave in such a system is additionally influenced by the interaction of the phases, it is recommended to take this into account for modelling. He specifies the interaction as the simultaneous occurrence of phase change processes, heat transfer, and momentum exchange between the phases. Petr [113] describes these processes induced by the propagation of the sound wave as irreversible. Depending on its frequency, the acoustic wave thus causes different degrees of disturbance to the thermal and mechanical equilibrium within the system. According to Bakhtar et al. [14], the reciprocal interaction of the sound wave and the two-phase mixture can also influence the stability of the thermodynamic equilibrium. The determination of the speed of sound for states within the two-phase region is, therefore, directly dependent on the phase change processes that occur. A detailed analysis is hence carried out in the context of the numerical application.

3.2 Mathematical Description of State Quantities

So far, the thermodynamic state quantities have only been described using symbolic relationships. However, in order to be able to calculate the state of a fluid as part of numerical investigations, it is necessary to introduce concrete modelling. The derivation of a definition of compressible non-ideal fluids should take the form of a successive delimitation.

A fluid is described as incompressible if its specific volume remains almost constant under the influence of an external force or pressure.

$$v = const. \tag{3.16}$$

Consequently, there is no pressure or temperature dependence of the specific volume or the density. The isothermal compressibility of a fluid modelled in this way also takes on the value zero. The model of the incompressible fluid represents a strong idealisation, which is mainly applied to liquids. Therefore, a fluid is described as compressible if the model of the incompressible fluid cannot suitably describe it. The specific volume of compressible fluids has to be determined as a function of pressure and temperature. [139]

Model of perfect gas

Another substantial simplification of real fluids is the model of perfect gases. According to its name, this can be applied to gaseous fluids whose state is characterised by a very low static pressure. The thermal equation of state of perfect gases is also known as the law of ideal gases:

$$pv = R_sT \qquad \text{with} \qquad R_s = \frac{R}{M} \tag{3.17}$$

The quotient of the universal gas constant R and the molar mass M defines the specific gas constant R_s. The law of ideal gases combines the laws of Boyle-Mariotte, Charles, and Avogadro, whereby the first two are only valid for $p \rightarrow 0$. Boyle-Mariotte's law is based on three assumptions of the kinetic theory of gases, which can, therefore, also be used to specify the model of perfect gases at the molecular level. Accordingly, the gas consists of molecules that move in random directions in space. In addition, the size of the molecules can be neglected due to their relative spatial distance from each other. Ultimately, the interaction between the molecules is limited to elastic collisions, which can be interpreted as a negation of intermolecular interactions. [8]

The caloric equation of state of perfect gases can be derived using Equation 3.4. As Gay-Lussac and Joule experimentally prove, the specific internal energy of perfect gases at constant temperature shows no dependence on the specific volume. Accordingly, the second differential coefficient can be set to zero, and the result is:

$$de = c_v dT \tag{3.18}$$

By combining this equation with a reformulation of Gibbs' fundamental equation from Equation 3.9, the change in entropy of a perfect gas can be written as follows:

$$ds = \frac{1}{T}de + \frac{p}{T}dv = c_v\frac{dT}{T} + R_s\frac{dv}{v} \tag{3.19}$$

The equations of state of the perfect gas can thus be completely defined on the basis of a specific heat capacity and the specific gas constant. From the definition of enthalpy in Equation 3.6, a further relation characteristic of a perfect gas can also be derived:

$$c_p = R_s + c_v \tag{3.20}$$

The definition of specific heat capacities leads to a subdivision of the model of perfect gases into two groups. A gas is described as calorically perfect if its specific heat capacities assume a constant value for any temperature. The monatomic noble gases can be described with sufficient accuracy using this model assumption. However, if the specific heat capacities are temperature-dependent, the gas modelled this way is described as thermally perfect. It should be noted that this distinction does not affect the validity of the law of ideal gases.
The derivation of an expression for the speed of sound of perfect gases uses the formulation of Gibbs' fundamental equation from Equation 3.19, whereby the specific enthalpy is used as the caloric defining quantity instead of the specific internal energy. Inserting Equation 3.17 and Equation 3.20 into this equation under the isentropic assumption valid for the speed of sound results in:

$$0 = c_v \frac{dp}{p} + c_p \frac{dv}{v} \qquad \Leftrightarrow \qquad \frac{dp}{p} = -\frac{c_p}{c_v}\frac{dv}{v} = -\kappa \frac{dv}{v} \tag{3.21}$$

The ratio of specific isobaric and isochoric heat capacity is referred to as the isentropic exponent of the perfect gas κ. A reformulation of the definition of the speed of sound from Equation 3.15 with regard to the specific volume in combination with Equation 3.21 leads to an expression for the isentropic speed of sound of perfect gases:

$$a = \sqrt{-v^2 \left(\frac{\partial p}{\partial v}\right)_s} = \sqrt{\kappa p v} = \sqrt{\kappa R_s T} \tag{3.22}$$

This formulation shows that knowledge of the static temperature is sufficient to determine the speed of sound of a perfect gas. If the state quantities of a fluid are all known, the deviation from the model of perfect gases can be quantified using a rearrangement of Equation 3.17:

$$Z = \frac{pv}{R_s T} \tag{3.23}$$

A compressibility factor Z of one thus indicates complete agreement with the model assumptions of the perfect gas. However, most fluids show a deviation of the compressibility factor from one, at least in parts of their region of state. For this reason, van der Waals [157] developed the first thermal equation of state, which, on the one hand, allows such a deviation from the model of the perfect gas and, on the other hand, can describe both liquid and gaseous states.

Cubic equations of state

The van der Waals equation of state is the best-known representative of the so-called cubic equations of state. The name of this group of model equations is based on their property that a rearrangement to the specific volume results in a third-degree function. The deviation from the model of perfect gases is taken into account through correction factors:

$$\left(p + \frac{a}{v^2}\right)(v - b) = RT \tag{3.24}$$

The coefficients a and b are called van der Waals coefficients. A comparison of the structure of Equation 3.24 and Equation 3.17 allows a physical interpretation of the correction factors. The term a/v^2 represents the consideration of intermolecular forces and is also referred to as cohesive pressure. The coefficient b represents a correction for the volume of the molecules and is therefore also known as the covolume. Other representatives of the cubic equations of state, such as the approaches according to Peng-Robinson or Soave-Redlich-Kwong, introduce an additional correction factor. This acentric factor takes into account a deviation of the molecular structure from the shape of a sphere. An exemplary van der Waals isotherm is shown in Figure 6 in comparison to the hyperbola that characterises the law of ideal gases. Unlike the isotherm of the perfect gas, the van der Waals isotherm passes through the two-phase region. Therefore, a distinction between liquid and gaseous states requires a definition of the boiling and dew line. This can be done using a criterion named after Maxwell:

$$g_{s,l} = g_{s,g} \qquad \Leftrightarrow \qquad p_s(v_{s,g} - v_{s,l}) = f_{s,l} - f_{s,g} = \int_{v_{s,l}}^{v_{s,g}} p\,dv \tag{3.25}$$

As introduced above, the Gibbs energies of the liquid and gaseous phases are equal along the vapour pressure curve for a one-component system in thermodynamic equilibrium. States along the vapour pressure curve are also referred to as saturation states and are indexed below by a s in combination with the phase. Quantities of the liquid phase have the index l, while the index g characterises the gas phase. According to the expression in Equation 3.25, the saturation vapour pressure can be determined iteratively using a geometric construction. The area below the isobaric connection line between the specific volume of the saturated liquid and that of the saturated gas phase must equal the area below the van der Waals isotherms in this volume interval [129]. This is equivalent to an equality of the areas coloured grey in Figure 6. The only isobar that fulfils this criterion is that of the saturation vapour pressure, meaning that it is uniquely defined by the Maxwell criterion. The Maxwell criterion is a generally necessary criterion for the formulation of thermal equations of state, which should be valid in the entire state region of a fluid [10]. This becomes particularly relevant in the context of multi-parameter equations of state.

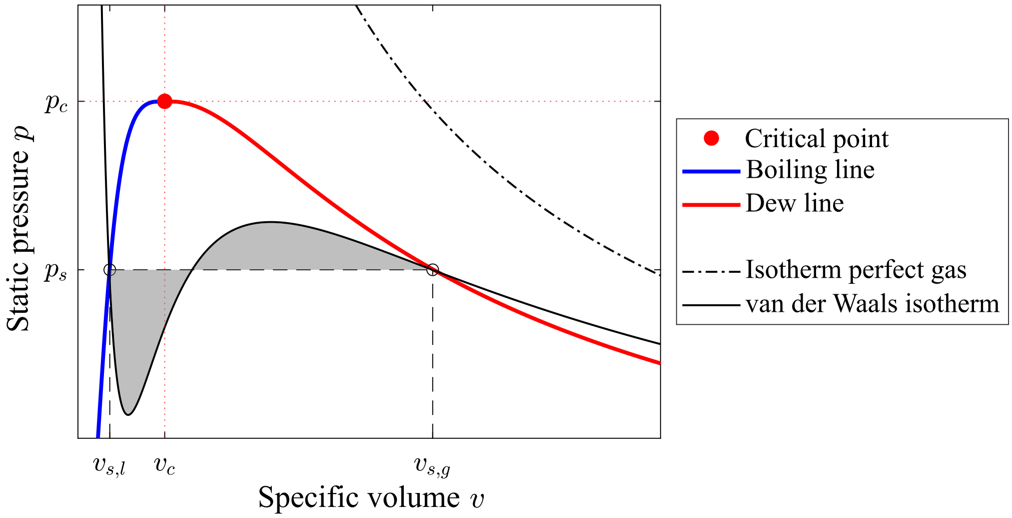

Figure 6: Comparison of the model of perfect gases and the van der Waals equation of state using isotherms in a p-v diagram

Multi-parameter equations of state

While the law of ideal gases and the cubic equations of state are physical modelling approaches for describing the thermal state quantities of the fluid, multi-parameter equations of state are fundamental equations that are approximated on the basis of experimental data. Pollak [118] formulates the first such fundamental equation, which is defined for the entire state region of a fluid for the medium water:

$$\Phi = \frac{f}{R_s T} \tag{3.26}$$

For this purpose, he introduces the dimensionless parameter Φ, referred to as the dimensionless Helmholtz energy. Splitting this parameter into two terms results in:

$$\Phi(\delta,\tau) = \Phi^0(\delta,\tau) + \Phi^r(\delta,\tau) \qquad \text{with} \qquad \delta = \frac{v_c}{v} = \frac{\rho}{\rho_c} \qquad \wedge \qquad \tau = \frac{T_c}{T} \tag{3.27}$$

Here, Φ^0 describes the so-called ideal part, while Φ^r represents the residual part of the dimensionless Helmholtz energy. According to the definition of the Helmholtz energy in Equation 3.10, this is formulated using the specific volume and the temperature. In Equation 3.27, the dimensionless density δ and the dimensionless temperature τ are therefore independent variables. Any state quantities of the fluid can be determined using expressions depending on the dimensionless Helmholtz energy and its derivatives. For example, the enthalpy can be written as:

$$h(\delta,\tau) = R_s T \left(1 + \tau(\Phi^0_\tau + \Phi^r_\tau) + \delta \Phi^r_\delta\right) \tag{3.28}$$

The use of τ as an index denotes the partial derivative with respect to the dimensionless temperature, while the partial derivative for the dimensionless density is indexed by δ. The Maxwell criterion from Equation 3.25 for defining the saturation quantities can also be expressed using the dimensionless Helmholtz energy and must be complied with when specifying the fundamental equation:

$$\frac{p_s}{R_s T}\left(\frac{1}{\rho_{s,g}} - \frac{1}{\rho_{s,l}}\right) - \ln\left(\frac{\rho_{s,l}}{\rho_{s,g}}\right) = \Phi^r(\delta_{s,l},\tau) - \Phi^r(\delta_{s,g},\tau) \tag{3.29}$$

In order to be able to evaluate this equation or Equation 3.28, explicit expressions for the ideal and the residual part of the dimensionless Helmholtz energy are required. The ideal part can be determined using the values of the specific enthalpy and the specific entropy in a state defined as a reference, as well as the temperature dependence of the specific isochoric heat capacity as a function of dimensionless temperature and density. The data required for this must be collected experimentally. The formulation of the residual part is also based on measurements of thermodynamic state quantities. However, the amount of data required is significantly larger than in the case of the ideal part, as not only the specific isochoric heat capacity must be considered, but almost all state quantities of the fluid. The function for the residual part of the fundamental equation determined from this approximation of the measured values is subsequently a polynomial of a higher degree. The inclusion of measurement data along the vapour pressure curve and in the immediate vicinity of the critical point has a considerable influence on the accuracy of the model.

In addition to such Helmholtz-based equations of state, it is also possible to formulate equations of state based on the Gibbs energy. This type of equation of state uses pressure and temperature as independent variables in accordance with the definition in Equation 3.11. The procedure for determining the functional relationship is the same as that described for Helmholtz-based approaches. However, a Gibbs-based equation of state is not able to cover the entire range of states of fluids, as pressure and temperature are not independent along the vapour pressure curve. In the context of fluids, Gibbs-based approaches can, therefore, only be found in combination with Helmholtz-based equations of state, whereby the region of state is divided into individual areas. [9]

The model types of equations of state presented in this subsection show that the complexity of the description of thermodynamic state quantities depends on the model. With an increasing number of parameters used to characterise the fluid, the accuracy of the description of the actual state increases. While the law of ideal gases only takes into account the molar mass of the fluid, cubic equations of state already utilise at least two fluid-specific parameters in the form of correction factors. Multi-parameter equations of state are based on the approximation of experimental data sets and consequently achieve the highest degree of accuracy. Accordingly, the state quantities resulting from their evaluation show a very high degree of agreement with the real thermodynamic quantities. However, their formulation is complex compared to the other two physical models. If fluids are analysed whose thermal state quantities can be described in good approximation by means of the law of ideal gases, it does not appear to make sense to use equations of state of higher complexity. However, if the state quantities calculated using the law of ideal gases show considerable deviations from the experimentally determined quantities, the fluids in the considered state range are labelled as non-ideal. Modelling of the thermal state quantities, which takes this non-ideality of the fluid into account, is then necessary. The extent of the deviation determines the complexity level of the equation of state to be selected.

3.3 Parameters for Classifying a Fluid as Non-Ideal

In order to quantify such a deviation and subsequently classify a compressible fluid as non-ideal, selecting suitable parameters is crucial. In addition to the thermodynamic properties of the fluid, it seems sensible to include the molecular structure as a criterion in the parameter selection. In this way, in addition to the assessment dependent on the state quantities, a categorisation based on material properties is also possible.

Compressibility factor

The compressibility factor, already defined in Equation 3.23, is the simplest way to quantify a deviation from the law of ideal gases. For this purpose, the terms of the left and right sides of the thermal equation of state of perfect gases are divided. The factor defined in this way takes the value one for a perfect gas. If the compressibility factor is determined for any given state of a fluid, it can have values both greater and less than one. To illustrate this, the compressibility factor for different reduced temperatures is plotted against the reduced pressure in Figure 7. Generally, gases at low pressures have a range of states in which the compressibility factor is approximately one. The interactions between the gas molecules are only very weak here due to the large relative distances between the molecules. On the other hand, compressibility factors greater than one can be detected for very high pressures, which indicates the presence of a larger specific volume than in the case of a gas modelled as perfect. This is due to the dominance of repulsive intermolecular forces in the high-pressure range, which can be attributed to the decrease in relative molecular distances with increasing pressure. In the transition range between low and high pressures, the compressibility factor shows a strong temperature- and fluid-dependent behaviour. While some fluids have compressibility factors greater than one for any temperature, most fluids have compressibility factors less than one at certain temperatures. For the latter group, attractive intermolecular forces dominate in a defined state range. [8]

In order to analyse the influence of temperature on the compressibility factor, it is helpful to make a division based on the critical isotherm, as described in Figure 7. As can be seen from the left-hand side of this figure, the compressibility factor increases with temperature at constant pressure in the supercritical case ($T_r > 1$). The formation of a transition region with compressibility factors less than one can only be observed up to a certain temperature, which is referred to as the Boyle temperature. Above this temperature, the profile of the compressibility factor along the pressure only shows values greater than one, as is also the case for the uppermost isotherm. The course of the critical isotherm ($T_r = 1$) is characterised by large gradients of the compressibility factor and represents the boundary to the subcritical isotherms ($T_r < 1$) in the right part of Figure 7. Unlike the supercritical isotherms, these have a discontinuity, which assigns two different compressibility factors to a pair of pressure and temperature and represents the two-phase region. The discontinuities of the isotherms can thus be used to define equivalent curves of the tau and boiling lines. The difference between the compressibility factors at the boundaries of the two-phase region decreases with increasing subcritical temperature and reaches a value of zero at the critical point. In the range of supercritical pressures, the subcritical isotherms tend towards the same value as the critical isotherm. Using Figure 7, it can be seen that the lowest compressibility factors of gaseous fluid states can be found in the immediate vicinity of the dew line and near the critical point. These areas are, therefore, particularly relevant for the investigation of compressible non-ideal fluids.

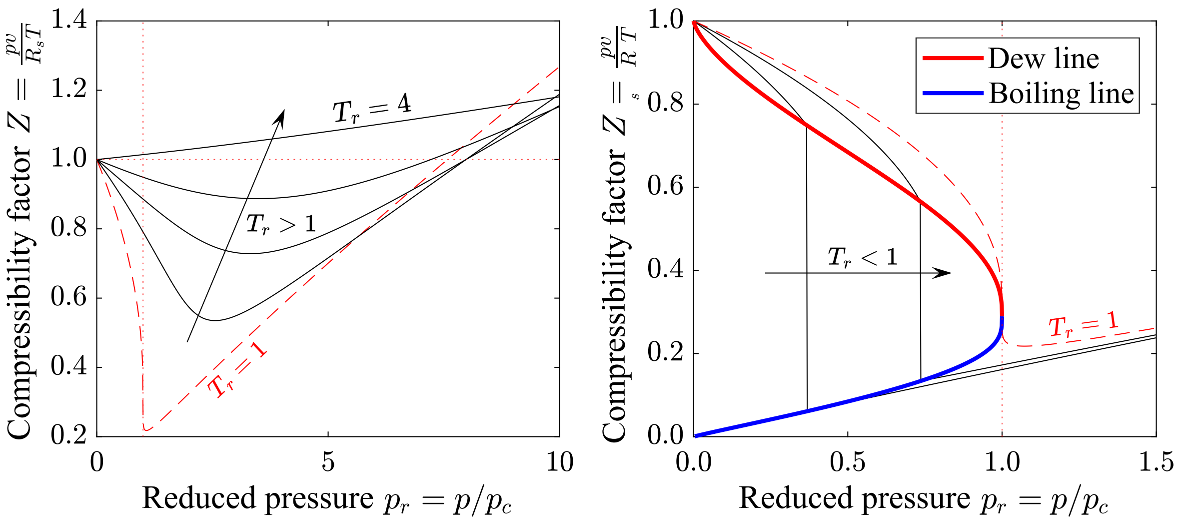

Figure 7: Graph of the compressibility factor over the reduced pressure for supercritical (left) and subcritical (right) isotherms

Isentropic pressure-volume exponent

Another parameter that can be used to classify a compressible fluid as non-ideal is the isentropic pressure-volume exponent κ_{pv}. According to Kouremenos and Kakatsios [85], this is an expression equivalent to the isentropic exponent of the perfect gas. If the entropy is expressed as a function of pressure and specific volume, an exact differential can be formulated:

$$ds = \left(\frac{\partial s}{\partial p}\right)_v dp + \left(\frac{\partial s}{\partial v}\right)_p dv \tag{3.30}$$

The isentropic change in pressure over the specific volume can be derived by applying the Maxwell relations [96] according to this equation:

$$\left(\frac{\partial p}{\partial v}\right)_s = -\frac{\left(\frac{\partial s}{\partial v}\right)_p}{\left(\frac{\partial s}{\partial p}\right)_v} = \frac{\left(\frac{\partial p}{\partial T}\right)_s}{\left(\frac{\partial v}{\partial T}\right)_s} = -\frac{c_p}{c_v}\left(\frac{\partial T}{\partial v}\right)_p\left(\frac{\partial p}{\partial T}\right)_v = \frac{c_p}{c_v}\left(\frac{\partial p}{\partial v}\right)_T \tag{3.31}$$

Using the definition of the isentropic exponent based on Equation 3.21, the isentropic pressure-volume exponent of non-ideal fluids can now be defined:

$$\kappa = -\frac{v}{p}\left(\frac{\partial p}{\partial v}\right)_s \quad \Leftrightarrow \quad \kappa_{pv} = -\frac{v}{p}\frac{c_p}{c_v}\left(\frac{\partial p}{\partial v}\right)_T = -\kappa\frac{v}{p}\left(\frac{\partial p}{\partial v}\right)_T \tag{3.32}$$

If the law of ideal gases is inserted into this expression, the isentropic pressure-volume exponent becomes the isentropic exponent of the perfect gas, which confirms the consistency of the method. Unlike the isentropic exponent of perfect gases, the value of the isentropic pressure-volume exponent varies along a change of state. Wheeler and Ong [161] therefore derive an alternative expression for the isentropic pressure-volume exponent, which describes the deviation from the isentropic exponent using a statistical correction factor. In order to quantify such a deviation, Giuffré and Pini [54] propose using an averaged value. Both the isentropic exponent and the isentropic pressure-volume exponent take on exclusively positive values due to their definition. However, the value range of the two exponents differs significantly. While the isentropic exponent adopts values greater than one in the entire range of states of a fluid, values less than one can also be observed for the isentropic pressure-volume exponent in the vicinity of the critical point. According to Tosto et al. [151], the deviation of the two exponents can be used as a measure of the non-ideality of a fluid. Deviations characterised by larger or smaller values of the isentropic pressure-volume exponent compared to the isentropic exponent must be considered equally.

Fundamental derivative of gas dynamics

A parameter closely related to the isentropic pressure-volume exponent is the fundamental derivative of gas dynamics Γ. This parameter defined by Thompson [146] is a dimensionless quantity for the curvature of the isentropes in a surface that is spanned by the pressure and the specific volume:

$$\Gamma = \frac{a^4}{2v^3}\left(\frac{\partial^2 v}{\partial p^2}\right)_s \tag{3.33}$$

Using the definition of the speed of sound in Equation 3.15, the fundamental derivative can also be described using the change in the speed of sound over the density along an isentropic change of state:

$$\Gamma = 1 + \frac{\rho}{a}\left(\frac{\partial a}{\partial \rho}\right)_s = \frac{1}{2}\left[\kappa_{pv} + 1 - \frac{v}{\kappa_{pv}}\left(\frac{\partial \kappa_{pv}}{\partial v}\right)_s\right] \tag{3.34}$$

For a perfect gas, the isentropic pressure-volume exponent is known to tend towards the isentropic exponent. The expression in Equation 3.34 thus takes the value $\Gamma = (\kappa + 1)/2$ for a perfect gas, which is always greater than one. For the classification of a compressible fluid based on the fundamental derivative, an isentropic increase in pressure is considered. Based on the perfect gas, a fluid is described as ideal if the value of the speed of sound increases in the course of a pressure increase. In this case, the fundamental derivative assumes values greater than one. If the value of the speed of sound decreases along with an increase in isentropic pressure, the fluid is classified as non-ideal. According to Equation 3.34, the negative sign of the differential of the speed of sound leads to values of the fundamental derivative less than one. Cramer [34] demonstrates such states for fluorocarbons near the critical point. Nannan et al. [106] extend this observation to the two-phase region of a large number of fluids directly below the respective critical point. According to Harinck et al. [68], the decrease in the speed of sound as the pressure increases can be attributed to the interaction of attractive and repulsive intermolecular forces. If the decrease in the speed of sound is so great that the fundamental derivative assumes negative values, the fluid is described as non-classical. Single-phase gaseous fluids in this category can also be found in the literature under Bethe-Zel'dovich-Thompson fluids. However, as Vimercati et al. [154] note, experimental proof of this group, unlike in the case of two-phase fluids, is still pending. Based on the fundamental derivative, it is possible to categorise the fluids into three groups, summarised and compared in Table 2.

Table 2: Classification of fluids based on the fundamental derivative of gas dynamics

$\Gamma \geq 1$	$(\partial a/\partial \rho)_s \geq 0$	classical ideal
$0 \leq \Gamma < 1$	$-a/\rho \leq (\partial a/\partial \rho)_s < 0$	classical non-ideal
$\Gamma < 0$	$(\partial a/\partial \rho)_s < -a/\rho$	non-classical

According to Colonna et al. [31], this classification is directly related to the molecular complexity of the fluid, as both the speed of sound and its isentropic change with density are influenced by this. Accordingly, the classical ideal case corresponds to a low molecular complexity, while classical non-ideal fluids have a high molecular complexity.

Parameters of molecular complexity

The distinction between ideal and non-ideal compressible fluids should, therefore, also include the molecular complexity of the fluid. According to Colonna and Guardone [29], this can be expressed by the number of active degrees of freedom N:

$$N = \frac{2}{\delta_\infty^c} = \frac{2c_{v,\infty}}{R_s} = M\frac{2c_{v,\infty}}{R} \tag{3.35}$$

The factor δ_∞^c denotes the dimensionless reciprocal value of the specific isochoric heat capacity defined by Bethe [20], which is evaluated at the critical temperature and assuming no intermolecular interactions. Therefore, many active degrees of freedom are associated with a high molecular complexity. According to Equation 3.35, the number of active degrees of freedom is directly proportional to the molar mass of the molecule. However, Tosto et al. [150] clarify that this relationship is weakened by the antiproportionality of specific isochoric heat capacity and molar mass stated by classical gas kinetics. Between the molecular complexity of a fluid and the isentropic pressure-volume exponent, there is also a reciprocal relationship. On the other hand, the ratio of specific heat capacities and the compressibility factor are not significantly influenced by the molecular complexity. Another approach to assessing molecular complexity by Guardone and Argrow [60] uses the minimum of the fundamental derivative along the dew line as a criterion. Likewise, the Grüneisen parameter Gr is used to describe molecular complexity. This parameter, originally defined to describe relations between thermodynamic quantities and the grid vibration within a solid, is generalised by Arp et al. [7] for application to fluids:

$$Gr = \frac{1}{\rho c_v}\left(\frac{\partial p}{\partial T}\right)_v = -\frac{v}{c_v}\left(\frac{\partial s}{\partial v}\right)_T = \kappa_{pv}\kappa_{pT} \qquad \text{with} \qquad \kappa_{pT} = \frac{p}{T}\left(\frac{\partial T}{\partial p}\right)_s \tag{3.36}$$

Using Maxwell's relations, it is also possible to formulate the Grüneisen parameter using only the isentropic pressure-volume exponent and the isentropic pressure-temperature exponent κ_{pT}. The latter can be defined analogue to the procedure presented for the isentropic pressure-volume exponent for non-ideal fluids. If the Grüneisen parameter is evaluated at the critical temperature, its value for a perfect gas tends towards the factor δ_∞^c [150]. This dependence can also be shown for a non-ideal fluid if its deviation from the model of the perfect gas is quantified by the compressibility factor:

$$Gr = \frac{1}{\delta_\infty^c}\frac{c_{v,\infty}}{c_v}\left[Z + T\left(\frac{\partial Z}{\partial T}\right)_\rho\right] \tag{3.37}$$

The Grüneisen parameter shows a maximum at the critical point for fluids with low molecular complexity, while it does not show an extremum for fluids with high molecular complexity. In order to describe the molecular complexity of fluids that are analysed in the context of a phase change, Invernizzi [80] defines a further parameter:

$$\sigma = \frac{T_c}{R_s}\left(\frac{ds}{dT}\right)_{s,v,T_r=0.7} \tag{3.38}$$

The value of σ is proportional to the slope of the dew line in a surface spanned by temperature and entropy. For fluids with low molecular complexity, σ has a negative value, which results in a negative slope of the dew line. According to this criterion, molecularly complex fluids can be identified by a positive slope of the dew line in a plot of temperature versus entropy.

In order to classify a compressible fluid as non-ideal, various parameters can be used, which differ significantly in their objective. The compressibility factor describes the deviation from the law of ideal gases. It can thus not only provide a binary classification regarding the non-ideality of a fluid, but also a quantification of this non-ideality. It thus represents a similarity parameter that enables the comparison of thermodynamic states as well as different fluids. As the counterpart of the isentropic exponent of perfect gases, the isentropic pressure-volume exponent is particularly suitable for distinguishing between ideal and non-ideal fluids in the context of analysing changes of state. It can also be used as an auxiliary parameter to define the fundamental derivative of gas dynamics, which emphasises the influence of wave propagation on the classification of the fluid. The Grüneisen parameter, which is linked to the number of active degrees of freedom via Equation 3.37, aims to quantify the molecular complexity as a function of a thermodynamic state. In addition, the fundamental derivative or the isentropic pressure-volume exponent and the molecular complexity are in a reciprocal relationship.

All the parameters introduced indicate that the non-ideality of a compressible fluid near the dew line is particularly significant. If there is a slight variation in pressure or temperature in this region of state, the dew line can be crossed into the two-phase region, which makes thermophysical modelling of the phase change process necessary.

3.4 Thermophysical Modelling of Phase Change

Given the study's emphasis on compressible media, the primary focus is on the phase change from the gaseous to the liquid phase. Consequently, the condensation process, which involves the formation of a liquid phase as the vapour pressure curve is crossed, is of particular importance. Two different types of condensation can be observed experimentally. Homogeneous condensation occurs when the liquid phase forms spontaneously as condensation nuclei directly from the gas phase. In contrast, heterogeneous condensation begins at the surface of solid particles, which serve as nucleation sites for the liquid phase. Heterogeneous condensation, occurring only in two- or multi-component systems, is therefore not considered in this work.

In addition to distinguishing between different physical condensation processes, various modelling approaches can be considered. Homogeneous condensation can be modelled by either assuming thermodynamic equilibrium or by negating it. These models differ significantly in their underlying assumptions and the mathematical descriptions of the phase change process. While the equilibrium model provides a highly abstracted representation, the non-equilibrium model offers a detailed description of homogeneous condensation, particularly through additional modelling steps.

Equilibrium Model of Homogeneous Condensation

The equilibrium model of homogeneous condensation assumes the existence of thermodynamic phase equilibrium. Thus, the liquid phase formed during condensation has the same specific Gibbs energy, temperature, and pressure as the gaseous phase. To describe the composition of the two-phase system, the wetness fraction y is introduced in the context of condensation. This fraction relates the mass of the liquid phase to the total mass of the system:

$$y = \frac{m_l}{m_l + m_g} \tag{3.39}$$

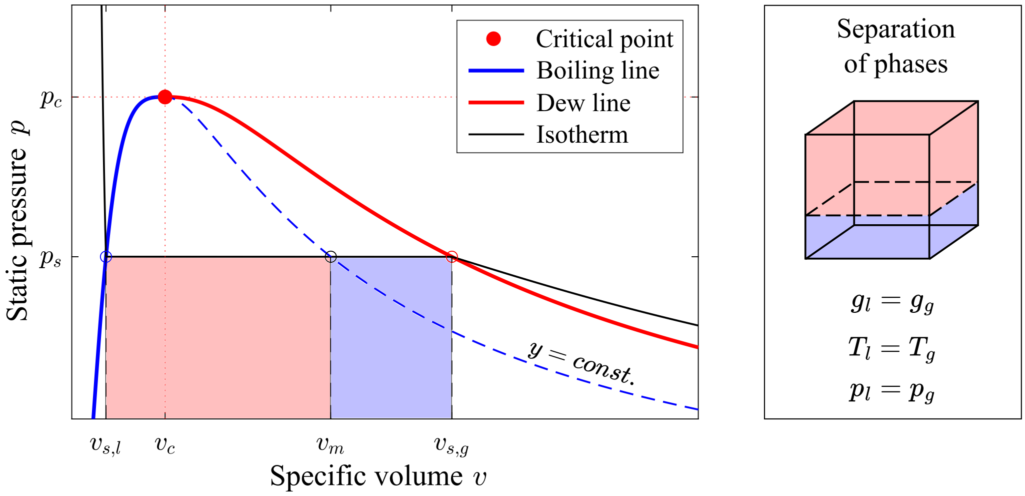

Figure 8: Definition of the wetness fraction for the equilibrium model of homogeneous condensation in a p-v diagram (left) and schematic representation of separation of phases (right)

If the equilibrium condition is met, the two phases present in the system can only reach saturated states. The extensive system volume can, therefore, be formulated as a function of the masses of the phases and the saturation quantities:

$$V_m = m_l v_{s,l} + m_g v_{s,g} \qquad \Leftrightarrow \qquad v_m = \frac{m_l v_{s,l} + m_g v_{s,g}}{m_l + m_g} \tag{3.40}$$

In Figure 8, this relationship between mixture and saturation quantities is illustrated through a pressure-volume diagram. If the pressure of a system that is initially gaseous is increased along the exemplary subcritical isotherm, the system enters the two-phase region when the saturation vapour pressure is reached, and a liquid phase is formed. The resulting state point is indicated in the diagram by the specific volume of the phase mixture v_m and the saturation vapour pressure. According to the equilibrium model of homogeneous condensation, the phases are separated by a single phase boundary. The state of each phase can be described by the saturation quantities along the boiling or dew line. The proportion of the blue liquid phase in the total system shown on the right in Figure 8 can also be expressed as the ratio of the specific volumes:

$$y = \frac{v_{s,g} - v_m}{v_{s,g} - v_{s,l}} \qquad \Leftrightarrow \qquad v_m = v_{s,g} - y(v_{s,g} - v_{s,l}) \tag{3.41}$$

This expression for the wetness fraction, which is derived graphically using the lever rule, can be formulated in the same way by combining Equation 3.39 and Equation 3.40. If a distribution is carried out using the lever rule for a large number of isotherms, the points constructed in this way can be connected to lines of constant wetness fraction. In addition to the specific volume, other state quantities, such as the specific enthalpy or the specific entropy, can be used as definition quantities:

$$h_m = h_{s,g} - y(h_{s,g} - h_{s,l}) = h_{s,g} - y h_v \tag{3.42}$$

The difference between the specific enthalpies of the saturated gas and liquid phases is referred to below as the specific enthalpy of vaporisation h_v. This quantity, also known as latent heat, quantifies the energy the system releases during a complete isothermal phase change from liquid to gaseous. An analytical determination of the state quantities of the two-phase system, particularly the wetness fraction, is thus possible in the case of the equilibrium model. However, the high degree of abstraction of the model compared to the physical formation of a liquid phase becomes clear from the theoretical definition of the phases. The physical processes that characterise the phase change are also not considered in the equilibrium model.

Non-equilibrium model of homogeneous condensation

In the course of homogeneous condensation, a metastable supersaturated or subcooled state initially occurs in natural processes when the vapour pressure curve is exceeded. This can be described both using the degree of saturation S and by means of the subcooling ΔT:

$$S = \frac{p}{p_s(T_g)} \qquad \rightleftharpoons \qquad \Delta T = T_s - T_g \tag{3.43}$$

Here, T_s denotes the saturation temperature defined by the vapour pressure curve. The pressure is not indexed as a gas quantity due to the presence of mechanical equilibrium and the resulting equality of phase and mixture pressure. For a degree of saturation greater than one or a subcooling greater than 0 K, fluctuations in density lead to the formation of clusters. However, these are not sufficiently stable for conditions of low supersaturation and disintegrate immediately. When a state known as critical supersaturation is reached, a large number of stable clusters, known as condensation nuclei, spontaneously form. This physical process of spontaneous nucleation is the initial step in the formation of a liquid phase. Therefore, the state of critical supersaturation marks the Wilson point, in which condensation can be measured for the first time in a phenomenological way using droplets. The condensation nuclei, usually modelled as spherical, are dispersed in the continuous gas phase.

Further molecules accumulate on their surface, causing the dispersed phase to grow. The energy released causes an increase in temperature within the gas phase, which, according to Equation 3.43, decreases the subcooling and inhibits nucleation. A combination of nucleation and droplet growth consequently leads to a self-regulation of the system, which strives to restore a thermodynamic equilibrium. After the onset of nucleation, nucleation, and droplet growth occur in parallel so that droplets with different radii r are present in the gas phase at a defined point in time. In order to be able to represent the dispersed phase mathematically, it is therefore necessary to divide it into a finite number of groups.

Each group i is characterised by the equality of its physical properties and, in particular, its radius. The wetness fraction can then be formulated as the ratio of the sum of the mass fractions of the individual groups to the total mass:

$$y = \sum y_i = \sum \frac{m_{l,i}}{m_m} = \sum \frac{n_i}{m_m} \cdot \frac{4}{3} \pi r_i^3 \cdot \rho_{l,i} \tag{3.44}$$

Where n_i denotes the number of droplets in the i-th group. The product of the volume of a sphere and the density of the liquid phase expresses the mass of a droplet. The state quantities of the two-phase mixture, such as the specific volume, for example, can be expressed based on the wetness fraction and the quantities of the gas and liquid phases:

$$v_m = (1-y)v_g + \sum y_i v_{l,i} \tag{3.45}$$

Unlike in the case of the equilibrium model, however, it is not possible to determine the state quantities of the individual phases analytically based on the saturation quantities. The processes of nucleation and droplet growth cause a time-resolved change in the phase composition and, consequently, in the wetness fraction. In addition, the distribution of the formed droplets to the individual size groups also varies during condensation. The influence of nucleation and growth on the change in the wetness fraction over time t can be mathematically separated:

$$\frac{dy}{dt} = \frac{dy_{Nucleation}}{dt} + \frac{dy_{Growth}}{dt} \tag{3.46}$$

The mechanism of nucleation can be quantified using the nucleation rate J. This represents the number of new nuclei that form per unit of time in a defined volume. The classical nucleation theory is based on the insight of Gibbs [52] that the energy ΔG required to form a cluster can be divided into a volumetric term ΔG_v and a surface term ΔG_s:

$$\Delta G = \Delta G_v + \Delta G_s = \frac{4}{3}\pi r^3 \rho_l (g_l - g_g) + 4\pi r^2 \sigma_{lg} \tag{3.47}$$

Here, σ_{lg} denotes the surface tension of the liquid phase at gas temperature. It should be noted that the difference between the specific Gibbs energies of the liquid and gaseous phases is usually simplified to $g_l - g_g = R_s T_g \ln(S)$ when applying the law of ideal gases. The maximum of the energy difference from Equation 3.47 represents the energy barrier ΔG_{crit}, which must be overcome to form a stable cluster, i.e., a nucleus. Based on this condition, an expression for the minimum nucleus radius or critical radius r_{crit} can be formulated:

$$r_{crit} = \frac{2\sigma_{lg}}{\rho_l R_s T_g \ln(S)} \qquad \Leftrightarrow \qquad \Delta G_{crit} = \frac{4}{3}\pi \sigma_{lg} r_{crit}^2 \tag{3.48}$$

Given this energetic description, Volmer and Weber [156] formulate an initial expression for the nucleation rate. They state that the nucleation rate is exponentially linked to the height of the energy barrier. The works of Becker and Döring [19], Frenkel [48], and Zeldovich [173] form the classical nucleation theory, which models the nucleation rate using an approach based on the Arrhenius equation:

$$J = J_0 \cdot \exp\left(-\frac{\Delta G_{crit}}{k_b T_g}\right) \qquad \text{with} \qquad J_0 = q_c \sqrt{\frac{2\sigma_{lg} N_A^3}{\pi M^3}} \cdot \frac{\rho_g^2}{\rho_l} \tag{3.49}$$

In this equation, q_c denotes the condensation coefficient, whose value is set to one in the following, and N_A denotes Avogadro's constant. The classical nucleation theory assumes that the gas phase in which nucleation is about to occur and the remaining gas volume have the same temperature. In reality, however, the gas phase is at a higher temperature just before nucleation occurs, so the isothermal assumption should not be maintained. To account for this when determining the nucleation rate, Kantrowitz [82] proposes introducing a correction factor ϕ.

According to Bakhtar and Zidi [12], the heat transfer between the phases must be taken into account when formulating this:

$$\phi = \phi_0 \cdot \left(\frac{h_v^2}{R_s T_g^2} - \frac{h_v}{2T_g} \right) \qquad \text{with} \qquad \phi_0 = q_c \frac{\rho_g}{\alpha_{crit}} \sqrt{\frac{R_s T_g}{2\pi}} \tag{3.50}$$

The heat transfer coefficient for a nucleus with critical radius α_{crit} is, for the sake of consistency, defined together with the description of the heat transfer during droplet growth by Equation 3.52. In the literature (see [13]), the correction factor ϕ is often simplified under the assumption of a perfect gas, though this simplification is dispensable for the purposes of this work. The change in the wetness fraction due to nucleation can then be formulated as a combination of Equation 3.49, Equation 3.50, and Equation 3.44:

$$\frac{dy_{Nucleation}}{dt} = \frac{4}{3} \pi r_{crit}^3 \frac{\rho_l}{\rho_m} \cdot \frac{J}{1+\phi} \tag{3.51}$$

Since nucleation events always occur at nuclei with a critical radius, further size groups do not need to be considered for this term, so the summation from Equation 3.44 is omitted. The division by the density of the mixture takes into account the change from volume-related nucleation rate to mass-related wetness fraction.

The droplet growth of the i-th size group is quantified using the growth function $G(r_i)$, which describes the change in radius per unit of time. The approach used in this work, according to Young [172], is a further development of the relationship originally formulated by Gyarmathy [63]. Gyarmathy models the time derivative of the radius change as the rate at which the evaporation enthalpy released during droplet growth is transferred to the gas phase:

$$G(r_i) = \frac{dr_i}{dt} = \frac{\alpha_i}{\rho_l h_v} (T_i - T_g) \qquad \text{with} \qquad \alpha_i = \frac{\lambda_g}{r_i (1 + 3.18 \cdot Kn)} \tag{3.52}$$

Thereby, α_i denotes the heat transfer coefficient at the interface of the i-th droplet size group, which is described using a Nusselt correlation valid for low Reynolds numbers of water. In this correlation, λ_g denotes the heat conductivity of the gas phase. The Knudsen number relates the mean free path $\bar{l}$ to a characteristic length:

$$Kn = \frac{\bar{l}}{2r_i} \qquad \text{with} \qquad \bar{l} = \frac{3\sqrt{\pi} \cdot \eta_g \cdot \sqrt{R_s T_g}}{\sqrt{8} p} \tag{3.53}$$

Since the mean free path is defined as the average distance a molecule can travel before colliding with another molecule, the diameter of the i-th group appears to be a suitable choice for the characteristic length of the droplet growth. The symbol η_g denotes the dynamic viscosity of the gas phase.

To evaluate the approach formulated in Equation 3.52, knowledge of the liquid phase temperature of each drop size group would be necessary. Alternatively, Gyarmathy suggests an approximation of the temperature difference:

$$T_i - T_g = \Delta T \left(1 - \frac{r_{crit}}{r_i} \right) \tag{3.54}$$

By comparing the model defined by Gyarmathy, which combines Equation 3.52 and Equation 3.54, with experimental findings, Young extends it by three empirical model parameters α, β and ν:

$$\frac{dr_i}{dt} = \frac{\lambda_g \Delta T (1 - \frac{r_{crit}}{r_i})}{\rho_l h_v r_i \left(\frac{1}{1+2\beta Kn} + 3.78(1-\nu)\frac{Kn}{Pr} \right)} \qquad \text{with} \qquad Pr = \frac{\eta_g c_{p,g}}{\lambda_g} \tag{3.55}$$

The Prandtl number Pr describes the ratio of momentum transport to heat transport within the gas phase. While the parameters α and β are initially set to $\alpha = 11$ and $\beta = 0$ based on the selection by Starzmann et al. [138], Young gives an explicit equation for the third parameter:

$$\nu = \frac{R_s T_s}{h_v} \left(\alpha - 0.5 - \frac{2-q_c}{2q_c} \left(\frac{\kappa+1}{2\kappa} \right) \left(\frac{c_{p,g} T_s}{h_v} \right) \right) \tag{3.56}$$

By suitably reformulating Equation 3.46, the contribution of droplet growth to the temporal change in wetness fraction can be formulated by differentiating Equation 3.44 with respect to radius r_i:

$$\frac{dy_{Growth}}{dt} = \frac{dy_{Growth}}{dr_i} \cdot \frac{dr_i}{dt} = \sum \frac{n_i}{m_m} \cdot 4 \cdot \pi r_i^2 \rho_i \cdot G(r_i) \tag{3.57}$$

Adding Equation 3.51 and Equation 3.57 yields the differential equation for the wetness fraction for the non-equilibrium model using the mass-based nucleation rate $\bar{J}$:

$$\frac{dy}{dt} = \frac{4}{3} \pi r_{crit}^3 \rho_l \cdot \frac{\bar{J}}{1+\phi} + \sum \frac{n_i}{m_m} \cdot 4 \cdot \pi r_i^2 \rho_i \cdot G(r_i) \qquad \text{with} \qquad \bar{J} = \frac{J}{\rho_m} \tag{3.58}$$

To solve this, an explicit description of the droplet radius distribution is needed. Assuming a monodispersed distribution, all droplets have the same mean radius, so only a single group is needed for modelling. The temporal change of the wetness fraction is obtained by substituting $i = 1$ in Equation 3.58.

However, due to the time lag between nucleation and droplet growth, the droplet radii, in reality, show a polydispersed distribution at any given time. Such a distribution is exemplarily shown in Figure 9. The critical radius characterises the group with the smallest diameter. As more and more molecules accumulate, the droplets grow and form groups of larger radii r_i. Due to the coagulation of droplets in the medium size range of the distribution, only a few droplets reach above-average radii.

For the mathematical description of such a droplet radius distribution, Hulburt and Katz [78] and Hill [72] propose modelling based on the central statistical moments. The kth moment of the distribution can be formulated by a Taylor series expansion of the number density function $f(r)$:

$$\mu_k = \int_0^\infty r^k f(r)\, dr \qquad \longrightarrow \qquad \frac{\partial \mu_k}{\partial t} = k \int_0^\infty r^{k-1} G(r) f(r) dr + \bar{J} r_{crit}^k \tag{3.59}$$

In order to be able to close the system of equations of the moments, White [162] gives three possible approximations for the expression of the growth rate. In this work, the approach that evaluates the growth function using the surface-averaged radius r_{20} is chosen from these.

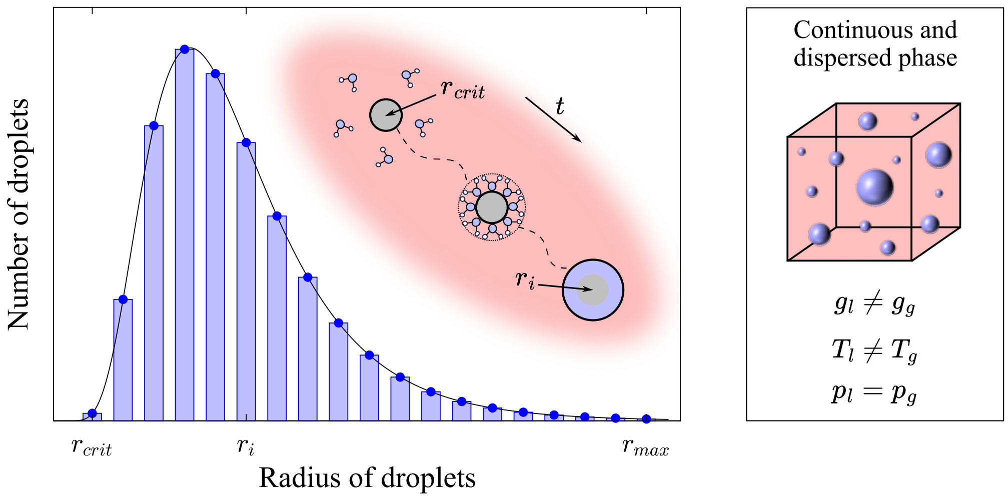

Figure 9: Exemplary polydispersed droplet radius distribution (left) and schematic distinction between the continuous and the dispersed phase (right)

If the integral in Equation 3.59 is replaced by a linear combination of μ_k and μ_{k-1}, which is omitted for $k = 0$, this results in:

$$\frac{\partial \mu_k}{\partial t} = k\mu^{k-1} G(r_{20}) + \bar{J} r_{crit}^k \qquad \text{with} \qquad r_{20} = \sqrt{\frac{\mu_2}{\mu_0}} \tag{3.60}$$

To avoid the use of such a closing condition and thus increase the accuracy of the method, McGraw [97] introduces weighting factors of the moments in Equation 3.59. These factors are then determined using an n-th order Gaussian quadrature. According to White and Hounslow [164], a description of the droplet radius distribution using the first four moments $k \in \{0, 1, 2, 3\}$ is usually sufficiently accurate even without such weighting.

The zeroth moment can be physically interpreted as the number of droplets per unit volume of the two-phase mixture. In addition, the Sauter radius r_{32} and the wetness fraction are in a proportional relationship to the third moment of the radius distribution:

$$r_{32} = \frac{\mu_3}{\mu_2} \qquad \wedge \qquad y = \frac{4}{3}\pi \rho_l \mu_3 \tag{3.61}$$

In the case of the non-equilibrium model of homogeneous condensation, determining the wetness fraction requires an iterative solution of the system of differential equations of the statistical moments. The modelling of the mechanisms occurring during condensation, which form the basis for specifying the system of equations, relies on a large number of thermophysical properties. It, therefore, seems appropriate to consider the unique features of the working fluids examined in the context of this work and to describe their thermophysical properties.

3.5 Special Properties of the Investigated Working Media

The determination of the thermophysical quantities of the working media considered below uses fluid-specific multi-parameter equations of state. Since the selection of these equations is highly relevant for the reproducibility of the results presented, a tabular overview of all model equations used for water, carbon dioxide, and octamethyltrisiloxane (MDM) can be found in Appendix A.

Water - H_2O

Water molecules consist of one oxygen atom and two hydrogen atoms. They exist as a liquid at standard atmospheric conditions. The three phases, solid, liquid, and gaseous, are in equilibrium at the triple point at a temperature of $T_{trip} = 273$ K and pressure of $p_{trip} = 6.12$ mbar. The critical point of water is defined by a temperature of $T_c = 647$ K and a critical pressure of $p_c = 220$ bar. When considering water as a working fluid, the area around the vapour pressure curve and the two-phase area are of particular relevance.

For this reason, this area is the focus of the analysis in Figure 10 in the form of a pressure-volume diagram and a pressure-temperature diagram. The p-v diagram (left) shows the distinction between the two-phase region and the single-phase state areas using the boiling line (blue) and the dew line (red). The metastable region extends from these boundary curves to the spinodal limits of the liquid and gaseous phases. In the illustrated range, the compressibility factor varies between values close to zero and one. The global minimum of this parameter is found in the liquid region. On the other hand, if only the gas phase is considered, the minimum of the compressibility factor lies in the vicinity of the critical point. Moderate pressures and temperatures, as they occur in the investigations of the condensation of water in the context of this work, are expected to cause only a slight non-ideality of the fluid.

The two-phase region is represented in the right part of Figure 10 by the vapour pressure curve (black). This separates the liquid from the gaseous phase and ends at the critical point. In order to determine the thermodynamic state quantities for the medium water, the equa-

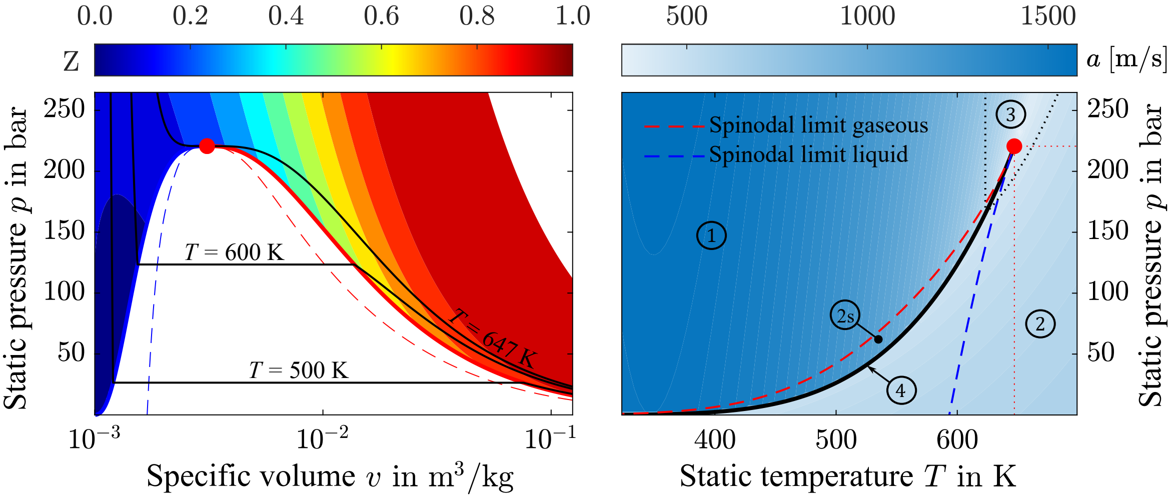

Figure 10: Variation of the compressibility factor Z in a p-v diagram (left) and distinction of the liquid and gaseous phase based on the speed of sound a and the definition ranges of the IAPWS-IF97 in a p-T diagram (right) for the medium water

tion of state named by the International Association for the Properties of Water and Steam (IAPWS) in 1997 as the Industrial Formulation (IAPWS-IF97) [160] is used in this work. The equation is characterised by a split of its definition range into sub-ranges. Circled numbers in Figure 10 indicate the regions relevant for further consideration. In order to favour the determination of the state quantities in industrial practice for the ranges 1 and 2, the corresponding equations are formulated using a Gibbs-based approach. On the other hand, the equation of state for region 3 uses a Helmholtz-based formulation. Another unique feature of the IAPWS-IF97 is the extension of region 2 to include the metastable region 2s, which is limited by the spinodal limit of the gas phase. A Gibbs-based equation of state is also available for this region, but unlike the other equations, it is not determined on the basis of experimental data. Rather, it is extrapolated from the single-phase region 2 using a specific equation of state for low-density gases [159]. By applying such an equation, the discontinuous transition of the state quantities from the gaseous to the liquid phase, as exemplarily shown in the right part of Figure 10 for the speed of sound, can be attenuated when considering phase change processes.

Carbon dioxide - CO_2

The structure of a carbon dioxide molecule (CO_2) consists of a linear arrangement of a carbon atom and two oxygen atoms. At standard atmospheric conditions, the fluid exists in the gaseous phase. Its triple point is defined by a temperature of $T_{trip} = 217$ K and a pressure of $p_{trip} = 5.2$ bar. A special feature of CO_2 relevant for technical applications is its critical state quantities. The critical temperature of $T_{crit} = 304$ K is close to typical ambient conditions and, in combination with a critical pressure of $p_{crit} = 73.8$ bar, enables efficient utilisation of the properties near the critical point.
In Figure 11, the state region around the critical point of CO_2 is therefore shown in a temperature-entropy diagram and a pressure-temperature diagram. In addition to the curves already presented for the medium water, which characterise the two-phase region, the Widom line is also plotted. The compressibility factor, visualised as a contour on the left side of the figure, varies in this region between approximately 0.1 and 0.7. In the immediate vicinity of

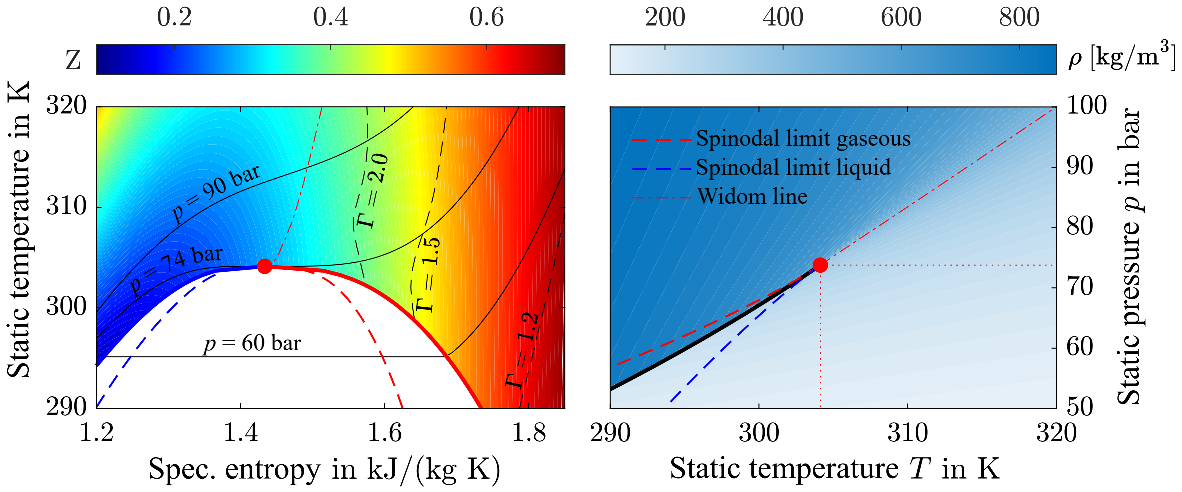

Figure 11: Variation of the compressibility factor Z and the fundamental derivative Γ in a T-s diagram (left) and density characteristic ρ near the critical point in a p-T diagram (right) for the medium CO_2

the critical point, the compressibility factor has a value of slightly above 0.2. In the literature (see [54], [150]), this region is often referred to as non-ideal in the sense of deviating from the law of ideal gases. However, the values of the fundamental derivative are above one, as shown by the isolines, which makes the influence of the parameter choice on the classification as non-ideal evident.

The equation of state according to Span and Wagner [136], on which the calculations of the state quantities of CO_2 are based, shows a high degree of accuracy in the sense of agreement with experimental data, particularly in the supercritical state range. Due to its Helmholtz-based formulation using a single function for the entire domain, it can also be easily implemented. An evaluation of this equation in terms of density is shown in the right part of Figure 11. The visible distinction between liquid and gaseous states above the critical point using the Widom line is particularly striking.

Octamethyltrisiloxane (MDM) - $C_8H_{24}O_2Si_3$

As its name suggests, octamethyltrisiloxane is characterised by eight methyl groups and three silicon atoms. In the nomenclature of siloxanes, a combination of three methyl groups and one silicon atom forms an M group. In comparison, two methyl groups and one silicon atom together characterise a D group. This results in the abbreviation MDM, which is most commonly used in the literature due to its brevity. The fluid, which is liquid at standard atmospheric conditions, has a temperature of $T_{trip} = 187$ K and a pressure of about $p_{trip} = 0.01$ mbar at the triple point. The critical point is defined by a temperature of $T_{crit} = 565$ K and a pressure of $p_{crit} = 14.4$ bar.

The characteristics of the thermodynamic state ranges of MDM are illustrated in Figure 12. In the left part of the figures, the gaseous and liquid state ranges, as well as the two-phase region, are shown in a plot of static pressure versus specific volume. Starting from the triple point, which is located near the origin, the value of the compressibility factor increases with increasing pressure and volume. Similar to the findings for water, the global minimum of this parameter is found in the liquid phase, while the minimum for gaseous states is found

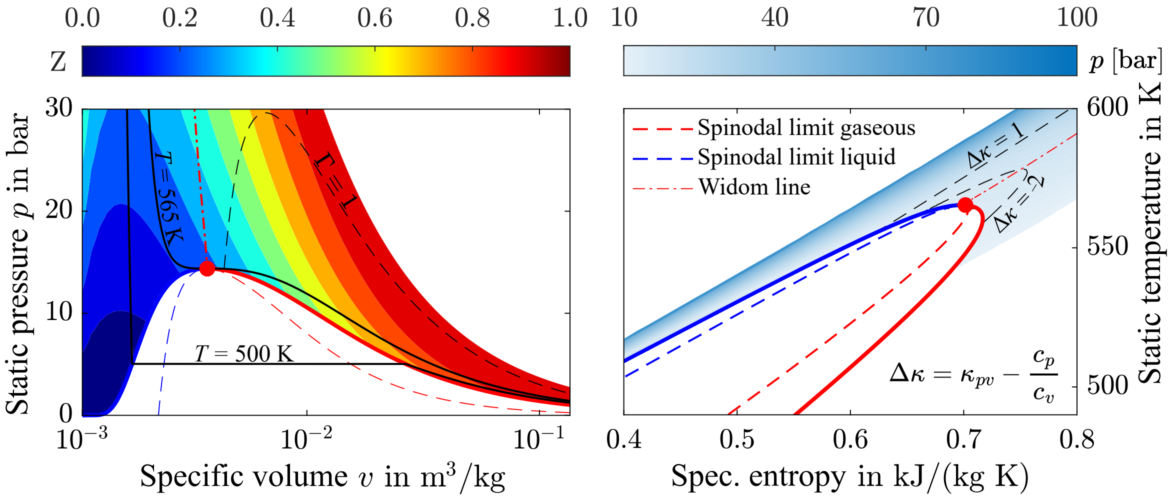

Figure 12: Variation of the compressibility factor Z and boundary of the non-ideal range of states in a p-v diagram (left) and deviation of the isentropic pressure-volume coefficient from the heat capacity ratio $\Delta\kappa$ in a T-s diagram (right) for the medium MDM

at the critical point. In contrast to the other two working media, a non-ideal state range can be defined for MDM by a fundamental derivative of less than one. This is located in the gas phase and runs almost along the entire dew line. It is noteworthy that the compressibility factor in this range has values between 0.3 and 1.0.
An evaluation of the Helmholtz-based equation of state according to Thol et al. [145] in terms of pressure forms the basis for the plot of static temperature over specific entropy shown in the right part of Figure 12. The deviation of the isentropic pressure-volume exponent from the ratio of specific heat capacities $\Delta\kappa$ is shown by two isolines. While the difference near the critical point assumes negative values, it shows positive values with increasing pressure. However, independently of its sign, the difference classifies significant deviations for the considered state region. Based on the representation of a T-s diagram, the negative slope of the dew line is also directly recognisable, which, in addition to its relevance for ORC applications in equivalence to the σ parameter, also indicates a high molecular complexity.

In order to examine this aspect comparatively for the three working media under consideration, the Grüneisen parameter and the isentropic pressure-volume exponent are plotted along the critical isotherm in the left part of Figure 13. The parameters shown are each related to their value when evaluated for a specific volume tending towards infinity. The curve of the Grüneisen parameter shows very different properties for the three fluids. While the curve for water falls monotonically, it rises monotonically for MDM. In the case of CO_2, a maximum is formed shortly before the critical pressure is reached. Also, the characteristics of the isentropic pressure-volume exponent differ considerably. While the curve for MDM falls monotonically, the curve for water shows almost no slope. The curves for water and CO_2 are very similar at low pressures. However, the isentropic pressure-volume exponent for CO_2 increases more steeply from a reduced pressure of about $p_r = 0.6$.
The results for MDM and CO_2 align with the findings of Tosto et al. [150]. According to them, the formation of a maximum in the curve of the Grüneisen parameter indicates moderate molecular complexity. In contrast, a monotonically increasing Grüneisen parameter and a monotonically decreasing isentropic pressure-volume exponent are characteristic of a fluid with high molecular complexity. The classification of the medium water thus indicates

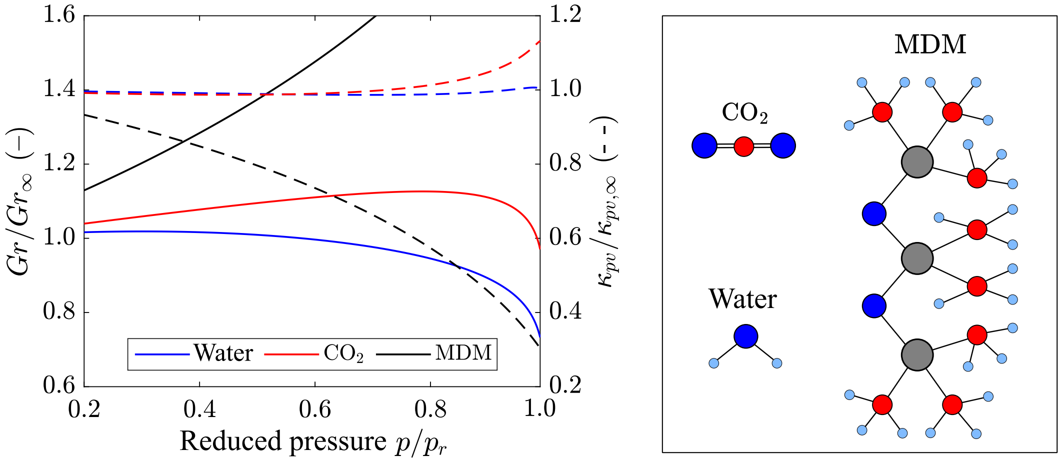

Figure 13: Variation of the Grüneisen parameter Gr and the isentropic pressure-volume coefficient κ_{pv} along the critical isotherm for the media water, CO_2 and MDM (left) and the molecular structure of the investigated fluids (right)

low molecular complexity but is not unambiguous. Therefore, an examination based on the molecular structures in the right part of Figure 13 seems helpful. The MDM molecule not only has the highest molar mass of $M = 237$ g/mol but also a significantly more complex branched structure. The molecules of CO_2 with a molar mass of $M = 44$ g/mol and water with $M = 18$ g/mol are comparatively simple in structure. The order of the working media selected in this subchapter consequently also corresponds to the order of their molecular complexity.

4 Numerical Modelling

Starting from the thermodynamic description of compressible non-ideal fluids using the concept of a spatially fixed fluid element presented in the previous chapter, the flow of a continuous fluid will now be examined. To do so, it is necessary to consider a finite number of fluid elements moving in three-dimensional space. Since each fluid element, in addition to different thermophysical properties, also potentially has its own direction and speed of movement, it is crucial to choose suitable system boundaries for modelling the flow. In continuation of the approach from Figure 1, for further considerations, this falls analogously to the fluid element on an infinitesimal control volume dV.

The motion of a continuous medium can be described by means of a vector field, which is also referred to as a flow field. A curve in space, whose point set is tangential to the velocity vectors of the flow field, defines a streamline. When considering a stationary volume, the motion of the fluid along such a streamline causes a flow across the bounding surfaces. This is illustrated in a Cartesian coordinate system in Figure 14.

Applying the fundamental physical principles of conservation of mass, momentum, and energy to the spatially fixed infinitesimal volume takes into account not only the spatial change but also the temporal dimension. Due to its relevance for further explanations, the concept of flux is exemplified by the conservation of mass:

$$\dot{m} = \rho \cdot \boldsymbol{v}_{\perp} \cdot A = const. \tag{4.1}$$

The mass flow rate $\dot{m}$ can be formulated using the product of the density, the component of the velocity vector perpendicular to the flow direction $\boldsymbol{v}$, and the area A through which the flow passes. A division of the mass flow rate into its Cartesian components leads to a definition of three flux terms, which are expressed using the three velocity components u, v, and w. The x-component of the mass flux ρu enters the volume over the surface $dy \cdot dz$. On the complementary surface displaced by dx, the quantity changed by $(\partial(\rho u)/\partial x) \cdot dx$ exits accordingly. The same applies to the other two spatial directions based on Figure 14. The sign convention defines a positive flow direction based on the outward-pointing normal vectors on the boundary surfaces of the volume. [4]

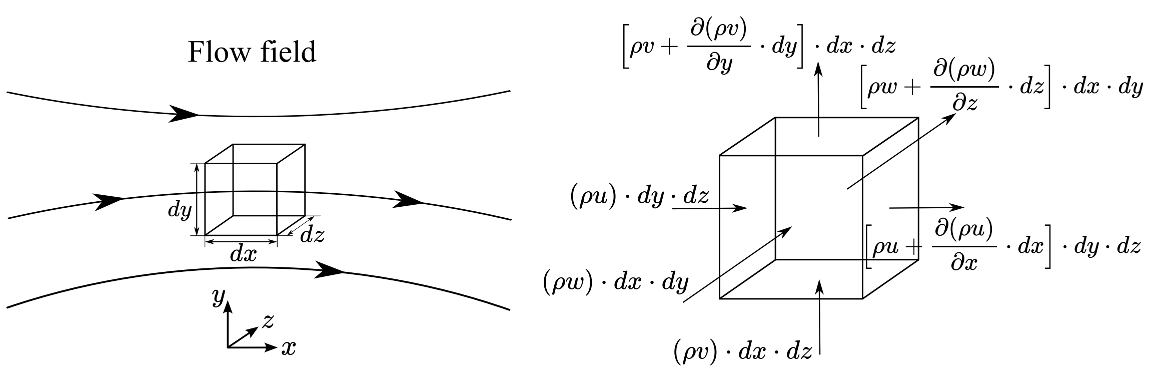

Figure 14: Infinitesimal control volume in a flow field (left) and fluxes across the volume boundaries as an example for the conservation of mass (right)

The variation of the mass with time is recorded over the entire control volume dV. Balancing the temporal change within the volume and the spatial change represented by the fluxes over the volume boundaries results in:

$$\begin{aligned}\frac{\partial \rho}{\partial t}(dx \cdot dy \cdot dz) &+ \left[\rho u + \frac{\partial(\rho u)}{\partial x} \cdot dx\right] \cdot dy \cdot dz - (\rho u) \cdot dy \cdot dz \\ &+ \left[\rho v + \frac{\partial(\rho v)}{\partial y} \cdot dy\right] \cdot dx \cdot dz - (\rho v) \cdot dx \cdot dz \\ &+ \left[\rho w + \frac{\partial(\rho w)}{\partial z} \cdot dz\right] \cdot dx \cdot dy - (\rho w) \cdot dx \cdot dy = 0\end{aligned} \tag{4.2}$$

A division of Equation 4.2 by $dx \cdot dy \cdot dz$ and a subsequent transformation yields the partial differential equation of mass conservation. The flux terms can be found in this notation in the numerator of the partial spatial derivatives:

$$\frac{\partial \rho}{\partial t} + \frac{\partial(\rho u)}{\partial x} + \frac{\partial(\rho v)}{\partial y} + \frac{\partial(\rho w)}{\partial z} = 0 \tag{4.3}$$

Applying the approach presented for the conservation of mass to the conservation quantities in the momentum equation in the three spatial directions, as well as the energy, leads to the following equations:

$$\begin{aligned}\frac{\partial(\rho u)}{\partial t} + \frac{\partial}{\partial x}(\rho u^2 + p - \tau_{xx}) + \frac{\partial}{\partial y}(\rho uv + \tau_{yx}) + \frac{\partial}{\partial z}(\rho uw + \tau_{zx}) - \rho f_x &= 0 \\ \frac{\partial(\rho v)}{\partial t} + \frac{\partial}{\partial x}(\rho vu + \tau_{xy}) + \frac{\partial}{\partial y}(\rho v^2 + p - \tau_{yy}) + \frac{\partial}{\partial z}(\rho vw + \tau_{zy}) - \rho f_y &= 0 \\ \frac{\partial(\rho w)}{\partial t} + \frac{\partial}{\partial x}(\rho wu + \tau_{xz}) + \frac{\partial}{\partial y}(\rho wv + \tau_{yz}) + \frac{\partial}{\partial z}(\rho w^2 + p - \tau_{zz}) - \rho f_z &= 0\end{aligned} \tag{4.4}$$

$$\begin{aligned}&\frac{\partial}{\partial t}\left[\rho \cdot \left(e + \frac{1}{2}\boldsymbol{v}^2\right)\right] - \rho \cdot (uf_x + vf_y + wf_z) - \rho \dot{q}_r \\ &+ \frac{\partial}{\partial x}\left[\rho u \cdot \left(h + \frac{1}{2}\boldsymbol{v}^2\right) - (u\tau_{xx} + v\tau_{xy} + w\tau_{xz}) - \lambda_g \cdot \frac{\partial T}{\partial x}\right] \\ &+ \frac{\partial}{\partial y}\left[\rho v \cdot \left(h + \frac{1}{2}\boldsymbol{v}^2\right) - (u\tau_{yx} + v\tau_{yy} + w\tau_{yz}) - \lambda_g \cdot \frac{\partial T}{\partial y}\right] \\ &+ \frac{\partial}{\partial z}\left[\rho w \cdot \left(h + \frac{1}{2}\boldsymbol{v}^2\right) - (u\tau_{zx} + v\tau_{zy} + w\tau_{zz}) - \lambda_g \cdot \frac{\partial T}{\partial z}\right] = 0\end{aligned} \tag{4.5}$$

In these, f_x, f_y and f_z denote the Cartesian components of the body forces, while $\dot{q}_r$ represents the heat flow due to radiation and τ_{ij} the shear stress. The stress components act on a surface orthogonal to index i in the direction of index j. They can be specified using the relations formulated by Stokes [141]. The velocity vector can also be formulated by its Cartesian components $\boldsymbol{v}^2 = u^2 + v^2 + w^2$. The set of mass conservation in Equation 4.3, momentum conservation in Equation 4.4, and energy conservation in Equation 4.5 form the complete Navier–Stokes equations.

4.1 Conservation and Transport Equations for Single- and Two-Phase Flows

This work numerically solves the Reynolds-averaged Navier-Stokes equations to describe continuous flows. These equations can be derived from the complete Navier-Stokes equations by applying Favre averaging to the physical quantities. The conserved quantities consequently result in the sum of a temporal mean and a fluctuation quantity. In the course of the averaging, the number of unknowns in the system of equations increases so that additional models are needed to describe the turbulent fluctuations [44]. Since the formal structure of the complete and the Reynolds-averaged Navier-Stokes equations match and the viscous terms are not the focus of further consideration, the averaged quantities will not be explicitly marked. In addition to a formulation as a system of partial differential equations, the Navier-Stokes equations can also be represented in vector form. In the context of deriving numerical solution methods, this appears particularly suitable due to its structured representation and similarity to the operators of linear algebra:

$$\frac{\partial}{\partial t}\boldsymbol{U} + \frac{\partial}{\partial x}(\boldsymbol{F}_c - \boldsymbol{F}_v) + \frac{\partial}{\partial y}(\boldsymbol{G}_c - \boldsymbol{G}_v) + \frac{\partial}{\partial z}(\boldsymbol{H}_c - \boldsymbol{H}_v) = \boldsymbol{Q} \tag{4.6}$$

with

$$\boldsymbol{U} = \begin{pmatrix} \rho \\ \rho u \\ \rho v \\ \rho w \\ \rho E \end{pmatrix}, \quad \boldsymbol{F}_c = \begin{pmatrix} \rho u \\ \rho u^2 + p \\ \rho v u \\ \rho w u \\ \rho u H \end{pmatrix}, \quad \boldsymbol{F}_v = \begin{pmatrix} 0 \\ \tau_{xx} \\ \tau_{xy} \\ \tau_{xz} \\ \lambda_g \cdot \frac{\partial T}{\partial x} + u\tau_{xx} + v\tau_{xy} + w\tau_{xz} \end{pmatrix},$$

$$\boldsymbol{G}_c = \begin{pmatrix} \rho v \\ \rho u v \\ \rho v^2 + p \\ \rho w v \\ \rho v H \end{pmatrix}, \quad \boldsymbol{G}_v = \begin{pmatrix} 0 \\ \tau_{yx} \\ \tau_{yy} \\ \tau_{yz} \\ \lambda_g \cdot \frac{\partial T}{\partial y} + u\tau_{yx} + v\tau_{yy} + w\tau_{yz} \end{pmatrix}, \quad \boldsymbol{H}_c = \begin{pmatrix} \rho w \\ \rho u w \\ \rho v w \\ \rho w^2 + p \\ \rho w H \end{pmatrix},$$

$$\boldsymbol{H}_v = \begin{pmatrix} 0 \\ \tau_{zx} \\ \tau_{zy} \\ \tau_{zz} \\ \lambda_g \cdot \frac{\partial T}{\partial z} + u\tau_{zx} + v\tau_{zy} + w\tau_{zz} \end{pmatrix}, \quad \boldsymbol{Q} = \begin{pmatrix} 0 \\ \rho f_x \\ \rho f_y \\ \rho f_z \\ \rho \cdot (u f_x + v f_y + w f_z + \rho \dot{q}_r) \end{pmatrix}$$

$$E = e + \frac{1}{2}\boldsymbol{v}^2, \qquad H = e + \frac{p}{\rho} + \frac{1}{2}\boldsymbol{v}^2$$

U is referred to as the conservation vector and **Q** as the source term vector, while **F**, **G** and **H** represent the flux vectors. The total specific internal energy E and the total specific internal enthalpy H are introduced for better readability. The splitting of the flux vector into a convective part $\boldsymbol{F}_c$ and a viscous part $\boldsymbol{F}_v$ allows a separate consideration of the methods used to calculate these terms. Due to the minor importance of heat conduction, heat radiation, and body forces in the present investigations, these terms are neglected in the following equations. Furthermore, the previous relationships are limited to single-phase flows. Before a detailed investigation of different formulations of the equation systems of two-phase flows, it seems useful to introduce the quantities required to model the interaction between phases.

Exchange of momentum between liquid and gaseous phase

If the liquid phase is dispersed in the gaseous continuous phase, the flow field causes an exchange of momentum between the two phases. This results in the formation of various aerodynamic force components. In addition to drag, these include, for example, buoyancy, Basset force, virtual mass effect and Magnus force [35]. The modelling of the momentum exchange is limited to drag in the following, which results in the other force components being neglected. In addition, it is assumed that the liquid phase in the form of droplets does not interact with each other.

A droplet moving in the flow field at velocity $\boldsymbol{v}_l$ experiences a force due to the flow around it at velocity $\boldsymbol{v}_g$. According to Newton's third law, an force of equal magnitude acts on the continuous gas phase in the opposite direction. In this way, the drag force causes the two phase velocities to approach each other. Assuming spherical droplets, it can be formulated using Newton's second law:

$$F_D = \frac{1}{2}\rho_g A_s C_D (\boldsymbol{v}_g - \boldsymbol{v}_l)|\boldsymbol{v}_g - \boldsymbol{v}_l| \qquad \text{with} \qquad A_s = \pi r^2 \tag{4.7}$$

In this equation, A_s denotes the surface area of a droplet, and C_D is the dimensionless drag coefficient, primarily determined by the Reynolds number prevailing in the flow. To formulate the ratio of the inertial forces acting on a droplet to the viscous force components on the basis of the Reynolds number, the velocity difference between the two phases is used as the velocity, and the droplet radius is used as the characteristic length:

$$Re = \frac{2r|\boldsymbol{v}_g - \boldsymbol{v}_l|\rho_g}{\eta_g} \tag{4.8}$$

For Reynolds numbers smaller than one, Stokes [140] derives an anti-proportionality of the drag coefficient to the Reynolds number. The approach, according to Schiller and Naumann [131], multiplies this by a correction term and thus enables modelling of the drag coefficient for Reynolds numbers up to 1000:

$$C_{D,SN} = \frac{24}{Re} \cdot \left(1 + 0.15 \cdot Re^{0.687}\right) \qquad \text{for} \qquad 1 < Re < 1000 \tag{4.9}$$

The description, according to Stokes, assumes that the velocity difference at the surface of the drop approaches a value of zero. This assumption is not fulfilled for drops whose diameter is of a similar order of magnitude to the mean free path of the gas. Cunningham [36] therefore proposes an empirical correction factor C_C that depends on the Knudsen number. Knudsen and Weber [84] found that the model constant A_C derived by Cunningham also depends on the Knudsen number. The parameters additionally introduced by them are determined by Davies [37] using a weighted average of experimental results, leading to the following formulation:

$$C_C = \frac{1}{1 + 2 \cdot A_C \cdot Kn} \qquad \text{with} \qquad A_C = 1.257 + 0.4 \cdot e^{-1.1 \cdot \frac{1}{2 \cdot Kn}} \tag{4.10}$$

By combining Equation 4.9 and Equation 4.10, the drag coefficient can be determined taking into account the influence of the Reynolds and Knudsen numbers:

$$C_D = C_{D,SN} \cdot C_C \tag{4.11}$$

The droplet radius can be identified as one of the dominant factors influencing the magnitude of the drag force using the above equations in combination with the definition of the Knudsen number from Equation 3.53. Small droplet radii are therefore regularly cited as justification for neglecting the drag force (see, for example, [165]). Another way to estimate the relevance of considering the drag force is to evaluate the Stokes number:

$$St = \frac{2r|\boldsymbol{v}_g - \boldsymbol{v}_l|\rho_l}{9\eta_g} \cdot \frac{24}{Re \cdot C_D} \tag{4.12}$$

It describes the ratio of the relaxation time of a droplet to a characteristic time scale of the flow. The relaxation time is the time it takes for the droplet to return to an equilibrium state with respect to its mass inertia. The second term in Equation 4.12 allows for the previously introduced correction factors [61]. If $St < 0.1$, the droplets follow the flow with a maximum deviation of 1% [153]. Therefore, the drag force is only taken into account in the modelling for $St > 0.1$.

Modelling approaches for two-phase flows

Two different frames of reference can be used to describe flows. The Eulerian frame of reference subdivides a volume through which flow passes into a finite number of spatially discrete points, each representing a fluid element. The change in the flow quantities over time is recorded at each of these fixed points. This makes it possible to describe the flow as a field characterised by streamlines and is the reason why the Eulerian frame of reference is used to describe continuous flows. In contrast to the fixed Eulerian frame of reference, the reference system moves with the flow when a Lagrangian frame of reference is applied. The temporal change of the flow quantities of a specific particle is described along its trajectory. Due to the necessity of identifying individual particles, the applicability of the Lagrangian approach for continuous flows is severely limited. However, a Lagrangian frame of reference appears to be a possible option for describing the dispersed phase of a two-phase flow. In this case, a particle is represented by a group of droplets of the same size, which are influenced along their trajectory by the mechanism of droplet growth. Since the flow of the continuous phase continues to be described in an Eulerian frame of reference, the differential equations can be solved separately for each phase. This enables a numerical integration of the system of equations of the dispersed phase that is independent of the grid discretisation and the time step used for the gas phase. The possibility of under-relaxation can also positively affect the solution process of the coupled differential equations. Due to a separate consideration of the droplet size groups, it is not necessary to model possible group changes. The applicability of the combination of a Lagrangian frame of reference for the dispersed phase with an Eulerian approach for the continuous phase is significantly limited by the difficulty of parallelising the calculation steps. This is due to a constant change between the frames of reference, which negatively influences calculation time efficiency.

If the dispersed phase is described in an Eulerian frame of reference, this favours parallelisation. However, the number of equations to be solved increases compared to an Eulerian-Lagrangian approach (E-L). This leads to a high dimension of the equation system, especially when a large number of discrete droplet size classes are taken into account. Furthermore, the spatial discretisation must be chosen more finely than in the single-phase case due to the description of nucleation and droplet growth. The strong coupling of the differential equations of the two phases does not allow for classical under-relaxation and can endanger the stability of the solution process for supersonic flows in the vicinity of shocks. In addition, modelling the dispersed phase in an Eulerian frame of reference raises the question of how the change of a droplet between two size groups can be described as part of the modelling. On the other hand, considering a velocity difference between the phases is favoured by the choice of an Eulerian-Eulerian approach (E-E).

In addition to the choice of the frame of reference, the formulation of the system of equations must also be distinguished with regard to mixture-based or phase-based quantities. In the case of a mixture-based formulation (M), the number of differential equations required is reduced using additional closure conditions, as exemplarily defined in Equation 3.45. This seems particularly useful if the investigation aims to determine global quantities such as pressure or wetness fraction. If, on the other hand, the flow quantities of the individual phases are the focus of the investigation or if the velocity difference between the phases, also known as the slip (S), is to be taken into account, a phase-based formulation (P) is used.

Another factor influencing the number of equations to be solved is the type of modelling of the dispersed phase. While the assumption of a monodispersed droplet size distribution (Mono) can be taken into account using two additional differential equations, a polydispersed description (Poly) based on statistical moments of the distribution requires four additional equations. The options explained in this paragraph concerning the frame of reference of the dispersed phase, the formulation of the physical quantities, and the modelling of the dispersed phase result in a multitude of possible combinations.

From these, four variants are selected, the specification of which can be found in Table 3. In addition to the model limitations explained above, the selection criteria include, on the one hand, the relevance for the validation cases presented in Chapter 5. On the other hand, the variants are selected in such a way that the derivations presented below can be applied to the remaining combinations.

The combinations of modelling approaches listed so far aim to describe the phase change using the model of homogeneous non-equilibrium condensation. If, on the other hand, the model of homogeneous equilibrium condensation is to be used, no separate modelling of a dispersed phase is required due to the lower physical level of detail. The system of equations for single-phase flow, using a mixture-based formulation in the form of the closing conditions formulated in Equation 3.41 and Equation 3.42, is sufficient for describing two-phase flow under this assumption.

Table 3: Selected combinations of modelling approaches for the description of two-phase flows

	Frame of reference of dispersed phase		Physical quantities		Droplet size distribution		Slip	
	Eulerian	Lagrangian	Phase	Mixture	Poly	Mono	Yes	No
E-L-M-Poly		x		x	x			x
E-E-M-Mono	x			x		x		x
E-E-M-Poly	x			x	x			x
E-E-P-Poly-S	x		x		x		x	

Specification of the systems of equations to be analysed

Due to the objective of deriving a scheme for calculating the convective flux terms, the specification of the systems of equations to be examined in the following is limited to the relevant vector quantities from Equation 4.6. For the sake of a compact presentation, the derivations are also explained in only one dimension. The vectors and matrices required for a formulation in three dimensions can be found in Appendix B. Starting with the definition of the system of equations for a single-phase flow, the variants are detailed in order of increasing model complexity.

Single-phase:

$$\boldsymbol{U} = \begin{pmatrix} \rho \\ \rho u \\ \rho E \end{pmatrix}, \quad \boldsymbol{F}_c = \begin{pmatrix} \rho u \\ \rho u^2 + p \\ \rho u H \end{pmatrix}, \quad \boldsymbol{Q} = \begin{pmatrix} 0 \\ 0 \\ 0 \end{pmatrix} \tag{4.13}$$

The system of equations describing a single-phase flow represents the starting point for the consideration of a second phase presented in this work. In addition, any two-phase modelling approach must reduce to the single-phase model for $y = 0 \wedge (n = 0 \vee \mu_k = 0)$. If, in Equation 4.13, the mixture density ρ_m and the specific internal energy of the mixture e_m are used instead of the single-phase quantities, whereby the phase change is described using the model of homogeneous equilibrium condensation, it is even possible to model a two-phase flow. By combining the use of the mixture density with a description of the dispersed phase in a Lagrangian frame of reference, the physical level of detail can also be increased by applying the model of non-equilibrium homogeneous condensation.

E-L-M-Poly:

$$\frac{\partial}{\partial t}\boldsymbol{M} = \boldsymbol{Q_L} \qquad \text{with} \qquad \boldsymbol{M} = \begin{pmatrix} y \\ \mu_0 \\ \mu_1 \\ \mu_2 \end{pmatrix}, \quad \boldsymbol{Q_L} = \begin{pmatrix} \Lambda_N + \Lambda_W \\ \bar{J} \\ \mu_0 G(r_{20}) + \bar{J} r_{crit} \\ 2\mu_1 G(r_{20}) + \bar{J} r_{crit}^2 \end{pmatrix} \tag{4.14}$$

with:

$$\Lambda_N = \frac{4}{3}\pi \rho_l \bar{J} r_{crit}^3, \qquad \Lambda_G = 4\pi \rho_l \mu_2 G(r_{20})$$

In the case of modelling the droplet size distribution as polydispersed, the differential equations of the wetness fraction and the statistical moments are solved separately from the system of equations of the continuous phase from Equation 4.13. Due to the moving frame of reference, a temporal integration of the quantities of the dispersed phase represented by $\boldsymbol{M}$ is necessary for this. When defining the source term in the Lagrangian frame of reference $\boldsymbol{Q}_L$, the mass transfer between the phases is divided into a term related to nucleation Λ_N and a term related to droplet growth Λ_G.

E-E-M-Mono:

$$\boldsymbol{U} = \begin{pmatrix} \rho_m \\ \rho_m u \\ \rho_m E_m \\ \rho_m y \\ \rho_m N_T \end{pmatrix}, \quad \boldsymbol{F}_c = \begin{pmatrix} \rho_m u \\ \rho_m u^2 + p \\ \rho_m u H_m \\ \rho_m u y \\ \rho_m u N_T \end{pmatrix}, \quad \boldsymbol{Q} = \begin{pmatrix} 0 \\ 0 \\ 0 \\ \rho_m(\Lambda_N + 4\pi r^2 \rho_l N_T G(r_{20})) \\ \rho_m \bar{J} \end{pmatrix} \tag{4.15}$$

Choosing an Eulerian frame of reference to describe the dispersed phase leads to two additional differential equations if monodispersed droplets are assumed. The quantity N_T is introduced for the number of droplets per unit mass of the mixture, which for $i = 1$ corresponds to the known expression from Equation 3.44. Unlike in the case of a Lagrangian approach, the equations of the two phases are now directly coupled.

E-E-M-Poly:

$$\boldsymbol{U} = \begin{pmatrix} \rho_m \\ \rho_m u \\ \rho_m E_m \\ \rho_m y \\ \rho_m \mu_0 \\ \rho_m \mu_1 \\ \rho_m \mu_2 \end{pmatrix}, \quad \boldsymbol{F}_c = \begin{pmatrix} \rho_m u \\ \rho_m u^2 + p \\ \rho_m u H_m \\ \rho_m u y \\ \rho_m u \mu_0 \\ \rho_m u \mu_1 \\ \rho_m u \mu_2 \end{pmatrix}, \quad \boldsymbol{Q} = \begin{pmatrix} 0 \\ 0 \\ 0 \\ \rho_m(\Lambda_N + \Lambda_G) \\ \rho_m \bar{J} \\ \rho_m(\mu_0 G(r_{20}) + \bar{J} r_{crit}) \\ \rho_m(2\mu_1 G(r_{20}) + \bar{J} r_{crit}^2) \end{pmatrix} \tag{4.16}$$

If a polydispersed droplet size distribution is assumed, the number of equations to be solved increases compared to the monodispersed consideration. However, the remaining structure of the system of equations in the Eulerian approach does not change.

E-E-P-Poly-S:

$$\boldsymbol{U} = \begin{pmatrix} \rho_m(1-y) \\ \rho_m(1-y)u_g \\ \rho_m(1-y)E_g \\ \rho_m y \\ \rho_m y u_l \\ \rho_m y E_l \\ \rho_m \mu_0 \\ \rho_m \mu_1 \\ \rho_m \mu_2 \end{pmatrix}, \quad \boldsymbol{F}_c = \begin{pmatrix} \rho_m(1-y)u_g \\ \rho_m(1-y)u_g^2 + \frac{\rho_m}{\rho_g}(1-y)p \\ \rho_m(1-y)u_g H_g \\ \rho_m y u_l \\ \rho_m y u_l^2 + \frac{\rho_m}{\rho_l} y p \\ \rho_m y u_l H_l \\ \rho_m u_l \mu_0 \\ \rho_m u_l \mu_1 \\ \rho_m u_l \mu_2 \end{pmatrix}, \tag{4.17}$$

$$\boldsymbol{Q} = \begin{pmatrix} -\Lambda_N - \Lambda_G \\ -\Lambda_G u_{int} - \frac{3}{4}\frac{\rho_m y}{\rho_l \pi r^3} F_D \\ -\Lambda_G (H_{g,int} - h_v) \\ \Lambda_N + \Lambda_G \\ \Lambda_G u_{int} + \frac{3}{4}\frac{\rho_m y}{\rho_l \pi r^3} F_D \\ \Lambda_G H_{l,int} \\ \rho_m \bar{J} \\ \rho_m(\mu_0 G(r_{20}) + \bar{J} r_{crit}) \\ \rho_m(2\mu_1 G(r_{20}) + \bar{J} r_{crit}^2) \end{pmatrix} \quad \text{with} \quad \begin{cases} u_{int} = y u_l + (1-y) u_g \\ H_{g,int} = h_{s,g} + u_{int} u_g - \frac{1}{2} u_g^2 \\ H_{l,int} = h_{s,l} + u_{int} u_l - \frac{1}{2} u_l^2 \end{cases}$$

A further increase in the level of detail of the modelling is achieved by writing the system of equations separately for each phase. In addition to considering the mechanisms of nucleation and droplet growth, as already found in the previous variants, the influence of momentum exchange due to a prevailing velocity difference and heat exchange between the phases is now also modelled. The definition of the velocity u_{int} as well as the specific total enthalpy of the gaseous $H_{g,int}$ and liquid phase at the phase interface $H_{l,int}$ is based on the formulations proposed by Wróblewski and Dykas [169]. Due to the assumptions made for the model of homogeneous non-equilibrium condensation, a pressure difference at the phase interface is neglected.

In order to solve the non-linear system of equations defined by Equation 4.13, Equation 4.15, Equation 4.16 and Equation 4.17, a scheme for determining the convective fluxes across the cell boundaries of the infinitesimal control volume is required in addition to numerical methods for spatial and temporal integration. The following subchapter is therefore focused on the extension of an established flow calculation scheme for single-phase flows of ideal fluids to the description of non-ideal single- and two-phase flows, where approaches of different complexity describe the phase change according to the presented equation systems.

4.2 Extension of a Roe Scheme for Application to Single- and Two-Phase Flows of Varying Complexity

The numerical integration of the hyperbolic system of equations defined by Equation 4.13 can be illustrated by restricting to a first-order method using an explicit formulation of the conservation vector at the next discrete point in time:

$$\boldsymbol{U}_j^{n+1} = \boldsymbol{U}_j^n - \frac{\Delta t}{\Delta x}\left(\boldsymbol{F}_{c,j+\frac{1}{2}} - \boldsymbol{F}_{c,j-\frac{1}{2}}\right) \qquad \text{with} \qquad \Delta t = t^{n+1} - t^n, \;\; \Delta x = x_{j+1} - x_j \tag{4.18}$$

The temporal dimension is denoted by a superscript index, where the integration takes place between two points in time n and $n+1$ separated by the time step Δt. The spatial integration takes into account two adjacent infinitesimal control volumes, which are identified by the indices j and $j+1$. The difference in the spatial coordinates between their centres is used to define the grid point spacing Δx. Equation 4.18 is closed by the unknown quantities of the fluxes across the two cell boundaries.

A visualisation of the nomenclature used can be found in the left part of Figure 15. In order to be able to determine the quantities of the next time step $\boldsymbol{U}_j^{n+1}$ based on the known conserved quantities $\boldsymbol{U}_j^n$, knowledge of these flux terms is thus necessary. A solution of the Riemann problem defined by combining Equation 4.13 with the following initial value condition represents a suitable approach for this:

$$\left.\begin{aligned} &\tfrac{\partial}{\partial t}\boldsymbol{U} + \tfrac{\partial}{\partial x}\boldsymbol{F}_c = \boldsymbol{Q} \\ &\boldsymbol{U}(x, t=0) = \begin{cases} \boldsymbol{U}_L, & x < x_{j+\frac{1}{2}} \\ \boldsymbol{U}_R, & x > x_{j+\frac{1}{2}} \end{cases} \end{aligned}\right\} \tag{4.19}$$

The spatial coordinate with the subscript $j+\frac{1}{2}$ marks the boundary between the two infinitesimal control volumes under consideration. The flux vector represents the change in the quantities between the non-linear waves shown in the right part of Figure 15, which are separated by an interface. The conservation quantities on the left side of the domain bounded by these waves form the vector $\boldsymbol{U}_L$, while the conservation vector $\boldsymbol{U}_R$ contains the quantities on the right side. For the boundary at the spatial coordinate indexed by $j-\frac{1}{2}$ an Riemann problem equivalent to Equation 4.19 can be formulated. In most cases, these initial value problems are solved using approximative methods such as the approach formulated by Roe [124].

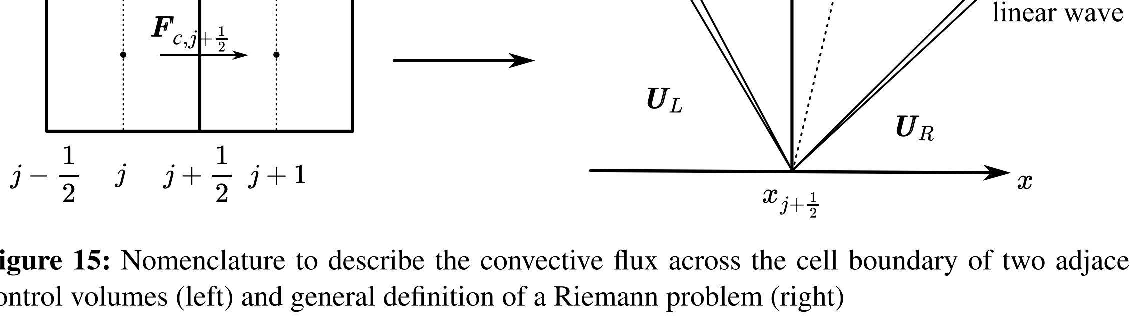

Figure 15: Nomenclature to describe the convective flux across the cell boundary of two adjacent control volumes (left) and general definition of a Riemann problem (right)

For this purpose, the system of equations is first linearised, whereby the convective flux vector is to be formulated as a function of the conservation vector:

$$\frac{\partial}{\partial t}\boldsymbol{U} + \boldsymbol{A}(\boldsymbol{U}) \cdot \frac{\partial}{\partial x}\boldsymbol{U} = \boldsymbol{Q} \qquad \text{with} \qquad \boldsymbol{A}(\boldsymbol{U}) = \frac{\partial \boldsymbol{F}_c}{\partial \boldsymbol{U}} \tag{4.20}$$

The matrix $\boldsymbol{A}(\boldsymbol{U})$ denotes the Jacobian matrix and is defined by the partial derivatives of the entries of the flux vector with respect to the components of the conservation vector. Roe replaces the Jacobian matrix by a constant matrix $\tilde{\boldsymbol{A}}(\boldsymbol{U}_L,\boldsymbol{U}_R)$, which describes the locally prevailing quantities of the states to the left and right of the interface.
This has to fulfil the following conditions:

(i) $\tilde{\boldsymbol{A}}$ defines a linear transformation of the conservation vector $\boldsymbol{U}$ onto the flux vector $\boldsymbol{F}_c$.

(ii) For $\boldsymbol{U}_L \rightarrow \boldsymbol{U} \wedge \boldsymbol{U}_R \rightarrow \boldsymbol{U}$ applies $\tilde{\boldsymbol{A}}(\boldsymbol{U}_L,\boldsymbol{U}_R) \rightarrow \boldsymbol{A}(\boldsymbol{U})$.

(iii) $\boldsymbol{F}_c(\boldsymbol{U}_L) - \boldsymbol{F}_c(\boldsymbol{U}_R) = \tilde{\boldsymbol{A}} \cdot (\boldsymbol{U}_R - \boldsymbol{U}_L)$ for any $\boldsymbol{U}_L$ and $\boldsymbol{U}_R$.

(iv) $\tilde{\boldsymbol{A}}$ has only real eigenvalues $\tilde{\lambda}$ and a complete system of linearly independent right eigenvectors $\tilde{\boldsymbol{R}}$. It is therefore diagonalisable.

As Toro [148] shows, the definition of a matrix that fulfils these conditions is very complicated for systems of equations that exceed the complexity of the three-dimensional Euler equations.
The approach proposed by Roe and Pike [125] avoids this obstacle by defining the eigenstructure required to determine the convective flux terms using the exact Jacobian matrix and then inserting selected algebraically averaged quantities. The eigenvalues of the exact Jacobian matrix can be determined as the roots of the characteristic polynomial:

$$\det\big(\boldsymbol{A}(\boldsymbol{U}) - \lambda \boldsymbol{I}\big) = 0 \qquad \longrightarrow \qquad \boldsymbol{A}(\boldsymbol{U})\boldsymbol{R} = \lambda \boldsymbol{R} \;\Leftrightarrow\; \big(\boldsymbol{A}(\boldsymbol{U}) - \lambda \boldsymbol{I}\big)\boldsymbol{R} = 0 \tag{4.21}$$

Here, $\boldsymbol{I}$ denotes the unit matrix. The eigenvectors are determined with the help of their defining property by solving a system of linear equations for each eigenvalue. As a result, the eigenstructure of the exact Jacobian matrix is uniquely determined in the form of the eigenvalues and eigenvectors. The definition of so-called Roe-averaged quantities $\tilde{q}$ algebraically links the quantities on the left and right sides:

$$\tilde{\rho} = \sqrt{\rho_L \rho_R}, \qquad \tilde{q} = \frac{\sqrt{\rho_L} q_L + \sqrt{\rho_R} q_R}{\sqrt{\rho_L} + \sqrt{\rho_R}} \qquad \text{with} \qquad q \in \{u, H, a\} \tag{4.22}$$

If these are inserted into the equations of the eigenstructure of the exact Jacobian matrix determined from Equation 4.21, the eigenstructure of the matrix $\tilde{\boldsymbol{A}}$ results. In this way, an explicit derivation of this matrix is not necessary. The convective flux across the cell boundary is formulated by Roe using the following expression:

$$\boldsymbol{F}_{c,j+\frac{1}{2}} = \frac{1}{2}\big(\boldsymbol{F}_c(\boldsymbol{U}_L) + \boldsymbol{F}_c(\boldsymbol{U}_R)\big) - \frac{1}{2}\sum_{d=1}^{3} \tilde{\alpha}_d \big|\tilde{\lambda}_d\big|^* \tilde{\boldsymbol{R}}_d \tag{4.23}$$

Where $\tilde{\alpha}$ denotes the wave strength and $|\tilde{\lambda}|^*$ denotes the corrected eigenvalue. The tilde over the formula symbols indicates that the respective quantity is determined by substituting the Roe-averaged quantities. A correction of the eigenvalues is necessary because of the possibility of violating the entropy condition for the method formulated by Roe. The entropy condition requires that the change of entropy over a shock must always be positive. To ensure this, Harten and Hyman [69] propose a correction of the eigenvalues according to the following case distinction:

$$|\tilde{\lambda}_i|^* = \begin{cases} |\tilde{\lambda}_d| & |\tilde{\lambda}_d| \geq \delta_d^* \\ \frac{1}{2}\left(\frac{\tilde{\lambda}_d^2}{\delta_d^*} + \delta_d^*\right) & |\tilde{\lambda}_d| < \delta_d^* \end{cases} \qquad \text{with} \qquad \delta_d^* = \max\left[0, \tilde{\lambda}_d - \lambda_{L,d}, \lambda_{R,d} - \tilde{\lambda}_d\right] \tag{4.24}$$

The parameter δ^* serves as a measure for the violation of the entropy condition. It is defined using a maximum function, which, in particular, ensures the positivity of the parameter. The function parameters λ_L and λ_R are determined by inserting the conservation quantities of the left and right sides, respectively, into the expressions of the eigenvalues derived from Equation 4.21. The evaluation is carried out separately for each equation d. If the absolute value of the Roe-averaged eigenvalue is greater than the value of δ^*, the entropy condition is not violated, and consequently, no correction is necessary. However, if the absolute value is smaller, the eigenvalue is corrected using the expression in Equation 4.24.

The wave strengths can be determined by projecting the change in the conservation quantities between the left and right sides, as defined by a jump, onto the Roe-averaged right eigenvectors:

$$\Delta\boldsymbol{U} = \boldsymbol{U}_R - \boldsymbol{U}_L = \sum_{d=1}^{3} \tilde{\alpha}_d \tilde{\boldsymbol{R}}_d \tag{4.25}$$

They result as coefficients of the linear system of equations defined by this equation. In order to calculate the convective flux terms using the method formulated by Roe in the context of a numerical flow solver, it is necessary to determine analytical expressions for the eigenvalues, the eigenvectors, and the Roe-averaged quantities, as described in Equation 4.23. An explicit formulation of the Jacobian matrix must also be formulated using a linearisation of the partial differential equations defining the Riemann problem to determine the eigenstructure. Roe provides corresponding expressions for the three-dimensional Euler equations under the assumption of a perfect gas.

For the extensions presented below for single- and two-phase flows of non-ideal fluids, equivalent formulations can be derived. In order to be able to make a statement in these cases about the fulfilment or violation of the conditions required by Roe for the matrix $\tilde{\boldsymbol{A}}$, this can be determined by applying a matrix transformation to the diagonal matrix of the Roe-averaged eigenvalues $\tilde{\boldsymbol{\Lambda}}$:

$$\tilde{\boldsymbol{A}} = \tilde{\boldsymbol{E}}\tilde{\boldsymbol{\Lambda}}\tilde{\boldsymbol{E}}^{-1} \qquad \longrightarrow \qquad \tilde{\boldsymbol{\alpha}} = \tilde{\boldsymbol{E}}^{-1}\Delta\boldsymbol{U} \tag{4.26}$$

The columns of the eigenvector matrix $\tilde{\boldsymbol{E}}$ contain the eigenvectors of the Jacobian matrix $\boldsymbol{A}$, which are defined by inserting the Roe-averaged quantities. Due to the property of the eigenvectors as a linearly independent basis, the eigenvector matrix is invertible. This allows an alternative way of calculating the wave strengths, which form the entries of the vector $\tilde{\boldsymbol{\alpha}}$.

Extension for application to single-phase non-ideal flows

As already discussed in Chapter 2.2, numerous approaches for extending Roe's original formulation to include single-phase non-ideal flows can be found in the literature. In most cases, the derivation focuses on a formulation of the partial derivatives of pressure contained in the Jacobian matrix that is as exact as possible, as well as on a unique definition of the Roe-averaged quantities. On the one hand, such an approach causes the scheme to depend on the type of the selected equation of state due to the specification of the defining quantities. On the other hand, the resulting formulation of the Jacobian matrix and its eigenstructure is highly complex, which can negatively affect the applicability and robustness of the method. The aim of the GIRoe scheme (*Generalised Ideal Roe*) [142] is, therefore, to ensure applicability to arbitrary equations of state while keeping the complexity of the formulation low and the robustness of the method as high as possible. To this end, it is first assumed, for the sake of simplicity, that the influence of the equation of state on the eigenstructure of the Jacobian matrix can be neglected. The derivation is thus carried out using the laws of perfect gases:

$$p = (\kappa - 1)\rho e, \qquad a^2 = \frac{\kappa p}{\rho} \tag{4.27}$$

By combining this approach with an evaluation of the thermodynamic quantities using an equation of state that deviates from the law of ideal gases, only a violation of the by Roe required condition (iii) (see page 52) is possible. The approach presented here thus belongs to the class of simplified Roe schemes.

The convective flux vector can be uniquely determined as a function of the conservation vector and the isentropic exponent:

$$\boldsymbol{F}_c(\boldsymbol{U}) = \begin{pmatrix} u_2 \\ \frac{1}{2}(3-\kappa)\frac{u_2^2}{u_1} + u_3(\kappa - 1) \\ \kappa\frac{u_2 u_3}{u_1} - \frac{1}{2}(\kappa - 1)\frac{u_2^3}{u_1^2} \end{pmatrix} \tag{4.28}$$

The systematic differentiation of the vector components with respect to the components of the conservation vector yields the following expression for the Jacobian matrix:

$$\boldsymbol{A}(\boldsymbol{U}) = \begin{pmatrix} 0 & 1 & 0 \\ \frac{1}{2}(\kappa-3)u^2 & (3-\kappa)u & \kappa - 1 \\ \frac{1}{2}(\kappa-2)u^3 - \frac{a^2 u}{\kappa-1} & \frac{3-2\kappa}{2}u^2 + \frac{a^2}{\kappa-1} & \kappa u \end{pmatrix} \tag{4.29}$$

Using Equation 4.21, the eigenstructure of the matrix can be determined as the set of its eigenvalues and eigenvectors:

$$\tilde{\lambda}_1 = \tilde{u} - \tilde{a}, \;\; \tilde{\lambda}_2 = \tilde{u}, \;\; \tilde{\lambda}_3 = \tilde{u} + \tilde{a} \tag{4.30}$$

$$\tilde{\boldsymbol{R}}_1 = \begin{pmatrix} 1 \\ \tilde{u} - \tilde{a} \\ \tilde{H} - \tilde{u}\tilde{a} \end{pmatrix}, \; \tilde{\boldsymbol{R}}_2 = \begin{pmatrix} 1 \\ \tilde{u} \\ \frac{1}{2}\tilde{u}^2 \end{pmatrix}, \; \tilde{\boldsymbol{R}}_3 = \begin{pmatrix} 1 \\ \tilde{u} + \tilde{a} \\ \tilde{H} + \tilde{u}\tilde{a} \end{pmatrix} \tag{4.31}$$

The evaluation of the Roe-averaged speed of sound is carried out using an equation of state that can be chosen freely. In addition to the classic Roe-averaged density from Equation 4.22, an additional thermodynamic state quantity is required for this. For Gibbs or Helmholtz-based multi-parameter equations of state, the Roe-averaged temperature is therefore introduced:

$$\tilde{T} = \frac{\sqrt{\rho_L} T_L + \sqrt{\rho_R} T_R}{\sqrt{\rho_L} + \sqrt{\rho_R}} \qquad \longrightarrow \qquad \tilde{a} = a_{EOS}(\tilde{\rho}, \tilde{T}) \tag{4.32}$$

If the method is to be applied to a different equation of state, the definition of Roe-averaging from Equation 4.22 must be applied to the respective pair of defining quantities. Regardless of the chosen equation of state, the thermodynamically consistent determination of the Roe-averaged state must be ensured. Since a thermodynamic state in the case of a single-phase flow is uniquely determined by an independent pair of state quantities, exactly two Roe-averaged thermodynamic quantities are to be determined using the expression from Equation 4.22. All other Roe-averaged thermodynamic quantities must be determined by evaluating the respective equation of state.

The way the Roe-averaged speed of sound is defined, as shown in Equation 4.32, has a significant influence on the stability of the method. An approach that seems comparable at first glance, which dispenses with the introduction of the Roe-averaged temperature, reads:

$$a_L = a_{EOS}(\rho_L, T_L), \quad a_R = a_{EOS}(\rho_R, T_R) \qquad \longrightarrow \qquad \tilde{a} = \frac{\sqrt{\rho_L} a_L + \sqrt{\rho_R} a_R}{\sqrt{\rho_L} + \sqrt{\rho_R}} \;\; \lightning \tag{4.33}$$

However, it turns out that such an approximation of the Roe-averaged speed of sound based on the respective quantities on the left and right sides causes numerical oscillations to develop. These negatively affect the convergence of the method and could be due to the introduction of a further numerical error caused by approximation. When extending the GIRoe scheme to the description of two-phase non-ideal flows of different complexity, the determination of the Roe-averaged quantities according to Equation 4.32 is therefore of particular relevance.

Extension for two-phase non-ideal flows of varying complexity

If the GIRoe scheme is to be used to describe two-phase flows, the way in which the phase transition is modelled determines the necessity and extent of any adjustments to be made. If the phase change is described using the model of homogeneous equilibrium condensation, the system of equations to be solved does not change, and thus, the formulation of the flux calculation scheme also remains unchanged.

E-L-M-Poly:

If the phase change is to be considered using the model of the non-equilibrium homogeneous condensation, the choice of the reference system of the dispersed phase decides whether the scheme needs to be extended.

If a Lagrangian frame of reference is chosen, it is possible to solve the conservation equations of the two-phase mixture and the transport equations of the dispersed phase separately. As a result, it is not necessary to adapt the GIRoe scheme. Instead of the quantities of the single-phase flow, the mixture quantities must be used. An explicit Euler method can be used for the temporal integration of the partial differential equations of the moments of the polydispersed droplet size distribution defined in Equation 4.14:

$$\boldsymbol{M}^{n+1} = \boldsymbol{M}^{n} + \frac{\Delta x}{u_m^n} \cdot \boldsymbol{Q}_L^n \tag{4.34}$$

The selected step size establishes a link between the spatial grid point spacing and the locally prevailing velocity of the two-phase mixture. Since the flow velocity is a solution variable of the conservation equations, a one-sided coupling of the iteration progress is possible in this way.

E-E-M-Mono:

If the dispersed phase is described in an Eulerian frame of reference, the system of equations is extended, which requires an adaptation of the flux calculation scheme. In the case of the mixture-based approach formulated by Equation 4.15, assuming a monodispersed droplet size distribution, two additional equations must be solved. Analogous to the procedure of the GIRoe scheme, the Jacobian matrix is derived using simplifying assumptions:

$$\begin{aligned} p = p_g = p_l = \rho_g(\kappa-1)e_g, &\qquad a_m^2 = \frac{p\kappa}{\rho_m} \\ \frac{1}{\rho_l} \ll 1 \ \rightarrow\ \rho_g = (1-y)\rho_m, &\qquad e_m = (1-y)e_g + ye_l \end{aligned} \tag{4.35}$$

With the help of the enthalpy of evaporation, an analytical expression can be formulated for the pressure prevailing in the two-phase mixture:

$$\begin{aligned} h_v =& \frac{p}{\rho_g(\kappa-1)} + \frac{p}{\rho_g} - \frac{1}{y}\left(e_m - \frac{(1-y)p}{\rho_g(\kappa-1)}\right) \\ \Leftrightarrow \qquad p =& \rho_m \frac{(1-y)(\kappa-1)}{(1+y(\kappa-1))}\left(yh_v + E_m - \frac{1}{2}u_m^2\right) \end{aligned} \tag{4.36}$$

The vector components of the flux vector from Equation 4.15 can thus be represented as a function of the components of the conservation vector:

$$\boldsymbol{F}_c(\boldsymbol{U}) = \begin{pmatrix} u_2 \\ \frac{u_2^2}{u_1} + (\kappa-1)\frac{1-\frac{u_4}{u_1}}{1+\frac{u_4}{u_1}\left(\kappa-1\right)}\left(u_3 - \frac{1}{2}\frac{u_2^2}{u_1} + u_4 h_v\right) \\ u_2\left[\frac{u_3}{u_1} + (\kappa-1)\frac{1-\frac{u_4}{u1}}{1+\frac{u_4}{u1}\left(\kappa-1\right)}\left(\frac{u_3}{u_1} - \frac{1}{2}\frac{u_2^2}{u_1^2} + \frac{u_4}{u_1}h_v\right)\right] \\ \frac{u_4 u_2}{u_1} \\ \frac{u_5 u_2}{u_1} \end{pmatrix} \tag{4.37}$$

The derivation of the Jacobian matrix results in the following expression:

$$\boldsymbol{A}(\boldsymbol{U}) = \begin{pmatrix} 0 & 1 & 0 & 0 & 0 \\ a_{21} & 2u_m - u_m(\kappa-1)\varepsilon_2 & (\kappa-1)\varepsilon_2 & a_{24} & 0 \\ a_{31} & a_{32} & \frac{\kappa u_m}{\kappa y - y + 1} & a_{34} & 0 \\ -yu_m & y & 0 & u_m & 0 \\ -N_T u_m & N_T & 0 & 0 & u_m \end{pmatrix} \tag{4.38}$$

with

$$\begin{aligned} a_{21} &= y\varepsilon_1 + \left(\frac{1}{2}(\kappa-1)\varepsilon_2 - 1\right)u_m^2, \qquad a_{24} = (\kappa-1)\varepsilon_2 h_v - \varepsilon_1, \\ a_{31} &= u_m\Big(y\varepsilon_1 + (\kappa-1)\varepsilon_2 u_m^2 - \big(1+(\kappa-1)\varepsilon_2\big)E_m - (\kappa-1)\varepsilon_2 y h_v\Big), \\ a_{32} &= \big(1+(\kappa-1)\varepsilon_2\big)E_m + (\kappa-1)\varepsilon_2 y h_v - \frac{3}{2}(\kappa-1)\varepsilon_2 u_m^2, \\ a_{34} &= u_m\big((\kappa-1)\varepsilon_2 h_v - \varepsilon_1\big) \end{aligned} \tag{4.39}$$

The two parameters ε_1 and ε_2 are auxiliary quantities that have been introduced for better readability:

$$\varepsilon_1 = \frac{a_m^2}{(1-y)(1+y(\kappa-1))}, \qquad \varepsilon_2 = \frac{(1-y)^2}{a_m^2}\varepsilon_1 \tag{4.40}$$

Given that $y = 0 \,\wedge\, (n = 0 \,\rightarrow\, N_T = 0)$ it is required that the Jacobian matrix from Equation 4.38 transforms into the matrix of the one-phase flow from Equation 4.29. The only exceptions to this are the columns associated with the transport equations since these are automatically dropped due to the zero rows of the flux vector involved in the matrix multiplication. Inserting the following limiting relations into Equation 4.38 and Equation 4.39 yields the proof:

$$\varepsilon_1(y=0) = a_g^2, \qquad \varepsilon_2(y=0) = 1 \tag{4.41}$$

The eigenstructure of the Jacobian matrix results in:

$$\tilde{\lambda}_1 = \tilde{u}_m - \sqrt{\varepsilon_2}\tilde{a}_m, \;\; \tilde{\lambda}_2 = \tilde{u}_m, \;\; \tilde{\lambda}_3 = \tilde{u}_m + \sqrt{\varepsilon_2}\tilde{a}_m, \;\; \tilde{\lambda}_{4,5} = \tilde{u}_m \tag{4.42}$$

$$\tilde{\boldsymbol{R}}_1 = \begin{pmatrix} 1 \\ \tilde{u}_m - \sqrt{\varepsilon_2}\tilde{a}_m \\ \tilde{H}_m - \tilde{u}_m\sqrt{\varepsilon_2}\tilde{a}_m \\ \tilde{y} \\ \tilde{N}_T \end{pmatrix}, \; \tilde{\boldsymbol{R}}_2 = \begin{pmatrix} 1 \\ \tilde{u}_m \\ \frac{1}{2}\tilde{u}_m^2 + \tilde{y}\tilde{h}_v \\ \tilde{y} \\ 0 \end{pmatrix}, \; \tilde{\boldsymbol{R}}_3 = \begin{pmatrix} 1 \\ \tilde{u}_m + \sqrt{\varepsilon_2}\tilde{a}_m \\ \tilde{H}_m + \tilde{u}_m\sqrt{\varepsilon_2}\tilde{a}_m \\ \tilde{y} \\ \tilde{N}_T \end{pmatrix}, \tag{4.43}$$

$$\tilde{\boldsymbol{R}}_4 = \begin{pmatrix} 1 \\ \tilde{u}_m \\ \tilde{H}_m - (1-\tilde{y})\tilde{h}_v \\ 1 \\ 0 \end{pmatrix}, \; \tilde{\boldsymbol{R}}_5 = \begin{pmatrix} 0 \\ 0 \\ 0 \\ 0 \\ 1 \end{pmatrix}$$

A comparison of these eigenvalues and eigenvectors with those for the case of a single-phase flow in Equation 4.30 and Equation 4.31 shows a structural similarity. Furthermore, the transferability to the single-phase limiting case can be demonstrated for the eigenstructure analogous to the Jacobian matrix.

Due to the additional transport equations, the algebraic Roe-averaging is to be applied not only to the temperature but also to the wetness fraction and the mass-related droplet number:

$$\begin{aligned} \tilde{q} = \frac{\sqrt{\rho_L} q_L + \sqrt{\rho_R} q_R}{\sqrt{\rho_L} + \sqrt{\rho_R}} \qquad & \text{with} \qquad q \in \{T, y, N_T\} \\ \longrightarrow \qquad \tilde{a}_m = a_{EOS}(\tilde{\rho}_m, \tilde{T}_m),\ \ & \tilde{h}_v = h_{v,EOS}(\tilde{T}_m),\ \ \tilde{\kappa} \approx \kappa_{pv,EOS}(\tilde{\rho}_m, \tilde{T}_m) \end{aligned} \tag{4.44}$$

Furthermore, in addition to the Roe-averaged speed of sound, the Roe-averaged evaporation enthalpy must also be determined using the equation of state. A peculiarity is the multiplication of the speed of sound of the mixture by the root of the auxiliary parameter ε_2. According to Equation 4.40, this is defined both by the wetness fraction and by the isentropic exponent. Due to the deviation of the isentropic pressure-volume exponent from the ratio of specific heat capacities in the case of compressible non-ideal fluids, as shown in Chapter 3.3, the use of the isentropic exponent, which is evaluated as the ratio of specific heat capacities, appears problematic. For this reason, the isentropic exponent is approximated by the isentropic pressure-volume exponent. The sensitivity of the overall scheme with regard to the selected formulation is checked as part of the validation.

E-E-M-Poly:

If the level of detail of the modelling of the dispersed phase is to be increased by describing the droplet size distribution as polydispersed, the number of equations increases further compared to the monodispersed description. In addition to the conservation equations of the mixture, the differential equation of the wetness fraction and the equations of the first three statistical moments of the distribution must be solved simultaneously.

The assumptions made previously in Equation 4.35 for the monodispersed approach also remain valid for the polydispersed modelling. The flux vector shown in Equation 4.16 can thus be formulated by analogy with the procedure explained above, using analytical expressions of the components of the conservation vector:

$$\boldsymbol{F}_c(\boldsymbol{U}) = \begin{pmatrix} u_2 \\ \frac{u_2^2}{u_1} + (\kappa - 1) \frac{1 - \frac{u_4}{u_1}}{1 + \frac{u_4}{u_1}\left(\kappa - 1\right)} \left(u_3 - \frac{1}{2}\frac{u_2^2}{u_1} + u_4 h_v\right) \\ u_2 \left[\frac{u_3}{u_1} + (\kappa - 1) \frac{1 - \frac{u_4}{u1}}{1 + \frac{u_4}{u1}\left(\kappa - 1\right)} \left(\frac{u_3}{u_1} - \frac{1}{2}\frac{u_2^2}{u_1^2} + \frac{u_4}{u_1} h_v\right)\right] \\ \frac{u_4 u_2}{u_1} \\ \frac{u_5 u_2}{u_1} \\ \frac{u_6 u_2}{u_1} \\ \frac{u_7 u_2}{u_1} \end{pmatrix} \tag{4.45}$$

Notably, the first three lines of the vector are identical to those of the flux vector of the monodispersed approach in Equation 4.37. Since a mixture-based notation is used in both cases and the flux terms of the mixture are linearly independent of the statistical moments of the droplet size distribution, this observation seems plausible. As a result, the Jacobian matrix can be divided into two diagonalisable submatrices:

$$\boldsymbol{A}(\boldsymbol{U}) = \begin{pmatrix} 0 & 1 & 0 & 0 & 0 & 0 & 0 \\ a_{21} & 2u_m - u_m(\kappa-1)\varepsilon_2 & (\kappa-1)\varepsilon_2 & a_{24} & 0 & 0 & 0 \\ a_{31} & a_{32} & \frac{\kappa u_m}{\kappa y - y + 1} & a_{34} & 0 & 0 & 0 \\ -y u_m & y & 0 & u_m & 0 & 0 & 0 \\ -\mu_0 u_m & \mu_0 & 0 & 0 & u_m & 0 & 0 \\ -\mu_1 u_m & \mu_1 & 0 & 0 & 0 & u_m & 0 \\ -\mu_2 u_m & \mu_2 & 0 & 0 & 0 & 0 & u_m \end{pmatrix} \tag{4.46}$$

The symbolic matrix components a_{ij} of the submatrix representing the conservation equations of the mixture match the expressions formulated in Equation 4.39 and Equation 4.40. Consequently, proof of the convertibility of the scheme for the limiting case of single-phase flow can be dispensed with. The following eigenvalues and eigenvectors give the eigenstructure of the Jacobian matrix:

$$\tilde{\lambda}_1 = \tilde{u}_m - \sqrt{\varepsilon_2}\tilde{a}_m, \;\; \tilde{\lambda}_2 = \tilde{u}_m, \;\; \tilde{\lambda}_3 = \tilde{u}_m + \sqrt{\varepsilon_2}\tilde{a}_m, \;\; \tilde{\lambda}_{4,5,6,7} = \tilde{u}_m \tag{4.47}$$

$$\tilde{\boldsymbol{R}}_1 = \begin{pmatrix} 1 \\ \tilde{u}_m - \sqrt{\varepsilon_2}\tilde{a}_m \\ \tilde{H}_m - \tilde{u}_m\sqrt{\varepsilon_2}\tilde{a}_m \\ \tilde{y} \\ \tilde{\mu}_0 \\ \tilde{\mu}_1 \\ \tilde{\mu}_2 \end{pmatrix}, \; \tilde{\boldsymbol{R}}_2 = \begin{pmatrix} 1 \\ \tilde{u}_m \\ \frac{1}{2}\tilde{u}_m^2 + \tilde{y}\tilde{h}_v \\ \tilde{y} \\ 0 \\ 0 \\ 0 \end{pmatrix}, \; \tilde{\boldsymbol{R}}_3 = \begin{pmatrix} 1 \\ \tilde{u}_m + \sqrt{\varepsilon_2}\tilde{a}_m \\ \tilde{H}_m + \tilde{u}_m\sqrt{\varepsilon_2}\tilde{a}_m \\ \tilde{y} \\ \tilde{\mu}_0 \\ \tilde{\mu}_1 \\ \tilde{\mu}_2 \end{pmatrix}, \tag{4.48}$$

$$\tilde{\boldsymbol{R}}_4 = \begin{pmatrix} 1 \\ \tilde{u}_m \\ \tilde{H}_m - (1-\tilde{y})\tilde{h}_v \\ 1 \\ 0 \\ 0 \\ 0 \end{pmatrix}, \; \tilde{\boldsymbol{R}}_5 = \begin{pmatrix} 0 \\ 0 \\ 0 \\ 0 \\ 1 \\ 0 \\ 0 \end{pmatrix}, \; \tilde{\boldsymbol{R}}_6 = \begin{pmatrix} 0 \\ 0 \\ 0 \\ 0 \\ 0 \\ 1 \\ 0 \end{pmatrix}, \; \tilde{\boldsymbol{R}}_7 = \begin{pmatrix} 0 \\ 0 \\ 0 \\ 0 \\ 0 \\ 0 \\ 1 \end{pmatrix}$$

The additional equations of the statistical moments require a further increase in Roe-averaged quantities. Algebraic Roe-averaging is applied to the temperature, the wetness fraction, and the first three statistical moments. The evaluation of the chosen equation of state also allows the determination of the Roe-averaged speed of sound and the Roe-averaged evaporation enthalpy.

Analogous to the monodispersed case, the isentropic exponent required to determine the auxiliary parameter ε_2 is approximated by the isentropic pressure-volume exponent.

$$\begin{aligned} &\tilde{q} = \frac{\sqrt{\rho_L} q_L + \sqrt{\rho_R} q_R}{\sqrt{\rho_L} + \sqrt{\rho_R}} \qquad \text{with} \qquad q \in \{T, y, \mu_0, \mu_1, \mu_2\} \\ &\longrightarrow \qquad \tilde{a}_m = a_{EOS}(\tilde{\rho}_m, \tilde{T}_m),\ \tilde{h}_v = h_{v,EOS}(\tilde{T}_m),\ \tilde{\kappa} \approx \kappa_{pv,EOS}(\tilde{\rho}_m, \tilde{T}_m) \end{aligned} \tag{4.49}$$

E-E-P-Poly-S:

In addition to a mixture-based notation, the conservation equations of the two phases can also be formulated separately. The resulting phase-based system of equations from Equation 4.17 represents not only the highest level of detail in terms of modelling the dispersed phase but also the highest degree of complexity of the system of equations. In particular, the formulation of the conservation of momentum for both phases allows for the consideration of different phase velocities. For the derivation of the Jacobian, the following simplifying assumptions are made:

$$p = p_g = p_l = \rho(\kappa_g - 1)e_g, \quad a_g^2 = \frac{p\kappa_g}{\rho_g}, \quad \rho_m = (1-y)\rho_g + y\rho_l, \quad \rho_l = const. \tag{4.50}$$

Unlike before, the liquid phase is now modelled as incompressible for the purpose of derivation. Since a derivative of the liquid density with respect to an arbitrary quantity always yields the value zero under this assumption, the determination of the phase-based Jacobian matrix can be simplified in this way. To ensure the equality of pressure required for the phase-based notation as a result of the existence of a mechanical equilibrium, a procedure that differs from the previous derivations is chosen when formulating the flux vector:

$$\boldsymbol{F}_c(\boldsymbol{U}) = \begin{pmatrix} u_2 \\ \frac{u_2^2}{u_1} + \varphi_g p \\ \frac{u_2}{u_1}\left(u_3 + \varphi_g p\right) \\ u_5 \\ \frac{u_5^2}{u_4} + \varphi_l p \\ \frac{u_5}{u_4}\left(u_6 + \varphi_l p\right) \\ \frac{u_7 u_5}{u_4} \\ \frac{u_8 u_5}{u_4} \\ \frac{u_9 u_5}{u_4} \end{pmatrix} \qquad \text{with} \qquad \begin{cases} \varphi_g = (1-y)\frac{\rho_m}{\rho_g} \\ \\ \varphi_l = y\frac{\rho_m}{\rho_l} \end{cases} \tag{4.51}$$

Toumi [152] proposes a division of the flux vector into two types of terms to determine the Jacobian matrix of a system of six differential equations, taking into account momentum exchange between the phases. While the majority of the entries of the flux vector are expressed as before in terms of the components of the conservation vector, the pressure now also remains as an explicit quantity.

The coefficients of the pressure terms can be expressed in terms of the volume fractions of the gaseous phase φ_g and the liquid phase φ_l in order to simplify the structure. This approach allows a unique analytical definition of the Jacobian matrix. The partial derivative of the pressure terms required for this is first split using the product rule:

$$\frac{\partial}{\partial u_i}\left(\varphi_{g/l}\cdot p\right)_i = \frac{\partial \varphi_{g/l}}{\partial u_i}\cdot p + \frac{\partial p}{\partial u_i}\cdot \varphi_{g/l} \tag{4.52}$$

By subsequently applying the chain rule in combination with the assumptions made in Equation 4.50, the Jacobian matrix can be formulated as follows:

$$\boldsymbol{A}(\boldsymbol{U}) = \begin{pmatrix} 0 & 1 & 0 & 0 & 0 & 0 & 0 & 0 & 0 \\ a_{21} & a_{22} & \kappa_g - 1 & a_{24} & 0 & 0 & 0 & 0 & 0 \\ a_{31} & a_{32} & \kappa_g u_g & 0 & a_{35} & 0 & 0 & 0 & 0 \\ 0 & 0 & 0 & 0 & 1 & 0 & 0 & 0 & 0 \\ a_{51} & a_{52} & a_{53} & a_{54} & 2u_l & 0 & 0 & 0 & 0 \\ a_{61} & a_{62} & a_{63} & a_{64} & a_{65} & u_l & 0 & 0 & 0 \\ 0 & 0 & 0 & -\frac{\mu_0 u_l}{y} & \frac{\mu_0}{y} & 0 & u_l & 0 & 0 \\ 0 & 0 & 0 & -\frac{\mu_1 u_l}{y} & \frac{\mu_1}{y} & 0 & 0 & u_l & 0 \\ 0 & 0 & 0 & -\frac{\mu_2 u_l}{y} & \frac{\mu_2}{y} & 0 & 0 & 0 & u_l \end{pmatrix} \tag{4.53}$$

with

$$a_{21} = \frac{1}{2}(\kappa_g - 3)u_g^2, \qquad a_{22} = (3-\kappa_g)u_g, \qquad a_{24} = \frac{\rho_g a_g^2}{\kappa_g \rho_l},$$

$$a_{31} = \frac{1}{2}(\kappa_g - 2)u_g^3 - \frac{a_g^2 u_g}{\kappa_g - 1}, \qquad a_{32} = \frac{3-2\kappa_g}{2}u_g^2 + \frac{a_g^2}{\kappa_g - 1}, \qquad a_{52} = (1-\kappa_g)\frac{y}{1-y}\frac{\rho_l}{\rho_g}u_g,$$

$$a_{64} = u_l\left(\frac{a_g^2\rho_g^2}{\kappa_g\rho_l\rho_m(1-y)} - h_l - \frac{1}{2}u_l^2\right), \qquad a_{35} = \frac{\rho_g a_g^2}{\kappa_g\rho_l}, \qquad a_{51} = \frac{(\kappa_g - 1)}{2}\frac{y}{1-y}\frac{\rho_l}{\rho_g}u_g^2,$$

$$a_{53} = (\kappa_g - 1)\frac{y}{1-y}\frac{\rho_l}{\rho_g}, \qquad a_{54} = \frac{y}{1-y}\frac{a_g^2}{\kappa_g} - u_l^2, \qquad a_{61} = \frac{(\kappa_g - 1)}{2}\frac{y}{1-y}\frac{\rho_l}{\rho_g}u_g^2 u_l,$$

$$a_{62} = (1-\kappa_g)\frac{y}{1-y}\frac{\rho_l}{\rho_g}u_g u_l, \qquad a_{63} = (\kappa_g - 1)\frac{y}{1-y}\frac{\rho_l}{\rho_g}u_l, \qquad a_{65} = h_l + \frac{1}{2}u_l^2 - \frac{\rho_g a_g^2}{\kappa_g\rho_l}$$

Due to the separate formulation of the two phases, the transferability of the matrix for the limiting case of single-phase flow can be easily recognised. If the physical quantities of the liquid phase and the statistical moments are set to zero, the entries of the submatrix in the upper left corner take on the values of the Jacobian matrix in the single-phase case. In addition, the entries below this submatrix become zero without exception so that the matrix merges completely into the system of equations of the single-phase flow.

The determination of the eigenstructure of the Jacobian matrix gives nine eigenvalues:

$$\begin{aligned} \tilde{\lambda}_1 &= \tilde{u}_g - \sqrt{\varepsilon_3}\tilde{a}_g, \ \tilde{\lambda}_2 = \tilde{u}_g, \ \tilde{\lambda}_3 = \tilde{u}_g + \sqrt{\varepsilon_3}\tilde{a}_g, \\ \tilde{\lambda}_4 &= 2\tilde{u}_l - \tilde{u}_g, \ \tilde{\lambda}_5 = \tilde{u}_l, \ \tilde{\lambda}_6 = \tilde{u}_g, \ \tilde{\lambda}_{7,8,9} = \tilde{u}_l \end{aligned} \tag{4.54}$$

The corresponding eigenvectors are:

$$\tilde{\boldsymbol{R}}_1 = \begin{pmatrix} (1-\tilde{y})\frac{\tilde{\rho}_m}{\tilde{\rho}_g}\left(1-\frac{\tilde{u}_g-\tilde{u}_l}{\sqrt{\varepsilon_3}\tilde{a}_g}\right) \\ (1-\tilde{y})\frac{\tilde{\rho}_m}{\tilde{\rho}_g}\left(1-\frac{\tilde{u}_g-\tilde{u}_l}{\sqrt{\varepsilon_3}\tilde{a}_g}\right)(\tilde{u}_g-\sqrt{\varepsilon_3}\tilde{a}_g) \\ (1-\tilde{y})\frac{\tilde{\rho}_m}{\tilde{\rho}_g}\left(1-\frac{\tilde{u}_g-\tilde{u}_l}{\sqrt{\varepsilon_3}\tilde{a}_g}\right)(\tilde{H}_g-\tilde{u}_g\sqrt{\varepsilon_3}\tilde{a}_g)+\tilde{y}\frac{\tilde{\rho}_m}{\tilde{\rho}_l}\left(1+\frac{\tilde{u}_g-\tilde{u}_l}{\sqrt{\varepsilon_3}\tilde{a}_g}\right)\frac{\tilde{p}}{\tilde{\rho}_l} \\ \tilde{y}\frac{\tilde{\rho}_m}{\tilde{\rho}_l}\left(1+\frac{\tilde{u}_g-\tilde{u}_l}{\sqrt{\varepsilon_3}\tilde{a}_g}\right) \\ \tilde{y}\frac{\tilde{\rho}_m}{\tilde{\rho}_l}\left(1+\frac{\tilde{u}_g-\tilde{u}_l}{\sqrt{\varepsilon_3}\tilde{a}_g}\right)(\tilde{u}_g-\sqrt{\varepsilon_3}\tilde{a}_g) \\ \tilde{y}\frac{\tilde{\rho}_m}{\tilde{\rho}_l}\left(1+\frac{\tilde{u}_g-\tilde{u}_l}{\sqrt{\varepsilon_3}\tilde{a}_g}\right)(\tilde{H}_l-\tilde{u}_l\sqrt{\varepsilon_3}\tilde{a}_g)-\tilde{y}\frac{\tilde{\rho}_m}{\tilde{\rho}_l}\left(1+\frac{\tilde{u}_g-\tilde{u}_l}{\sqrt{\varepsilon_3}\tilde{a}_g}\right)\frac{\tilde{p}}{\tilde{\rho}_l} \\ 0 \\ 0 \\ 0 \end{pmatrix}, \tag{4.55}$$

$$\tilde{\boldsymbol{R}}_2 = \begin{pmatrix} 1 \\ \tilde{u}_g \\ \frac{1}{2}\tilde{u}_g^2 \\ 0 \\ 0 \\ 0 \\ 0 \\ 0 \\ 0 \end{pmatrix}, \tilde{\boldsymbol{R}}_3 = \begin{pmatrix} (1-\tilde{y})\frac{\tilde{\rho}_m}{\tilde{\rho}_g}\left(1+\frac{\tilde{u}_g-\tilde{u}_l}{\sqrt{\varepsilon_3}\tilde{a}_g}\right) \\ (1-\tilde{y})\frac{\tilde{\rho}_m}{\tilde{\rho}_g}\left(1+\frac{\tilde{u}_g-\tilde{u}_l}{\sqrt{\varepsilon_3}\tilde{a}_g}\right)(\tilde{u}_g+\sqrt{\varepsilon_3}\tilde{a}_g) \\ (1-\tilde{y})\frac{\tilde{\rho}_m}{\tilde{\rho}_g}\left(1+\frac{\tilde{u}_g-\tilde{u}_l}{\sqrt{\varepsilon_3}\tilde{a}_g}\right)(\tilde{H}_g+\tilde{u}_g\sqrt{\varepsilon_3}\tilde{a}_g)+\tilde{y}\frac{\tilde{\rho}_m}{\tilde{\rho}_l}\left(1-\frac{\tilde{u}_g-\tilde{u}_l}{\sqrt{\varepsilon_3}\tilde{a}_g}\right)\frac{\tilde{p}}{\tilde{\rho}_l} \\ \tilde{y}\frac{\tilde{\rho}_m}{\tilde{\rho}_l}\left(1-\frac{\tilde{u}_g+\tilde{u}_l}{\sqrt{\varepsilon_3}\tilde{a}_g}\right) \\ \tilde{y}\frac{\tilde{\rho}_m}{\tilde{\rho}_l}\left(1-\frac{\tilde{u}_g-\tilde{u}_l}{\sqrt{\varepsilon_3}\tilde{a}_g}\right)(\tilde{u}_g+\sqrt{\varepsilon_3}\tilde{a}_g) \\ \tilde{y}\frac{\tilde{\rho}_m}{\tilde{\rho}_l}\left(1-\frac{\tilde{u}_g-\tilde{u}_l}{\sqrt{\varepsilon_3}\tilde{a}_g}\right)(\tilde{H}_l+\tilde{u}_l\sqrt{\varepsilon_3}\tilde{a}_g)-\tilde{y}\frac{\tilde{\rho}_m}{\tilde{\rho}_l}\left(1-\frac{\tilde{u}_g-\tilde{u}_l}{\sqrt{\varepsilon_3}\tilde{a}_g}\right)\frac{\tilde{p}}{\tilde{\rho}_l} \\ 0 \\ 0 \\ 0 \end{pmatrix},$$

$$\tilde{\boldsymbol{R}}_4 = \begin{pmatrix} 1 \\ 2\tilde{u}_l-\tilde{u}_g \\ \frac{\tilde{p}}{\tilde{\rho}_g\tilde{a}_g}\left(\tilde{H}_g-\frac{1}{2}\tilde{u}_g^2\right)+\tilde{u}_g\left(\frac{1}{2}\tilde{u}_g-2\tilde{u}_l\right) \\ 0 \\ 0 \\ 0 \\ \tilde{\mu}_0 \\ \tilde{\mu}_1 \\ \tilde{\mu}_2 \end{pmatrix}, \tilde{\boldsymbol{R}}_5 = \begin{pmatrix} 0 \\ 0 \\ 0 \\ 0 \\ 0 \\ \tilde{u}_l \\ 0 \\ 0 \\ 0 \end{pmatrix}, \tilde{\boldsymbol{R}}_6 = \begin{pmatrix} 1 \\ \tilde{u}_g \\ \frac{\tilde{p}}{\tilde{\rho}_g\tilde{a}_g}\left(\tilde{H}_g-\frac{1}{2}\tilde{u}_g^2\right)+\frac{1}{2}\tilde{u}_g^2 \\ 0 \\ 0 \\ 0 \\ \tilde{\mu}_0 \\ \tilde{\mu}_1 \\ \tilde{\mu}_2 \end{pmatrix},$$

$$\tilde{\boldsymbol{R}}_7 = \begin{pmatrix} 0 & 0 & 0 & 0 & 0 & 0 & 1 & 0 & 0 \end{pmatrix}^{\mathsf{T}}, \qquad \tilde{\boldsymbol{R}}_8 = \begin{pmatrix} 0 & 0 & 0 & 0 & 0 & 0 & 0 & 1 & 0 \end{pmatrix}^{\mathsf{T}},$$

$$\tilde{\boldsymbol{R}}_9 = \begin{pmatrix} 0 & 0 & 0 & 0 & 0 & 0 & 0 & 0 & 1 \end{pmatrix}^{\mathsf{T}} \qquad \text{with} \qquad \varepsilon_3 = \frac{(1-\tilde{y})\tilde{\rho}_l^2+\tilde{y}\tilde{\rho}_g^2}{\tilde{\rho}_g\tilde{\rho}_l}$$

Analogous to the previously introduced auxiliary quantities, the parameter ε_3 serves to improve readability. The determination of the variables required in addition to those Roe-averaged quantities defined by Equation 4.22 is limited to the Roe-averaged speed of sound of the gas phase and the Roe-averaged pressure, along with the typical representatives for the polydispersed approach:

$$\begin{aligned} \tilde{q} &= \frac{\sqrt{\rho_L} q_L + \sqrt{\rho_R} q_R}{\sqrt{\rho_L} + \sqrt{\rho_R}} \qquad \text{with} \qquad q \in \{T, y, \mu_0, \mu_1, \mu_2\} \\ \longrightarrow \qquad & \tilde{a}_g = a_{EOS}(\tilde{\rho}_g, \tilde{T}_g), \;\; \tilde{p} = p_{EOS}(\tilde{\rho}_g, \tilde{T}_g) \end{aligned} \tag{4.56}$$

Especially in this case, however, the previously explained thermodynamic consistency must be maintained due to the large number of quantities to be determined. A comparison of the structure of the eigenvalues and eigenvectors of the phase-based notation with those of the mixture-based approach in Equation 4.48, which is equivalent in terms of modelling the droplet size distribution, illustrates the algebraic similarity. In both cases, the quantity of the speed of sound, which is central to the Roe scheme, is multiplied by a factor that has a dominant dependence on the wetness fraction.

A characteristic systematic of the eigenstructures can be recognized for all considered variants, including the single-phase formulation. With an increasing level of detail in the thermophysical modelling of the phase change, only the number of variables and terms to be considered increases. The derived extensions of the GIRoe scheme for two-phase non-ideal flows of different complexity are thus characterised by three distinctive properties:

(i) Their derivation is based on simplifying assumptions regarding the modelling of the thermodynamic state quantities so that the resulting matrices have relatively low complexity.

(ii) By evaluating all thermophysical quantities based on an arbitrary, explicitly selected equation of state, any simplifications are isolated to the area of derivation. This becomes particularly evident by determining selected Roe-averaged quantities by means of the equation of state.

(iii) Each of the formulations presented above is transformed into the single-phase GIRoe scheme by negating a liquid phase. In addition, their eigenstructures have a characteristic structure that is retained regardless of the type of liquid phase modelling selected.

In the interests of uniform nomenclature the methods presented are therefore referred to below as the *Phase Generalised Ideal Roe* (PGIRoe) scheme. Since the GIRoe scheme is also incorporated into this designation, the PGIRoe scheme is able to describe single-phase and two-phase flows of compressible non-ideal fluids. A variety of different modelling approaches can be selected for modelling the liquid phase. In order to be able to validate the introduced variants of flow calculation schemes using physical test cases, a modular implementation in the flow solver TRACE is carried out.

4.3 Implementation of the PGIRoe Scheme in the Flow Solver TRACE

TRACE is a density-based flow solver developed by the DLR specifically for use in turbomachinery. It is used in both academic and industrial environments to investigate research questions in aerodynamics, aeroelastics, aeroacoustics, and aerothermodynamics. To this end, the three-dimensional Reynolds-averaged Navier-Stokes equations are solved. While a second-order Roe scheme is used to determine the convective flux terms, the viscous flux terms are discretised using second-order central differences. Several methods with different levels of accuracy are available for spatial discretisation. The second-order formulations include, among others, a Monotonic Upstream-centred Scheme for Conservation Laws (MUSCL). The temporal integration of the system of equations can be carried out using a Gauß-Seidel approach or a *predictor-corrector* formulation based on implicit first- and second-order methods. If the flow is to be investigated in a temporally resolved manner, higher-order methods are used for the temporal integration. Moreover, TRACE is able to calculate corresponding solutions of the flow field for both structured and unstructured grids, as well as combinations of these two types. It also offers a variety of turbulence models to choose from. However, the underlying modelling of thermophysical quantities represents a significant limitation to the applicability of the flow solver.

Evaluation of thermophysical quantities in TRACE

The gas models in TRACE are limited to the models of the caloric perfect and the thermally perfect gas. Consequently, the law of ideal gases is the only thermal equation of state available. When modelling as a thermally perfect gas, the temperature-dependent specific heat capacities are determined by polynomials characterised by fluid-specific coefficients. A model equation formulated by Sutherland is used to calculate the dynamic viscosity, which contains a fluid-specific constant and the temperature as parameters. However, it is not possible to describe the fluid as non-ideal on the basis of the models implemented in TRACE. Therefore, due to the objective of the present work, an additional gas model for non-ideal fluids is implemented first.

As shown in Chapter 3.2, multi-parameter equations of state allow the thermophysical quantities to be determined with a high degree of accuracy. They are, therefore, selected for the description of non-ideal fluids in TRACE. Since multi-parameter equations of state are fluid-specific formulations, this choice requires the implementation of one equation of state per fluid species. Furthermore, different combinations of state quantities arise in the course of the iterative solution, so further iterative routines are needed alongside the explicit form of the equation of state. If all these equations and routines are to be implemented directly in TRACE, limiting the number of fluid species seems unavoidable. However, by integrating the REFPROP database of the National Institute of Standards and Technology (NIST) [91], such a limitation can be avoided. The results presented below are based on version 10 of this database. It contains 147 pure substances as well as a large number of mixtures. In addition to the equations of state and the iterative routines, the database also provides corresponding model equations for determining the transport quantities for each fluid.

The routines in REFPROP for evaluating the thermophysical quantities can be called up directly in TRACE via a corresponding interface. When selecting the routines, particular attention should be paid to possible limitations concerning specific state ranges. In particular, suitable routines must be used for the supercritical range as well as the two-phase region.

Otherwise, unphysical values may be calculated. The metastable state range of the gas phase can be evaluated by forcing a search for solutions in the gaseous state or by means of a bilinear extrapolation. Since the REFPROP database only includes Helmholtz-based equations of state $\mathscr{F}_\Phi$, an additional equation of state for the medium water in terms of the IAPWS-IF97 is implemented directly in TRACE. Wagner and Kretzschmar [158] provide explicit polynomial equations for this equation of state as a replacement for the required iterative routines. The equations used to calculate the transport quantities of water are implemented according to the sources given in Appendix A. In this way, the evaluation of the thermophysical quantities of non-ideal fluids in general and those to be investigated in the context of this work can be ensured in TRACE.

However, it turns out that a direct evaluation of the equation of state and, in particular, the iterative calculation of state quantities is very computationally expensive. Since a large number of these operations have to be performed per iteration step and node of the spatial grid, this leads to very long computing times when investigating non-ideal fluids. One way to address this challenge is to store the thermophysical quantities in tables.

Storage of thermophysical quantities as tables

Such an approach is already established in the field of thermodynamics using classical steam tables. For this purpose, arbitrary state quantities z are determined as a function of two independent quantities and stored in a table together with these. To be able to map a large number of states, the two defining quantities are varied within selected intervals. The number of elements in these intervals determines the discretisation of the state range defined by the interval boundaries. If an arbitrary state within these limits is to be evaluated, an interpolation between the discrete entries in the table must be carried out.

In addition to the classic linear approach, various higher-order formulations are available. These include the method proposed by Miyagawa and Hill [100], which expresses the quantity z using a Taylor series expansion truncated after the second term. Consequently, it is a second-order formulation that takes the following form for a Helmholtz-based equation of state:

$$\begin{aligned} z = z_{i,j} &+ (\rho-\rho_i)\left(\frac{\partial z}{\partial \rho}\right)_{i,j} + (T-T_j)\left(\frac{\partial z}{\partial T}\right)_{i,j} \\ &+ \frac{1}{2}(\rho-\rho_i)^2\left(\frac{\partial^2 z}{\partial \rho^2}\right)_{i,j} + \frac{1}{2}(T-T_j)^2\left(\frac{\partial^2 z}{\partial T^2}\right)_{i,j} \\ &+ (\rho-\rho_i)(T-T_j)\left(\frac{\partial^2 z}{\partial \rho \partial T}\right)_{i,j} \end{aligned} \tag{4.57}$$

The table used for storage can also be interpreted as a two-dimensional structure whose dimension is directly linked to the chosen discretisation of the tabulated state range. If an equal number n_T of different values is chosen for both defining quantities, then n_T^2 uniquely determined thermodynamic states result. Consequently, the resulting square matrix of the storage structure must also have the dimension n_T.

To be able to interpolate the state quantity z using Equation 4.57, all equation terms must be known. These include, in particular, the required first and second-order derivatives.

For a Helmholtz-based equation of state, a suitable memory structure would be as follows:

$$\begin{array}{c|cccc|}
 & T_1 & \cdots & \cdots & T_{n_T-1}+\Delta T \\
\rho_1 & z_{1,1},\Delta_{1,1} & \cdots & \cdots & z_{1,n_T},\Delta_{1,n_T} \\
\vdots & \vdots & \ddots & & \vdots \\
\vdots & \vdots & & \ddots & \vdots \\
\rho_{n_T-1}+\Delta\rho & z_{n_T,1},\Delta_{n_T,1} & \cdots & \cdots & z_{n_T,n_T},\Delta_{n_T,n_T}
\end{array} \tag{4.58}$$

$$\text{with} \qquad \Delta_{i,j} = \left\{ \left(\frac{\partial z}{\partial \rho}\right)_{i,j}, \left(\frac{\partial z}{\partial T}\right)_{i,j}, \left(\frac{\partial^2 z}{\partial \rho^2}\right)_{i,j}, \left(\frac{\partial^2 z}{\partial T^2}\right)_{i,j}, \left(\frac{\partial^2 z}{\partial \rho \partial T}\right)_{i,j} \right\}$$

For the sake of clarity, the set Δ represents the derivative terms. Using such a matrix structure, it is possible to store the terms required for the interpolation of any number of quantities z. It is only necessary to ensure that the choice of defining quantities remains unchanged. Separate memory structures must be created for the quantities to be determined using iterative routines $\mathscr{F}_{\Phi}^{iter}$. These differ from the form shown in Equation 4.58 in terms of their defining quantities. Both the thermophysical equations and the iterative routines are evaluated multiple times in each iteration step during CFD calculations.

According to an overview in the left part of Figure 16, three possible types of evaluation of the thermophysical routines can be distinguished. In addition to a direct evaluation of any quantity, a gradual use of memory structures, indicated by the index *tab*, is possible. The latter distinguishes between tabulating all quantities or only those determined by the iterative routines. The reason for such a gradual approach lies in the observation that a particularly high computing time is required to evaluate the iterative routines.

In order to examine this in detail, the computing time for different numbers of queries n_A to be performed is examined as a function of the three types of evaluation, using the example of the medium CO_2. A representative set of routines, which TRACE runs through per spatial and temporal iteration, forms the basis of the analysis. The random selection of different thermodynamic states is carried out within a defined state range of CO_2. The multiplication of the number of selected states with the number of routines included in the set yields the number of queries. To ensure the comparability of the test results, the three types of evaluation are each subjected to identical queries. The tables generated for the considered state range are also used in the same way for all types of evaluations. In addition, three repetitions are carried out for each type of evaluation to determine the required computing times. The respective results of these three runs are then arithmetically averaged.

The right part of Figure 16 shows a plot of the computing time obtained in this way versus the number of queries in millions for direct evaluation and the two different levels of memory structure usage. As expected, storing all thermophysical quantities in the form of tables leads to a significant decrease in computing time compared to direct evaluation. Since the tables in TRACE are created before runtime and can be reused as often as required due to their storage in the input file, the computing time of the tabulated variants includes reading the storage structure into the main memory. However, even for the lowest number of queries examined, the additional time required for this does not result in any disadvantage compared to direct evaluation. If a linear regression is applied to the data points of the three evaluation types, a high degree of correlation with the respective regression lines can be seen in

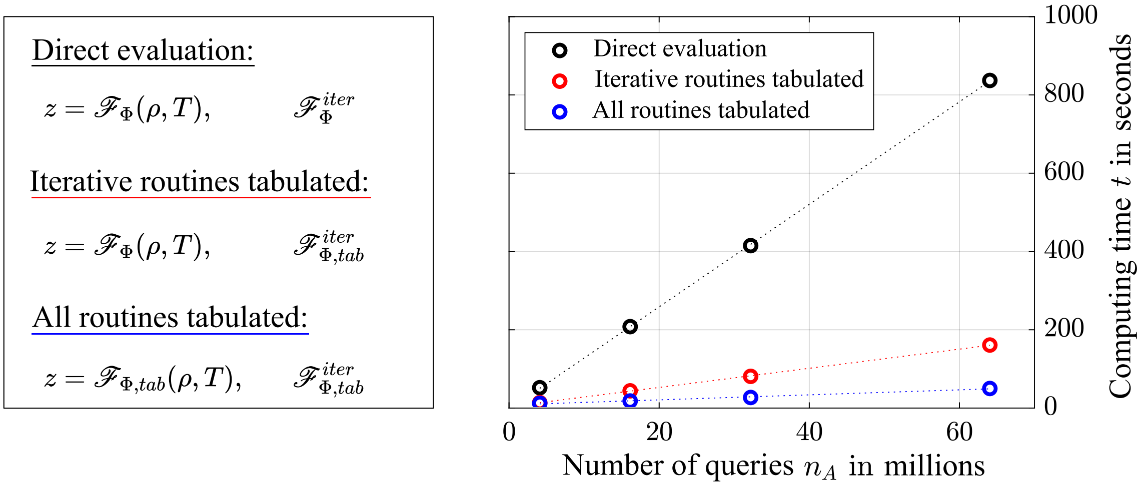

Figure 16: Required computing time as a function of number of queries for different types of evaluation of the thermophysical routines taking the medium CO_2 as an example; dotted lines represent a linear regression of data points

all three cases. The computing time thus scales approximately linearly with the number of queries, whereby the slopes of the lines show strongly differing values. This is particularly evident for the highest number of queries examined. In this case, using a table for the iterative routines instead of a direct evaluation reduces the computing time by a factor of five. If the remaining thermophysical routines are also stored in tabular form, a further reduction in computing time by a factor of three can be achieved. However, the advantage in terms of computing time is inevitably accompanied by a decrease in the accuracy of the evaluated thermophysical quantities. The discretisation of the table and the gradients of the thermophysical quantities in the state range under consideration significantly influence the resulting accuracy of the results.

To illustrate this, two state regions of CO_2 are highlighted in colour in the left part of Figure 17, whose interval boundaries are characterised by equal pressure and temperature differences. Region I in red encompasses the immediate vicinity of the critical point, which, in addition to low values of the compressibility factor, also exhibits particularly large gradients of the state quantities at the limiting curves of the continuous and discontinuous phase transitions. By selecting the blue region II at a suitable distance from the critical point, states that are characterised by a less pronounced non-ideality can be found within its boundaries. Suppose the same dimension of the table is selected when tabulating the thermophysical quantities of the two regions. In that case, the definition-dependent equal pressure and temperature differences also result in a corresponding discretisation. This property is now to be used to examine the influence of the state region on the accuracy of the tabulated quantities in isolation. In addition to the density, the speed of sound and the specific isobaric heat capacity are selected as parameters for investigation. As discussed in Chapter 3, the speed of sound in the vicinity of the saturated vapour line and the isobaric heat capacity in the immediate vicinity of the Widom line exhibit large gradients, making their evaluation particularly sensitive.

For each of the two regions, the state quantities are tabulated according to their defining quantities, with four different table dimensions being selected in each case. A dimension of 100 represents the lowest resolution, while the table with the finest discretisation has a dimension of 1000. Within the two regions to be examined, 250,000 different thermody-

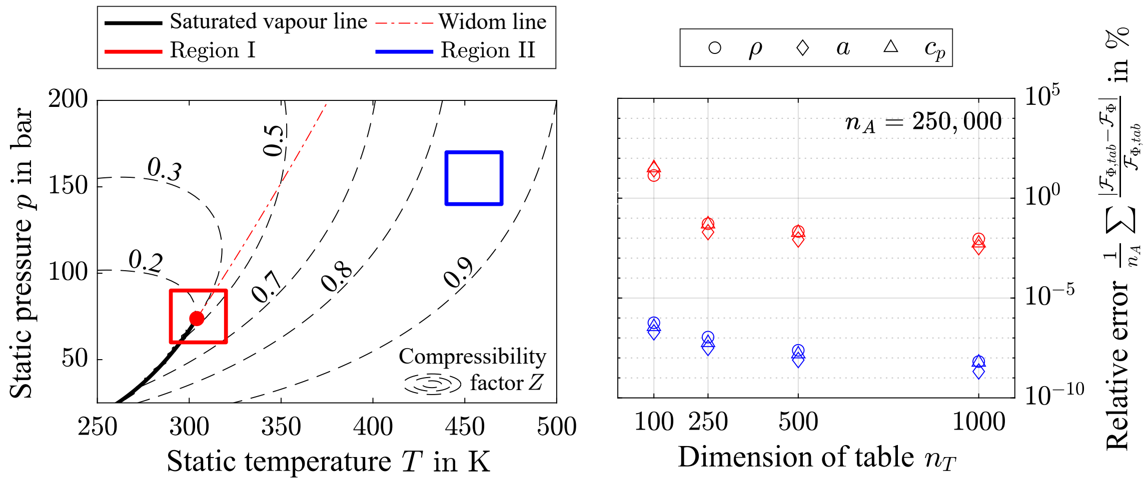

Figure 17: Definition of two investigation regions of CO_2 in a p-T diagram (left) and graph of the relative error of the evaluation of density, speed of sound and specific isobaric heat capacity using tables of different dimensions (right)

namic states are randomly selected as representative sample sets. Their number is equivalent to the already known quantity of the number of queries. The three examination parameters are determined for each of these states by direct evaluation and interpolating the four tables. For each query, the absolute difference between the interpolation results and the result of the direct evaluation is calculated and related to the former. Subsequently, the related differences are summed up for each parameter and table dimension. Dividing this result by the number of queries yields the relative error of the tabular evaluation, which is plotted in percent in the right part of Figure 17. The values for Region I are shown in red, corresponding to the previous colour scheme, and the results for Region II appear in blue.

The relative error values of the table-based evaluation of the state for Region II are at least five orders of magnitude smaller than for Region I, regardless of the table dimension considered. This observation seems plausible since Region I, unlike Region II, is characterised by large gradients of the examination parameters. For both regions, the value of the relative error decreases with increasing table dimension, although this effect is much more pronounced for low dimensions. In addition, the three test parameters show only slightly different values of the relative error for each selected region and table dimension, so the validity of the derived conclusions can be assumed independently of the table type. While the tables generated for Region II all seem suitable for CFD calculations, this has to be checked for Region I due to the comparatively high relative error values for the specific application. As part of such an investigation, a table dimension suitable for compliance with a defined error bound can be determined for any state region.

In particular, for a high number of queries, as they occur, for example, when using very fine spatial grids, the evaluation using tabulated data shows great potential by combining a considerable saving of computing time with sufficient result accuracy. In addition, a refinement of the tables by simply increasing the dimension only leads to an increase in the time required for the initial reading of the memory structures and an increased demand for memory. However, up to a dimension of 1000, the influence of these two factors appears negligible for TRACE. The number of required memory structures, which depends on the type of flow to be examined, must be taken into account. While two memory structures are to be processed in the case of a single-phase flow, this number increases to five for two-phase flows.

If the phase change is described using the model of homogeneous equilibrium condensation, only the saturation quantities need to be stored alongside the gas quantities as an additional structure. However, modelling the liquid phase as dispersed in the continuous phase requires tabulating the state quantities comparable to that for the gas phase, using two additional memory structures. This is one of many factors to be considered when conceptualising a module to take a second phase into account in TRACE.

Conceptual design of a module to take into account a second phase

While the already introduced gas model of non-ideal fluids is integrated into the group of gas models available in TRACE, the development of a separate module, called *TwoPhase*, seems useful for taking a second phase into account. This is essentially motivated by three aspects. Firstly, the separation of the routines enables a minimally invasive implementation. If a two-phase flow is to be calculated with TRACE, the single-phase main code merely calls the module once per spatial and temporal iteration, triggered by a binary parameter defined in the input file. On the other hand, the module can be deactivated at any time without affecting the functionality of the rest of the flow solver due to its self-contained nature. This is particularly relevant because the developed implementation is an external enhancement of the code quality assured by the DLR. Finally, the modular structure provides a way to develop further and expand the modelling approaches that are almost entirely decoupled from the developments in the main code.
To support the latter aspect, the module is divided into three sub-modules, as visualised in Figure 18. The first of these sub-modules includes the evaluation of the thermophysical

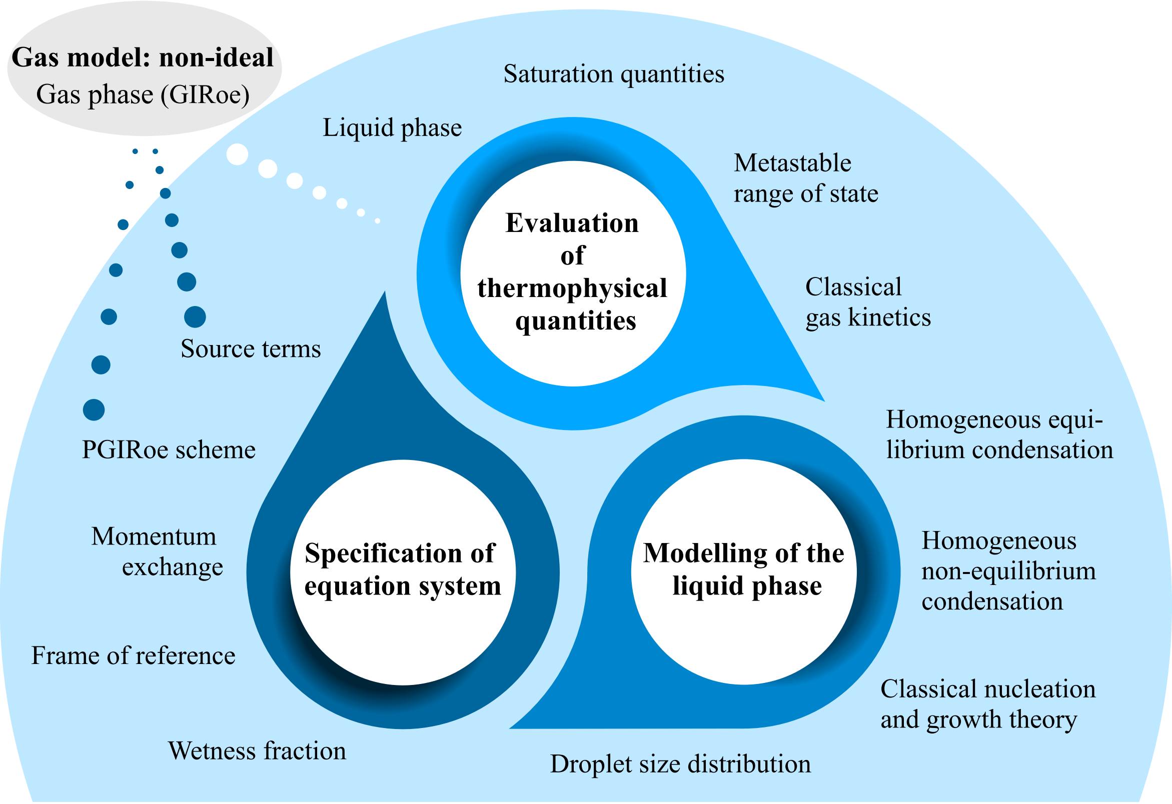

Figure 18: Structure of the module TwoPhase for the consideration of a second phase in TRACE

quantities of both phases. While the routines for determining the quantities of the liquid phase, the saturation states, the metastable state range, and the classical gas kinetics can be found directly in this submodule, the evaluation of the gas quantities is based on an interface to the gas model of the non-ideal fluid. The decision between a direct or tabulated evaluation of the routines is made via a further binary parameter in the input file.

The routines associated with modelling the liquid phase can be found in the second submodule. These include, in particular, the modelling approaches of the phase change as homogeneous equilibrium and non-equilibrium condensation. In the case of the latter, a determination of different quantities of the classical nucleation and growth theory, as well as a mathematical specification of the droplet size distribution, is necessary. Similar to the binary parameter, which activates the consideration of a second phase at the beginning of the calculation, further input options allow the user to choose between the different types of phase change modelling and the respective sub-models.

The combination of these results in the formulation of the wetness fraction, which is part of the routines of the third submodule for specifying the system of equations. The choice of the reference system, which is also controlled by binary input file parameters, and the consideration of momentum exchange between the phases, leads to a unique definition of the modelling of the second phase. Based on this, the formulation of the system of equations to be solved can be specified by the source terms and the PGIRoe scheme.

In combination with the routines available in TRACE for solving single-phase flows and the boundary conditions adapted for considering a second phase, the iterative calculation of the two-phase flow field is possible. In order to ensure the functionality of the single-phase implementation for non-ideal fluids independently of the *TwoPhase* module, the GIRoe scheme contained in the PGIRoe scheme is additionally implemented in the single-phase main code. In this way, the desired type of flow modelling can be defined in the input file by combining the binary parameters that act as mathematical switches. Before the extension of the flow solver TRACE, with the inclusion of a second phase and thus the PGIRoe scheme contained in it, is validated using a selection of physical test cases, it seems useful to introduce the methods used to assess numerical solutions.

4.4 Methods for Evaluating Numerical Solutions

The nomenclature used in this context is based on the guideline formulated by the American Institute of Aeronautics and Astronautics (AIAA) for verifying and validating CFD calculations. Verification ensures that the implementation correctly reproduces a solution derived from the underlying models. An example of this could be comparing an analytically determined solution to a specific problem with the numerical calculation results. A plausibility check based on fundamental physical relationships is also conceivable.

Validation, on the other hand, refers to a procedure that checks the extent to which the results of a CFD calculation match the flow quantities observed in reality. The comparison of experimentally collected data with the results of a corresponding CFD simulation can be used for this purpose. In order to validate the model of the PGIRoe scheme and its implementation in TRACE, a staged approach involving verification prior to validation is therefore required.

Since CFD methods inevitably simplify reality on the basis of a large number of different model assumptions, the concept of error is at the centre of every verification and validation. A distinction can be made between different types of error. If the source of the error can be clearly identified, as is the case with programming or usage errors, the influence of the error on the calculation results can be eliminated by means of a corresponding correction. However, if the error is based on an underlying assumption or procedural aspect of the modelling, it remains intrinsic to the respective CFD method. In addition to discretisation errors, approximation errors of physical models, and errors associated with the iterative solution of the system of equations, this type of error also includes rounding errors caused by the use of computers. These errors must be systematically investigated to assess the significance of the numerical solution to a physical problem.

In order for a numerical representation of a physical test case to be considered validated, the influence of the individual sources of error must either be negated, or it must be possible to qualitatively and quantitatively classify them. For discretisation errors and errors caused by the iterative solution, proof of the independence of a numerical solution from the source of the error is often sought. Maintaining methodological consistency and falling below a defined error threshold serve as sufficient criteria for this.

Independence of the solution from the spatial discretisation

Since the present work is concerned exclusively with calculating flows that can be assumed to be stationary, the consideration of the classical discretisation errors is limited to the spatial extent. For this purpose, the procedure documented by Roache [123] is followed.

Starting from a coarse spatial grid identified by index 4 in the following, a systematic grid refinement is carried out. The respective number of nodes in the three spatial directions is multiplied by a factor r_G, which is to be chosen as an integer. The resulting medium grid is designated by the index 2. A further refinement using the previously defined factor leads to a further increase in the number of nodes and forms the finest grid with index 1.

Based on the spatial grids generated in this way, a flow solver can determine three numerical solutions of the flow field for a specific case. The quantity z is chosen such that it represents a characteristic quantity for the case under consideration. By evaluating it for the three different grids, an expression for calculating the convergence order of the grid θ_G can be formulated:

$$\theta_G = \ln\left(\frac{z_4 - z_2}{z_2 - z_1}\right) / \ln(r_G) \tag{4.59}$$

The calculated convergence order can be compared with the theoretical convergence order of the solution method. TRACE uses a second-order method for spatial discretisation so that the theoretical convergence order also takes the value of two. To ensure the consistency of the method, the calculated convergence order must, therefore, have a value of approximately two.

If this criterion is met, an estimate can be made using a Richardson extrapolation, from which node number onwards, a further grid refinement no longer has a relevant influence on the numerical solution. By neglecting all terms with an order greater than two, Roache derives an expression for the Richardson extrapolation z_{RE} for the quantity under investigation, which depends on the results of the medium and fine grid, as well as the grid refinement factor and the order of convergence:

$$z_{RE} = z_1 + \frac{z_1 - z_2}{r_G^{\theta_G} - 1} \tag{4.60}$$

Its value can be interpreted as an approximation of the solution on a spatial grid with an infinite number of nodes and, thus, a grid point spacing of zero. Since a comparison of the Richardson extrapolation with an analytical solution is not possible for most numerical test cases due to the lack of an analytical solution, it serves as a benchmark. The independence of the solution from the spatial discretisation can be assumed for the corresponding grid if the relative deviation of the characteristic quantity determined for the three grids from the value of the Richardson extrapolation falls below a predefined error threshold. The error threshold must be selected appropriately for the case under investigation. As shown earlier in this chapter, evaluating tabulated data of thermophysical quantities also involves a discretisation and, thus an associated error.

Independence of the solution from the discretisation of the tabulated quantities

Unlike the case of classical discretisation errors, there is no standardised procedure in the literature for investigating this type of error. However, the property of a table as a two-dimensional structure can also be used here by interpreting it as a grid in two spatial directions.

Similar to the procedure for examining spatial grid independence, a coarse table marked with the index 4 is generated first. Multiplying the table dimension by an integer refinement factor r_T results in a medium table marked with the index 2. The finest table indexed with 1 represents a further increase in dimension based on the previously selected factor. Unlike in the context of spatial discretisation, the evaluation of characteristic quantities of a flow simulation does not appear to be sufficient here. Rather, an investigation of the independence of the solution from the discretisation of the tabulated quantities aims at the deviation between the direct evaluation and an evaluation based on tables. When quantifying this, it is essential to use a representative sample size; otherwise, repeatability cannot be guaranteed.

The deviation χ averaged based on the number of queries is therefore used as a parameter. If this is evaluated for the coarse, medium, and fine table, the order of convergence of the table θ_T can be calculated as follows:

$$\theta_T = \ln\left(\frac{\chi_4 - \chi_2}{\chi_2 - \chi_1}\right) / \ln(r_T) \qquad \text{with} \qquad \chi = \frac{1}{n_A} \sum |\mathscr{F}_{\Phi,tab} - \mathscr{F}_{\Phi}| \tag{4.61}$$

According to Equation 4.57, the interpolation of the tabulated quantities has a second-order truncation error. Consequently, the theoretical convergence order of the table is two. To ensure the consistency of the method, the calculated convergence order must not deviate significantly from this value. If this criterion is met, a statement about the dimension required for the independence of the results from the discretisation of the table can be derived using the Richardson extrapolation χ_{RE}. The formulation for this follows the procedure presented for spatial discretisation:

$$\chi_{RE} = \chi_1 + \frac{\chi_1 - \chi_2}{r_T^{\theta_T} - 1} \xrightarrow{!} 0 \tag{4.62}$$

Its value can be interpreted as the mean error of evaluating a representative set of samples based on a table with infinite dimensions. As a result, the Richardson extrapolation must inevitably tend towards a very small value. If the relative error determined based on a selected table falls below a suitably chosen error threshold, it can be stated that the solution is independent of the discretisation of the table.

For this statement to be valid for associated CFD calculations, it must be ensured that the thermodynamic states to be evaluated lie within the interval limits of the table. If the tabulated range were to be left during the calculations, the thermophysical quantities would be evaluated directly. Although this would not negatively affect the accuracy of the results, it would question the purpose of the presented detailed analysis. In addition to the approaches for examining the discretisation errors, an analysis of the error caused by the iterative nature of the solution process also needs to be carried out.

Proving the convergence of the iterative solution procedure

When solving a mathematically defined problem iteratively, the underlying system of equations is repeatedly evaluated. The aim is to approximate the exact solution with the highest possible accuracy in a reasonable number of iterations. If the calculated solution approaches the exact solution during the iterative process, the procedure converges. However, a termination criterion must be defined since the exact solution cannot be achieved in a finite number of iterations. This criterion must strike a balance between the two objectives of accuracy and the number of iterations required.

The value of the residual is one way of assessing the deviation between the exact and the approximated solution. This is determined for each iteration step, grid point, and equation to be solved. It can be formed by subtracting the right-hand side from the left-hand side of the system of equations. A normalisation of the residual is often used to make a statement about the deviation for all the equations and node points of the grid. The L1 norm applied below to assess convergence weights all the absolute values of the residual equally. For a stationary approach, TRACE determines the residual $ResL1$ normalised in the above way using the following equation:

$$ResL1 = \frac{1}{n_V} \sum_{j=1}^{n_V} \sum_{d=1}^{n_G} \left| \frac{\Delta t_j}{V_{V,j} \cdot CFL} \left(\left(\boldsymbol{F}_{j+\frac{1}{2},d} - \boldsymbol{F}_{j-\frac{1}{2},d} \right) - \boldsymbol{Q}_{j,d} \right) \right| \tag{4.63}$$

Here, n_V denotes the number of cells in the spatial grid, while n_G represents the number of equations to be solved. The locally prevailing time increment Δt_j and the respective cell volume $V_{V,j}$, which is defined by the local distances between the grid points, together with the CFL number, represent the dimensionless parameters introduced in the course of spatial and temporal integration.

The CFL number defined by Courant, Friedrichs, and Lewy [33] relates the step sizes of spatial and temporal integration to a characteristic velocity:

$$CFL = a \cdot \frac{\Delta t}{\Delta x} \tag{4.64}$$

According to this definition, its value can also be interpreted as information propagation speed per grid point and time step. An analysis of the stability of numerical methods according to von Neumann [26] yields a stability criterion of $CFL \leq 1$ for explicit formulations of the temporal integration. Consequently, the information can propagate at a maximum of the speed of sound. Implicit methods of time integration are not subject to this limitation and also achieve stable solutions for $CFL > 1$. However, the required number of arithmetic operations per iteration step increases compared to the explicit methods, in particular, due to the necessity of additional matrix inversions. In this context, the term stable refers to the determination of a converged solution in the absence of strong numerical oscillations. A solution is considered to have converged if the convergence criterion is met, as evidenced by a defined value of the residuum. The absolute value of this criterion thus indicates the maximum permissible deviation of the iterative solution from the exact solution. An additional indication of convergence can be derived by analysing the trends of global flow quantities.

Verification using a flow solver independent of TRACE

To minimise the influence of possible errors made during the implementation of the *TwoPhase* module in TRACE and to also be able to validate the PGIRoe scheme for explicit methods of temporal integration, a completely independent implementation from TRACE is carried out using a separate density-based flow solver.

Unlike TRACE, this can solve the Reynolds-averaged Navier-Stokes equations as well as the Euler equations not only in three but optionally also in one or two dimensions. While the convective flux terms are determined with second-order accuracy using the PGIRoe scheme, the viscous flux terms are calculated using second-order central differences. The spatial discretisation is based on a second-order MUSCL scheme, where a limiter function formulated by van Leer [89] is applied. An explicit second-order Runge-Kutta method is used for the temporal integration. The turbulence modelling is based on the one-equation model by Spalart and Allmaras [135]. By integrating the REFPROP database, the user can choose between the gas models of the calorically perfect gas and the non-ideal fluid. For the latter, tabulated thermophysical data can be used. The model equations for considering a second phase contained in the *TwoPhase* module in TRACE can also be found in a comparable way in the in-house implementation. This also serves as a development environment for the adaptations of the boundary conditions made in TRACE to take a second phase into account. The applicability of the method is limited to structured grids and stationary flows.

The resulting flow solver is able to calculate single- and two-phase flows of compressible non-ideal fluids, taking into account the formation of a second phase. In this way, it can be applied in the same way as TRACE to all physical test cases examined for validation. For the sake of clarity, the independently implemented flow solver will be referred to below as *Explicit Phase Generalised Ideal Roe* (EPGIRoe) in combination with the number of spatial dimensions chosen for modelling.

5 Application of the Model to Various Validation Cases

Seven test cases were selected to verify and validate the PGIRoe scheme comprehensively. These can be divided into three groups based on their underlying geometries. In addition to the investigation of single- and two-phase flows in Laval nozzles, the compression of CO_2 in a supercritical state using a radial compressor and the interaction of the gaseous and liquid phases in an axial turbine cascade are also investigated. The selection of the test cases is motivated by different validation objectives for single- and two-phase flows.

In the single-phase case, it must first be demonstrated that the PGIRoe scheme is capable of adequately describing arbitrary compressible non-ideal flows. Since the original Roe method is characterised by a high degree of robustness and thus the ability to describe discontinuities and, in particular shocks, with high accuracy, the preservation of this property must be verified for the PGIRoe scheme. Laval nozzles are particularly suitable for this purpose since the flow conditions prevailing in those can be easily varied by means of the applied pressure ratio. In addition, the geometry data of a large number of Laval nozzles, such as NASA's *Converging Diverging Verification* (CDV) nozzle [92], are documented in the literature as part of established CFD validation cases. Due to their simple geometry compared to three-dimensional turbomachinery, it is possible to characterise them solely in terms of their area change along the nozzle axis, thus enabling the derivation of quasi-analytical solutions. In the context of ORC turbines, Laval nozzles are of high practical relevance as low-complexity substitute models for investigating the expansion from subsonic to supersonic conditions. The influence of non-ideality and molecular complexity of the working fluid on the flow characteristics of the expansion can be considered in isolation from other factors. An example of this is the experimental investigations by Spinelli et al. [137], which are documented both in terms of the underlying geometry and the measurement data and can, therefore, be used as a validation case in the context of this work. In order to analyse the robustness of the PGIRoe scheme with respect to large gradients in the flow field, the flow of CO_2 in a supercritical state through a radial compressor is considered. The operating range of the compressor designed by Hacks et al. [66] is in the immediate vicinity of the critical point and, thus, also of the two-phase region. In addition, it is a three-dimensional turbomachinery test case for which experimental measurement data is available.

After verification and validation of the PGIRoe scheme using these three single-phase test cases, a similar process must be carried out for two-phase flows. First, the different configurations of the scheme with regard to the modelling of the liquid phase must be verified. In particular, it is to be ensured that the PGIRoe scheme adequately reproduces the mechanisms of nucleation and droplet growth and the resulting flow phenomena such as condensation fronts. The extent to which the scheme is able to map the interaction of the phases and, thus, the heat and momentum exchange also has to be examined. To this end, simple geometries in the form of Laval nozzles are first analysed, similar to the single-phase case. These can be interpreted as a substitute model of the blade channel of low-pressure steam turbines by setting appropriate values for the expansion rate $\dot{p}$, the Mach number Ma, and the subcooling. For the medium steam, a large number of experimental investigations are available, including, in particular, the work of Moore et al. [101], Moses and Stein [102] and Barschdorff [17]. While the nozzle geometries of the first two mentioned make it difficult to consider condensation effects in isolation due to boundary layer effects and the formation of flow discontinuities, no original measurement data regarding the size of the droplets are available for the latter. However, since a validation, as shown by Young [172], should be carried out using a combination of pressure and droplet radius curves, Maqueo Martinez et al. [94] carry out supplementary measurements of the droplet radii for the nozzle geometry according to Barschdorff. In addition, a complementary test case is chosen, which is the *Mystery* nozzle that was numerically investigated as part of the *International Wet Steam Modelling Project* (IWSMP) [138]. In order to validate the applicability of the PGIRoe scheme to two-phase flows of different fluid species, a nozzle geometry experimentally investigated by Theis [144] for CO_2 is also analysed. Following the consideration of Laval nozzles, a further approach to the three-dimensional flow prevailing in turbomachinery appears useful in the course of validation. This is confirmed by the experimental evidence provided by numerous authors (see [11, 170, 130]) of increased interaction between the dispersed and continuous phases in the presence of flow discontinuities in the last stages of low-pressure steam turbines. An axial turbine cascade investigated by White et al. [165] is particularly suitable as a basis for a corresponding numerical test case due to its systematic variation of flow conditions. Therefore, the quasi-two-dimensional investigation of this geometry rounds off the PGIRoe scheme's validation for two-phase flows.

5.1 Single-Phase Flows

Verification and validation of the PGIRoe scheme for single-phase flows are necessary prerequisites for investigating its applicability to the description of phase change processes. The focus here is on three requirements. The thermophysical quantities of the flow must be calculated correctly by the PGIRoe scheme. Furthermore, it needs to be able to describe discontinuities and gradients in the flow field as accurately as possible and achieve a converged solution despite these. It must be demonstrated that it can be applied to any dimensional modelling of the flow. Finally, the consistency of the procedure is to be checked by ensuring that the PGIRoe scheme, regardless of the selected setting concerning a second phase, must transition into the GIRoe scheme in the single-phase case.

5.1.1 Expansion of CO_2 and MDM in Laval Nozzles

One challenge in selecting a test case to verify the PGIRoe scheme for single-phase flows of non-ideal fluids is the availability of suitable reference data. While a large number of established CFD test cases with corresponding analytical and experimental reference data are available in the literature for ideal fluids, there is no comparable database for non-ideal fluids. For this reason, the NASA CDV nozzle test case, which in its original formulation requires a calorically perfect gas, is first adapted for the medium CO_2 modelled as non-ideal.

Formation of a shock front in a Laval nozzle flowed through by CO_2

The geometry of the NASA CDV nozzle can be found in the left part of Figure 19. As the name suggests, it is a nozzle consisting of a convergent and a divergent part. Two parameters are introduced to enable a dimensionless consideration of the geometric characteristics. The ratio of the cross-sectional area A and the nozzle's narrowest cross-section A^* denotes the relative area, while the relative length refers to the coordinate along the nozzle axis x in relation to the total length of the nozzle L. The NASA CDV nozzle is characterised by a narrowest cross-section of 645.16 mm^2 and a total length of 0.254 m, with the transition from the convergent to the divergent part occurring at half the nozzle length. The flow characteristics within the nozzle can be varied by adjusting the ratio of static pressure at the outlet p_{out} to total pressure at the inlet p_{in}. One parameter for classifying this variation is the Mach number:

$$Ma = \frac{v}{a} \tag{5.1}$$

It relates the flow velocity to the speed of sound and provides a way to distinguish between different types of flow within the nozzle. A Mach number of one characterises the flow as sonic. If the value of the Mach number is below one throughout the entire nozzle, then the flow is purely subsonic. However, if the Mach number in the divergent part of the nozzle exceeds one, the flow is locally referred to as supersonic. The limiting case in which sonic conditions prevail only at the narrowest cross-section, while the rest of the flow remains subsonic, is characterised by the critical pressure ratio. Falling below the critical pressure ratio leads to the formation of a discontinuity in the form of a shock front in the divergent part of the nozzle. While supersonic conditions prevail immediately in front of the shock front, the flow downstream is subsonic. The position of the shock front moves towards the outlet of the nozzle as the pressure ratio decreases. If the outlet is just reached, supersonic conditions prevail throughout the entire divergent part of the nozzle.

Assuming an adiabatic and inviscid flow, two characteristic cases can be distinguished according to Table 4. The case *Isentropic* is characterised by a purely supersonic flow through the divergent part of the nozzle, whereby the specified pressure ratio of 0.08 results directly from the nozzle geometry as well as the choice of fluid and the thermodynamic state at the inlet. When a pressure ratio of 0.75 is set, a shock front forms for CO_2, which indicates the designation of the associated test case as *Shock*.

The inlet boundary condition is chosen in such a way that, on the one hand, the highest possible variation of the compressibility factor along the nozzle axis is achieved and, on the other hand, the state at the outlet of the supersonic nozzle is in the vicinity of the critical point and the two-phase region of CO_2. The static thermodynamic states resulting from the total quantities listed in Table 4 are shown in the right part of Figure 19 using a T-s diagram. Both test cases have the same inlet state, characterised by a static pressure of 1120 bar. Starting

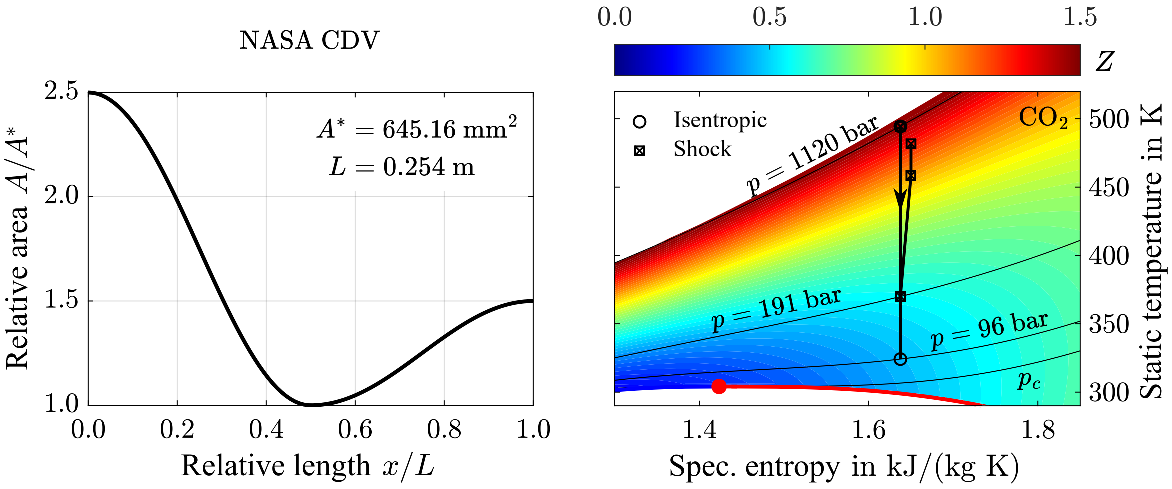

Figure 19: Geometric characteristics of the NASA CDV nozzle [92] (left) and specification of two test cases (○ Isentropic and ⊠ Shock) in a T-s diagram of CO_2 (right)

Table 4: Boundary conditions for the NASA CDV nozzle for the medium CO_2

	$p_{out}/p_{t,in}$	$p_{t,in}$	$T_{t,in}$
Isentropic	0.08	1200 bar	500 K
Shock	0.75		

from this, an isentropic expansion occurs, which, for the case *Isentropic* marked by a circle, proceeds up to a pressure of 96 bar. In the case *Shock*, which is symbolised by a cross in a square, a shock occurs at a temperature of about 370 K, as a result of which the entropy, pressure, and temperature increase. In both cases, a high variation of the compressibility factor can be observed. In the case *Isentropic*, this takes on values between 0.5 and 1.5.

It should be noted that the results shown are the results of quasi-one-dimensional quasi-analytical calculations, which will be used as a reference solution to verify the PGIRoe scheme. The term quasi-one-dimensional indicates that only the change in area along one dimension corresponding to the nozzle axis is considered in the course of the solution. Quasi-analytical refers to a calculation that solves the flow field analytically, whereby the determination of selected thermodynamic state quantities must be carried out iteratively due to the use of a multi-parameter equation of state.

To calculate the flow through the NASA CDV nozzle using the PGIRoe scheme implemented in TRACE, a suitable spatial grid must first be selected. It should be noted that the TRACE flow solver requires three-dimensional modelling of the nozzle for this purpose. In order to minimise the influence of the resulting symmetry boundary condition on the flow along the nozzle axis and thus to enable a quasi-two-dimensional description, the depth of the nozzle is chosen to be $0.1L$. Following the procedure presented in Chapter 4.4, a coarse structured grid is generated first. The geometry of the NASA CDV nozzle is meshed with 100 node points in the direction of the x-coordinate, 50 points in the direction of the y-coordinate, and 3 points in the direction of the z-coordinate. The coarse grid thus has a total node count of $15,000$. The refinement factor is chosen to be $r_G = 2$. Consequently, the middle grid is defined by $120,000$ nodes and the fine grid by $960,000$ nodes. A systematic list of the parameters for investigating the discretisation error of the spatial grid can be found in the left part of Figure 20. For all three grids, a numerical solution for the case *Isentropic* is determined using the flow solver TRACE. In doing so, both spatial and temporal methods with a second-order accuracy are chosen so that the theoretical convergence order assumes the value two. The convergence of the iterative solutions is ensured by falling below a convergence criterion of $ResL1 = 1.0 \times 10^{-6}$. The area-averaged Mach number at the outlet of the nozzle is chosen as the characteristic quantity. An evaluation of this using the three calculated solutions yields a convergence order of $\theta_G = 2.08$ when applying Equation 4.59. Due to the only very slight deviation of the calculated and theoretical convergence order, the consistency of the method can be considered confirmed. Consequently, the Richardson extrapolation can be calculated based on Equation 4.60. The resulting Mach number $Ma_{RE} = 2.6764$ is plotted together with the values determined for the three spatial grids in the right part of Figure 20 represented by blue circles. The order of convergence is reflected in the parabolic shape of the plotted points. The scale used shows that the variation of the Mach number is very small for the three grids considered. Refinement beyond the medium grid only leads to a change in the Mach number of 0.04%. Consequently, it can be assumed that the solution for the medium grid is sufficiently independent of the spatial discretisation, which justifies its use for further calculations.

	Spatial grid ○	Table $\mathscr{F}_\Phi$ △
Coarse Index 4	$15,000$	250 $\Delta p = 4.44$ bar $\Delta T = 0.80$ K
Medium Index 2	$120,000$	500 $\Delta p = 2.22$ bar $\Delta T = 0.40$ K
Fine Index 1	$960,000$	1000 $\Delta p = 1.11$ bar $\Delta T = 0.20$ K

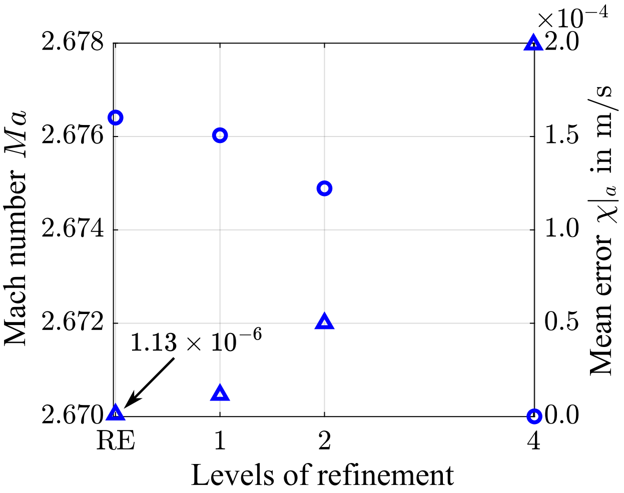

Figure 20: Systematic analysis of the discretisation errors of the NASA CDV nozzle spatial grid as well as the tabulated thermophysical quantities of CO_2 for $p \in [90;1200]$ bar and $T \in [300;500]$ K using three levels of refinement and the Richardson extrapolation

Since the evaluation of the thermophysical quantities for the purpose of computing time efficiency is to be carried out using tabulated data, the associated discretisation error must also be analysed. Similar to the approaches known from Chapter 4.3 and Chapter 4.4, the state region to be tabulated must first be defined. This can be estimated using Figure 19 to $p \in [90;1200]$ bar and $T \in [300;500]$ K. The dimension of the coarse table is set to 250 so that the step size of the pressure has a value of $\Delta p = 4.44$ bar and the step size of the temperature has a value of $\Delta T = 0.8$ K. The tables are refined with the factor $r_T = 2$, which results in a dimension of 500 for the medium table and 1000 for the fine table. A listing of the corresponding step sizes of the tables can be found in the left part of Figure 20. The number of randomly selected queries is $n_A = 250,000$. Based on these, an evaluation of the thermophysical quantities can be carried out for all three tables. As exemplarily shown in Chapter 4.3, the relative errors of the individual quantities per table tend to similar values. However, since this statement would have to be proven individually for each state region, the variable with the highest relative error is chosen as the characteristic quantity. In the case considered here, this is the speed of sound, whose mean error $\chi|_a$ is therefore determined for all three tables. Determining the convergence order based on Equation 4.61 yields a value of $\theta_T|_a = 1.96$, which sufficiently approximates the theoretical convergence order of the table $\theta_T = 2$. From this, the Richardson extrapolation can be determined using Equation 4.62 to be $\chi_{RE}|_a = 1.13 \times 10^{-6}$ m/s. When this is plotted together with the error values determined for the three tables over the level of refinement, the parabolic trend shown in the right part of Figure 20 using triangles results. According to the requirements formulated in Chapter 4.4, the Richardson extrapolation and thus the mean error for an infinitely fine table tends towards a very small value. However, due to the large extent of the state region to be tabulated, caused by the low pressure ratio in the case *Isentropic*, only the finest table falls below an error bound of 5.0×10^{-5} m/s. Therefore, the final calculations are carried out using the finest tables on the medium spatial grid.

Based on the presented results, it is assumed that for this combination, the solution is independent of the discretisation of the grid and the table. Since the investigations of the discretisation errors show qualitatively comparable results for all test cases presented in this work, a detailed description is omitted in the following in order to avoid repetition. The explanations are, therefore, limited to the specification of the spatial grids and the tables for which independence of the solution from the discretisation can be ensured using the procedure presented. A detailed overview of the parameters selected for the investigation of the discretisation errors can be found in Appendix C.

The left part of Figure 21 shows the results of the PGIRoe scheme when solving the Euler equations for the two test cases examined, depicted as the pressure ratio of static to total inlet pressure over the relative length of the nozzle. The results of the test case *Isentropic* are represented by blue circles, while the blue squares symbolise the case *Shock*. In order to better assess the resolution of the shock by the PGIRoe scheme, the number of points displayed in the vicinity of the shock front is increased. For reference, the quasi-analytical solutions are also plotted as black solid lines. For both cases, the results of the PGIRoe scheme show a high degree of agreement with the respective quasi-analytical solution. This applies, in particular, to the regions of the inlet and outlet boundary conditions. In the case *Shock*, the position of the shock is mapped with very high accuracy by the PGIRoe scheme. Furthermore, no oscillations are visible in front of or behind the shock front. This indicates that the robustness of the scheme formulated by Roe for calorically perfect gases with respect to discontinuities is preserved for the PGIRoe scheme.

A further indication of this is the investigation of the Mach number, which is plotted on the right side of Figure 21. Also, for the quotient of flow velocity and speed of sound, the PGIRoe scheme shows a high degree of agreement with the quasi-analytical solution. The curve of the compressibility factor Z, which is also plotted for the case *Isentropic* over the nozzle length, confirms the expected variation between values from about 0.5 to 1.5. On the one hand, this means that based on the compressibility factor the fluid can be classified as non-ideal in large parts of the nozzle. On the other hand, the flow within the nozzle is characterised by large gradients of the thermophysical quantities. This is particularly evident in the vicinity of the shock front, where there is a sudden change in the compressibility factor of about 0.5. However, the values of the fundamental derivative Γ only take on values greater than one, which would indicate a classification as classically ideal. This confirms the dependence of the classification of CO_2 on the choice of the considered parameter, as already shown in Chapter 3.5, and could be attributed to the aforementioned moderate molecular complexity of CO_2.

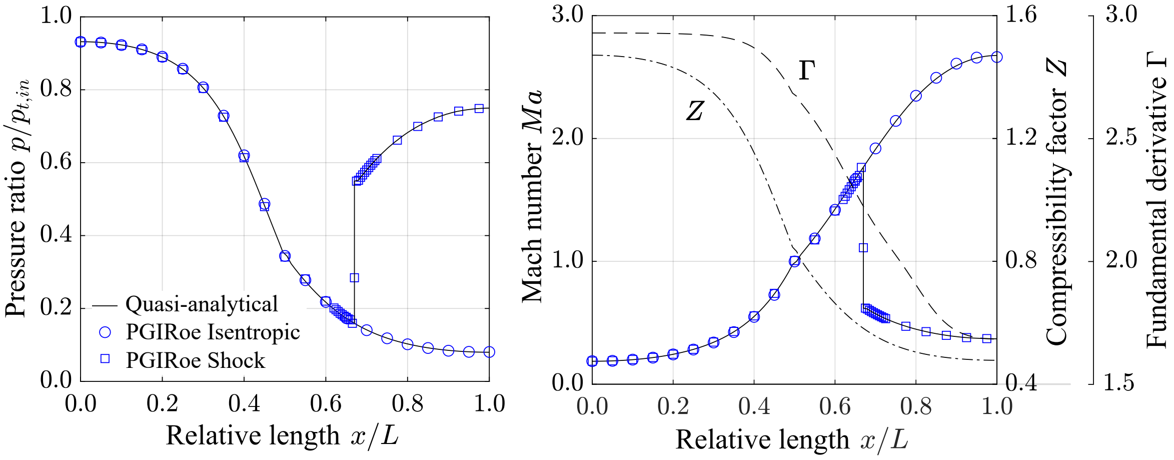

Figure 21: Curves of pressure (left) and Mach number (right) for two test cases of the NASA CDV nozzle based on a quasi-analytical calculation (line) and the PGIRoe scheme (symbols) for the medium CO_2; additional curves of compressibility factor and fundamental derivative

The consistency of the PGIRoe scheme in the single-phase case can be checked by means of a variation calculation. If the calculation of the case *Isentropic* is repeated with explicit activation of the two-phase module in the input file, the deviation from the displayed results is of the same order of magnitude as the machine accuracy for double precision. Consequently, the PGIRoe scheme transitions to the GIRoe scheme in the single-phase case. Verification using the quasi-analytical solution also indicates that the PGIRoe scheme can reproduce the physical relationships of single-phase flows correctly and accurately describe shocks. For this reason, a validation of the scheme using experimental data seems reasonable.

Comparison of experimental data of a Laval nozzle flowed through by MDM

For this purpose, a nozzle geometry experimentally investigated for the working fluid MDM by Spinelli et al. [137] is prepared as a CFD test case. It is a Laval nozzle with a narrowest cross-section of 314.16 mm^2 and a total length of 0.1804 m. The contour of the nozzle can be found on the left part of Figure 22. This figure also shows a detailed view of a special feature of the nozzle consisting of a backward-facing step at the height of the nozzle throat. The height of the step is about 0.1 mm and, for supersonic flow through the divergent part of the nozzle, causes the formation of an oblique shock. The nozzle's cross-section is rectangular, with a depth of 18.7 mm.

Spinelli et al. investigate the flow experimentally by measuring the static pressure at nine measuring points along the nozzle axis. The total conditions at the inlet of the nozzle are set once before the start of the experiment by measurements in a still flow section in front of the test section. At the start of the experiment, the fluid flows into the measuring section due to the opening of a valve, causing a steady pressure drop in the pressure vessel. As a result, a maximum pressure and a minimum compressibility factor prevail at the inlet of the nozzle at the beginning of the experiment. For this point in time, the data of the measured static pressure are available in the literature. Spinelli et al. also prove by comparing the relaxation time of the nozzle with that of the emptying of the pressure vessel that the nozzle flow can be assumed to be stationary at each measurement time.

Two different total inlet states are considered to investigate the influence of the non-ideality of the molecular complex fluid MDM on the flow characteristics. *Case L* represents an inlet state that is characterised by a low deviation from the law of ideal gases, while the compressibility factor for *Case H* assumes a value that differs significantly from one. The static inlet and outlet states for the two cases are plotted in a T-s diagram for the medium MDM in the right part of Figure 22. The state at the outlet is approximated by assuming an isentropic flow through the nozzle. The total inlet conditions, in combination with the total compressibility factors characterising the test cases, are listed in Table 5.

Based on the coloured contour of the compressibility factor in the T-s diagram, it is easy to see that, in line with the objective of the test case, no significant deviation from the law of ideal gases is to be expected for *Case L*. However, the fundamental derivative shows values smaller than one over the entire length of the nozzle, resulting in a classification as classically non-ideal. The same applies to *Case H*, where the compressibility factor for this case at the inlet of the nozzle ranges around 0.7. For both cases, an increase of the compressibility factor and of the value of the fundamental derivative along the nozzle axis is to be expected. The non-ideality thus decreases in the direction of the flow.

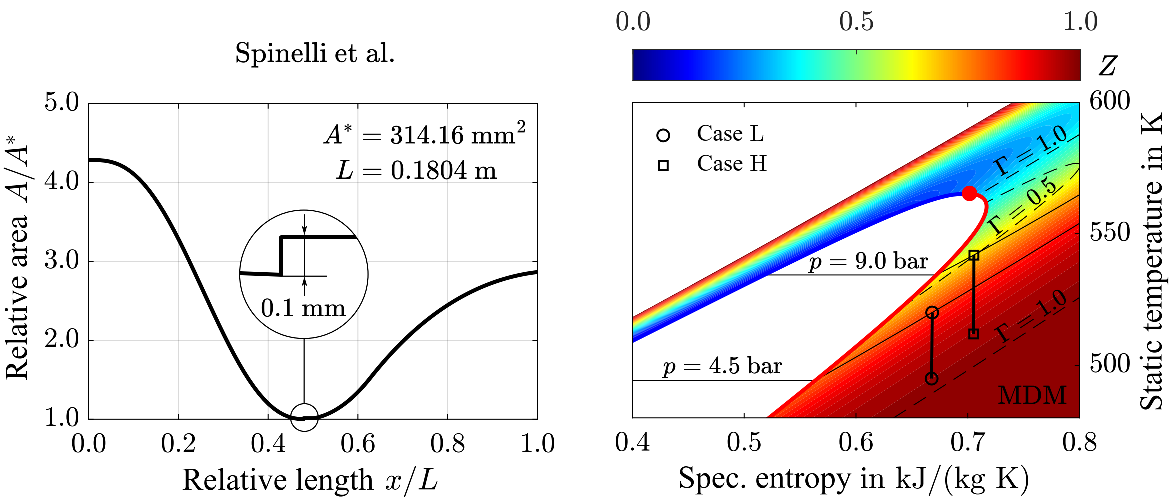

Figure 22: Geometric characteristics of the nozzle according to Spinelli et al. [137] (left) and specification of two test cases (○ Case L and □ Case H) in a T-s diagram of MDM (right)

In order to make the two test cases accessible to an investigation using CFD methods, the geometry is completely reconstructed from the geometry data documented by Spinelli et al. and a structured mesh is created. The resolution of the expected oblique shock in the divergent part of the nozzle requires a sufficiently fine grid so that a grid refinement is carried out for the range of relative length from 0.4 to 1.0. To be able to describe the separation at the step appropriately, the number of nodes in this area is increased in particular. The Reynolds-averaged Navier-Stokes equations are solved using the *Shear Stress Transport* (SST) turbulence model according to Menter et al. [99], which is implemented in TRACE. Since using wall functions to describe the turbulence near the wall is omitted, a rigid restriction of the dimensionless wall distance y^+, which represents a measure of the distance of the first grid point from the wall, is necessary. The refinement of the grid near the walls is therefore assumed to be sufficient if the criterion $y^+ < 1$ is met. For a spatial grid with 1.92 million nodes, the grid independence of the solution can be demonstrated by examining the discretisation error. The tabulation of the thermophysical quantities is done for a pressure interval of $p \in [0.5; 10]$ bar and a temperature range of $T \in [490; 550]$ K. Both test cases are calculated using the specified spatial grid and a table with dimension 500. A residual of $ResL1 = 1.0 \times 10^{-6}$ is chosen as the convergence criterion for the iterative solution.

Figure 23 compares the results calculated using the PGIRoe scheme with the experimental data. Red dots symbolise the experiment, while blue circles represent the results of the PGIRoe scheme implemented in TRACE. For *Case L*, the ratio of static pressure to total inlet pressure is plotted over the nozzle length in the left part of the figure. Experimental data is available for eight measuring points along the nozzle axis. A comparison of these with the values determined using the PGIRoe scheme shows qualitative agreement over the entire nozzle length. However, the deviation increases in the divergent part and, thus, in the region downstream of the step. This is particularly evident for the data point of the last measuring

Table 5: Boundary conditions for the nozzle according to Spinelli et al. for the medium MDM

	$p_{t,in}$	$T_{t,in}$	$Z_{t,in}$
Case L	4.58 bar	520 K	0.83
Case H	9.02 bar	542 K	0.65

point, which shows the highest deviation from the CFD results. The compressibility factor, plotted on the right-hand ordinate, shows an increase of about 0.15 along the nozzle axis. At the nozzle exit, its value tends towards a value close to one, which is in agreement with the range of values shown in Figure 22.

Since the exact position of the oblique shock cannot be determined from the experimental pressure data, a comparison of the results of the PGIRoe scheme with those of the EPGIRoe scheme seems helpful. To ensure the comparability of the results and to take into account the restriction of the EPGIRoe scheme to the Spalart and Allmaras turbulence model, the calculation of the PGIRoe scheme previously carried out with the SST model is repeated using the Spalart and Allmaras model implemented in TRACE. Furthermore, the two-dimensional grid for the calculations of the EPGIRoe scheme is chosen to have the same number of nodes and structure in both spatial directions as the three-dimensional grid generated for the PGIRoe scheme. The results of the EPGIRoe scheme are shown in Figure 23 by a dotted line. It should be noted that the point density is sufficiently high due to the number of nodes of the grid. Therefore, the influence of the linear interpolation on the representation of the results can be negated. The change of the turbulence model from SST to Spalart and Allmaras shows no influence on the pressure profile along the nozzle axis, so for the sake of clarity, no additional data series is shown for the PGIRoe scheme. As can be seen from the close-up, for *Case L*, the position of the intersection of the shock fronts caused by the upper and lower steps of the nozzle geometry, which will be referred to in the following as the position of the oblique shock, is predicted by both schemes to be the same. However, there is a slight deviation in the characteristics of the pressure curves. The pressure change over the shock front seems to be resolved with slightly higher accuracy by the EPGIRoe scheme. Nevertheless, the deviation is of such a small extent and local limitation that it seems explainable by the differences between the two methods in terms of their underlying temporal discretisation and their implementation. This can be interpreted as a plausibility check of the results of the PGIRoe scheme.

A further indication of the validity of the results can be obtained from the investigations by Gori et al. [57]. The authors use a CFD method to investigate the influence of fluid modeling on the flow characteristics for *Case L*. They, too, do not find any relevant influence of the

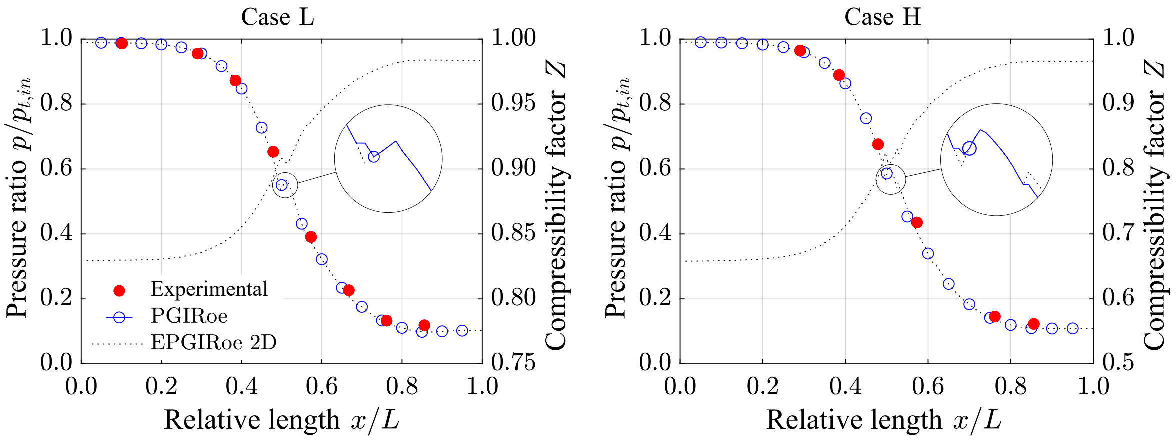

Figure 23: Comparison of the pressure curves for Case L (left) and Case H (right) of the nozzle according to Spinelli et al. [137] based on the PGIRoe scheme (symbols) with the experimental data (dots) for the medium MDM; additional curves of compressibility factor and pressure curves for the two-dimensional EPGIRoe scheme (dotted line)

choice of the turbulence model on the pressure curve along the nozzle axis. In addition, the results they obtain are very similar to the results shown in the left part of Figure 23 in terms of both the position of the oblique shock and the pressure characteristics in the divergent part of the nozzle. This indicates that the deviation of the PGIRoe scheme results from the experimental data in the divergent part of the nozzle is not due to the scheme itself. Rather, the CFD calculations may underestimate the intensity of reflected shock waves. The schlieren images documented by Spinelli et al. display the intersection points of two shocks reflected at the nozzle walls, which are not determined with comparable intensity by the PGIRoe scheme, in the vicinity of the last two measuring points. This could explain the local underestimation of the static pressure. However, a further investigation is not possible due to the lack of a scale for the experimental schlieren images.

Nevertheless, a possible influence of the non-ideality of the fluid on this observation can be examined using the results shown for *Case H* in the right part of Figure 23. Here, too, the red dots symbolise the experimental data, with Spinelli et al. only documenting corresponding pressure data for six measuring points. The results of the PGIRoe scheme, shown as blue circles, achieve similarly high agreement with the experimental data as in *Case L*. The compressibility factor increases by about 0.3 along the nozzle axis, with the non-ideality of the fluid likely influencing the flow characteristics, particularly in the convergent part of the nozzle. If the results of the EPGIRoe scheme are also used to analyse the position of the oblique shock in detail, it is noticeable that the two methods show a slight deviation in the vicinity of the shock even for *Case H*. While the shock position is located similarly by both, the EPGIRoe scheme seems to resolve the shock front with slightly higher accuracy in this case as well. In addition, it predicts a slightly higher intensity for a further shock downstream of the first. However, the difference between the two methods is again very small and limited to the oblique shock's immediate vicinity. The deviation of the CFD results from the experimental data in the divergent part of the nozzle, which has already been discussed for *Case L*, can also be observed in a comparable way for *Case H*.

However, the generally high agreement between the results of the PGIRoe scheme and the experimental data appears to be sufficient for validation. This is confirmed by the investigation of two test cases, which are characterised by a different degree of non-ideality of the fluid. It can thus be assumed that the PGIRoe scheme is able to describe flows of non-ideal fluids of moderate and high molecular complexity in a suitable manner. It also excels at resolving shock fronts with high accuracy. However, the previous investigations to validate the PGIRoe scheme are limited to quasi-two-dimensional flows. To validate the method for three-dimensional applications, the compression of CO_2 in a supercritical state is now to be investigated using the geometry of a radial compressor. The selected test case consequently represents a rotating flow, for which large gradients in the flow field are to be expected due to the proximity of their thermodynamic states to the critical point. In this way, it is particularly suitable for demonstrating the numerical stability of the PGIRoe scheme.

5.1.2 Compression of CO_2 in Supercritical State

The geometry under investigation is a single-stage centrifugal compressor for a turbomachine developed as part of the sCO_2-HeRo project. The compressor will, therefore, be referred to as the HeRo compressor in the following. The inflow is parallel to the axis of rotation, with a part of the inlet upstream of the rotor also rotating at rotor speed. The rotor itself consists of 15 two-dimensional purely radial blades and has an outer diameter of about 40 mm. Its

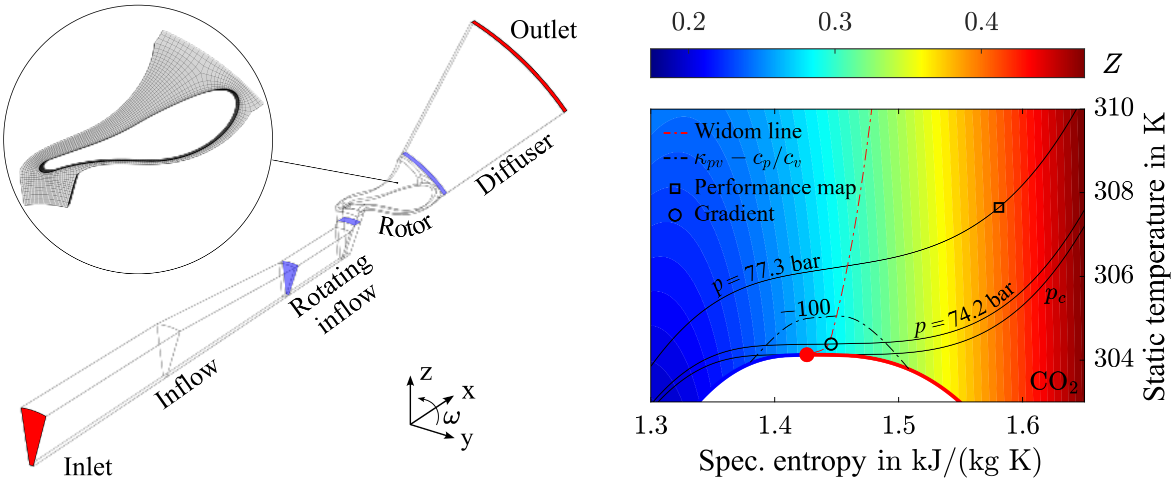

Figure 24: Geometry and setup of the analysed segment of the HeRo compressor with a detailed view of the meshing strategy for the rotor (left) and specification of the analysed inlet states in a T-s-diagram of CO_2 (right)

dimensions are thus comparable to those of another radial compressor impeller frequently examined in the literature, that of the *Sandia sCO$_2$ compression loop facility* [168]. The fluid flows out of the rotor into a parallel radial diffuser, which in turn diverts the flow into a volute. With the exception of the volute, the design of the HeRo compressor can be seen in the left-hand part of Figure 24 where ω denotes the angular velocity of the counterclockwise rotation about the x axis. Hacks et al. [64, 65] conduct a large number of experimental investigations on the HeRo compressor, which form an extensive database of measured values. In combination with the known geometry, these enable a further validation of the PGIRoe scheme for two selected test cases.

A specification of the total thermodynamic states at the compressor inlet can be found in Table 6. Since a pair of values consisting of pressure and density is measured in the experiment, the given temperature values are quantities calculated using the equation of state. In the right part of Figure 24, the defined inlet conditions of the test case *Performance map* are shown by a square, and the case *Gradient* is shown as a circle in a T-s diagram of the medium CO_2. In order to be able to classify the states in relation to the gradients to be expected in their surroundings in the flow field, the Widom line is also plotted as a red dash-dot line in addition to the limiting curves of the two-phase region. Moreover, the coloured contour of the compressibility factor and an isoline of the difference between the isentropic pressure-volume exponent and the ratio of specific heat capacities, represented by a black dash-dot line, allow an estimation of the non-ideality. For the test case *Performance map*, the compressibility factor at the compressor inlet takes on a value of about 0.41. At the same time, the state point is to the right of the critical point, and the Widom line, whereby the scaling used greatly exaggerates the small distance to the critical point of about 3.5 bar and 3.5 K. The case *Gradient* represents a further approaching of the critical point and is therefore in

Table 6: Boundary conditions for the HeRo compressor for the medium CO_2

	$p_{t,in}$	$T_{t,in}$	n_s	$\dot{m}_{out}$
Performance map	77.3 bar	307.65 K	10,000 - 25,000 rpm	0.04 - 0.33 kg/s
Gradient	74.2 bar	304.39 K	30,392 rpm	0.31 kg/s

close proximity to the two-phase region and the Widom line. With a compressibility factor of about 0.28 at the inlet of the compressor, it exhibits a non-ideality comparable to that at the critical point. The difference between the isentropic pressure volume exponent and the ratio of specific heat capacities is approximately -288. This corresponds to a relative deviation of the isentropic pressure volume exponent of about 100% and illustrates the significant deviation from the model assumption of a calorically perfect gas at this point. Thus, for both cases, *Performance map* and *Gradient*, the fluid states are classified as non-ideal. For the case *Gradient*, according to its designation, large gradients of the thermophysical quantities are to be expected in the flow field.

The flow through the HeRo compressor is examined for both test cases using a model simplification. This involves reducing the geometry to a 24° segment, which requires the application of a periodic boundary condition in the circumferential direction. However, since the cross-sectional area of the volute exhibits a continuous change in this direction, it can no longer be taken into account effectively using this approach. Consequently, it is neglected in the modelling, just like the leakage mass flows that occur in the real machine. It should be emphasised that these simplifying assumptions do not counteract the present objective. By reducing the number of nodes by more than a factor of 15, the required computing time can be significantly reduced. In addition, as a stationary component, the volute tends to have a rather advantageous effect on the numerical stability of the solution, so even if it is neglected, a corresponding gain in knowledge seems possible.

The faces of the inlet and outlet boundary conditions are shown in red in the left part of Figure 24, while blue faces indicate the interfaces between the components. At the inlet, a swirl-free inflow is assumed, which is characterised by a specified total pressure and a total temperature. The rotating components rotate at a defined rotor speed n_s. In addition, a specification of the mass flow $\dot{m}_{out}$ serves as the outlet boundary condition. An overview of the complete boundary conditions of the two test cases examined is given in Table 6. The interfaces between the components can also be considered as boundary conditions, which are described using the *mixing plane* model. Unlike the model of the *frozen rotor*, which calculates the boundary condition at the interface using a local snapshot of the rotation, the *mixing plane* model allows the rotational movement to be taken into account. For this purpose, the circular segments are subdivided into defined radial profiles within which the flow quantities are averaged in the circumferential direction. This approach is applied to both sides of the interface and leads to an update of the boundary condition in each iteration step.

The structured meshing of the geometry is carried out for each component, and thus, the inflow, the rotor, and the diffuser separately. In doing so, a systematic grid refinement is carried out for the near-wall regions. A close-up of the meshing strategy of the rotor is shown in Figure 24.

Pečnik et al. [115] provide an overview of the challenges associated with turbulence modelling of compressible non-ideal fluids in a supercritical state. A comparative study of different *eddy viscosity* models with regard to their ability to describe turbulence effects in flows of compressible non-ideal fluids is undertaken by Otero et al. [111]. They point out that the turbulence models established for ideal fluids, such as the SST model, can provide insufficient results for flows of non-ideal fluids, especially in the presence of large gradients in the flow field. Only the model, according to Spalart and Allmaras, despite the simplicity of its formulation, is in good agreement with the results obtained from DNS. For investigations of CO_2 near the critical point, as in the case of the HeRo compressor, this model, therefore, appears to be an appropriate choice. Due to its ability to describe the turbulence up to the wall, the viscosity-affected region of the boundary layer, in particular, must be sufficiently resolved by the spatial grid. To ensure this, a criterion of $y^+ < 1$ is selected for the dimensionless wall distance. By meeting this condition, an investigation of the spatial grid-correlated discretisation error is carried out. Based on this, grid independence can be obtained for a grid with $949,000$ nodes. For the case *Performance map*, the tabulation of the thermophysical quantities is carried out in a pressure interval of $p \in [65; 95]$ bar and a temperature interval of $T \in [295; 320]$ K. Due to the large gradients in the vicinity of the critical point, which place particularly high demands on the discretisation of the table, a dimension of 1000 is chosen. If the table exhibits insufficient resolution in the vicinity of the saturation vapour line, this can endanger the stability of the iterative solution process. For this reason, a confidence interval is stored together with the tabulated quantities within this range. If this interval is exceeded, the equation of state is evaluated directly. In order not to jeopardise the objective of tabulation, it is ensured that at least 95% of the states to be evaluated are determined on the basis of the table. In the case *Gradient*, the tabulated range includes a pressure interval of $p \in [65; 90]$ bar and a temperature interval of $T \in [295; 315]$ K. Again, in accordance with the above explanations, the table dimension is chosen to be 1000. A detailed description of the investigations of the discretisation errors of the spatial grid and the tabulated thermophysical quantities in the case *Gradient* can be found in Tegethoff et al. [143]. The convergence of the iterative solution is assessed using a criterion of $ResL1 = 1.0 \times 10^{-6}$. An additional indication can be obtained from the trend of global quantities during the iteration process. Besides the mass flow at the inlet, the pressure ratio π is also suitable for this purpose:

$$\pi = \frac{p_{out}}{p_{in}} \tag{5.2}$$

Neither of these quantities is directly dependent on the imposed boundary conditions and can be used to characterise the flow fully. If constant values are reached for them, then no further changes to the flow field seem to occur in the course of the iterative solution. Taking into account the convergence criterion, this constitutes a converged solution.

For the case *Performance map*, a multitude of converged solutions are calculated in this way, whereby both the rotational speed and the mass flow at the outlet are varied in a predefined range. This makes it possible to determine a performance map for the HeRo compressor numerically. The left part of Figure 25 shows a typical representation of such a map by plotting the pressure ratio over the mass flow at the compressor inlet. Blue indicates a rotational speed of $10,000$ rpm, red a rotational speed of $20,000$ rpm, and black a rotational speed of $25,000$ rpm. Based on the investigations by Hacks et al. [65], the experimental data and the associated error estimates are visualised using circles and error bars for the mass flow and pressure ratio. Squares represent the results of the PGIRoe scheme, while triangles symbolise the results of the three-dimensional EPGIRoe scheme. To ensure comparability of the results obtained using the PGIRoe scheme and the EPGIRoe scheme, the results are calculated using identical spatial grids and tabulated state quantities. However, for the purpose of visual differentiation, the calculations of the schemes usually differ slightly with regard to the value of the mass flow boundary condition at the outlet.

A comparison of the experimental data with the results of the PGIRoe scheme shows a high qualitative agreement of the resulting curves. In addition, the numerically determined values are, without exception, within the ranges encompassed by the error bars, with the pressure

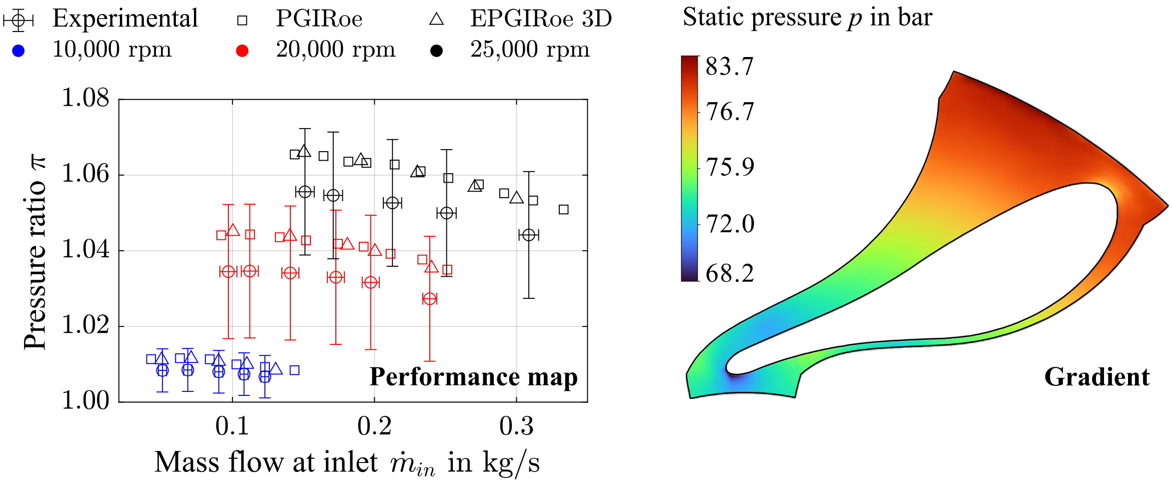

Figure 25: Characteristic map of the HeRo compressor in the form of experimental data (○) with error bars, calculations of the PGIRoe scheme (□) and the three-dimensional EPGIRoe scheme (△) (left) as well as coloured contour of the static pressure in the rotor of the compressor for the test case Gradient calculated by the PGIRoe scheme (right)

ratio increasing with rotational speed as expected. The numerical investigations lead to an overestimation of the pressure ratio, which can, however, be checked for plausibility using the assumptions on which the model is based. Due to the pressure losses to be expected as a result of a flow through the volute, which are neglected by the model investigated, the pressure ratio would decrease. Neglecting the leakage mass flows could also shift the numerically determined characteristic curves of constant rotational speed since the mass flow set at the outlet, taking into account the leakage, no longer matches the mass flow at the inlet as plotted in the performance map. The results of the PGIRoe scheme, therefore, appear plausible both qualitatively and quantitatively. This is additionally confirmed by the similarity of the characteristic curves of constant rotational speed determined on the basis of the PGIRoe scheme and the EPGIRoe scheme. The PGIRoe scheme thus seems to be able to describe three-dimensional flows of non-ideal fluids in turbomachinery.

By tabulating the thermophysical quantities, the computing time can also be reduced to a magnitude suitable for practical application, which is illustrated by the number of data points required for a performance map. When investigating the test case *Gradient* using the PGIRoe scheme, achieving a converged solution can already be considered a success due to the state range present within the compressor geometry. Proof of the convergence of the iterative solution of this test case, as well as a detailed description of the procedure for achieving such a solution, can be found in Tegethoff et al. [143].

The right part of Figure 25 visualises the static pressure contour in the rotor of the HeRo compressor for the case *Gradient*. The colour scale indicates that the pressure value varies between 68.2 bar and 83.7 bar. Localised regions of lower pressure can be seen near the leading and trailing edges of the blade. The pressure minimum is reached at the blade's leading edge and, with the pressure falling below the dew line, indicates the formation of a second phase. Due to the restriction to single-phase considerations in this subchapter, the evaluation of the equation of state by REFPROP is constrained to a gaseous fluid. This approach enables a determination of the thermophysical quantities of the gas phase within the limits of the gas-side metastable state range, even beyond the dew line. However, if the Spinodal limit is exceeded, on the one hand the physical significance of the determined values must

be doubted. On the other hand, the iterative determination of the pressure and temperature can fail due to the lack of a converged solution. Therefore, a bilinear extrapolation of the gas quantities into the two-phase region is carried out for this region.
If the pressure ratio for the test case *Gradient* is determined according to Equation 5.2 in this way, the result is a value of $\pi = 1.121$. The pressure ratio calculated using the measurement data documented by Hacks et al. [64] is $\pi = 1.113$. Thus, the numerical method leads to a slight overestimation of the pressure ratio for this case as well, which can be verified by means of the model simplifications explained above. An analysis of the compressibility factor within the geometry of the rotor shows a particularly high variation of the parameter at the blade's leading edge and the adjacent pressure-side blade profile. From this observation, in combination with the indication of a local drop below the dew curve, a particular challenge for the stability of the numerical method can be identified. The PGIRoe scheme thus seems to be able to achieve a numerically stable solution even in the presence of large gradients of the thermophysical quantities in the flow field and in the immediate vicinity of the two-phase region. This can be interpreted as a validation of the PGIRoe scheme for flows of compressible non-ideal fluids in the immediate vicinity of the critical point of CO_2. Furthermore, this test case highlights the necessity of including a second phase in the numerical model when dealing with a real-life application.

5.2 Two-Phase Flows

Nevertheless, before the PGIRoe scheme can be applied to such a problem, it must first be verified and validated using different test cases of two-phase flows. Three aspects are of particular relevance here. The configurations of the PGIRoe scheme, which differ significantly in the way they describe a dispersed phase, are to be examined with regard to their ability to numerically represent the phase change appropriately. In particular, the mechanisms of nucleation and droplet growth must be correctly reproduced by the schemes. Moreover, it must be ensured that the schemes can be applied to any non-ideal fluid. As part of the validation, not only the non-ideality of the gas phase but also the way the speed of sound in the two-phase region is determined must be taken into account. Finally, the PGIRoe scheme shall be able to describe both condensation and shock fronts in multi-dimensional two-phase flows as accurately as possible.

5.2.1 Condensation of Steam and CO_2 in Laval Nozzles

Verifying different configurations of the PGIRoe scheme requires a test case for which a wide range of comparative data on different modelling approaches for the dispersed phase is available. However, since two-phase flows, in reality, always exhibit a polydispersed droplet size distribution as well as velocity differences between the phases, experimental data appear unsuitable for this purpose. Furthermore, it is not possible to derive analytical solutions for practical problems due to interactions between the phases. This means that verification can only be carried out on the basis of suitable numerical data. The numerical results published in the IWSMP [138] are based on the use of fourteen different flow solvers, which differ, among other things, in the choice of the reference system and the description of the droplet size distribution. Based on this data, the influence of the modelling of the dispersed phase on the numerical results of the PGIRoe scheme can thus be classified.

Influence of the modelling of the dispersed phase on the numerical results

The geometry examined for this purpose is a Laval nozzle specially designed for the IWSMP's objective, through which steam flows. Due to its characteristic as a blind test case, it is called the Mystery nozzle and is distinguished from other nozzle geometries by an operating section free of discontinuities. In addition, it was designed to have an almost constant expansion rate $\dot{p}$ for single-phase flows.

$$\dot{p} = -\frac{1}{p} \cdot \frac{dp}{dt} = -\frac{u}{p} \cdot \frac{dp}{dx} \tag{5.3}$$

According to its definition in Equation 5.3, the expansion rate is proportional to the temporal change of the pressure. If the flow velocity is interpreted as the differential of the local coordinate with respect to time, it can also be formulated in terms of the pressure change along the nozzle axis. A constant value of the expansion rate presupposes the continuity of the pressure curve and thus indicates the absence of discontinuities.

The IWSMP is investigating two variants of the Mystery nozzle, from which the one with an expansion rate of $\dot{p} = 3500\ 1/s$ is selected for further consideration. A plot of the relative area over the relative nozzle length can be found in the left part of Figure 26. The Mystery nozzle has a narrowest cross-section of 40 mm^2. It should be noted that, due to the purely two-dimensional definition of the geometry, this is a pseudo-surface representing the height of the nozzle throat. The length of the nozzle is 0.5 m and is divided into a convergent and a divergent section in the ratio 0.3 to 0.7.

For the test case referred to below as *Case M*, the flow in the divergent section can be assumed to be purely supersonic. Therefore, the explicit formulation of a boundary condition at the outlet of the nozzle is omitted. The inlet boundary condition as a total pressure of 1.1 bar and a total temperature of 417 K is formulated together with the expansion rate characterising the change of state within the nozzle in Table 7. The thermodynamic state defined by the static quantities at the inlet is marked by a circle in the right part of Figure 26. It can be seen that this is above the dew line and thus in the single-phase region of the gas phase so that a wetness fraction of $y = 0$ can be selected as an additional boundary condition at the inlet. Furthermore, the inlet condition is characterised by a compressibility factor of about 0.99, indicating only a weak non-ideality of the single-phase flow. The deviation of the isentropic pressure-volume exponent from the ratio of specific heat capacities is about -0.013, corresponding to a relative deviation of 1% and confirming the indication of the compressibility factor.

In order to meet the requirement of a geometry meshed in three dimensions, as necessitated by the flow solver, while at the same time approximating the conditions of a two-dimensional investigation, the depth of the nozzle is modelled as $0.1L$, comparable to the approach used for the NASA CDV nozzle. To compare the results with those of the IWSMP, turbulence effects present in the flow are taken into account, which are described using the Spalart and Allmaras turbulence model. Therefore, a criterion of the dimensionless wall distance of $y^+ < 1$ is chosen for the meshing of the geometry. An investigation of the spatial discretisation error shows the grid-independence of the solution for a spatial grid with $576,000$ nodes, which has appropriate refinements near the walls. The thermophysical quantities are tabulated separately for the gas and liquid phases. For the gas quantities, a pressure interval of $p \in [0.1; 1.15]$ bar and a temperature interval of $T \in [300; 430]$ K is selected.

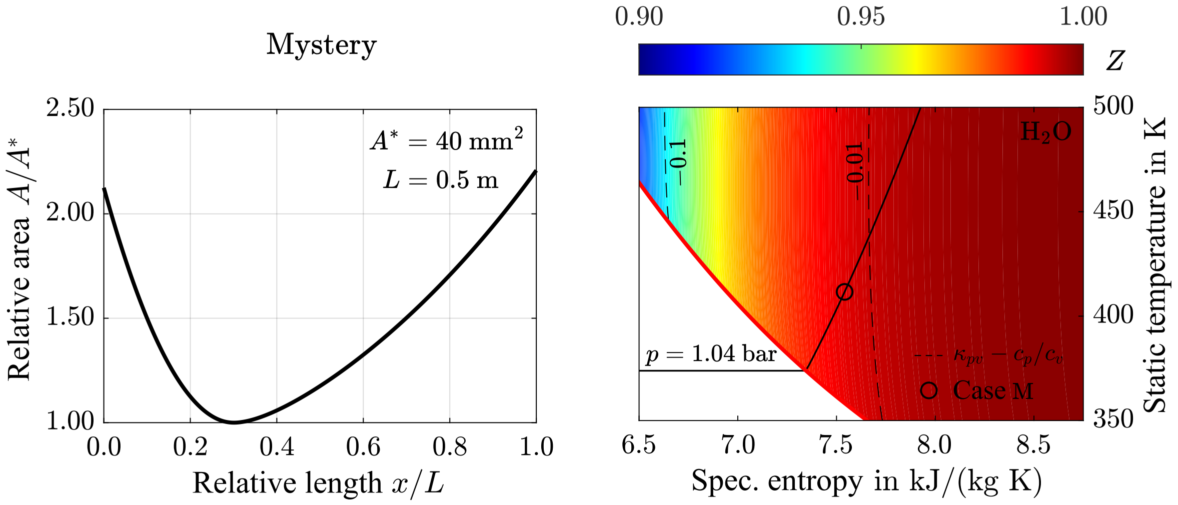

Figure 26: Geometric characteristics of the Mystery nozzle [138] (left) and specification of the test Case M (○) in a T-s diagram of water (right)

In contrast to a purely single-phase consideration, the determination of the thermophysical quantities in the two-phase region is now of particular importance. If the thermodynamic state to be tabulated lies within the two-phase region, the first question to be answered is which model should be used to describe the phase change. In the case of the model of homogeneous equilibrium condensation, it is not necessary to tabulate the states within the two-phase region. Storing the thermophysical quantities of the gas phase and the saturation quantities of the gas and liquid phases is sufficient to determine the state completely.

If the model of homogeneous non-equilibrium condensation is to be applied, it must first be checked whether the state point to be tabulated falls within the boundaries of the metastable range. If this is the case, the equation of state is evaluated with restriction to gaseous states. If, on the other hand, the state point lies beyond the spinodal limit, it has no physical significance, which is why the value minus one is stored in the table. If such a table entry is queried during the iterative calculations of the flow solver, a warning message is issued. The negative sign is used to activate a bilinear extrapolation beyond the spinodal limit using direct evaluation. Such a solution may only be used for a short-term stabilisation of the solution process and makes it possible to achieve a convergent solution, especially in the vicinity of the critical point, despite the very small extent of the metastable state range there. To ensure the physical significance of the final calculation results, the activation of the bilinear extrapolation in the last 500 iterations is prevented. If the spinodal limit is exceeded at this stage of the solution, the negative sign of the tabulated values causes the calculations to be aborted.

The tables of thermophysical quantities in the gas phase consequently consist of regions of pure single-phase and metastable states in the two-phase region. In order to be able to resolve the delimitation of these areas with sufficient accuracy, the saturated vapour line and the dew line within the considered definition range are additionally tabulated as a function of temperature.

Table 7: Boundary conditions for the Mystery nozzle for the medium water

	$p_{t,in}$	$T_{t,in}$	$\dot{p}$
Case M	1.1 bar	417 K	3500 1/s

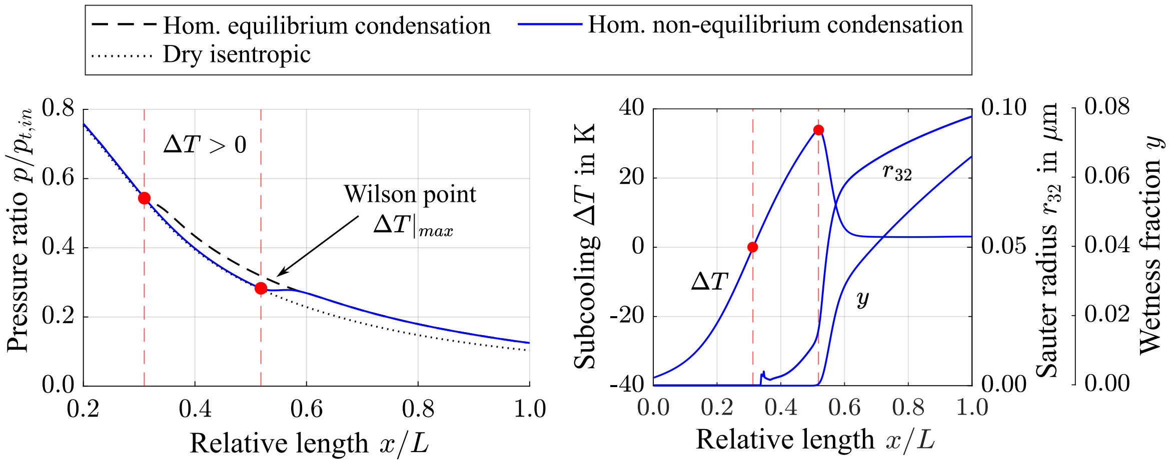

Figure 27: Comparison of different models for describing condensation based on pressure curve along the Mystery nozzle (left) and curves of characteristic quantities assuming homogeneous non-equilibrium condensation (right) for the medium water

For the liquid phase, the thermophysical quantities are tabulated within a pressure interval of $p \in [0.1; 0.55]$ bar and a temperature interval of $T \in [310; 355]$ K. Here, the equation of state is evaluated with an explicit restriction to liquid states. The investigation of the discretisation error of the tables shows a peculiarity with regard to the table dimensions required for a sufficient resolution of the state region. While the tables for the gas phase already show a sufficiently low value of the mean error of the speed of sound for a dimension of 500, such a value is only achieved for the liquid phase when using the next higher dimension of 1000. Since the pressure and temperature interval for the gas phase covers a larger range of values, this does not initially correspond to expectations. However, it turns out that the equation of state of the IAPWS-IF97 for region 1 and thus liquid states within the examined interval limits has significantly higher sensitivity with regard to changes in the definition parameters than the equations of the regions 2 and 2s for the gas phase.

According to Chapter 3.4, a phase change can be described on the basis of different model assumptions. To demonstrate that the PGIRoe scheme is able to correctly reflect the underlying physical processes, the results of three modelling types are compared first. This enables a plausibility check and also shows the phase change characteristics within the Mystery nozzle for *Case M*. In the left part of Figure 27, the pressure curve of the dry flow of steam is compared with the curves assuming homogeneous equilibrium condensation and homogeneous non-equilibrium condensation. The focus of the diagram is on the divergent part of the nozzle. To enable an analysis that is as isolated as possible from the influence of the modelling of the phase change on the flow quantities, the effects of friction are not taken into account for all three calculations by solving the Euler equations. As for all subsequent calculations of this test case, the convergence of the iterative solution is assessed using a criterion of $ResL1 = 1.0 \times 10^{-7}$.

The flow modelled as dry exhibits an isentropic characteristic and is represented by a black dotted line. Its pressure curve resembles those already seen in Chapter 5.1 for Laval nozzles with supersonic outlet boundary conditions. The pressure curve of the PGIRoe scheme, when describing the phase change using the model of homogeneous equilibrium condensation, represented by a black dashed line, initially matches that of the dry flow. However, with the expansion along the nozzle axis, as a result of the decrease in pressure and temperature, the saturated vapour line is crossed at a defined position. In Figure 27, this is marked by a red dot at a relative length of 0.32. According to the model of homogeneous equilibrium condensation, the resulting subcooling greater than zero marks the onset of condensation and, thus, the formation of a second phase. Since the model assumes the existence of an equilibrium state between the phases, the thermodynamic state of the phase mixture downstream is uniquely determined by the respective saturation quantities and the wetness fraction, resulting in a pressure curve approximately parallel to that of the dry flow.

However, the assumption of a phase equilibrium must be abandoned to describe the physical processes of condensation and the interaction of the phases. The pressure curve of the PGIRoe scheme for the model of homogeneous non-equilibrium condensation, represented by a blue line, should, therefore, be explained by the mechanisms of nucleation and droplet growth. Initially, this curve also shows a characteristic similar to that of the dry flow. In contrast to when assuming equilibrium condensation, however, falling below the saturated vapour line does not immediately lead to the formation of a second phase. Instead, clusters form first, but these are smaller than the critical nucleation radius and thus decay. As can be seen in the right part of Figure 27, the subcooling continues to increase. A sudden nucleation event then leads to the formation of a large number of stable condensation nuclei, forming a liquid phase dispersed in the gas phase. The position along the nozzle axis at which such a nucleation event occurs is highlighted by another red dot at a relative nozzle length of 0.52. It marks the point of maximum subcooling, also known as the Wilson point, which, for *Case M*, is at a pressure of about 0.31 bar and a subcooling of 33 K.

The enthalpy of evaporation released from the liquid phase during nucleation and droplet growth causes the pressure and temperature of the gas phase to rise. As a result, the subcooling decreases. In addition, the thermodynamic state of the phase mixture approaches an equilibrium state. This can be seen both in the subcooling and in the pressure curve by means of a characteristic pressure increase, often referred to as condensation front, and the subsequent approximation to the pressure curve assuming an equilibrium state in the left part of Figure 27. The droplet radius, which is plotted as the Sauter radius, increases downstream of the Wilson point as a result of growth of the droplets, reaching values of up to just under 0.1 µm. Since nucleation is inhibited downstream of the condensation front due to the temperature increase, the mechanism of droplet growth dominates from a relative nozzle length of about 0.6 onwards. The value of the wetness fraction reaches a value greater than zero for the first time at the Wilson point. It increases to a value of just over 0.06, which corresponds to a wetness fraction of about 6% of the total mass of the phase mixture. The increase in the droplet radii, which contribute to the volume of the liquid phase to the power of three and are thus directly linked to the liquid mass, is consistent with a further increase in the wetness fraction above a relative nozzle length of about 0.6.

The results of the PGIRoe scheme for the two different modelling types of condensation shown in Figure 27 thus appear plausible in the context of the expected physical processes. In particular, the PGIRoe scheme is able to correctly represent the physical mechanisms associated with condensation. In order to derive a statement about the quantitative agreement of the results of the PGIRoe scheme with reference data and thus to be able to verify the scheme, a choice must first be made regarding the configurations to be examined.

According to Chapter 4.1 the Stokes number can be interpreted as an indicator of the ability of the dispersed phase to follow the continuous flow in terms of direction and magnitude of the flow velocity. Based on its definition in Equation 4.12, it can be seen that its value is

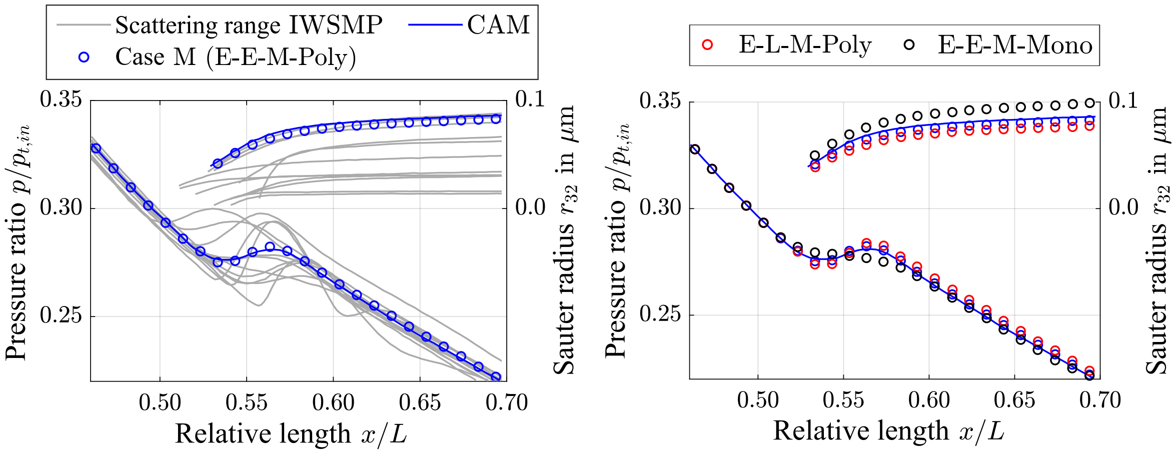

Figure 28: Curves of pressure and Sauter radius for Case M of the Mystery nozzle as determined by the IWSMP [138] (grey lines), by a flow solver from the University of Cambridge (blue line) and using the PGIRoe scheme (symbols) (left) as well as comparison of different types of modelling the dispersed phase using the PGIRoe scheme (right)

influenced by the absolute value of the velocity difference between the phases. A calculation of *Case M* using the PGIRoe scheme for the *E-E-P-Poly-S* configuration, taking frictional effects into account, indicates that the maximum velocity difference between the phases is reached at the walls of the nozzle in the immediate vicinity of the outlet. A calculation of the Stokes number based on the flow quantities prevailing in this area yields a value of 0.09 and thus does not fulfil the criterion of $St > 0.1$ formulated for the consideration of momentum exchange.

For this reason, only the configurations *E-L-M-Poly*, *E-E-M-Mono*, and *E-E-M-Poly* will be examined for the Mystery Nozzle in the following. The first two mentioned differ from the latter only in one of the four categories of variation specified in Table 3. This allows an isolated analysis of the influence of the choice of the reference system and the description of the droplet size distribution by comparing it with the results of the configuration *E-E-M-Poly*. However, beforehand, a verification of the configuration *E-E-M-Poly* based on reference data from the IWSMP is required.

For this purpose, the ratio of static pressure to total inlet pressure is plotted on the left abscissa of the left part of Figure 28. The values calculated using the PGIRoe scheme and displayed in the form of blue circles are compared with the results of the IWSMP. An equivalent procedure is followed using the right abscissa for the Sauter radius. For the sake of clarity, the scatter of the IWSMP results is represented by a set of grey curves. It can be seen that the different flow solvers show high deviations in terms of both the pressure curves and the droplet radii. Although it should be noted that the section shown represents only a small part of the nozzle geometry, the position and shape of the pressure increase, and, in particular, the quantity of the droplet radii vary considerably. This can be partly explained by the different types and implementations of the flow solvers examined. Starzmann et al. [138] also mention differences in the models of nucleation and growth rates used, as well as in the thermophysical model equations, as possible influencing factors. Since, consequently, the verification of the PGIRoe scheme cannot be carried out solely on the basis of this scatter range, the flow solver of the University of Cambridge is chosen as a reference for a more extensive quantitative comparison of the results.

This appears to be particularly suitable due to its similarity to the implementation of the PGIRoe scheme in TRACE. It is based on the same modelling approaches of nucleation and droplet growth, uses identical model parameters to describe droplet growth according to Young, and evaluates the thermophysical quantities based on the same model equations. The dispersed phase is described in an identical manner to the configuration *E-E-M-Poly* using an Eulerian frame of reference in mixture-based notation, whereby the polydispersed droplet size distribution is described using its statistical moments. Since the Spalart and Allmaras approach is also chosen to model turbulence, besides the type of implementation, only two differences to the PGIRoe scheme in TRACE can be identified. The flow solver from the University of Cambridge uses an explicit method for the temporal integration of the system of equations and calculates the numerical flux terms using a scheme that, by definition, adds to the formation of numerical dissipation.

Despite these differences, the results of the PGIRoe scheme show a high degree of agreement with the reference data, both in terms of the pressure curve and the Sauter radius. The condensation starts marginally later for the PGIRoe scheme. This causes a slightly higher subcooling and could lead to the formation of a larger number of droplets, which consequently have smaller radii. However, the deviation of the results, especially in comparison to the scatter range of the IWSMP, is so small that the configuration *E-E-M-Poly* of the PGIRoe scheme can be considered verified. It should, therefore, now be used to verify two further configurations.

For this purpose, the right part of Figure 28 shows a comparison of the results of the configurations *E-L-M-Poly* and *E-E-M-Mono* with the already verified data. The calculations using a description of the dispersed phase in a Lagrangian frame of reference are shown as red circles, while black circles represent the results assuming a monodispersed droplet size distribution. The nozzle section shown and the scales of the two abscissas are chosen analogously to the results already presented. Both the pressure and the radius curves show slight deviations between the configurations and from the reference data. When the frame of reference of the dispersed phase is changed from Eulerian to Lagrangian, condensation sets in a little further downstream, which, as explained above based on the presented results, can lead to a reduction in the droplet radius.

However, compared to the investigations of a change of the frame of reference according to White [162], the deviation between the results is very small. White suggests that the discrepancy he observed may be due to an error introduced by the scheme for calculating the numerical flux terms. The description of the dispersed phase in the Lagrangian frame of reference requires the solution of a system of equations that is separate from the conservation equations of the continuous gas phase. As a result, the numerical flux terms are to be formulated exclusively for the Navier-Stokes equations. This significantly reduces the influence of the applied flux calculation scheme and its accuracy on the quantities of the liquid phase compared to a formulation in the Eulerian frame of reference and could explain a deviation between the results of different frames of reference. Since the formulation of the PGIRoe scheme, unlike the method used by White, contains no artificial damping terms and, due to its origin from the scheme according to Roe, does not tend to produce numerical dissipation, this justification also seems suitable to explain the absence of a deviation and thus indicate a verification. Despite the high degree of agreement between the results, it should be noted that the use of an Eulerian frame of reference in the context of the implementation in TRACE shows a significant advantage in terms of computing time.

As expected, the description of the dispersed phase in the Lagrangian frame of reference makes it possible to achieve a grid-independent solution even on a grid with a smaller number of nodes. However, the reduction in computing time associated with this is cancelled out by the increased time required to achieve a convergent solution in TRACE. Solving the differential equations of the statistical moments separately from the conservation equations increases the number of iterations required to reach the convergence criterion. Since this behaviour can be observed in a similar way for the EPGIRoe scheme, it seems unlikely that this is due to the implementation. Rather, in the present case, the solution of the equations coupled by an Eulerian frame of reference could lead to an acceleration of convergence with no negative influence on stability.

A comparison of the results assuming a monodispersed droplet size distribution with the already verified polydispersed configuration shows a stronger deviation than in the case of a change of the frame of reference. The increase in pressure in the vicinity of the condensation front appears slightly compressed. Also, the radius of the droplets is overestimated compared to the *E-E-M-Poly* variant. It should be noted that the formulation of a volume-averaged radius replaces the calculation of the Sauter radius in the monodispersed case due to the lack of a way to determine the droplet surface. However, Starzmann et al. [138] show that the way the droplet radius is averaged is of secondary importance for the accuracy of the results in the case of nozzle flows. The compressed characteristic of the pressure curve also corresponds to similar observations in the literature. White and Hounslow [164] attribute this to an inadequate description of the heat exchange between the phases under the simplifying assumption of a monodispersed droplet size distribution. The heat exchange between the phases, which can be localised at the surface of the droplets, is thus directly dependent on the surface area as a quantity that cannot be clearly determined in the monodispersed case. The resulting error also affects the subcooling and the maximum of the nucleation rate. It leads to an upstream shift in the onset of condensation, favouring an overestimation of the droplet radii.

Since the configuration *E-E-M-Mono* of the PGIRoe scheme also matches the trends found in the literature, all three configurations examined on the basis of *Case M* of the Mystery nozzle can be assumed to be verified. Furthermore, based on the discussed relations between the three configurations, it seems reasonable to limit a validation of the PGIRoe scheme to the two variants *E-E-M-Poly* and *E-E-P-Poly-S*. To this end, the numerical results of the PGIRoe scheme will now be compared with experimental data of a flow characterised by moderate differences in phase velocities.

Comparison with experimental data of moderate difference in phase velocities

The geometry considered below was originally used by Barschdorff [17] to study condensation in supersonic flows of humid air when exposed to heat. In later experiments, Barschdorff [18] also measured the expansion of pure steam using the same Laval nozzle, with the focus again being on the phase change by means of condensation. Due to the measurement methods used, his documented results are limited to pressure curves measured along the nozzle axis. However, since validation of numerical methods requires not only measurement data of the continuous phase but also measurement results of at least one quantity of the dispersed phase, Maqueo Martinez et al. [94] investigate the nozzle geometry according to Barschdorff both in terms of pressure and droplet radius.

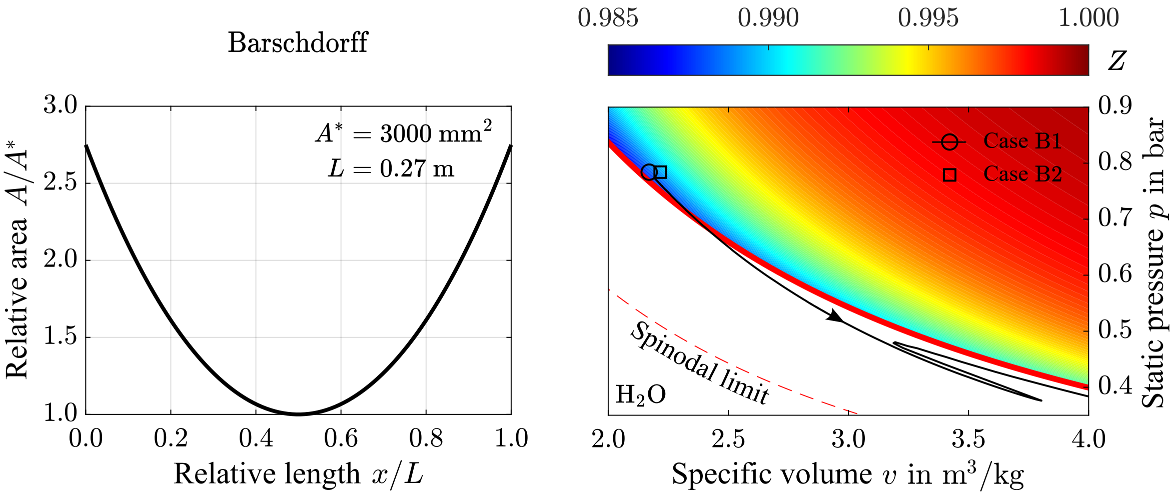

Figure 29: Geometric characteristics of the nozzle according to Barschdorff [17] (left) and specification of two test cases (○ Case B1 and □ Case B2) in a *p*-*v* diagram of water (right)

The geometry they use corresponds to the circular arc nozzle with a rectangular cross-section, which Barschdorff calls Düse II and which is characterised by a radius of curvature of 584 mm. The corresponding curve of the relative area along the relative length is shown in the left part of Figure 29. Due to the shape of the arc, which appears slightly distorted due to the plotting of the related quantities, there is a direct geometric dependency between the length of the nozzle and the cross-sectional area at the inlet and outlet, given the radius, the nozzle depth and the narrowest cross-section. This means that the characteristic of the change in area along the nozzle axis remains the same regardless of the choice of nozzle length. The narrowest cross-section of the nozzle, according to Barschdorff, is obtained by multiplying the height of the nozzle throat of 60 mm by a nozzle depth of 50 mm, resulting in 3000 mm^2. The length of the nozzle is modelled as 0.27 m, in accordance with Barschdorff's documentation. Unlike in the case of the Mystery nozzle, the expansion rate here is not constant.

From the eleven inlet states measured by Barschdorff two test cases were selected to validate the PGIRoe scheme. The total pressure at the inlet is 0.7839 bar in both cases. *Case B1* is characterised by a total temperature at the inlet of 373.35 K, while for *Case B2*, a total temperature of 380.55 K is specified. An overview of this data can be found in Table 8.

The static thermodynamic states resulting from the total quantities are plotted in the right part of Figure 29 in a *p*-*v* diagram of the medium water. In this diagram, *Case B1* is represented by a circle and *Case B2* by a square. Both state points are above the dew line and thus in the gaseous single-phase state region. A closer look at the compressibility factor, which is shown as a coloured contour, reveals that no significant non-ideality of the gas phase is to be expected for the test cases of the nozzle according to Barschdorff either. The compressibility factor is in the range of about 0.987, with the value for *Case B1* being slightly lower than in *Case B2*.

Table 8: Boundary conditions for the Barschdorff nozzle for the medium water

	$p_{t,in}$	$T_{t,in}$
Case B1	0.7839 bar	373.35 K
Case B2		380.55 K

A special feature becomes apparent if the expected change of state along the nozzle axis for *Case B1* is visualised as a black line. Starting from the state at the inlet of the nozzle, which is already in close proximity to the dew line, the expansion within the Laval nozzle leads to an entry into the two-phase region. As already shown by the results for the Mystery nozzle, the subcooling continues to increase downstream, although the spinodal limit, shown as a red dashed line, is not exceeded. The state in which stable condensation nuclei first form is characterised by reaching a maximum subcooling and can be located in the p-v diagram of Figure 29 in the local minimum of the black curve.

As a result of the formation of a liquid phase, the evaporation enthalpy is released, which can be interpreted as thermal energy. While the quantities of pressure and temperature increase, the heat release causes a local drop in the Mach number. If this happens relatively close to the narrowest cross-section of the nozzle, in which sonic conditions prevail, as in *Case B1*, and if the heat release is sufficiently high, a localised subsonic area forms in the divergent part of the nozzle. The heat load at which exactly a Mach number of one is reached in the vicinity of the condensation front is referred to as the critical heat addition. If the released amount of energy has a higher value, it is referred to as a supercritical heat addition and causes large gradients in the flow field due to an abrupt change from subsonic to supersonic conditions.

To be able to map these appropriately within the scope of the numerical investigations, the spatial grid is refined in the divergent part of the nozzle. Analogous to the Mystery nozzle, the Spalart and Allmaras model with a corresponding criterion of the dimensionless wall distance is chosen for the turbulence modelling of the nozzle according to Barschdorff. On the basis of an investigation of the discretisation error of the spatial grid, the grid independence of the solution can be stated for a grid with 960,000 node points. The tabulation of the thermophysical quantities of the gas phase and the saturation quantities is carried out for a pressure interval of $p \in [0.15;0.8]$ bar and a temperature interval of $T \in [300;385]$ K, while the quantities of the liquid phase are tabulated in a pressure interval of $p \in [0.15;0.5]$ bar and a temperature interval of $T \in [300;360]$ K. An investigation of the independence of the solution from the discretisation results in the choice of a table dimension of 500 for the gas phase and 1000 for the liquid phase. The criterion for assessing the convergence of the iterative solution is set to $ResL1 = 1.0 \times 10^{-7}$.

To be able to assess the necessity of considering the momentum exchange between the phases, the Stokes number is evaluated for both test cases of the nozzle according to Barschdorff. Calculations using the configuration *E-E-P-Poly-S* of the PGIRoe scheme show that similar to the case of the Mystery nozzle, a maximum difference in phase velocities in the vicinity of the walls close to the outlet boundary condition is to be expected. Based on the quantities determined in this way, a Stokes number of 0.51 is obtained for *Case B1* and of 0.37 for *Case B2* using Equation 4.12. Thus, combined with the previously formulated criterion of $St > 0.1$, it seems reasonable to take into account the momentum exchange between the phases, especially for *Case B1*. At this point, it should be noted that when using the configuration *E-E-P-Poly-S* of the PGIRoe scheme, the consideration of frictional effects in the form of turbulence modelling is carried out exclusively for the gas phase.

To be able to compare the influence of the consideration of the momentum exchange between the phases on the numerical results, the two test cases of the nozzle according to Barschdorff are first calculated using the already verified configuration *E-E-M-Poly*. The results obtained in this way are compared with the experimental data in the left part of Figure 30. The pres-

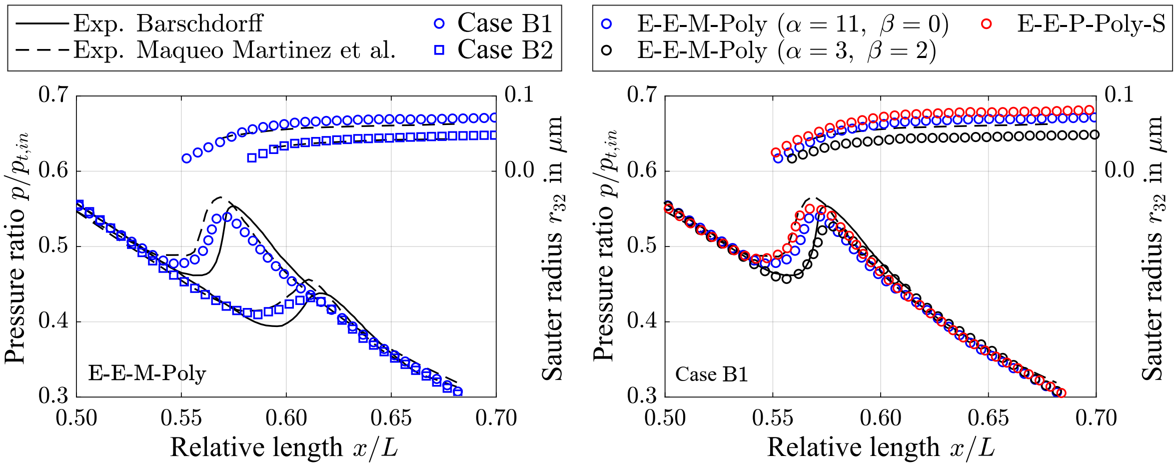

Figure 30: Pressure and Sauter radius curves for Case B1 (○) and Case B2 (□) of the nozzle according to Barschdorff as measured by Barschdorff [18] (black lines), by Maqueo Martinez [94] (black dashed line) and determined numerically using the PGIRoe scheme *E-E-M-Poly* (symbols) (left) as well as comparison of different types of modelling of the dispersed phase using the PGIRoe scheme (right) for the medium water

sure curves according to Barschdorff [18] are shown as black lines and are based on a digital reconstruction of the measurement data published as a graphic. A similar approach is also followed for the experimental data according to Maqueo Martinez et al. [94]. Black dashed lines represent the resulting pressure and Sauter radius curves. Blue circles symbolise the results of the *E-E-M-Poly* configuration of the PGIRoe scheme for *Case B1*, while blue squares indicate the curves calculated for *Case B2*. Since the narrowest cross-section lies at half the nozzle length, its coordinates are selected as the origin of the ordinates.

Prior to the onset of condensation, all of the displayed pressure curves correspond well with one another, with the numerical results being somewhat closer to the data according to Barschdorff. The Wilson point for *Case B1* is characterised by the PGIRoe scheme by a pressure of about 0.38 bar and a maximum subcooling of 33 K. A comparison of the experimental data sets against each other shows a deviation with regard to the onset of condensation and the resulting pressure increase. The results of Maqueo Martinez et al. indicate an earlier onset of condensation than the data according to Barschdorff, whereby the characteristic of the pressure increase shows a similar shape for both data sets. The results of the PGIRoe scheme fall within the range of the experimental data with regard to the onset of condensation. However, the pressure increase has a lower slope and, consequently, a lower maximum. Since *Case B1* is a test case with a supercritical heat addition, this deviation could indicate an underestimation of the released thermal energy by the PGIRoe scheme. Downstream of the pressure increase, the numerical results show agreement with the experimental data according to Maqueo Martinez et al., while the data according to Barschdorff indicate slightly higher values of the pressure. The trend of the droplet radius determined by the PGIRoe scheme shows qualitative agreement with the experimental data over the entire measuring section. In the last data point documented by Maqueo-Martinez et al., the Sauter radius determined numerically for *Case B1* shows a relative deviation of about 16%.

An investigation of *Case B2* using the PGIRoe scheme leads to a determination of the Wilson point at a pressure of about 0.33 bar and a maximum subcooling of 34 K. Similar to *Case B1*, the experimental data show a deviation concerning the onset of condensation. In

Case B2, the results of the PGIRoe scheme again lie between the experimentally determined pressure curves. The onset of condensation is predicted by the PGIRoe scheme both in terms of the nozzle coordinate and the pressure level in a way that is comparable to the data from Maqueo-Martinez et al.. However, the shape of the pressure increase shows a lower gradient and a lower maximum in this case as well. Since *Case B2* is not characterised by a supercritical heat addition, no specific cause can be identified for this so far. An analysis of the droplet radii shows a qualitative agreement between the numerical results and the experimental data. The relative deviation of the Sauter radius determined using the PGIRoe scheme in the last data point documented by Maqueo Martinez et al. for *Case B2* is about 7%. With reference to the scatter range of numerical results demonstrated by the IWSMP for the Mystery nozzle when investigating the condensation of steam in Laval nozzles, as well as the similarity of the numerical results to the experimental measurement data in the case of the nozzle according to Barschdorff, the configuration *E-E-M-Poly* of the PGIRoe scheme can be considered validated.

Maqueo Martinez et al. show on the basis of their own numerical calculations that an adjustment of the parameters of Young's droplet growth model can lead to an improved agreement with the experimental results. The values of $\alpha = 3$ and $\beta = 2$ used by the authors are rather unusual compared to the parameters recommended by the IWSMP of $\alpha = 11$ and $\beta = 0$. To investigate the influence of the droplet growth modelling on the numerical results of the PGIRoe scheme, a case study is carried out in the right part of Figure 30 using *Case B1*. The blue circles symbolise the results of the PGIRoe scheme using the configuration *E-E-M-Poly* and the standard parameters of the droplet growth model, as before. The results when adjusting the model parameters according to the choice of Maqueo Martinez et al. with otherwise the same modelling of the dispersed phase are shown as black circles. A comparison of the pressure curves reveals no relevant deviation until condensation sets in. This seems plausible since the adjustment of the droplet growth model parameters in the absence of droplets must not influence the results. Based on the modified parameters, the onset of condensation is predicted by the PGIRoe scheme further downstream. This is consistent with the trend observed by Maqueo Martinez et al. and, in the case of the PGIRoe scheme, leads to an approaching of the experimental data according to Barschdorff. The choice of parameters does not significantly influence the shape of the pressure rise. Since the influence of nucleation can be assumed to be dominant in this area, this is in line with the physical modelling. As already explained for the Mystery nozzle, the later onset of condensation and the associated higher subcooling lead to the formation of a larger number of droplets with a smaller radius. An analysis of Equation 3.55 and Equation 3.56 shows that the adjustment of the parameters of the droplet growth model proposed by Maqueo Martinez et al. in the present case tends to lead to lower growth rate values than when using the default parameters. The strong decrease in the droplet radii when adjusting the parameters can thus be explained by a combination of a downstream displacement of the onset of condensation with a reduction in the droplet growth rate. For the PGIRoe scheme, adjusting the parameters does not improve the agreement with the experimental results. Rather, the droplet radii now deviate by up to 29%. The numerical calculations by Maqueo Martinez et al. are based on the assumption of a monodispersed droplet size distribution, which, as shown for the Mystery nozzle and confirmed by Wróblewski and Dykas [169] for the Barschdorff nozzle, can lead to a numerical overestimation of the radii. In their case, a reduction of the droplet radii, therefore, appears expedient, in contrast to the configuration *E-E-M-Poly* of the PGIRoe scheme.

Regardless of the effect achieved for the PGIRoe scheme, however, the variation of the model parameters according to Young, illustrates the high sensitivity of the numerical solution with respect to the model approaches used to describe the condensation. As indicated by the previously calculated Stokes numbers, the consideration of momentum exchange between the phases is also likely to influence the numerical results. In the right part of Figure 30, in addition to the data series already described, the results of the PGIRoe scheme of the configuration *E-E-P-Poly-S* for *Case B1* are therefore also plotted using red circles. A comparison of the pressure curve with the experimental data according to Maqueo Martinez et al. shows a high degree of agreement both in terms of the onset of condensation and the shape of the pressure increase. Only in the direct vicinity of the local pressure maximum, the PGIRoe scheme underestimates the pressure. Compared to the configuration *E-E-M-Poly*, which describes the flow using the mixture quantities, the pressure rise shows a steeper characteristic and a higher pressure value. The qualitative trend of the droplet radii is retained even when momentum transfer between the phases is taken into account. However, the configuration *E-E-P-Poly-S* calculates larger droplet radii. Although this seems plausible, given the condensation occurring comparatively further upstream, it leads to an increased discrepancy with the experimental data. In this case, the droplet radii's relative deviation is about 25%. Dykas and Wróblewski [40] examine the Barschdorff nozzle for *Case B1* using two model approaches, where, similar to the PGIRoe scheme, only one of the variants takes into account the momentum exchange between the phases. They observe comparable tendencies with regard to both the pressure curve and the droplet radii.

The results of all four configurations of the PGIRoe scheme thus appear physically consistent and also qualitatively agree with corresponding investigations represented in the literature. A comparison of the results of the PGIRoe scheme with experimental data for the nozzle according to Barschdorff also shows a high level of quantitative agreement, particularly when the momentum exchange between the phases is considered. A successful validation of the PGIRoe scheme for Laval nozzles flowed through with steam can be derived from this. In order to expand the scope of the scheme with regard to the working medium, a validation based on a test case with a medium other than water seems promising. The choice of the medium CO_2 in combination with a state at the inlet of the Laval nozzle, which is close to the usual operating limits of sCO_2 compressors, allows a simplified investigation of condensation, as it occurs in particular at blade leading edges. For this purpose, similar to the previously investigated case, a comparison of experimentally obtained results is carried out.

Comparison of experimental data of a Laval nozzle flowed through by CO_2

Theis [144] conducts investigations into homogeneous condensation in flows of CO_2 and difluorodichloromethane using five different Laval nozzle geometries. The measurement data he documented includes, in particular, Wilson lines plotted for various parameter combinations, which cover almost the entire state range between triple point and critical point. Based on these findings, Bier et al. [21, 22] investigate flows of air-CO_2 mixtures and other refrigerants. Since the literature usually erroneously refers to Bier instead of Theis in the context of the investigation of pure CO_2, in the interests of integrity, the test case will be referred to in the following as a combination of both authors' names.

Theis distinguishes the nozzles he examined based on the shape of their cross-sectional area and their expansion rate. For the validation of the PGIRoe scheme, a nozzle designated by Theis as B1 with a rectangular cross-section and an expansion rate of about $23{,}000$ 1/s is selected. The latter quantity is an estimate by Theis, obtained by averaging along the nozzle axis, and is therefore not a constant. In the left part of Figure 31, the relative area of the nozzle is plotted over the relative length. The narrowest cross-section is 1.88 mm^2 and is composed of a height of 0.75 mm and a nozzle depth of 2.51 mm. The total length of the nozzle is 34.4 mm, with the convergent and divergent parts in a ratio of 0.29 to 0.71.

For the nozzle investigated, the formation of a boundary layer is to be expected, which could significantly influence the flow and, thus also, the phase change due to the very small dimensions of the geometry. Theis therefore proposes to determine the effective flow cross-section based on an experimentally determined pressure curve for the case of a dry flow. Assuming an isentropic core flow, a quasi-analytical derivation of the effective cross-sectional area is possible if the total inlet boundary condition and the static pressure along the nozzle axis are known. Its course is shown as a dashed line in the left part of Figure 31. The difference between the geometric and effective cross-sections can be interpreted as a flow displacement resulting from a boundary layer. Accordingly, the wall friction acquires a particular significance from the narrowest cross-section of the nozzle onwards, which is further intensified in the divergent part. In addition, there is an effective displacement of the narrowest cross-section in the positive flow direction. Since the boundary conditions formulated by Theis, which will be explained in more detail below, only apply in certain part of the nozzle, this is highlighted in grey.

For the selected nozzle geometry, four test cases are examined using the medium CO$_2$, where the total pressure at the inlet is uniformly 45 bar. The total inlet temperatures vary between 300.12 K and 325.76 K. A complete overview of the inlet boundary conditions can be found in Table 9. The static conditions at the geometric inlet of the nozzle for all four cases are also shown in a T-s diagram in the right part of Figure 31. While *Case T1* is symbolised by a circle, a square marks *Case T2*. The initial condition for *Case T3* is represented by a rhombus, and that for *Case T4* by a triangle. The critical isobar illustrates that the fluid conditions

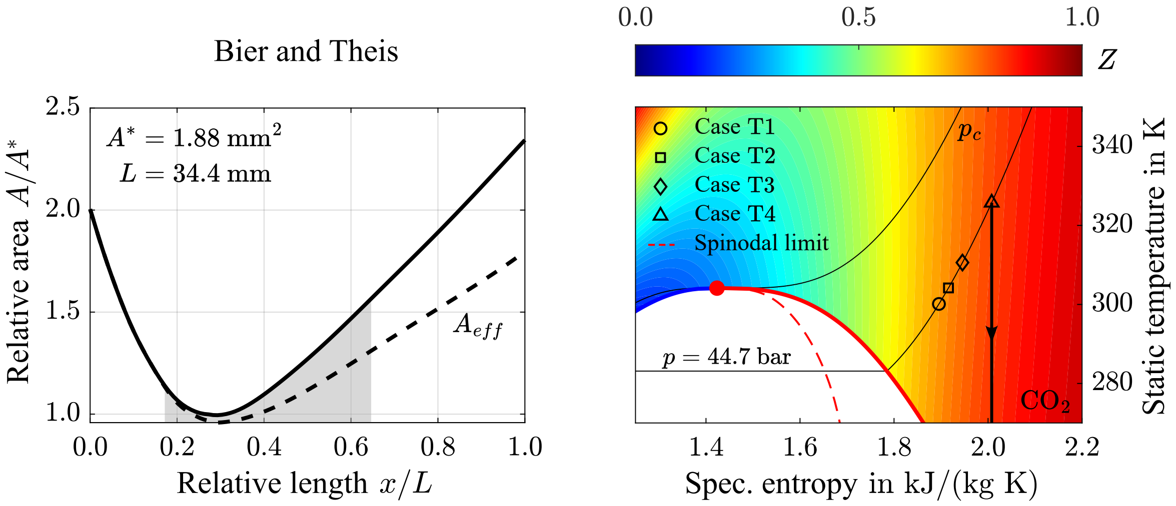

Figure 31: Geometric characteristics of the nozzle according to Bier and Theis [144] with grey shaded test section and effective cross-section represented by a black dashed line (left) as well as specification of four test cases in a T-s diagram of CO$_2$ (right)

Table 9: Boundary conditions for the nozzle according to Bier and Theis for the medium CO_2

	Case T1	Case T2	Case T3	Case T4
$p_{t,in}$	45 bar			
$T_{t,in}$	300.12 K	304.18 K	310.60 K	325.76 K

examined exhibit supercritical temperatures in some parts but a subcritical pressure value at around 44.7 bar. *Case T4* is characterised by Theis as a test case of a dry flow. However, it should be noted that this assumption is only valid within the grey-shaded test section. As a second phase also occurs for *Case T4* in the further downstream course of the nozzle, it is important to place the outlet boundary condition appropriately, particularly for determining the effective cross-sectional area. For the other three test cases, as a result of condensation, the entry into the metastable range of the two-phase region already occurs within the test section.

An analysis of the compressibility factor based on the coloured contour shown on the right in Figure 31 shows, unlike previously for the medium water, a relevant deviation from the value $Z = 1$. With decreasing temperature at the inlet of the nozzle, the compressibility factor also decreases at constant pressure. For *Case T4*, it has a value of about 0.81 and for *Case T1* of 0.73. This results in a classification of the fluid states as non-ideal, so validating the PGIRoe scheme for flows of non-ideal fluids with the formation of a second phase seems possible using the nozzle according to Bier and Theis.

Due to the indicated influence of boundary layer effects, two different approaches are pursued to investigate the flow. On the basis of the EPGIRoe scheme, which, unlike TRACE, enables a quasi-one-dimensional description of the flow, the previously calculated effective cross-sectional area can be used to dispense with explicit modelling of the wall friction. In addition, the PGIRoe scheme implemented in TRACE is used in a similar way to the previous nozzle test cases to examine the flow in a quasi-two-dimensional manner, with explicit consideration of friction. A comparison of the results obtained by these two approaches could provide information about the sensitivity of the modelling of the phase change with regard to the influence of frictional effects.

Since the turbulence model according to Spalart and Allmaras is chosen for the calculations in TRACE and thus a criterion of the dimensionless wall distance smaller than one is to be adhered to, a refinement of the spatial grid in wall proximity is carried out. In order to ensure uniformity of the calculation approaches with regard to the spatial discretisation, an identical number of nodes in the direction of the x-coordinate and thus along the nozzle axis is selected for the quasi-one-dimensional description as for the quasi-two-dimensional modelling. Based on an investigation of the spatial discretisation error, taking into account all three spatial directions, the grid independence of the solution can be assumed for a grid with $638,000$ nodes. The tabulation of the thermophysical quantities is carried out for the gas phase and the saturation quantities in a pressure range of $p \in [9;40]$ bar and a temperature range of $T \in [230;300]$ K. For the liquid phase, a pressure interval of $p \in [9;23]$ bar and a temperature interval of $T \in [250;270]$ K are tabulated. For both phases, the solution can be assumed to be independent of the selected discretisation for a table dimension of 500. To ensure the convergence of the iterative solution, a criterion of $ResL1 = 1.0 \times 10^{-7}$ is selected. Performing a calculation of *Case T1* based on the configuration *E-E-P-Poly-S* of the PGIRoe scheme allows for the estimation of a Stokes number of 0.06. Consequently, it does not appear necessary to take into account the momentum exchange between the phases.

Accordingly, a sufficiently high level of detail with regard to the description of the dispersed phase can be achieved by modelling the droplet size distribution as polydispersed. Unlike the previous investigations, no correction of the nucleation rate is applied with regard to the presence of a temperature gradient in the gas phase immediately preceding nucleation. The resulting neglect of the factor formulated in Equation 3.50 limits the influence of the model adaptations verified exclusively for steam on the droplet growth model according to Young.
However, before an investigation of condensation can be carried out, a calculation of the dry flow through the nozzle geometry according to Bier and Theis first has to be carried out. The numerical results of the pressure for *Case T4* are compared in the left part of Figure 32 with the data experimentally collected by Theis [144]. Since the measurement data is only available in the literature as figures, the corresponding curves are digitally reconstructed. A black line indicates the experimental values acquired in this way, while black triangles represent the results of the quasi-one-dimensional calculation of the EPGIRoe scheme. The pressure curve resulting from quasi-two-dimensional modelling based on the PGIRoe scheme is indicated by blue triangles. Both the calculations of the EPGIRoe scheme and those of the PGIRoe scheme are based on modelling the dispersed phase using the configuration *E-E-M-Poly*. In the absence of a liquid phase, this transitions to the GIRoe scheme, as verified using the test case of the NASA CDV nozzle.
The numerical results for *Case T4* show high agreement with the experimentally determined data. The EPGIRoe scheme almost precisely matches the measured pressure curve. However, this only confirms the consistency of the method since the effective cross-sectional area used for the calculation was previously calculated using the same measurement data. The results of the PGIRoe scheme, which are based on a description of the nozzle using its geometric contour, also match the measured data in the convergent part of the nozzle to a good approximation. Downstream of the narrowest cross-section, which is located at a relative length of about 0.29, there is a slight deviation from the experimentally determined data. This deviation increases along the nozzle axis and reaches a maximum of about 3%. In order to check a potential influence of the numerical method, a quasi-two-dimensional calculation is carried out using the EPGIRoe scheme while maintaining all boundary conditions. Since the results obtained in this way show a maximum deviation of only 0.002% from the calculations of the PGIRoe scheme, an additional data series is not shown. The description of the area through which the flow passes using the effective cross-section thus seems to lead to a slight overestimation of the influence of the boundary layer in the divergent part of the nozzle. However, it should be noted that both the experimental pressure curve shown and the nozzle contour are determined graphically and thus exhibit inaccuracies, which could affect the comparison of results and at least partially explain the deviation. Due to the slight difference and qualitative similarity of the curves, further investigation using the PGIRoe scheme seems justified.
The right part of Figure 32 therefore shows the results of the PGIRoe scheme of the test cases for which a second phase occurs within the test section. *Case T1* is represented by blue circles, *Case T2* by blue squares and *Case T3* by blue diamonds. The Wilson point is characterised by the PGIRoe scheme exemplarily for *Case T1* by a pressure of about 20.3 bar and a maximum subcooling of 8 K. A comparison of this data pair with the Wilson line determined by Theis confirms the low value of the maximum subcooling compared to the test cases for steam examined so far.

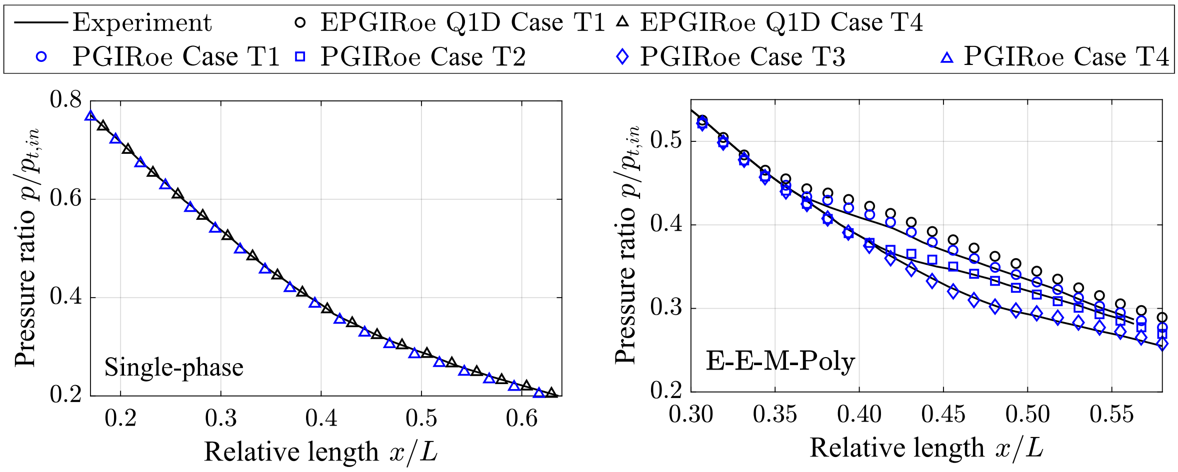

Figure 32: Pressure curves for Case T4 assuming a single-phase flow as determined experimentally by Theis [144] and numerically using the PGIRoe scheme (blue symbols) and the EPGIRoe scheme (black symbols) (left) as well as pressure curves for all four test cases taking into account a second phase (right) for the medium CO_2

A high degree of agreement with the experimental data can be seen for all three test cases. For *Case T3*, for example, the values of the pressure calculated using the PGIRoe scheme lie almost exactly on the measured pressure curve. The position of the Wilson point and the subsequent pressure rise are also well approximated by the PGIRoe scheme. The relatively low maximum subcooling is reflected in a flat pressure rise. In order to examine the influence of the cross-sectional area on the onset of condensation and also to simplify comparison with investigations represented in the literature, the quasi-one-dimensional results of the EPGIRoe scheme for *Case T1* are also plotted in the right part of Figure 32 as black circles. The Wilson point is predicted by the EPGIRoe scheme a little further upstream. As a result, the condensation and the pressure increase associated with it occur at a slightly higher pressure. This causes a quantitative deviation from the experimental measurement data, which is more pronounced than in the case of the quasi-two-dimensional calculations of the PGIRoe scheme. In order to be able to exclude an influence of the implementation here as well, a quasi-two-dimensional comparative calculation is again carried out using the EPGIRoe scheme.

The deviation from the results of the PGIRoe scheme is of a similar order of magnitude as in the dry case and can, therefore, be neglected. The purely quantitative offset of the pressure rise thus seems to be due to the way the influence of friction is modelled. This could be interpreted as an indication of the particular relevance of an exact modelling of the nozzle contour and the boundary layer effects occurring on it in the context of phase change processes. An influence of the interaction of the dispersed phase and the turbulent boundary layer cannot be excluded either.

Since Theis does not measure the droplet radii, a final assessment of the results in terms of the accuracy of description of the dispersed phase is unfortunately not possible. The necessity of adapting the formulation of the critical radius from Equation 3.48 with regard to the non-ideality of the gas phase, as stated by Petruccelli et al. [114], cannot be confirmed by the present study. Using numerical calculations, the authors demonstrate that the way the critical radius is modelled significantly influences the Wilson point. For this purpose, they examine a nozzle designated as B2 by Theis, which has a higher expansion rate. The underlying description of the nozzle geometry is based on an apparently inappropriate combination of effective cross-sectional area and additional turbulence modelling. A comparison of the results presented by the authors with the experimental measurement data according to Theis also shows considerable deviations, which unfortunately are not discussed.

In principle, an investigation of adaptations of the model approaches established for the medium steam, which also assume the ideality of the gas phase, seems quite promising. In addition to a detailed theoretical analysis of the gas-kinetic relationships, however, a corresponding database is required to validate the developed model adaptations. In particular, the lack of availability of measurement data for the droplet radii has a limiting effect, so that such a consideration is dispensed with in the context of this work.

Since the speed of sound in particular, but also an expression equivalent to the isentropic exponent of calorically perfect gases, are central parameters of the PGIRoe scheme, it seems sensible to investigate these with regard to flows of non-ideal fluids forming a second phase. It turns out that the way the speed of sound in the two-phase region is calculated has no significant influence on the results of *Case T1*. Even an approximation of the isentropic exponent in Equation 4.49 that differs from the isentropic pressure-volume coefficient leads only to a relative deviation of the pressure in the direct vicinity of the Wilson point of up to 0.01 bar, which corresponds to a relative deviation of 0.05%. A detailed description of the underlying investigation can be found in Appendix D. This indicates that the procedure followed to determine the thermophysical state quantities in the two-phase region appears to be valid, at least for the test cases examined in the context of this work.

The high degree of agreement between the results of the PGIRoe scheme and the experimental data for the medium CO_2 obtained for the nozzle according to Bier and Theis also shows that the PGIRoe scheme is able to describe the phase change in flows of non-ideal fluids in a suitable manner. The previous numerical investigation of condensation in Laval nozzles places the focus of validation on the accuracy of the description associated with modelling the phase change. With the exception of the near-wall regions, the flows examined for this purpose exhibit a quasi-one-dimensional characteristic, which, however, cannot be found in real turbomachinery. To validate the PGIRoe scheme also for flows, which, in addition to the formation of a second phase, are characterised by the presence of two-dimensional discontinuities, an axial turbine cascade provides a suitable test case.

5.2.2 Phase Interaction of Steam in a Turbine Cascade

As a result of the flow around turbine blades, shock fronts can form at the trailing edge, in the vicinity of which interaction between the dispersed and the continuous phase can be observed in terms of an increased heat and momentum exchange. To be able to map the resulting flow characteristics numerically and thus to estimate the occurring flow losses, high demands are placed on the method used in terms of robustness and accuracy of description of the phase change. White et al. [165] investigate the flow of steam within an axial turbine cascade both experimentally and using a two-dimensional time-marching method developed by White [163] that describes the dispersed phase in a Lagrangian frame of reference.

The blade profiles used are the stator blades of the fifth stage of a real low-pressure steam turbine. The cascade consists of four profiles arranged in parallel. Using an optical access in the region of the trailing edges of the blades, the flow field can be visualised using Schlieren images. Pressure taps along the suction and pressure sides of the two central profiles also enable a spatially resolved measurement of the static pressure on the blade surface. To enable a

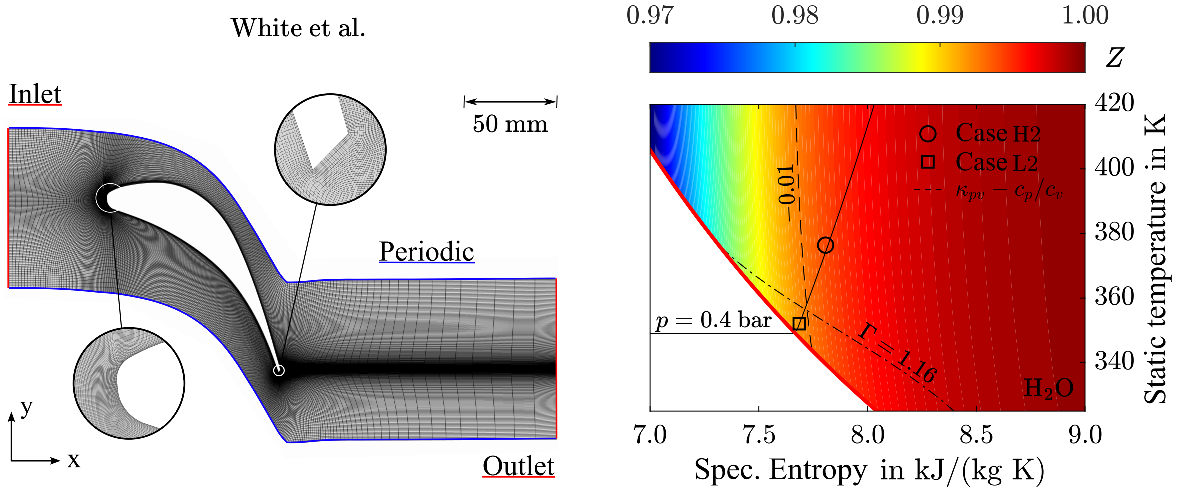

Figure 33: Geometry of the cascade according to White et al. [165], localisation of the boundary conditions and detailed views of the meshing strategy at the leading and trailing edge of the blade (left) as well as specification of two test cases (○ Case H2 and □ Case L2) in a T-s diagram of water (right)

validation of two-dimensional numerical methods, the depth of the passage with 152 mm is chosen in such a way that no relevant influence from the limitation in depth is to be expected in the spatial symmetry plane. The mean expansion rate is given by White et al. as 1156 1/s and matches the value of the actual turbine due to the choice of blading.

In order to make the test case accessible to investigation using CFD methods, the flow channel around one of the four blades is modelled. Homogeneous distribution of the flow quantities at the inlet is ensured by positioning the inlet boundary condition at a sufficient distance from the blade's leading edge. In addition, maintaining an appropriate distance between the trailing edge of the blade and the outlet prevents the shock systems to be expected in the wake area of the blade from affecting the outlet boundary condition. The physical total length of the modelled section, which is shown in the left part of Figure 33, is 300 mm. The definition of the delimiting surface, which is almost parallel to the blade contour of the pressure side, as a periodic boundary condition makes it possible to describe the complete flow field within the cascade using only one profile.

White et al. define 22 test cases, which are classified both by the subcooling at the inlet and the Mach number at the outlet. They distinguish between low, medium, high, and very high subcooling, where the latter always assumes positive values and is therefore also referred to as superheat. For each of these groups, the Mach number at the outlet is varied by controlling the back pressure of the condenser. The test case with the highest Mach number and, thus, the lowest outlet pressure is indicated by the number one, while the lowest Mach number and the highest outlet pressure are achieved for the test case with the number three.

Table 10: Boundary conditions for the cascade according to White et al. for the medium water

	$p_{t,in}$	$T_{t,in}$	p_{out}
Case H2	0.419 bar	378.5 K	0.177 bar
Case L2	0.409 bar	354.0 K	0.194 bar

The validation of the PGIRoe scheme is carried out by means of two characteristic test cases. These are notable for significant differences in their flow characteristics as well as sufficient representation in the literature in the form of comparable numerical investigations. Both test cases have a total inlet pressure of just over 0.4 bar. *Case H2* is defined by White et al. as having a total inlet temperature of 378.5 K and is classified as a test case with high superheat. If it is determined based on the total quantities at the inlet, this yields a value of 28 K. The number two in the designation indicates that the Mach number at the outlet corresponds to a medium supersonic value for this group. The same applies to *Case L2*, where the total inlet temperature of 354 K causes an overheating of 4 K and thus places the test case in the low superheat group.

An overview of the inlet and outlet boundary conditions can be found in Table 10, where the static pressure at the outlet is interpreted as an area-averaged value. The static inlet conditions of the two test cases are also shown in the right-hand part of Figure 33 in a T-s diagram. A circle symbolises *Case H2*, while *Case L2* is represented by a square. The already highlighted distinction between the test cases based on superheat is made clear by different distances of the illustrated inlet states from the dew line. For example, *Case L2* as a result of low superheat is different from *Case H2* in that it is in close proximity to the dew line. An analysis of the compressibility factor, which is represented by a coloured contour, shows no significant deviation from the value of one for both initial states. This is consistent with the validation cases examined so far for the medium water and indicates only a slight non-ideality of the gas phase. The deviation of the isentropic pressure-volume exponent from the ratio of specific heat capacities, plotted as a dashed isoline, and the dash-dot line of the fundamental derivative also confirm this classification. The fundamental derivative takes on a value greater than one for both test cases. The isentropic pressure-volume exponent differs only by about -0.01 and thus 0.83% from the ratio of specific heat capacities for both *Case H2* and *Case L2*.

A numerical investigation of the change of state within the turbine cascade requires a spatial grid that is generated based on the geometry. To ensure sufficient resolution in the near-wall region of the turbine blades and thus to comply with the criterion of the dimensionless wall distance for the turbulence model according to Spalart and Allmaras, the grid is refined close to the walls. Particular attention is paid to the structure in the vicinity of the leading and trailing edges of the blade, which are shown enlarged in the left part of Figure 33. While a sufficient resolution of the stagnation point is to be ensured at the blade's leading edge, the grid structure in the vicinity of the trailing edge of the blade is particularly relevant in the context of the shock systems that form here. In order to ensure as high a level of accuracy as possible in describing the flow characteristics, the grid is locally refined and optimised in terms of the arrangement of its nodes. Based on an investigation of the spatial discretisation error of the grid generated in this way, grid independence of the solution can be demonstrated for a node number of 1.16 million.

The tabulation of the thermophysical quantities of the gas phase and the saturation quantities is carried out in a pressure range of $p \in [0.05; 0.45]$ bar and a temperature range of $T \in [250; 400]$ K. For the liquid phase, a pressure interval of $p \in [0.05; 0.35]$ bar and a temperature interval of $T \in [250; 380]$ K are tabulated. The solution can be assumed to be independent of the selected table discretisation with a table dimension of 500 for the gas phase and a dimension of 1000 for the liquid phase. In addition, the iterative solution is considered to have converged if a criterion of $ResL1 = 1.0 \times 10^{-6}$ is undercut.

To assess whether considering the momentum exchange between the phases for the examined test cases of the turbine cascade according to White et al. could provide additional insights, a calculation of both cases is carried out using the configuration *E-E-P-Poly-S* of the PGIRoe scheme. The highest difference between the velocities of the gas and liquid phases is predicted in the region of the flow separation at the blade's trailing edge. A calculation of the Stokes number at the point of maximum difference in phase velocities yields a value of 0.74 for *Case H2*, while a value of 0.92 is obtained for *Case L2*. As a result, both test cases fulfil the criterion defined as $St > 0.1$, which is why the further calculations take into account a momentum exchange between the phases by using the configuration *E-E-P-Poly-S*.

At this stage, it should be noted that the phase-based notation allows for a comprehensive determination of the flow quantities of both phases and, thus, in particular, a description of the droplet trajectories in the flow field. Thereby, considering a possible interaction of the droplets with each other is omitted. Furthermore, the heat transfer at the interface between the liquid phase and the blade surface is not modelled.

In the left part of Figure 34, the numerical results of the static pressure on the blade surface for *Case H2* are compared with the data experimentally obtained by White et al. [165]. For this purpose, the ratio of static pressure to total inlet pressure is plotted over the relative arc length of the profile, which is defined as the ratio of the coordinate in the x direction to the arc length of the blade. The trailing edge of the blade, which, due to its shape, is defined by a pressure-side and a suction-side coordinate, is excluded from the determination of the relative arc length. While the experimental data points for *Case H2* are shown as circular symbols, the results of the PGIRoe scheme are represented by a blue line. It should be noted that the representation of the CFD results as a continuous function requires a linear interpolation between the data points. However, due to the high node density in the vicinity of the wall, any influence of this interpolation on the significance of the representation can be neglected. The results of the PGIRoe scheme show a high degree of agreement with the experimental data for *Case H2*.

Starting from the stagnation point, which forms the origin of the ordinate, the curve of pressure-side static pressure on the blade surface closely matches the measured data points, with the deviation decreasing along the relative arc length. Since the flow field near the

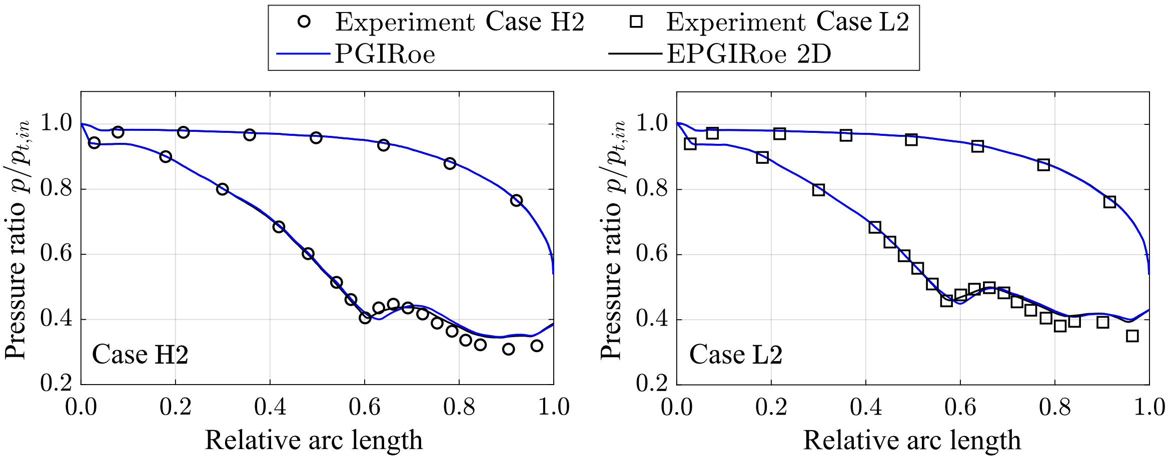

Figure 34: Comparison of pressure curves along the blade surface for Case H2 (left) and Case L2 (right) of the cascade according to White et al. using the PGIRoe scheme (blue line) and the EPGIRoe scheme (black line) with experimental data from White [163] (symbols) for the medium water

pressure side of the profile is characterised by higher pressure and lower velocity values compared to the suction side, condensation is not expected to influence the pressure curve significantly. This is confirmed by the steady decrease in pressure along the relative arc length. The suction-side pressure curve also shows a characteristic similar to the experimental data. A relevant deviation of the numerical results first becomes visible at a relative arc length of about 0.6. Due to the prevailing supersonic conditions in the vicinity of the blade's trailing edge, oblique shock waves are formed as a result of its angular shape.

White et al. distinguish these shock fronts on the basis of their localisation in the flow field into pressure- and suction-side discontinuities. An analysis of the two-dimensional flow field determined by the PGIRoe scheme shows that a pressure-side shock originating from the profile located above the investigated blade meets the suction side of the investigated profile at about a relative arc length of 0.62. This is qualitatively consistent with the Schlieren images documented by White et al., which are discussed in detail below in the context of *Case L2*. Consequently, the local pressure rise, seen in the left part of Figure 34, can be explained by an interaction between the flow near the blade and the shock front. However, there is a slight deviation in terms of the position and slope of the pressure rise. The deviation also increases downstream of the shock. Thus, the pressure downstream of the shock front is slightly overestimated, resulting in a maximum deviation of about 0.016 bar and thus 12%. However, the qualitative similarity of the curves is maintained along the entire arc length.

A comparative calculation is carried out using the two-dimensional EPGIRoe scheme to investigate possible numerical factors influencing the prediction of the position of the pressure-side shock. The results, which, with the exception of the flow solver used, are based on identical boundary conditions, are shown in Figure 34 as a black line. While, for the most part, the results of the EPGIRoe scheme correspond almost exactly with the results of the PGIRoe scheme, there is a noticeable deviation in the region of the pressure rise. The EPGIRoe scheme predicts a slightly upstream shifted position of the shock front, which is reflected in a corresponding offset of the pressure rise and leads to a higher agreement with the experimental data. Downstream of the shock front, the results of the EPGIRoe scheme gradually approach the values determined using the PGIRoe scheme. Similar to the single-phase case of the nozzle according to Spinelli et al., the EPGIRoe scheme seems to be able to describe the flow in the direct vicinity of shock fronts with slightly higher accuracy. However, a discussion of these seems necessary since no quantitatively comparable deviations are observed for the investigations presented earlier in this chapter.

Unlike for the EPGIRoe scheme, the flow channel for the PGIRoe scheme implemented in TRACE is modelled as three-dimensional. To investigate a possible influence of the spatial depth on the numerical results, the calculation of *Case H2* is therefore repeated using the three-dimensional EPGIRoe scheme. For spatial discretisation, the grid already generated for the calculations of the PGIRoe scheme is used. The results of the EPGIRoe scheme obtained in this way show no significant deviation from the two-dimensional calculations and are therefore not shown. Based on this, the modelling of spatial depth can be ruled out as the cause of the observed deviation.

The other potentially relevant differences between the flow solvers considered in this study are limited to the method used for temporal integration and the type of implementation. However, without making significant changes to the existing structures, the influence of the temporal integration can only be examined superficially. To do this, the implicit method implemented in TRACE must be approximated to the integration conditions of the explicit approach. This is done by adjusting the CFL number, which, according to Equation 4.64, is proportional to the time step of the integration. Lowering the CFL number to the value of one does not lead to any relevant change in the results of the PGIRoe scheme. However, from this, only the consistency of the implicit method for different integration step sizes can be concluded. Due to the present study's focus on validating the formulated flux calculation scheme, an analysis going beyond the already presented approaches does not appear to be useful at this point.

A greater gain in knowledge for the validation of the PGIRoe scheme promises the investigation of a further test case as *Case L2*. For this case, according to White et al., and in contrast to *Case H2*, the condensation is expected to have an influence on the pressure curve at the blade surface due to the lower superheat. A comparison of the results calculated using the PGIRoe scheme with the experimental data is shown in the right part of Figure 34. Analogous to *Case H2*, the symbols, which have a quadratic shape for *Case L2*, represent the measurement data, while a blue line indicates the numerical results of the PGIRoe scheme. The trend of the pressure along the pressure side of the blade shows a high degree of agreement with the experimental data comparable to *Case H2*. An increase in pressure can be seen in the range of a relative arc length of about 0.58, which is again predicted by the PGIRoe scheme to be slightly offset downstream. However, unlike in *Case H2*, the slope of the pressure rise in this case resembles that indicated by the experiment. An examination of the two-dimensional flow field, which will be described in detail below, shows the formation of a condensation front on the suction side of the blade. It is located in close proximity to a shock front emanating from the trailing edge of the neighbouring profile, which is why the observed increase in pressure at the blade surface appears to be explainable by a combination of both phenomena. This is confirmed by an analysis of the point of maximum subcooling on the blade surface, which marks the local onset of condensation and, for the PGIRoe scheme, coincides with the onset of the pressure rise. Further downstream, the deviation of the results of the PGIRoe scheme from the experimental data increases similarly to *Case H2*.

However, unlike for the latter, both the measurement data and the numerical results show a second, weaker pressure increase. According to White et al., the temperature increase in the vicinity of the pressure-side shock causes the condensation front to split into two parts. One part, which is in close proximity to the suction side, remains at the level of the shock front, while the second part appears to be shifted downstream. A reaction of the latter on the flow quantities of the suction side could cause a renewed increase in pressure. Again, this is qualitatively represented by the PGIRoe scheme, whereby the deviation from the measured data downstream assumes a maximum value of about 0.021 bar and thus 19%.

If the results of the PGIRoe scheme are also compared with those of the EPGIRoe scheme for *Case L2*, a comparable picture to *Case H2* emerges. A relevant deviation between the implementations occurs exclusively in the vicinity of the shock. The EPGIRoe scheme again matches the experimental data locally with slightly higher accuracy, whereby the deviation from the PGIRoe scheme is smaller than in *Case H2*. This seems surprising at first glance due to the somewhat more complex flow characteristics, but could be due to a reduced dominance of the discontinuity caused by the condensation front.

In order to assess the deviations of the PGIRoe scheme shown in Figure 34 from the experimental data, a comparison with corresponding literature references is useful. The time-marching method developed by White [163] shows deviations of up to 30% concerning the pressure at the blade surface in *Case H2*. Dykas and Wróblewski [41] analyse two test cases complementary to *Case L2* using a flow solver similar to the configuration *E-E-P-Poly-S*. Unlike White, they take into account a momentum exchange between the phases. The resulting maximum deviation of their results from the measurement data occurs in the vicinity of the shock and amounts to about 29%. Grübel et al. [59] calculate *Case L2* using different model approaches to describe droplet growth. Irrespective of this variation, their results show a maximum deviation in the region of the blade's trailing edge of about 23%. The PGIRoe scheme thus seems to describe the flow characteristics in both test cases with comparatively high accuracy. The remaining deviation could further be explained by the assumption of a periodic boundary condition, which, according to White [163], cannot necessarily be sufficiently justified by the flow. Also, there are changes in the flow field over time as a result of the flow through the cascade, which are not resolved by the method used.

In order to be able to conclusively assess the suitability of the PGIRoe scheme for describing discontinuities and condensation fronts, as well as the resulting phase interaction, a study of the two-dimensional flow field is required. Given the interaction between the shock and condensation front that has already been indicated, *Case L2* appears particularly suitable for this. To visualise the two-dimensional flow within the cascade based on the calculation results of the PGIRoe scheme, the spatial density gradients are evaluated. A qualitative contour plot of these can be found in the left part of Figure 35. Black-coloured areas represent a high value of the density gradient and are thus characteristic of discontinuities, while low values of the density gradient are shown in white. The periodic boundary condition and the blade contour can be identified through the colouring used in Figure 33.

The comparison of a Schlieren image measured experimentally by White [163] in the right part of Figure 35 allows a qualitative comparison. In contrast to the numerical Schlieren image, the colour blue is used to indicate shocks in the experiment, while the colour green indicates regions of small gradients. For better orientation, in addition to the periodic boundary condition, the limits of the numerical Schlieren image are shown in the measured frame as black dotted lines. On the pressure side of the blade profile, a discontinuity originating from the trailing edge of the blade can be seen, which White refers to as the pressure-side shock S_{DS} and is already discussed in the context of the pressure curves in Figure 34. Both the shock's position and geometric orientation are consistent with the experimental results. However, according to the numerical description, the shock front consists of two slightly offset discontinuities. White points out that an oscillation of the shock fronts results in a blurred representation in the experimental Schlieren images. This could also be a possible

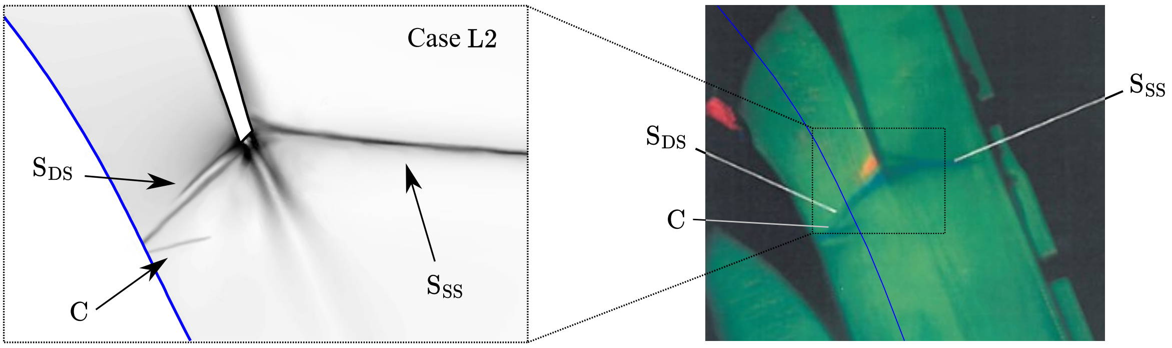

Figure 35: Qualitative contour plots of density gradients for Case L2 of the cascade according to White et al. numerically calculated using the PGIRoe scheme (left) and experimentally measured by White [163] (right)

explanation for the deviation in the numerical results. Another shock front marked $\mathrm{S_{SS}}$ can be seen on the suction side of the blade profile. Unlike the shock $\mathrm{S_{DS}}$, this discontinuity is described by the numerical calculations as clearly separated from the rest of the flow field. Similar to $\mathrm{S_{DS}}$, there is a high degree of agreement with the experimental data in terms of the position and orientation of the shock front.

As already shown by the pressure curve on the blade surface, a condensation front forms for *Case L2*, which can also be seen from the numerical density gradients and is marked by the letter C in Figure 34. It spreads from the suction side of the profile into the flow channel and has a similar shape to that in the experimental Schlieren image. The onset of condensation and, thus, the formation of a second phase in the direct vicinity of a discontinuity in the flow appears to lead to a weakening of the shock intensity. In particular, there is no reflection of $\mathrm{S_{DS}}$ on the suction side of the profile, which could indicate an increased phase interaction in this region. This is consistent with the observation of local maxima in the difference in phase velocities calculated using the PGIRoe scheme. Immediately downstream of the blade profile, the numerical results indicate regions of large density gradients, which are not confirmed by the experiment. However, the experimental results also show regions of larger gradients in the wake of the blade. An analysis of the wetness fraction downstream of the blade's trailing edge shows that the PGIRoe scheme also predicts large gradients for this. The turbulent separation could cause the droplets to remain in this region for longer and, as a result, lead to locally increased droplet growth.

The level of detail of the numerical Schlieren image illustrates the accuracy of the description achieved by the PGIRoe scheme. Both the two-dimensional discontinuities of the flow and the phase change mechanisms are predicted in close agreement with the experimental results. In combination with the validation of different configurations of the PGIRoe scheme using Laval nozzles presented in Chapter 5.2.1, this indicates the applicability of the method to problems of varying complexity and dimension.

6 Summary and Outlook

The present work aims to contribute to the development of numerical methods for the investigation of phase change processes of compressible non-ideal fluids. For this purpose, a method for calculating numerical flux terms originally formulated by Roe for calorically perfect gases is extended for application to one- and two-phase flows of non-ideal fluids. The resulting PGIRoe scheme is characterised by a low complexity based on its derivation and can be applied to any equation of state. It also offers the possibility of describing a dispersed phase formed during phase change using different modelling assumptions. In addition to the frame of reference of the dispersed phase, the type of modelling of the droplet size distribution can be selected as required. In addition, the PGIRoe scheme allows the momentum exchange between the phases to be taken into account so that the movement of the dispersed phase can be described separately from the continuous phase. By formulating different configurations implemented in parallel and transitioning into one another in the single-phase case, the scheme can map the level of detail required for a specific problem to a very high degree of accuracy. A modular structure also enables using various models to describe the phase change processes. By implementing the PGIRoe scheme in the three-dimensional flow solver TRACE, the developed approach will be made accessible to the scientific community and industrial applications. In this way, validation will be performed based on an established flow solver for the calculation of turbomachinery flows. The option of tabulating the thermophysical quantities can lead to a considerable increase in calculation time efficiency. This results in an increase in availability and thus enables a potential use of the PGIRoe scheme as part of the numerical design of turbomachinery. With this objective in mind, the scheme is comprehensively verified and validated using a representative selection of suitable single-phase and two-phase test cases. To prove the applicability of the PGIRoe scheme for both implicit and explicit methods of temporal integration, additional validation is carried out using a three-dimensional flow solver implemented independently of TRACE itself. In addition, a validation staged according to the number of phases enables individual characteristics to be analysed in as much isolation as possible. An investigation of the single-phase flow through Laval nozzles shows that the PGIRoe scheme can describe discontinuities in the flow with high accuracy. This can be demonstrated by analysing different working media for fluids of both moderate and high molecular complexity and non-ideality. The robustness of the PGIRoe scheme against large gradients in the flow field is also confirmed by the investigation of the flow through a sCO_2 compressor. Despite the direct proximity of the operating points to the critical point and the two-phase region, a converged solution can be achieved, showing sufficient agreement with the experimentally determined values. The validity of the PGIRoe scheme for the description of single-phase flows indicated in this way serves as the basis for the subsequent consideration of two-phase test cases. The different configurations of the scheme are analysed using condensation in Laval nozzles. This shows that the PGIRoe scheme is able to describe the phase change using both the homogeneous equilibrium condensation model and the homogeneous non-equilibrium condensation model. In addition, consistent results can be achieved for different modelling types of the dispersed phase, which show only minor deviations from experimentally determined data, both qualitatively and quantitatively. To enable verification of the models implemented to describe nucleation and droplet growth, the droplet radius is also included in the validation as a representative of the dispersed phase alongside a measured quantity of the continuous phase. The investigation of the flow through an axial turbine cascade shows that the PGIRoe scheme describes both discontinuities and condensation fronts and the associated interaction between the phases in agreement with experimental results. The PGIRoe scheme thus appears to be applicable to single-phase and two-phase flows of compressible non-ideal fluids of different molecular complexity. A restriction to compressible media requires a dominance of the gaseous phase within the flow, which limits the range of application with regard to the wetness fraction $y < 0.5$. However, no practical limitation is expected for the investigation of homogeneous condensation in turbomachinery due to the low values of the wetness fraction that can be observed. Therefore, determining the speed of sound in the two-phase region, assuming a state of equilibrium, also appears to be sufficient. Since the condensation of non-ideal fluids could lead to the local formation of higher values of the wetness fraction, a possible influence on the determination of the speed of sound in the two-phase region must be examined on a case-by-case basis. If the assumption of an equilibrium state can no longer be justified, a formulation considering the wetness fraction can be used.

Initial studies on multi-component flows, which are not part of the present work, indicate the validity of the PGIRoe scheme for mixtures. However, this should be proven in the future through comprehensive validation. An investigation of the HeRo compressor with consideration of a second phase also appears promising. As the single-phase calculations indicate that the saturated vapour line is crossed near the blade's leading edge, a second phase could form in this area due to phase change processes. A calculation of the three-dimensional flow field under the assumption of homogeneous non-equilibrium condensation enables a more detailed analysis of the local changes of state. Considering a momentum exchange between the phases by the PGIRoe scheme could also contribute to an ambiguity discussed in the literature regarding the time scales associated with condensation.

Another way to describe such processes with even greater accuracy is to use LES methods. An application of the PGIRoe scheme in this context appears to be possible with minor adjustments to the existing approaches in TRACE and could provide added value in terms of modelling the fluid for a variety of issues. For example, the established turbulence models, most of which are based on the assumption of a calorically perfect gas, could be checked for application to non-ideal fluids using LES calculations and adapted if necessary. As a result, an increase in the confidence range of the RANS calculations would be conceivable. In addition, LES calculations enable a time-resolved investigation of boundary layer effects. In this way, a possible interaction of the boundary layer with the dispersed phase in the vicinity of condensation fronts could be investigated in more detail using numerical methods. Such investigations could also offer added value concerning the uncertainty mentioned above regarding the onset of condensation in the immediate vicinity of the critical point.

Due to the high technical relevance of evaporation in the context of a short-term increase in compressor efficiency, modelling this physical process, which is complementary to condensation, could also represent an interesting extension. By adapting the source terms accordingly, the PGIRoe scheme can potentially describe any phase change processes. Due to the modular implementation, a simple extension of the existing model equations can be realised, whereby a reversal of the droplet growth could already be a first approach to describe evaporation. If, in addition to the aerodynamic drag force, further force components are taken into account concerning the momentum balance of the phases, this could enable an increase in the accuracy of the description for two-phase flows. Once again, an adaptation of the source terms of the PGIRoe scheme for the configuration that allows momentum exchange between the phases appears to be a suitable starting point. In this way, an investigation of the deposition of liquid droplets on walls and the resulting film formation would likewise be conceivable.

Since the model equations for describing nucleation and droplet growth are based on the assumption of a calorically perfect gas and are also historically optimised for describing the medium of steam, a detailed theoretical study in the context of flows of non-ideal fluids seems advisable. Such a study requires an analysis of the underlying molecular gas kinetics and could lead to an adaptation of the existing models. However, the validation of these models requires a corresponding experimental database, which is not currently available. In particular, a need for experimental measurements of droplet radii in condensing flows of non-ideal fluids can be derived from this. If such data is available, the PGIRoe scheme appears to be particularly suitable for validating the adapted models based on the results outlined in the present work.

7 Appendix

A Thermophysical model equations

Table A.1: Thermophysical model equations used for the media water, CO_2 and MDM in accordance with the standards of IAPWS-IF97 or the REFPROP-10 implementation [91]

Fluid	Fundamental equation	Dynamic viscosity	Thermal conductivity	Surface tension
Water	IAPWS-IF97 [160]	Huber et al. [76]	Huber et al. [75]	IAPWS 2014 [79]
CO_2	Span and Wagner [136]	Laesecke and Muzny [86]	Huber et al. [77]	Mulero et al. [105]
MDM $C_8H_{24}O_2Si_3$	Thol et al. [145]	Huber [74]	Huber [74]	Mulero and Cachadina [104]

B Vectors and matrices for implementing the PGIRoe scheme in three dimensions

Single-phase (GIRoe):

$$\boldsymbol{U} = \begin{pmatrix} \rho \\ \rho u \\ \rho v \\ \rho w \\ \rho E \end{pmatrix}, \quad \boldsymbol{F}_c = \begin{pmatrix} \rho \boldsymbol{u} \\ \rho u \boldsymbol{u} + p n_x \\ \rho v \boldsymbol{u} + p n_y \\ \rho w \boldsymbol{u} + p n_z \\ \rho \boldsymbol{u} H \end{pmatrix}, \quad \boldsymbol{Q} = \begin{pmatrix} 0 \\ 0 \\ 0 \\ 0 \\ 0 \end{pmatrix} \tag{B.1}$$

Jacobian matrix:

$$\boldsymbol{A}(\boldsymbol{U}) = \begin{pmatrix} 0 & n_x & n_y & n_z & 0 \\ \frac{1}{2}(\kappa-1)\boldsymbol{v}^2 n_x - u\boldsymbol{u} & \boldsymbol{u} - (\kappa-2)u n_x & u n_y - (\kappa-1) v n_x & u n_z - (\kappa-1) w n_x & (\kappa-1) n_x \\ \frac{1}{2}(\kappa-1)\boldsymbol{v}^2 n_y - v\boldsymbol{u} & v n_x - (\kappa-1) u n_y & \boldsymbol{u} - (\kappa-2) v n_y & v n_z - (\kappa-1) w n_y & (\kappa-1) n_y \\ \frac{1}{2}(\kappa-1)\boldsymbol{v}^2 n_z - w\boldsymbol{u} & w n_x - (\kappa-1) u n_z & w n_y - (\kappa-1) v n_z & \boldsymbol{u} - (\kappa-2) w n_z & (\kappa-1) n_z \\ \left[\frac{1}{2}(\kappa-2)\boldsymbol{v}^2 - h\right]\boldsymbol{u} & \left(h + \frac{1}{2}\boldsymbol{v}^2\right) n_x - (\kappa-1) u \boldsymbol{u} & \left(h + \frac{1}{2}\boldsymbol{v}^2\right) n_y - (\kappa-1) v \boldsymbol{u} & \left(h + \frac{1}{2}\boldsymbol{v}^2\right) n_z - (\kappa-1) w \boldsymbol{u} & \kappa \boldsymbol{u} \end{pmatrix} \tag{B.2}$$

$$n_x^2 + n_y^2 + n_z^2 = 1, \qquad \boldsymbol{u} = u n_x + v n_y + w n_z, \qquad \boldsymbol{v}^2 = u^2 + v^2 + w^2$$

Eigenstructure:

$$\tilde{\lambda}_1 = \tilde{\boldsymbol{u}} - \tilde{a}, \;\; \tilde{\lambda}_2 = \tilde{\boldsymbol{u}}, \;\; \tilde{\lambda}_3 = \tilde{\boldsymbol{u}}, \;\; \tilde{\lambda}_4 = \tilde{\boldsymbol{u}}, \;\; \tilde{\lambda}_5 = \tilde{\boldsymbol{u}} + \tilde{a} \tag{B.3}$$

$$\boldsymbol{E} = \begin{pmatrix} 1 & 1 & 0 & 0 & 1 \\ \tilde{u} - \tilde{a} n_x & \tilde{u} & n_y & -n_z & \tilde{u} + \tilde{a} n_x \\ \tilde{v} - \tilde{a} n_y & \tilde{v} & -n_x & 0 & \tilde{v} + \tilde{a} n_y \\ \tilde{w} - \tilde{a} n_z & \tilde{w} & 0 & n_x & \tilde{w} + \tilde{a} n_z \\ \tilde{H} - \tilde{a}\tilde{\boldsymbol{u}} & \frac{1}{2}\tilde{\boldsymbol{v}}^2 & \tilde{u} n_y - \tilde{v} n_x & \tilde{w} n_x - \tilde{u} n_z & \tilde{H} + \tilde{a}\tilde{\boldsymbol{u}} \end{pmatrix} \tag{B.4}$$

Additional Roe-averaged quantity:

$$\tilde{T} = \frac{\sqrt{\rho_L} T_L + \sqrt{\rho_R} T_R}{\sqrt{\rho_L} + \sqrt{\rho_R}} \qquad \longrightarrow \qquad \tilde{a} = a_{EOS}(\tilde{\rho}, \tilde{T}) \tag{B.5}$$

E-E-M-Mono:

$$\boldsymbol{U}=\begin{pmatrix}\rho_m\\ \rho_m u\\ \rho_m v\\ \rho_m w\\ \rho_m E\\ \rho_m y\\ \rho_m N_T\end{pmatrix},\ \boldsymbol{F}_c=\begin{pmatrix}\rho_m\boldsymbol{u}\\ \rho_m u\boldsymbol{u}+pn_x\\ \rho_m v\boldsymbol{u}+pn_y\\ \rho_m w\boldsymbol{u}+pn_z\\ \rho_m\boldsymbol{u}H\\ \rho_m y\boldsymbol{u}\\ \rho_m N_T\boldsymbol{u}\end{pmatrix},\ \boldsymbol{Q}=\begin{pmatrix}0\\0\\0\\0\\0\\ \rho_m(\Lambda_N+4\pi r^2\rho_l N_T G(r_{20}))\\ \rho_m\bar{J}\end{pmatrix} \tag{B.6}$$

Jacobian matrix:

$$\boldsymbol{A}(\boldsymbol{U})=\begin{pmatrix}0 & n_x & n_y & n_z & 0 & 0 & 0\\ (y\varepsilon_1+\frac{1}{2}\varepsilon_4\boldsymbol{v}^2)n_x-u\boldsymbol{u} & \boldsymbol{u}-(\varepsilon_4-1)un_x & un_y-\varepsilon_4 vn_x & un_z-\varepsilon_4 wn_x & \varepsilon_4 n_x & (\varepsilon_4 h_v-\varepsilon_1)n_x & 0\\ (y\varepsilon_1+\frac{1}{2}\varepsilon_4\boldsymbol{v}^2)n_y-v\boldsymbol{u} & vn_x-\varepsilon_4 un_y & \boldsymbol{u}-(\varepsilon_4-1)vn_y & vn_z-\varepsilon_4 wn_y & \varepsilon_4 n_y & (\varepsilon_4 h_v-\varepsilon_1)n_y & 0\\ (y\varepsilon_1+\frac{1}{2}\varepsilon_4\boldsymbol{v}^2)n_z-w\boldsymbol{u} & wn_x-\varepsilon_4 un_z & wn_y-\varepsilon_4 vn_z & \boldsymbol{u}-(\varepsilon_4-1)wn_z & \varepsilon_4 n_z & (\varepsilon_4 h_v-\varepsilon_1)n_z & 0\\ \big(y\varepsilon_1+\frac{1}{2}(\varepsilon_4-1)\boldsymbol{v}^2-h\big)\boldsymbol{u} & \big(h+\frac{1}{2}\boldsymbol{v}^2\big)n_x-\varepsilon_4 u\boldsymbol{u} & \big(h+\frac{1}{2}\boldsymbol{v}^2\big)n_y-\varepsilon_4 v\boldsymbol{u} & \big(h+\frac{1}{2}\boldsymbol{v}^2\big)n_z-\varepsilon_4 w\boldsymbol{u} & (1+\varepsilon_4)\boldsymbol{u} & (\varepsilon_4 h_v-\varepsilon_1)\boldsymbol{u} & 0\\ -y\boldsymbol{u} & yn_x & yn_y & yn_z & 0 & \boldsymbol{u} & 0\\ -N_T\boldsymbol{u} & N_T n_x & N_T n_y & N_T n_z & 0 & 0 & \boldsymbol{u}\end{pmatrix}$$

$$n_x^2+n_y^2+n_z^2=1,\qquad \boldsymbol{u}=un_x+vn_y+wn_z,\qquad \boldsymbol{v}^2=u^2+v^2+w^2 \tag{B.7}$$

$$\varepsilon_1=\frac{a^2}{(1-y)\big(1+y(\kappa-1)\big)},\qquad \varepsilon_2=\frac{(1-y)^2}{a^2}\varepsilon_1,\qquad \varepsilon_4=(\kappa-1)\varepsilon_2$$

Eigenstructure:

$$\tilde{\lambda}_1 = \tilde{\boldsymbol{u}} - \sqrt{\varepsilon_2}\tilde{a}, \;\; \tilde{\lambda}_{2,3,4,5,6} = \tilde{\boldsymbol{u}}, \;\; \tilde{\lambda}_7 = \tilde{\boldsymbol{u}} + \sqrt{\varepsilon_2}\tilde{a} \tag{B.8}$$

$$\boldsymbol{E} = \begin{pmatrix} 1 & 1 & 0 & 0 & 1 & 0 & 0 \\ \tilde{u} - \sqrt{\varepsilon_2}\tilde{a}n_x & \tilde{u} & n_y & -n_z & \tilde{u} + \sqrt{\varepsilon_2}\tilde{a}n_x & 0 & 0 \\ \tilde{v} - \sqrt{\varepsilon_2}\tilde{a}n_y & \tilde{v} & -n_x & 0 & \tilde{v} + \sqrt{\varepsilon_2}\tilde{a}n_y & 0 & 0 \\ \tilde{w} - \sqrt{\varepsilon_2}\tilde{a}n_z & \tilde{w} & 0 & n_x & \tilde{w} + \sqrt{\varepsilon_2}\tilde{a}n_z & 0 & 0 \\ \tilde{H} - \sqrt{\varepsilon_2}\tilde{a}\tilde{\boldsymbol{u}} & \frac{1}{2}\tilde{\boldsymbol{v}}^2 & \tilde{u}n_y - \tilde{v}n_x & \tilde{w}n_x - \tilde{u}n_z & \tilde{H} + \sqrt{\varepsilon_2}\tilde{a}\tilde{\boldsymbol{u}} & \tilde{H} - (1-\tilde{y})\tilde{h}_v & 0 \\ \tilde{y} & \tilde{y} & 0 & 0 & \tilde{y} & 1 & 0 \\ \tilde{N}_T & 0 & 0 & 0 & \tilde{N}_T & 0 & 1 \end{pmatrix} \tag{B.9}$$

Additional Roe-averaged quantities:

$$\begin{aligned} &\tilde{q} = \frac{\sqrt{\rho_L}q_L + \sqrt{\rho_R}q_R}{\sqrt{\rho_L} + \sqrt{\rho_R}} \qquad \text{with} \qquad q \in \{T, y, N_T\} \\ &\longrightarrow \qquad \tilde{a} = a_{EOS}(\tilde{\rho}_m, \tilde{T}), \;\; \tilde{h}_v = h_{v,EOS}(\tilde{T}), \;\; \tilde{\boldsymbol{\kappa}} \approx \kappa_{pv,EOS}(\tilde{\rho}_m, \tilde{T}) \end{aligned} \tag{B.10}$$

E-E-M-Poly:

$$\boldsymbol{U}=\begin{pmatrix}\rho_m\\ \rho_m u\\ \rho_m v\\ \rho_m w\\ \rho_m E\\ \rho_m y\\ \rho_m\mu_0\\ \rho_m\mu_1\\ \rho_m\mu_2\end{pmatrix},\ \boldsymbol{F}_c=\begin{pmatrix}\rho_m\boldsymbol{u}\\ \rho_m u\boldsymbol{u}+pn_x\\ \rho_m v\boldsymbol{u}+pn_y\\ \rho_m w\boldsymbol{u}+pn_z\\ \rho_m\boldsymbol{u}H\\ \rho_m y\boldsymbol{u}\\ \rho_m\mu_0\boldsymbol{u}\\ \rho_m\mu_1\boldsymbol{u}\\ \rho_m\mu_2\boldsymbol{u}\end{pmatrix},\ \boldsymbol{Q}=\begin{pmatrix}0\\ 0\\ 0\\ 0\\ 0\\ \rho_m(\Lambda_N+\Lambda_G)\\ \rho_m\bar{J}\\ \rho_m(\mu_0G(r_{20})+\bar{J}r_{crit})\\ \rho_m(2\mu_1G(r_{20})+\bar{J}r_{crit}^2)\end{pmatrix} \tag{B.11}$$

<u>Jacobian matrix:</u>

$$\boldsymbol{A}(\boldsymbol{U})=\begin{pmatrix}
0 & n_x & n_y & n_z & 0 & 0 & 0 & 0 & 0\\
(y\varepsilon_1+\frac{1}{2}\varepsilon_4\boldsymbol{v}^2)n_x-u\boldsymbol{u} & \boldsymbol{u}-(\varepsilon_4-1)un_x & un_y-\varepsilon_4vn_x & un_z-\varepsilon_4wn_x & \varepsilon_4n_x & (\varepsilon_4h_v-\varepsilon_1)n_x & 0 & 0 & 0\\
(y\varepsilon_1+\frac{1}{2}\varepsilon_4\boldsymbol{v}^2)n_y-v\boldsymbol{u} & vn_x-\varepsilon_4un_y & \boldsymbol{u}-(\varepsilon_4-1)vn_y & vn_z-\varepsilon_4wn_y & \varepsilon_4n_y & (\varepsilon_4h_v-\varepsilon_1)n_y & 0 & 0 & 0\\
(y\varepsilon_1+\frac{1}{2}\varepsilon_4\boldsymbol{v}^2)n_z-w\boldsymbol{u} & wn_x-\varepsilon_4un_z & wn_y-\varepsilon_4vn_z & \boldsymbol{u}-(\varepsilon_4-1)wn_z & \varepsilon_4n_z & (\varepsilon_4h_v-\varepsilon_1)n_z & 0 & 0 & 0\\
\big(y\varepsilon_1+\frac{1}{2}(\varepsilon_4-1)\boldsymbol{v}^2-h\big)\boldsymbol{u} & \big(h+\frac{1}{2}\boldsymbol{v}^2\big)n_x-\varepsilon_4u\boldsymbol{u} & \big(h+\frac{1}{2}\boldsymbol{v}^2\big)n_y-\varepsilon_4v\boldsymbol{u} & \big(h+\frac{1}{2}\boldsymbol{v}^2\big)n_z-\varepsilon_4w\boldsymbol{u} & (1+\varepsilon_4)\boldsymbol{u} & (\varepsilon_4h_v-\varepsilon_1)\boldsymbol{u} & 0 & 0 & 0\\
-y\boldsymbol{u} & yn_x & yn_y & yn_z & 0 & \boldsymbol{u} & 0 & 0 & 0\\
-\mu_0\boldsymbol{u} & \mu_0n_x & \mu_0n_y & \mu_0n_z & 0 & 0 & \boldsymbol{u} & 0 & 0\\
-\mu_1\boldsymbol{u} & \mu_1n_x & \mu_1n_y & \mu_1n_z & 0 & 0 & 0 & \boldsymbol{u} & 0\\
-\mu_2\boldsymbol{u} & \mu_2n_x & \mu_2n_y & \mu_2n_z & 0 & 0 & 0 & 0 & \boldsymbol{u}
\end{pmatrix}$$

$$n_x^2+n_y^2+n_z^2=1,\qquad \boldsymbol{u}=un_x+vn_y+wn_z,\qquad \boldsymbol{v}^2=u^2+v^2+w^2 \tag{B.12}$$

$$\varepsilon_1=\frac{a^2}{(1-y)\big(1+y(\kappa-1)\big)},\qquad \varepsilon_2=\frac{(1-y)^2}{a^2}\varepsilon_1,\qquad \varepsilon_4=(\kappa-1)\varepsilon_2$$

Eigenstructure:

$$\tilde{\lambda}_1 = \tilde{\boldsymbol{u}} - \sqrt{\varepsilon_2}\tilde{a}, \;\; \tilde{\lambda}_{2,3,4,5,6,7,8} = \tilde{\boldsymbol{u}}, \;\; \tilde{\lambda}_9 = \tilde{\boldsymbol{u}} + \sqrt{\varepsilon_2}\tilde{a} \tag{B.13}$$

$$\boldsymbol{E} = \begin{pmatrix} 1 & 1 & 0 & 0 & 1 & 0 & 0 & 0 & 0 \\ \tilde{u} - \sqrt{\varepsilon_2}\tilde{a}n_x & \tilde{u} & n_y & -n_z & \tilde{u} + \sqrt{\varepsilon_2}\tilde{a}n_x & 0 & 0 & 0 & 0 \\ \tilde{v} - \sqrt{\varepsilon_2}\tilde{a}n_y & \tilde{v} & -n_x & 0 & \tilde{v} + \sqrt{\varepsilon_2}\tilde{a}n_y & 0 & 0 & 0 & 0 \\ \tilde{w} - \sqrt{\varepsilon_2}\tilde{a}n_z & \tilde{w} & 0 & n_x & \tilde{w} + \sqrt{\varepsilon_2}\tilde{a}n_z & 0 & 0 & 0 & 0 \\ \tilde{H} - \sqrt{\varepsilon_2}\tilde{a}\tilde{\boldsymbol{u}} & \frac{1}{2}\tilde{\boldsymbol{v}}^2 & \tilde{u}n_y - \tilde{v}n_x & \tilde{w}n_x - \tilde{u}n_z & \tilde{H} + \sqrt{\varepsilon_2}\tilde{a}\tilde{\boldsymbol{u}} & \tilde{H} - (1-\tilde{y})\tilde{h}_v & 0 & 0 & 0 \\ \tilde{y} & \tilde{y} & 0 & 0 & \tilde{y} & 1 & 0 & 0 & 0 \\ \tilde{\mu}_0 & 0 & 0 & 0 & \tilde{\mu}_0 & 0 & 1 & 0 & 0 \\ \tilde{\mu}_1 & 0 & 0 & 0 & \tilde{\mu}_1 & 0 & 0 & 1 & 0 \\ \tilde{\mu}_2 & 0 & 0 & 0 & \tilde{\mu}_2 & 0 & 0 & 0 & 1 \end{pmatrix} \tag{B.14}$$

Additional Roe-averaged quantities:

$$\tilde{q} = \frac{\sqrt{\rho_L}q_L + \sqrt{\rho_R}q_R}{\sqrt{\rho_L} + \sqrt{\rho_R}} \qquad \text{with} \qquad q \in \{T, y, \mu_0, \mu_1, \mu_2\}$$
$$\longrightarrow \qquad \tilde{a} = a_{EOS}(\tilde{\rho}_m, \tilde{T}), \;\; \tilde{h}_v = h_{v,EOS}(\tilde{T}), \;\; \tilde{\kappa} \approx \kappa_{pv,EOS}(\tilde{\rho}_m, \tilde{T}) \tag{B.15}$$

E-E-P-Poly-S:

$$\boldsymbol{U} = \begin{pmatrix} \rho_m(1-y) \\ \rho_m(1-y)u_g \\ \rho_m(1-y)v_g \\ \rho_m(1-y)w_g \\ \rho_m(1-y)E_g \\ \rho_m y \\ \rho_m y u_l \\ \rho_m y v_l \\ \rho_m y w_l \\ \rho_m y E_l \\ \rho_m y \mu_0 \\ \rho_m y \mu_1 \\ \rho_m y \mu_2 \end{pmatrix}, \quad \boldsymbol{F}_c = \begin{pmatrix} \rho_m(1-y)\boldsymbol{u}_g \\ \rho_m(1-y)u_g\boldsymbol{u}_g + \frac{\rho_m}{\rho_g}(1-y)pn_x \\ \rho_m(1-y)v_g\boldsymbol{u}_g + \frac{\rho_m}{\rho_g}(1-y)pn_y \\ \rho_m(1-y)w_g\boldsymbol{u}_g + \frac{\rho_m}{\rho_g}(1-y)pn_z \\ \rho_m(1-y)\boldsymbol{u}_g H_g \\ \rho_m y \boldsymbol{u}_l \\ \rho_m y u \boldsymbol{u}_l + \frac{\rho_m}{\rho_l} y p n_x \\ \rho_m y v \boldsymbol{u}_l + \frac{\rho_m}{\rho_l} y p n_y \\ \rho_m y w \boldsymbol{u}_l + \frac{\rho_m}{\rho_l} y p n_z \\ \rho_m y \boldsymbol{u}_l H_l \\ \rho_m \mu_0 \boldsymbol{u}_l \\ \rho_m \mu_1 \boldsymbol{u}_l \\ \rho_m \mu_2 \boldsymbol{u}_l \end{pmatrix}, \quad \boldsymbol{Q} = \begin{pmatrix} -\Lambda_N - \Lambda_G \\ -\Lambda_G u_{int} - \frac{3}{4}\frac{\rho_m y}{\rho_l \pi r^3} F_{D,x} \\ -\Lambda_G v_{int} - \frac{3}{4}\frac{\rho_m y}{\rho_l \pi r^3} F_{D,y} \\ -\Lambda_G w_{int} - \frac{3}{4}\frac{\rho_m y}{\rho_l \pi r^3} F_{D,z} \\ -\Lambda_G (H_{g,int} - h_v) \\ \Lambda_N + \Lambda_G \\ \Lambda_G u_{int} + \frac{3}{4}\frac{\rho_m y}{\rho_l \pi r^3} F_{D,x} \\ \Lambda_G v_{int} + \frac{3}{4}\frac{\rho_m y}{\rho_l \pi r^3} F_{D,y} \\ \Lambda_G w_{int} + \frac{3}{4}\frac{\rho_m y}{\rho_l \pi r^3} F_{D,z} \\ \Lambda_G H_{l,int} \\ \rho_m \bar{J} \\ \rho_m(\mu_0 G(r_{20}) + \bar{J} r_{crit}) \\ \rho_m(2\mu_1 G(r_{20}) + \bar{J} r_{crit}^2) \end{pmatrix} \tag{B.16}$$

Jacobian matrix:

$$\boldsymbol{A}(\boldsymbol{U}) = \left(\begin{array}{ccccccccccccc}
0 & n_x & n_y & n_z & 0 & 0 & 0 & 0 & 0 & 0 & 0 & 0 & 0 \\
a_{2,1} & a_{2,2} & a_{2,3} & a_{2,4} & a_{2,5} & a_{2,6} & 0 & 0 & 0 & 0 & 0 & 0 & 0 \\
a_{3,1} & a_{3,2} & a_{3,3} & a_{3,4} & a_{3,5} & a_{3,6} & 0 & 0 & 0 & 0 & 0 & 0 & 0 \\
a_{4,1} & a_{4,2} & a_{4,3} & a_{4,4} & a_{4,5} & a_{4,6} & 0 & 0 & 0 & 0 & 0 & 0 & 0 \\
a_{5,1} & a_{5,2} & a_{5,3} & a_{5,4} & a_{5,5} & 0 & a_{5,7} & a_{5,8} & a_{5,9} & 0 & 0 & 0 & 0 \\
0 & 0 & 0 & 0 & 0 & 0 & n_x & n_y & n_z & 0 & 0 & 0 & 0 \\
a_{7,1} & a_{7,2} & a_{7,3} & a_{7,4} & a_{7,5} & a_{7,6} & a_{7,7} & a_{7,8} & a_{7,9} & 0 & 0 & 0 & 0 \\
a_{8,1} & a_{8,2} & a_{8,3} & a_{8,4} & a_{8,5} & a_{8,6} & a_{8,7} & a_{8,8} & a_{8,9} & 0 & 0 & 0 & 0 \\
a_{9,1} & a_{9,2} & a_{9,3} & a_{9,4} & a_{9,5} & a_{9,6} & a_{9,7} & a_{9,8} & a_{9,9} & 0 & 0 & 0 & 0 \\
a_{10,1} & a_{10,2} & a_{10,3} & a_{10,4} & a_{10,5} & a_{10,6} & a_{10,7} & a_{10,8} & a_{10,9} & \boldsymbol{u}_l & 0 & 0 & 0 \\
0 & 0 & 0 & 0 & 0 & \frac{-\mu_0 \boldsymbol{u}_l}{y} & \frac{\mu_0 n_x}{y} & \frac{\mu_0 n_y}{y} & \frac{\mu_0 n_z}{y} & 0 & \boldsymbol{u}_l & 0 & 0 \\
0 & 0 & 0 & 0 & 0 & \frac{-\mu_1 \boldsymbol{u}_l}{y} & \frac{\mu_1 n_x}{y} & \frac{\mu_1 n_y}{y} & \frac{\mu_1 n_z}{y} & 0 & 0 & \boldsymbol{u}_l & 0 \\
0 & 0 & 0 & 0 & 0 & \frac{-\mu_2 \boldsymbol{u}_l}{y} & \frac{\mu_2 n_x}{y} & \frac{\mu_2 n_y}{y} & \frac{\mu_2 n_z}{y} & 0 & 0 & 0 & \boldsymbol{u}_l
\end{array}\right) \tag{B.17}$$

$$n_x^2 + n_y^2 + n_z^2 = 1, \qquad \boldsymbol{u}_g = u_g n_x + v_g n_y + w_g n_z, \qquad \boldsymbol{u}_l = u_l n_x + v_l n_y + w_l n_z,$$

$$\boldsymbol{v}_g^2 = u_g^2 + v_g^2 + w_g^2, \qquad \boldsymbol{v}_l^2 = u_l^2 + v_l^2 + w_l^2$$

with

$$a_{2,1} = \frac{1}{2}(\kappa_g - 1)\boldsymbol{v}_g^2 n_x - u_g \boldsymbol{u}_g, \quad a_{2,2} = \boldsymbol{u}_g - (\kappa_g - 2)u_g n_x, \quad a_{2,3} = u_g n_y - (\kappa_g - 1)v_g n_x, \quad a_{2,4} = u_g n_z - (\kappa_g - 1)w_g n_x, \quad a_{2,5} = (\kappa_g - 1)n_x,$$

$$a_{2,6} = \frac{p}{\rho_l} n_x, \quad a_{3,1} = \frac{1}{2}(\kappa_g - 1)\boldsymbol{v}_g^2 n_y - v_g \boldsymbol{u}_g, \quad a_{3,2} = v_g n_x - (\kappa_g - 1)u_g n_y, \quad a_{3,3} = \boldsymbol{u}_g - (\kappa_g - 2)v_g n_y, \quad a_{3,4} = v_g n_z - (\kappa_g - 1)w_g n_y,$$

$$a_{3,5} = (\kappa_g - 1)n_y, \quad a_{3,6} = \frac{p}{\rho_l} n_y, \quad a_{4,1} = \frac{1}{2}(\kappa_g - 1)\boldsymbol{v}_g^2 n_z - w_g \boldsymbol{u}_g, \quad a_{4,2} = w_g n_x - (\kappa_g - 1)u_g n_z, \quad a_{4,3} = w_g n_y - (\kappa_g - 1)v_g n_z,$$

$$a_{4,4} = \boldsymbol{u}_g - (\kappa_g - 2)w_g n_z, \quad a_{4,5} = (\kappa_g - 1)n_z, \quad a_{4,6} = \frac{p}{\rho_l} n_z, \quad a_{5,1} = \left[\frac{1}{2}(\kappa_g - 2)\boldsymbol{v}_g^2 - h_g\right]\boldsymbol{u}_g, \quad a_{5,2} = \left(h_g + \frac{1}{2}\boldsymbol{v}_g^2\right)n_x - (\kappa_g - 1)u_g \boldsymbol{u}_g,$$

$$a_{5,3} = \left(h_g + \frac{1}{2}\boldsymbol{v}_g^2\right)n_y - (\kappa_g - 1)v_g \boldsymbol{u}_g, \quad a_{5,4} = \left(h_g + \frac{1}{2}\boldsymbol{v}_g^2\right)n_z - (\kappa_g - 1)w_g \boldsymbol{u}_g, \quad a_{5,5} = \kappa_g \boldsymbol{u}_g, \quad a_{5,7} = \frac{p}{\rho_l} n_x, \quad a_{5,8} = \frac{p}{\rho_l} n_y, \quad a_{5,9} = \frac{p}{\rho_l} n_z,$$

$$a_{7,1} = \frac{1}{2}(\kappa_g - 1)\frac{y}{1-y}\frac{\rho_l}{\rho_g}\boldsymbol{v}_l^2 n_x, \quad a_{7,2} = \frac{y}{1-y}\frac{\rho_l}{\rho_g}(\boldsymbol{u}_l - \kappa_g u_l n_x), \quad a_{7,3} = \frac{y}{1-y}\frac{\rho_l}{\rho_g}\big(u_l n_y - (\kappa_g + 1)v_l n_x\big), \quad a_{7,4} = \frac{y}{1-y}\frac{\rho_l}{\rho_g}\big(u_l n_z - (\kappa_g + 1)w_l n_x\big),$$

$$a_{7,5} = (\kappa_g - 1)\frac{y}{1-y}\frac{\rho_l}{\rho_g} n_x, \quad a_{7,6} = \frac{y}{1-y}\frac{p}{\rho_g} n_x - u_l \boldsymbol{u}_l, \quad a_{7,7} = \boldsymbol{u}_l + u_l n_x, \quad a_{7,8} = u_l n_y + v_l n_x, \quad a_{7,9} = u_l n_z + w n_x,$$

$$a_{8,1} = \frac{1}{2}(\kappa_g - 1)\frac{y}{1-y}\frac{\rho_l}{\rho_g}\boldsymbol{v}_l^2 n_y, \quad a_{8,2} = \frac{y}{1-y}\frac{\rho_l}{\rho_g}\big(v_l n_x - (\kappa_g + 1)u_l n_y\big), \quad a_{8,3} = \frac{y}{1-y}\frac{\rho_l}{\rho_g}(\boldsymbol{u}_l - \kappa_g v_l n_y), \quad a_{8,4} = \frac{y}{1-y}\frac{\rho_l}{\rho_g}\big(v_l n_z - (\kappa_g + 1)w_l n_y\big),$$

$$a_{8,5} = (\kappa_g - 1)\frac{y}{1-y}\frac{\rho_l}{\rho_g} n_y, \quad a_{8,6} = \frac{y}{1-y}\frac{p}{\rho_g} n_y - v_l \boldsymbol{u}_l, \quad a_{8,7} = v_l n_x + u_l n_y, \quad a_{8,8} = \boldsymbol{u}_l + v_l n_y, \quad a_{8,9} = v_l n_z + w_l n_y,$$

$$a_{9,1} = \frac{1}{2}(\kappa_g - 1)\frac{y}{1-y}\frac{\rho_l}{\rho_g}\boldsymbol{v}_l^2 n_z, \quad a_{9,2} = \frac{y}{1-y}\frac{\rho_l}{\rho_g}\big(w_l n_x - (\kappa_g + 1)u_l n_z\big), \quad a_{9,3} = \frac{y}{1-y}\frac{\rho_l}{\rho_g}\big(w_l n_y - (\kappa_g + 1)v_l n_z\big), \quad a_{9,4} = \frac{y}{1-y}\frac{\rho_l}{\rho_g}(\boldsymbol{u}_l - \kappa_g w_l n_z),$$

$$a_{9,5} = (\kappa_g - 1)\frac{y}{1-y}\frac{\rho_l}{\rho_g} n_z, \quad a_{9,6} = \frac{y}{1-y}\frac{p}{\rho_g} n_z - w_l \boldsymbol{u}_l, \quad a_{9,7} = w_l n_x + u_l n_z, \quad a_{9,8} = w_l n_y + v_l n_z, \quad a_{9,9} = \boldsymbol{u}_l + w_l n_z,$$

$$a_{10,1} = \frac{1}{2}(\kappa_g - 1)\frac{y}{1-y}\frac{\rho_l}{\rho_g}\boldsymbol{v}_l^2 \boldsymbol{u}_l, \quad a_{10,2} = (1 - \kappa_g)\frac{y}{1-y}\frac{\rho_l}{\rho_g} u_g \boldsymbol{u}_l, \quad a_{10,3} = (1 - \kappa_g)\frac{y}{1-y}\frac{\rho_l}{\rho_g} v_g \boldsymbol{u}_l, \quad a_{10,4} = (1 - \kappa_g)\frac{y}{1-y}\frac{\rho_l}{\rho_g} w_g \boldsymbol{u}_l,$$

$$a_{10,5} = (\kappa_g - 1)\frac{y}{1-y}\frac{\rho_l}{\rho_g}\boldsymbol{u}_l, \quad a_{10,6} = \left(\frac{p}{y\rho_m} - h_l - \frac{1}{2}\boldsymbol{v}_l^2\right)\boldsymbol{u}_l, \quad a_{10,7} = h_l + \frac{1}{2}\boldsymbol{v}_l^2 - \frac{p}{\rho_l} n_x, \quad a_{10,8} = h_l + \frac{1}{2}\boldsymbol{v}_l^2 - \frac{p}{\rho_l} n_y, \quad a_{10,9} = h_l + \frac{1}{2}\boldsymbol{v}_l^2 - \frac{p}{\rho_l} n_z$$

Eigenstructure:

$$\tilde{\lambda}_1 = \tilde{\boldsymbol{u}}_g - \sqrt{\varepsilon_3}\tilde{a}_g,\ \ \tilde{\lambda}_{2,3,4} = \tilde{\boldsymbol{u}}_g,\ \ \tilde{\lambda}_5 = \tilde{\boldsymbol{u}}_g + \sqrt{\varepsilon_3}\tilde{a}_g,\ \ \tilde{\lambda}_6 = 2\tilde{\boldsymbol{u}}_l - \tilde{\boldsymbol{u}}_g,\ \ \tilde{\lambda}_{7,8,9} = \tilde{\boldsymbol{u}}_l,\ \ \tilde{\lambda}_{10} = \tilde{\boldsymbol{u}}_g,\ \ \tilde{\lambda}_{11,12,13} = \tilde{\boldsymbol{u}}_l \tag{B.18}$$

$$\boldsymbol{E} = \begin{pmatrix}
e_{1,1} & 1 & 0 & 0 & e_{1,5} & 1 & 0 & 0 & 0 & 1 & 0 & 0 & 0 \\
e_{2,1} & \tilde{u}_g & n_y & -n_z & e_{2,5} & e_{2,6} & 0 & 0 & 0 & \tilde{u}_g & 0 & 0 & 0 \\
e_{3,1} & \tilde{v}_g & -n_x & 0 & e_{3,5} & e_{3,6} & 0 & 0 & 0 & \tilde{v}_g & 0 & 0 & 0 \\
e_{4,1} & \tilde{w}_g & 0 & n_x & e_{4,5} & e_{4,6} & 0 & 0 & 0 & \tilde{w}_g & 0 & 0 & 0 \\
e_{5,1} & \frac{1}{2}\tilde{\boldsymbol{v}}_g^2 & e_{5,3} & e_{5,4} & e_{5,5} & e_{5,6} & 0 & 0 & 0 & e_{5,10} & 0 & 0 & 0 \\
e_{6,1} & 0 & 0 & 0 & e_{6,5} & 0 & 0 & 0 & 0 & 0 & 0 & 0 & 0 \\
e_{7,1} & 0 & 0 & 0 & e_{7,5} & 0 & \tilde{u}_l & 0 & 0 & 0 & 0 & 0 & 0 \\
e_{8,1} & 0 & 0 & 0 & e_{8,5} & 0 & 0 & \tilde{v}_l & 0 & 0 & 0 & 0 & 0 \\
e_{9,1} & 0 & 0 & 0 & e_{9,5} & 0 & 0 & 0 & \tilde{w}_l & 0 & 0 & 0 & 0 \\
e_{10,1} & 0 & 0 & 0 & e_{10,5} & 0 & 0 & 0 & 0 & 0 & 0 & 0 & 0 \\
0 & 0 & 0 & 0 & 0 & \tilde{\mu}_0 & 0 & 0 & 0 & \tilde{\mu}_0 & 1 & 0 & 0 \\
0 & 0 & 0 & 0 & 0 & \tilde{\mu}_1 & 0 & 0 & 0 & \tilde{\mu}_1 & 0 & 1 & 0 \\
0 & 0 & 0 & 0 & 0 & \tilde{\mu}_2 & 0 & 0 & 0 & \tilde{\mu}_2 & 0 & 0 & 1
\end{pmatrix} \tag{B.19}$$

$$\varepsilon_3 = \frac{(1-\tilde{y})\tilde{\rho}_l^2 + \tilde{y}\tilde{\rho}_g^2}{\tilde{\rho}_g\tilde{\rho}_l}, \qquad \varepsilon_5 = \frac{\tilde{u}_g - \tilde{u}_l}{\sqrt{\varepsilon_3}\tilde{a}_g}$$

with

$$
\begin{aligned}
&e_{1,1} = (1-\tilde{y})(1-\varepsilon_5)\frac{\tilde{\rho}_m}{\tilde{\rho}_g}, \quad e_{1,5} = (1-\tilde{y})(1+\varepsilon_5)\frac{\tilde{\rho}_m}{\tilde{\rho}_g}, \quad e_{2,1} = (1-\tilde{y})(1-\varepsilon_5)\frac{\tilde{\rho}_m}{\tilde{\rho}_g}\big(\tilde{u}_g - \sqrt{\varepsilon_3}\tilde{a}_g n_x\big),\\
&e_{2,5} = (1-\tilde{y})(1+\varepsilon_5)\frac{\tilde{\rho}_m}{\tilde{\rho}_g}\big(\tilde{u}_g + \sqrt{\varepsilon_3}\tilde{a}_g n_x\big), \quad e_{2,6} = 2\boldsymbol{u}_l - u_g, \quad e_{3,1} = (1-\tilde{y})(1-\varepsilon_5)\frac{\tilde{\rho}_m}{\tilde{\rho}_g}\big(\tilde{v}_g - \sqrt{\varepsilon_3}\tilde{a}_g n_y\big),\\
&e_{3,5} = (1-\tilde{y})(1+\varepsilon_5)\frac{\tilde{\rho}_m}{\tilde{\rho}_g}\big(\tilde{v}_g + \sqrt{\varepsilon_3}\tilde{a}_g n_y\big), \quad e_{3,6} = 2\boldsymbol{u}_l - v_g, \quad e_{4,1} = (1-\tilde{y})(1-\varepsilon_5)\frac{\tilde{\rho}_m}{\tilde{\rho}_g}\big(\tilde{w}_g - \sqrt{\varepsilon_3}\tilde{a}_g n_z\big),\\
&e_{4,5} = (1-\tilde{y})(1+\varepsilon_5)\frac{\tilde{\rho}_m}{\tilde{\rho}_g}\big(\tilde{w}_g + \sqrt{\varepsilon_3}\tilde{a}_g n_z\big), \quad e_{4,6} = 2\boldsymbol{u}_l - w_g, \quad e_{5,1} = (1-\tilde{y})(1-\varepsilon_5)\frac{\tilde{\rho}_m}{\tilde{\rho}_g}\Big(\tilde{H}_g - \tilde{\boldsymbol{u}}_g\sqrt{\varepsilon_3}\tilde{a}_g\Big) + \tilde{y}(1+\varepsilon_5)\frac{\tilde{\rho}_m\tilde{p}}{\tilde{\rho}_l^2},\\
&e_{5,3} = \tilde{u}_g n_y - \tilde{v}_g n_x, \quad e_{5,4} = \tilde{w}_g n_x - \tilde{u}_g n_z, \quad e_{5,5} = (1-\tilde{y})(1+\varepsilon_5)\frac{\tilde{\rho}_m}{\tilde{\rho}_g}\Big(\tilde{H}_g + \tilde{\boldsymbol{u}}_g\sqrt{\varepsilon_3}\tilde{a}_g\Big) + \tilde{y}(1-\varepsilon_5)\frac{\tilde{\rho}_m\tilde{p}}{\tilde{\rho}_l^2},\\
&e_{5,6} = \frac{\tilde{p}}{\tilde{\rho}_g\tilde{a}_g}\left(\tilde{H}_g - \frac{1}{2}\tilde{\boldsymbol{v}}_g^2\right) - 2\boldsymbol{u}_l\boldsymbol{u}_g + \frac{1}{2}\tilde{\boldsymbol{v}}_g^2, \quad e_{5,10} = \frac{\tilde{p}}{\tilde{\rho}_g\tilde{a}_g}\left(\tilde{H}_g - \frac{1}{2}\tilde{\boldsymbol{v}}_g^2\right) + \frac{1}{2}\tilde{\boldsymbol{v}}_g^2, \quad e_{6,1} = \tilde{y}(1+\varepsilon_5)\frac{\tilde{\rho}_m}{\tilde{\rho}_l}, \quad e_{6,5} = \tilde{y}(1-\varepsilon_5)\frac{\tilde{\rho}_m}{\tilde{\rho}_l},\\
&e_{7,1} = \tilde{y}(1+\varepsilon_5)\frac{\tilde{\rho}_m}{\tilde{\rho}_l}\big(\tilde{u}_g - \sqrt{\varepsilon_3}\tilde{a}_g n_x\big), \quad e_{7,5} = \tilde{y}(1-\varepsilon_5)\frac{\tilde{\rho}_m}{\tilde{\rho}_l}\big(\tilde{u}_g + \sqrt{\varepsilon_3}\tilde{a}_g n_x\big), \quad e_{8,1} = \tilde{y}(1+\varepsilon_5)\frac{\tilde{\rho}_m}{\tilde{\rho}_l}\big(\tilde{v}_g - \sqrt{\varepsilon_3}\tilde{a}_g n_y\big),\\
&e_{8,5} = \tilde{y}(1-\varepsilon_5)\frac{\tilde{\rho}_m}{\tilde{\rho}_l}\big(\tilde{v}_g + \sqrt{\varepsilon_3}\tilde{a}_g n_y\big), \quad e_{9,1} = \tilde{y}(1+\varepsilon_5)\frac{\tilde{\rho}_m}{\tilde{\rho}_l}\big(\tilde{w}_g - \sqrt{\varepsilon_3}\tilde{a}_g n_z\big), \quad e_{9,5} = \tilde{y}(1-\varepsilon_5)\frac{\tilde{\rho}_m}{\tilde{\rho}_l}\big(\tilde{w}_g + \sqrt{\varepsilon_3}\tilde{a}_g n_z\big),\\
&e_{10,1} = \tilde{y}(1+\varepsilon_5)\frac{\tilde{\rho}_m}{\tilde{\rho}_l}\big(\tilde{H}_l - \tilde{\boldsymbol{u}}_l\sqrt{\varepsilon_3}\tilde{a}_g\big) - \tilde{y}(1+\varepsilon_5)\frac{\tilde{\rho}_m\tilde{p}}{\tilde{\rho}_l^2}, \quad e_{10,5} = \tilde{y}(1-\varepsilon_5)\frac{\tilde{\rho}_m}{\tilde{\rho}_l}\big(\tilde{H}_l + \tilde{\boldsymbol{u}}_l\sqrt{\varepsilon_3}\tilde{a}_g\big) - \tilde{y}(1-\varepsilon_5)\frac{\tilde{\rho}_m\tilde{p}}{\tilde{\rho}_l^2}
\end{aligned}
$$

Additional Roe-averaged quantities:

$$
\begin{aligned}
&\tilde{q} = \frac{\sqrt{\rho_L}q_L + \sqrt{\rho_R}q_R}{\sqrt{\rho_L} + \sqrt{\rho_R}} \qquad \text{with} \qquad q \in \{T, y, \mu_0, \mu_1, \mu_2\}\\
&\longrightarrow \qquad \tilde{a}_g = a_{EOS}(\tilde{\rho}_g, \tilde{T}_g), \ \tilde{p} = p_{EOS}(\tilde{\rho}_g, \tilde{T}_g)
\end{aligned}
\tag{B.20}
$$

C Independence of the solutions from the discretisation of the spatial grid and the thermophysical tables

Table C.1 summarises the characteristic quantities used to investigate the spatial discretisation error are summarised for all validation cases considered. Based on the procedure presented in Chapter 4.4, the maximum tolerated relative deviation of the characteristic quantity when refining the grid by the refinement factor r_G is designated as the criterion. The number of nodes for which this error bound is undercut for the first time subsequently represents the grid for which independence of the solution from the selected discretisation can be assumed.

Table C.1: Parameters for investigating the spatial discretisation error of all validation cases considered

	Characteristic quantities	Criterion	Number of nodes
NASA CDV nozzle	Mach number at outlet	0.1%	120,000
Nozzle according to Spinelli et al.	Mach number at outlet	0.01%	1.92 million
HeRo compressor	Mach number at outlet	0.1%	949,000
Mystery nozzle	Mach number and Sauter radius at outlet	0.1%	576,000
Nozzle according to Barschdorff	Mach number and Sauter radius at outlet	0.1%	960,000
Nozzle according to Bier and Theis	Mach number and Sauter radius at outlet	0.1%	638,000
Cascade according to White et al.	Mach number and Sauter radius at outlet	0.1%	1.16 million

The parameters required for an investigation of the discretisation error of the tabulated thermophysical quantities are listed in Table C.2 for the single-phase and in Table C.3 for the two-phase validation cases. The mean error of the characteristic value is calculated within the range of states defined by the limits of the pressure and temperature intervals. The thermophysical quantity with the most significant relative error in the range of states under consideration is selected as a characteristic quantity. The solution can be assumed to be independent of the selected table dimension if the mean error of the characteristic quantity falls below an error limit defined as a criterion.

Table C.2: Parameters for investigating the discretisation error of the tabulated thermophysical quantities for the single-phase validation cases

	NASA CDV nozzle	**Nozzle according to Spinelli et al.**	**HeRo compressor**
Pressure interval	[90;1200] bar	[0.5;10] bar	[65;95] bar
Temperature interval	[300;500] K	[490;550] K	[295;320] K
Characteristic quantity	Speed of sound	Speed of sound	Isobaric heat capacity
Criterion	5.0×10^{-5} m/s	5.0×10^{-5} m/s	0.1 J/(kg·K)
Table dimension	1000	500	1000

Table C.3: Parameters for investigating the discretisation error of the tabulated thermophysical quantities for the two-phase validation cases

Gas phase	**Mystery nozzle**	**Nozzle according to Barschdorff**	**Nozzle according to Bier and Theis**	**Cascade according to White et al.**
Pressure interval	[0.1;1.15] bar	[0.15;0.8] bar	[9;40] bar	[0.05;0.45] bar
Temperature interval	[300;430] K	[300;385] K	[230;300] K	[250;400] K
Characteristic quantity	Speed of sound	Speed of sound	Speed of sound	Speed of sound
Criterion	1.0×10^{-4} m/s	1.0×10^{-4} m/s	1.0×10^{-4} m/s	1.0×10^{-4} m/s
Table dimension	500	500	500	500

Liquid phase	**Mystery nozzle**	**Nozzle according to Barschdorff**	**Nozzle according to Bier and Theis**	**Cascade according to White et al.**
Pressure interval	[0.1;0.55] bar	[0.15;0.5] bar	[9;23] bar	[0.05;0.35] bar
Temperature interval	[310;355] K	[300;360] K	[250;270] K	[250;380] K
Characteristic quantity	Speed of sound	Isochoric heat capacity	Speed of sound	Isochoric heat capacity
Criterion	1.0×10^{-4} m/s	0.1 J/(kg·K)	1.0×10^{-4} m/s	0.1 J/(kg·K)
Table dimension	1000	1000	500	1000

D Evaluation of thermophysical parameters in the two-phase region

Since the speed of sound is not uniquely defined in the two-phase region, as already explained in Chapter 3.1, it seems necessary to investigate the influence of different ways of formulation on the numerical solution. Here, the metastable region of state of the gas phase is of particular relevance due to a consideration of phase change processes, which lead to the formation of a liquid phase and, thus, an entry into the two-phase region to the right of the critical point. If a thermodynamic state lies within the two-phase region but beyond the spinodal limit, which delimits the metastable state region, it is unstable and, therefore, has no physical significance. An investigation to determine the speed of sound in the two-phase region can be limited to metastable states. In the present work, the speed of sound is calculated assuming an equilibrium state a_{eq}. For this purpose, the equation of state is analysed in the metastable region, restricting the calculation to gaseous states. The speed of sound values determined in this way, and the pressure curves along the nozzle axis calculated on that basis therefore serve as a reference in the following. In order to enable a comprehensive comparison with other ways of formulating the speed of sound represented in the literature, three approaches are selected. Firstly, a comparison with the speed of sound of a calorically perfect gas defined in Equation 3.22 appears to be useful, as it can be taken as an upper limit for possible deviations. Another approach to describing the speed of sound is presented in detail by Guha [62] and Petr [113]. According to them, the propagation of a sound wave results in different degrees of disturbance of the thermal and mechanical equilibrium within the flow, depending on its frequency. While a high-frequency sound wave has already passed through the area under investigation before the flow is able to react to the local gradients caused by it, low-frequency sound waves allow the flow quantities to be adjusted without disturbing the state of equilibrium. The concept of *frozen speed of sound* represents the case of high-frequency sound waves and leads to a formulation of the speed of sound as a function of the saturation quantities. Šafarík [176] proposes an evaluation of the equation of state based on the saturation state of the gas phase defined by its pressure:

$$\text{Frozen:} \qquad a = a_{EOS}(\rho_{s,g}, T_{s,g}) \tag{D.1}$$

While both the determination of the speed of sound in the equilibrium state and the concept of *frozen speed of sound* assume dominance of the gaseous phase, the formulation according to Wood [167] leads to an equivalent consideration of the proportions of both phases:

$$\text{Wood:} \qquad a = \sqrt{\frac{1}{\rho_m}\left(\frac{1-y}{\rho_g a_g^2} + \frac{y}{\rho_l a_l^2}\right)^{-1}} \tag{D.2}$$

The speed of sound of the gas and liquid phase included in this equation is determined by evaluating the equation of state. By implementing the three approaches introduced for determining the speed of sound in TRACE, a numerical solution for *Case T1* of the nozzle according to Bier and Theis can be calculated for each of the formulations using the PGIRoe scheme. On this basis, a relative deviation of the speed of sound and the pressure from the reference data is calculated for each point calculated along the nozzle axis. In the left part of Figure D.1, the values of the deviation obtained for the three formulation types are plotted against the relative nozzle length. While the relative deviation of the speed of sound can be found on the left-hand abscissa and is indicated by the colour blue, the right-hand abscissa shows the relative deviation of the pressure in black. The data series labelled *Ideal* and represented by a dash-dot line represents the calculations using the speed of sound of the calorically perfect gas. The solution calculated using Equation D.1 is referred to as *Frozen*, the deviation of which is characterised by a dashed line. Using the approach according to Wood from Equation D.2 also allows the determination of relative deviations plotted as a solid line. The position of the Wilson point for the test case described in detail in Chapter 5.2.1 is marked as a red dashed line to provide orientation regarding the presence of a second phase within the nozzle geometry. Since the qualitative trends of the deviations play a subordinate role in an investigation of the influence of the type of speed of sound calculation, the focus of further considerations will be on a quantitative comparison. A systematic analysis of the relative deviation of the speed of sound and thus the blue curves shows that the highest value of around 10% is achieved for the data series *Ideal*. This seems plausible since the assumption of a calorically perfect gas cannot be justified for the present test case. The formulation *Frozen* leads to a maximum relative deviation of the speed of sound of about 1%, while Wood's formula shows the smallest deviation of about 0.13%. It can also be seen that the curve only starts at the Wilson point. Since a deviation of the calculated speed of sound from the value in the equilibrium state according to Equation D.2 is only possible for states with $y > 0$, this appears consistent. A comparison with the data series *Ideal* also shows that the maximum deviations of the cases *Frozen* and *Wood* are relatively small. A closer look at the associated relative deviations of the pressure makes it possible to estimate how the speed of sound determined in the two-phase region affects the calculation of the flow field. If the black curves are analysed for this purpose, a characteristic similar to the speed of sound can be seen. While the highest deviation of 1.7% is achieved for the case *Ideal*, the maximum deviation for the case *Frozen* is only 0.01%. The case *Wood* has the lowest maximum value of 0.0004%. This makes it clear that the way in which the speed of sound is determined in the two-phase region has no relevance, at least for the present case. With the exception of the case *Ideal*, which only serves as a reference value, each of the formulations leads to the calculation of an almost identical pressure curve. Moreover, since the speed of

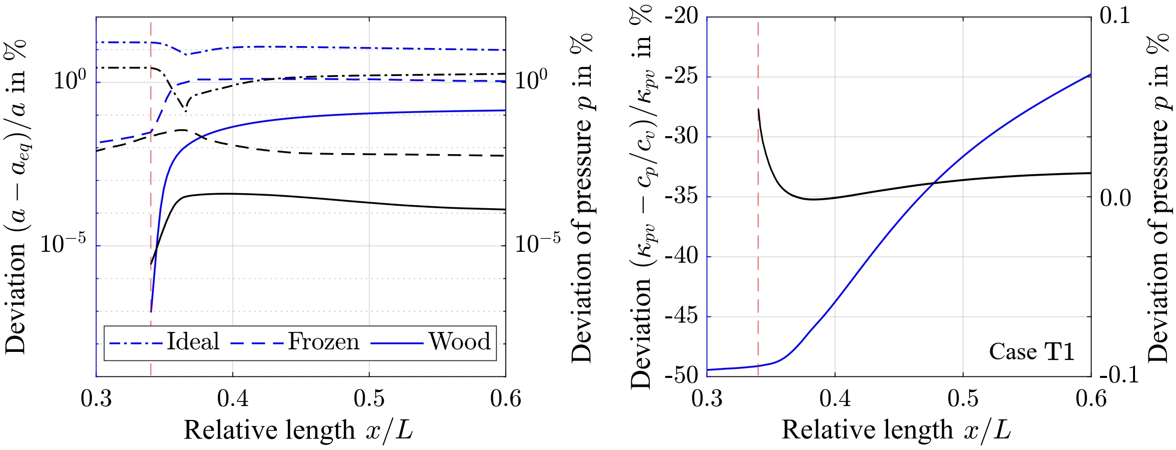

Figure D.1: Relative deviation of speed of sound and pressure along the nozzle according to Bier and Theis for different ways of determining the speed of sound in Case T1 (left) and relative deviation of isentropic pressure-volume exponent from ratio of specific heat capacities as well as the resulting deviation of pressure (right) sound is not directly included in the modelling of the disperse phase, the influence of its determination on the droplet radius can be estimated by the value determined on the basis of the pressure. Wood's formula indicates that for larger wetness fractions there could also be a higher deviation in the speed of sound and thus the calculated flow quantities. For the phase change processes investigated in the present work in the form of homogeneous condensation in turbomachines, however, only wetness fractions of the order of 0.1 are usually achieved. The maximum wetness fraction that can be achieved during homogeneous condensation is also thermodynamically limited by the spinodal limit.

The isentropic pressure-volume exponent is another thermophysical quantity that must be determined in the course of the calculations of the PGIRoe scheme. Due to its use as an expression equivalent to the isentropic exponent, the influence of its formulation is to be investigated in the same way as for the speed of sound. For this purpose, a calculation is carried out for *Case T1* of the nozzle according to Bier and Theis, which replaces the isentropic pressure-volume exponent with the ratio of specific heat capacities. The deviation of these results from the reference data is plotted in blue on the left abscissa in the right part of Figure D.1. While the deviation prior to the onset of condensation has a value of just over -50%, it decreases downstream of the Wilson point and reaches a value of -25% at the outlet of the test section, which could indicate an approach to the equilibrium state. If the effect of using the ratio of specific heat capacities on the pressure curve is considered using the right-hand abscissa, a maximum deviation of around -0.05% is shown, which coincides locally with the Wilson point. Since, in the context of the PGIRoe scheme, the analysed quantity is only determined in the presence of a second phase, this also forms the starting point of the curve. The deviation shown decreases steadily downstream and reaches a value of around 0.01% at the exit of the test section. As a result, the type of approximation of the isentropic exponent does not appear to have any relevant influence on the results. However, it should be noted that the above variation influences only the factor of the PGIRoe scheme formulated in Equation 4.49. However, using the ratio of specific heat capacities in the course of the modelling equations of condensation remains unaffected.

Bibliography

[1] **Abgrall, Rémi**. 'An extension of Roe's upwind scheme to algebraic equilibrium real gas models'. In: *Computers & Fluids* 19.2 (1991), pp. 171–182. ISSN: 0045-7930. DOI: `10.1016/0045-7930(91)90032-D`.

[2] **Allison, Timothy C., Moore, Jeffrey, Pelton, Robert, Wilkes, Jason, and Ertas, Bugra**. '7 - Turbomachinery'. In: *Fundamentals and Applications of Supercritical Carbon Dioxide (sCO2) Based Power Cycles*. Ed. by Klaus Brun, Peter Friedman, and Richard Dennis. Woodhead Publishing, 2017, pp. 147–215. ISBN: 978-0-08-100804-1. DOI: `10.1016/B978-0-08-100804-1.00007-4`.

[3] **Ameli, Alireza, Turunen-Saaresti, Teemu, and Backman, Jari**. 'Numerical Investigation of the Flow Behavior Inside a Supercritical CO2 Centrifugal Compressor'. In: *Journal of Engineering for Gas Turbines and Power* 140 (July 2018). DOI: `10.1115/1.4040577`.

[4] **Anderson, John D.** *Computational Fluid Dynamics - The Basics with Applications*. McGraw-Hill, 1995, pp. 41–42,53–55,62. ISBN: 9780071132107.

[5] **Angelino, Gianfranco**. 'Carbon Dioxide Condensation Cycles For Power Production'. In: *Journal of Engineering for Power* 90.3 (July 1968), pp. 287–295. ISSN: 0022-0825. DOI: `10.1115/1.3609190`.

[6] **Ansermet, Jean-Philippe and Brechet, Sylvain**. *Principles of Thermodynamics*. Dec. 2018, p. 140. ISBN: 9781108426091. DOI: `10.1017/9781108620932`.

[7] **Arp, Vincent, Persichetti, John M., and Chen, Guo-Bang**. 'The Grüneisen Parameter in Fluids'. In: *Journal of Fluids Engineering* 106.2 (June 1984), pp. 193–200. ISSN: 0098-2202. DOI: `10.1115/1.3243100`.

[8] **Atkins, Peter and Paula, Julio**. *Atkins' physical chemistry*. Oxford University press, 2008, pp. 7–9. ISBN: 9780195685220.

[9] **Baehr, Hans Dieter**. 'Thermodynamische Fundamentalgleichungen und charakteristische Funktionen'. In: *Forschung im Ingenieurwesen* 64.1 (May 1998), pp. 35–43.

[10] **Baehr, Hans Dieter and Kabelac, Stephan**. *Thermodynamik: Grundlagen und technische Anwendungen*. 16. Aufl. 2016. Berlin, Heidelberg: Springer Berlin Heidelberg, 2016, pp. 14–18, 254–256, 183–184, 221, 181–183. ISBN: 9783662495674.

[11] **Bakhtar, Farhang, Ebrahimi, Mojtaba, and Webb, Richard A.** 'On the Performance of a Cascade of Turbine Rotor Tip Section Blading in Nucleating Steam: Part 1: Surface Pressure Distributions'. In: *Proceedings of the Institution of Mechanical Engineers, Part C: Journal of Mechanical Engineering Science* 209.2 (1995), pp. 115–124. DOI: `10.1243/PIME_PROC_1995_209_131_02`.

[12] **Bakhtar, Farhang and Zidi, Kaddour**. 'Nucleation Phenomena in Flowing High-Pressure Steam Part 2: Theoretical Analysis'. In: *Proceedings of the Institution of Mechanical Engineers, Part A: Journal of Power and Energy* 204.4 (1990), pp. 233–242. DOI: `10.1243/PIME_PROC_1990_204_032_02`.

[13] **Bakhtar, Farhang, Young, John B., White, Alexander J., and Simpson, David. A.** 'Classical Nucleation Theory and Its Application to Condensing Steam Flow Calculations'. In: *Proceedings of the Institution of Mechanical Engineers, Part C: Journal of Mechanical Engineering Science* 219.12 (2005), pp. 1315–1333. DOI: `10.1243/095440605X8379`.

[14] **Bakhtar, Farhang, Otto, Steven R., Zamri, Mohd, and Sarkies, Jonathan Michael**. 'Instability in Two-Phase Flows of Steam'. In: *Proceedings: Mathematical, Physical and Engineering Sciences* 464.2091 (2008), pp. 537–553. ISSN: 13645021.

[15] **Baltadjiev, Nikola, Spakovszky, Zoltan, and Lettieri, Claudio**. 'An Investigation of Real Gas Effects In Supercritical CO2 Centrifugal Ccompressors'. In: *Journal of Turbomachinery* 137 (Sept. 2015). DOI: `10.1115/1.4029616`.

[16] **Banuti, Daniel T., Raju, Muralikrishna, and Ihme, Matthias**. 'Between supercritical liquids and gases – Reconciling dynamic and thermodynamic state transitions'. In: *The Journal of Supercritical Fluids* 165 (2020), p. 104895. ISSN: 0896-8446. DOI: `10.1016/j.supflu.2020.104895`.

[17] **Barschdorff, Dieter**. 'Kurzzeitfeuchtemessung und ihre Anwendung bei Kondensationserscheinungen in Lavaldüsen'. Doctoral Thesis. Karlsruhe: Institut Strömungslehre und Strömungsmaschinen, 1967, pp. 29–30.

[18] **Barschdorff, Dieter**. 'Verlauf der Zustandsgrößen und gasdynamische Zusammenhänge bei der spontanen Kondensation reinen Wasserdampfes in Lavaldüsen'. In: *Forschung im Ingenieurwesen A* 37 (1971), pp. 146–157.

[19] **Becker, Richard and Döring, Werner**. 'Kinetische Behandlung der Keimbildung in übersättigten Dämpfen'. In: *Annalen der Physik* 416.8 (1935), pp. 719–752. DOI: `10.1002/andp.19354160806`.

[20] **Bethe, Hans A.** 'On the Theory of Shock Waves for an Arbitrary Equation of State'. In: *Classic Papers in Shock Compression Science*. Ed. by James N. Johnson and Roger Chéret. New York, NY: Springer New York, 1998, pp. 421–495. ISBN: 978-1-4612-2218-7. DOI: `10.1007/978-1-4612-2218-7_11`.

[21] **Bier, Konrad, Ehrler, Friedrich, and Niekrawietz, Martin**. 'Experimental Investigation and Computer Analysis of Sontaneous Condensation in Stationary Nozzle Flow of CO2-Air Mixtures'. In: *Adiabatic Waves in Liquid-Vapor Systems*. Ed. by Gerd E. A. Meier and Philip A. Thompson. Berlin, Heidelberg: Springer Berlin Heidelberg, 1990, pp. 113–127. ISBN: 978-3-642-83587-2.

[22] **Bier, Konrad, Ehrler, Friedrich, and Theis, Gerhard**. 'Spontaneous Condensation in Stationary Nozzle Flow of Carbon Dioxide in a Wide Range of Density'. In: *Adiabatic Waves in Liquid-Vapor Systems*. Ed. by Gerd E. A. Meier and Philip A. Thompson. Berlin, Heidelberg: Springer Berlin Heidelberg, 1990, pp. 129–141. ISBN: 978-3-642-83587-2.

[23] **Bolmatov, Dima, Brazhkin, Vadim V., and Trachenko, Kostya**. 'Thermodynamic behaviour of supercritical matter'. In: *Nature communications* 4 (Aug. 2013), p. 2331. DOI: `10.1038/ncomms3331`.

[24] **Brazhkin, Vadim V. and Trachenko, Kostya**. 'What separates a liquid from a gas?' In: *Physics Today* 65.11 (Nov. 2012), pp. 68–69. ISSN: 0031-9228. DOI: `10.1063/PT.3.1796`.

[25] **Brazhkin, Vadim V., Fomin, Yury D., Lyapin, Alexander G., Ryzhov, Valentin N., and Tsiok, Elena N.** 'Widom Line for the Liquid–Gas Transition in Lennard-Jones System'. In: *The Journal of Physical Chemistry B* 115.48 (2011), pp. 14112–14115. DOI: `10.1021/jp2039898`.

[26] **Charney, Jule G., Fjörtoft, Ragnar, and Neumann, John von**. 'Numerical Integration of the Barotropic Vorticity Equation'. In: *Tellus* 2 (1950), pp. 237–254.

[27] **Cinnella, Paola**. 'Roe-type schemes for dense gas flow computations'. In: *Computers & Fluids* 35.10 (2006), pp. 1264–1281. ISSN: 0045-7930. DOI: `10.1016/j.compfluid.2005.04.007`.

[28] **Cockrell, Cillian, Brazhkin, Vadim V., and Trachenko, Kostya**. 'Transition in the supercritical state of matter: Review of experimental evidence'. In: *Physics Reports* 941 (2021), pp. 1–27. ISSN: 0370-1573. DOI: `10.1016/j.physrep.2021.10.002`.

[29] **Colonna, Piero and Guardone, Alberto**. 'Molecular interpretation of nonclassical gas dynamics of dense vapors under the van der Waals model'. In: *Physics of Fluids* 18 (May 2006). DOI: `10.1063/1.2196095`.

[30] **Colonna, Piero and Reynolds, William**. *Thermodynamics: Fundamentals and Engineering Applications*. Sept. 2018, pp. 136–137. ISBN: 9780521862738. DOI: `10.1017/9781139050616`.

[31] **Colonna, Piero, Nannan, Nawin R., Guardone, Alberto, and van der Stelt, Teus P.** 'On the computation of the fundamental derivative of gas dynamics using equations of state'. In: *Fluid Phase Equilibria* 286.1 (2009), pp. 43–54. ISSN: 0378-3812. DOI: `10.1016/j.fluid.2009.07.021`.

[32] **Colonna, Piero, Casati, Emiliano, Trapp, Carsten, Mathijssen, Tiemo, Larjola, Jaakko, Turunen-Saaresti, Teemu, and Uusitalo, Antti**. 'Organic Rankine Cycle Power Systems: From the Concept to Current Technology, Applications, and an Outlook to the Future'. In: *Journal of Engineering for Gas Turbines and Power* 137.10 (Oct. 2015). ISSN: 0742-4795. DOI: `10.1115/1.4029884`.

[33] **Courant, Richard, Friedrichs, Kurt, and Lewy, Hans**. 'Über die partiellen Differenzengleichungen der mathematischen Physik'. In: *Mathematische Annalen* 100 (1928), pp. 32–74. ISSN: 0025-5831.

[34] **Cramer, Mark S.** 'Negative nonlinearity in selected fluorocarbons'. In: *Physics of Fluids A: Fluid Dynamics* 1.11 (Nov. 1989), pp. 1894–1897. ISSN: 0899-8213. DOI: `10.1063/1.857514`.

[35] **Crowe, Clayton, Schwarzkopf, John, Sommerfeld, Martin, and Tsuji, Yutaka**. *Multiphase flows with droplets and particles*. CRC Press, Jan. 2011, pp. 67–100. ISBN: 1439840504. DOI: `10.1201/b11103`.

[36] **Cunningham, Ebenezer and Larmor, Joseph**. 'On the velocity of steady fall of spherical particles through fluid medium'. In: *Proceedings of the Royal Society of London. Series A, Containing Papers of a Mathematical and Physical Character* 83.563 (1910), pp. 357–365. DOI: `10.1098/rspa.1910.0024`.

[37] **Davies, Charles N.** 'Definitive equations for the fluid resistance of spheres'. In: *Proceedings of the Physical Society* 57.4 (1945), p. 259. DOI: `10.1088/0959-5309/57/4/301`.

[38] **Demirel, Yaşar**. 'Chapter 14 - Extended nonequilibrium thermodynamics'. In: *Nonequilibrium Thermodynamics*. Amsterdam: Elsevier Science, 2002, pp. 373–394. ISBN: 978-0-444-50886-7. DOI: `10.1016/B978-044450886-7/50014-X`.

[39] **Dostál, Václav**. *A supercritical carbon dioxide cycle for next generation nuclear reactors*. Massachusetts Institute of Technology, Dept. of Nuclear Engineering, Mar. 2004, pp. 114–155.

[40] **Dykas, Sławomir and Wróblewski, Włodzimierz**. 'Single- and two-fluid models for steam condensing flow modeling'. In: *International Journal of Multiphase Flow* 37.9 (2011), pp. 1245–1253. ISSN: 0301-9322. DOI: `10.1016/j.ijmultiphaseflow.2011.05.008`.

[41] **Dykas, Sławomir and Wróblewski, Włodzimierz**. 'Two-fluid model for prediction of wet steam transonic flow'. In: *International Journal of Heat and Mass Transfer* 60 (2013), pp. 88–94. ISSN: 0017-9310. DOI: `10.1016/j.ijheatmasstransfer.2012.12.024`.

[42] **Ehrenfest, Paul**. *Phasenumwandlungen im ueblichen und erweiterten Sinn, classifiziert nach den entsprechenden Singularitaeten des thermodynamischen Potentiales*. NV Noord-Hollandsche Uitgevers Maatschappij, 1933.

[43] **Einfeldt, Bernd**. 'On Godunov-Type Methods for Gas Dynamics'. In: *Siam Journal on Numerical Analysis - SIAM J NUMER ANAL* 25 (Apr. 1988), pp. 294–318. DOI: `10.1137/0725021`.

[44] **Ferziger, Joel H. and Perić, Milovan**. *Numerische Strömungsmechanik*. ger. Berlin [u.a: Springer, 2008, pp. 345–347. ISBN: 9783540675860.

[45] **Fisher, Michael E. and Widom, Benjamin**. 'Decay of Correlations in Linear Systems'. In: *The Journal of Chemical Physics* 50.9 (Dec. 1969), pp. 3756–3772. ISSN: 0021-9606. DOI: `10.1063/1.1671624`.

[46] **Franco, Alessandro**. 'Power production from a moderate temperature geothermal resource with regenerative Organic Rankine Cycles'. In: *Energy for Sustainable Development* 15.4 (2011), pp. 411–419. ISSN: 0973-0826. DOI: `10.1016/j.esd.2011.06.002`.

[47] **Freeman, James, Hellgardt, Klaus, and Markides, Christos N.** 'An assessment of solar-powered organic Rankine cycle systems for combined heating and power in UK domestic applications'. In: *Applied Energy* 138 (2015), pp. 605–620. ISSN: 0306-2619. DOI: `10.1016/j.apenergy.2014.10.035`.

[48] **Frenkel, Yakov**. 'Statistical Theory of Condensation Phenomena'. In: *The Journal of Chemical Physics* 7.3 (Mar. 1939), pp. 200–201. ISSN: 0021-9606. DOI: `10.1063/1.1750413`.

[49] **Friend, Daniel G.** '7. Speed of sound as a thermodynamic property of fluids'. In: *Modern Acoustical Techniques for the Measurennent of Mechanical Properties*. Ed. by Moises Levy, Henry E. Bass, and Richard Stern. Vol. 39. Experimental Methods in the Physical Sciences. Academic Press, 2001, pp. 237–306. DOI: `10.1016/S1079-4042(01)80090-4`.

[50] **Gerber, Andrew G.** 'Two-Phase Eulerian/Lagrangian Model for Nucleating Steam Flow '. In: *Journal of Fluids Engineering* 124.2 (May 2002), pp. 465–475. ISSN: 0098-2202. DOI: `10.1115/1.1454109`.

[51] **Gibbs, Josiah Willard**. 'On the Equilibrium of Heterogeneous Substances'. In: *Repertorium der literarischen Arbeiten aus dem Gebiete der reinen und angewandten Mathematik : Originalberichte der Verfasser* 2 (1879), pp. 300–320.

[52] **Gibbs, Josiah Willard**. *The Collected Works of J. Willard Gibbs*. Volume I - Thermodynamics. Longmans, Green and Co., 1928, ff.253.

[53] **Giordano, Michele and Cinnella, Paola**. 'Numerical Method for Wet-Steam Flows with Polydispersed Droplet Spectra'. In: June 2008. DOI: `10.2514/6.2008-3843`.

[54] **Giuffré, Andrea and Pini, Matteo**. 'Design Guidelines for Axial Turbines Operating With Non-Ideal Compressible Flows'. In: *Journal of Engineering for Gas Turbines and Power* 143.1 (Dec. 2020), p. 011004. ISSN: 0742-4795. DOI: `10.1115/1.4049137`.

[55] **Glaister, Paul**. 'An approximate linearised Riemann solver for the Euler equations for real gases'. In: *Journal of Computational Physics* 74.2 (1988), pp. 382–408. ISSN: 0021-9991. DOI: `10.1016/0021-9991(88)90084-8`.

[56] **Godunov, Sergei K. and Bohachevsky, Ihor**. 'Finite difference method for numerical computation of discontinuous solutions of the equations of fluid dynamics'. In: *Matematičeskij sbornik* 47(89).3 (1959), pp. 271–306.

[57] **Gori, Giulio, Zocca, Marta, Cammi, Giorgia, Spinelli, Andrea, and Guardone, Alberto**. 'Experimental assessment of the open-source SU2 CFD suite for ORC applications'. In: *Energy Procedia* 129 (2017). 4th International Seminar on ORC Power Systems, pp. 256–263. ISSN: 1876-6102. DOI: `10.1016/j.egypro.2017.09.151`.

[58] **Grossman, Ben and Walters, Robert W.** 'Flux-split algorithms for the multi-dimensional Euler equations with real gases'. In: *Computers & Fluids* 17.1 (1989), pp. 99–112. ISSN: 0045-7930. DOI: `10.1016/0045-7930(89)90009-1`.

[59] **Grübel, Marius, Starzmann, Jörg, Schatz, Markus, Eberle, Timo, Vogt, Damian M., and Sieverding, Frank**. 'Two-Phase Flow Modeling and Measurements in Low-Pressure Turbines—Part I: Numerical Validation of Wet Steam Models and Turbine Modeling'. In: *Journal of Engineering for Gas Turbines and Power* 137.4 (Apr. 2015), p. 042602. ISSN: 0742-4795. DOI: `10.1115/1.4028468`.

[60] **Guardone, Alberto and Argrow, Brian**. 'Nonclassical gasdynamic region of selected fluorocarbons'. In: *Physics of Fluids - PHYS FLUIDS* 17 (Nov. 2005). DOI: `10.1063/1.2131922`.

[61] **Guha, Abhijit**. 'Transport and Deposition of Particles in Turbulent and Laminar Flow'. In: *Annu. Rev. Fluid Mech* 40 (Jan. 2008), pp. 311–41. DOI: `10.1146/annurev.fluid.40.111406.102220`.

[62] **Guha, Abhijit**. *Two-Phase Flows with Phase Transition*. von Karman Institute Lecture Series, June 1995, pp. 50–51.

[63] **Gyarmathy, Georg**. 'Grundlagen einer Theorie der Nassdampfturbine'. Doctoral Thesis. Zürich: ETH Zurich, 1962. DOI: `10.3929/ethz-a-000087803`.

[64] **Hacks, Alexander J., Abd El Hussein, Ihab, Ren, Haikun, Schuster, Sebastian, and Brillert, Dieter**. 'Experimental Data of Supercritical Carbon Dioxide (sCO2) Compressor at Various Fluid States'. In: *Journal of Engineering for Gas Turbines and Power* 144.4 (Jan. 2022), p. 041012. ISSN: 0742-4795. DOI: `10.1115/1.4052954`.

[65] **Hacks, Alexander J., Vojacek, Ales, Dohmen, Hans Josef, and Brillert, Dieter**. 'Experimental investigation of the sCO2-HeRo compressor'. In: *2nd European sCO2 Conference 2018* (2018). DOI: `10.17185/duepublico/46088`.

[66] **Hacks, Alexander J., Schuster, Sebastian, Dohmen, Hans Josef, Benra, Friedrich-Karl, and Brillert, Dieter**. 'Turbomachine Design for Supercritical Carbon Dioxide Within the sCO2-HeRo.eu Project'. In: *Journal of Engineering for Gas Turbines and Power* 140.12 (Nov. 2018), p. 121017. ISSN: 0742-4795. DOI: `10.1115/1.4040861`.

[67] **Halama, Jan, Benkhaldoun, Fayssal, and Fořt, Jaroslav**. 'Flux schemes based finite volume method for internal transonic flow with condensation'. In: *International Journal for Numerical Methods in Fluids* 65 (Mar. 2011), pp. 953 –968. DOI: `10.1002/fld.2223`.

[68] **Harinck, John, Guardone, Alberto, and Colonna, Piero**. 'The influence of molecular complexity on expanding flows of ideal and dense gases'. In: *Physics of Fluids* 21.8 (Aug. 2009), p. 086101. ISSN: 1070-6631. DOI: `10.1063/1.3194308`.

[69] **Harten, Amiram and Hyman, James M.** 'Self adjusting grid methods for one-dimensional hyperbolic conservation laws'. In: *Journal of Computational Physics* 50.2 (1983), pp. 235–269. ISSN: 0021-9991. DOI: `10.1016/0021-9991(83)90066-9`.

[70] **Harten, Amiram, Lax, Peter D., and Leer, Bram van**. 'On Upstream Differencing and Godunov-Type Schemes for Hyperbolic Conservation Laws'. In: *SIAM Rev* 25 (Jan. 1983), pp. 35–61.

[71] **Hauke, Guillermo**. *An Introduction to Fluid Mechanics and Transport Phenomena*. Vol. 86. Jan. 2008, pp. 5–10. ISBN: 978-1-4020-8536-9. DOI: `10.1007/978-1-4020-8537-6`.

[72] **Hill, Philip G.** 'Condensation of water vapour during supersonic expansion in nozzles'. In: *Journal of Fluid Mechanics* 25.3 (1966), 593–620. DOI: `\url{10.1017/S0022112066000284}`.

[73] **Hu, Guojun and Kozlowski, Tomasz**. 'A Roe-type numerical solver for the two-phase two-fluid six-equation model with realistic equation of state'. In: *Nuclear Engineering and Design* 326 (2018), pp. 354–370. ISSN: 0029-5493. DOI: `10.1016/j.nucengdes.2017.11.023`.

[74] **Huber, Marcia**. 'Models for Viscosity, Thermal Conductivity, and Surface Tension of Selected Pure Fluids as Implemented in REFPROP v10.0'. en. Aug. 2018. DOI: `10.6028/NIST.IR.8209`.

[75] **Huber, Marcia, Perkins, Richard, Friend, Daniel, Sengers, Jan, Assael, Marc, Metaxa, Ifigeneia, Miyagawa, Kiyoshi, Hellmann, Robert, and Vogel, Eckhard**. 'New International Formulation for the Thermal Conductivity of H2O'. In: *Journal of Physical and Chemical Reference Data* 41 (Sept. 2012), p. 033102. DOI: `10.1063/1.4738955`.

[76] **Huber, Marcia, Perkins, Richard, Laesecke, Arno, Friend, Daniel, Sengers, Jan, Assael, Marc, Metaxa, Ifigeneia, Vogel, Eckhard, Mareš, Radim, and Miyagawa, Kiyoshi**. 'New International Formulation for the Viscosity of H2O'. In: *Journal of Physical and Chemical Reference Data - J PHYS CHEM REF DATA* 38 (June 2009), pp. 101–125. DOI: `10.1063/1.3088050`.

[77] **Huber, Marcia, Sykioti, Evrydiki, Assael, Marc, and Perkins, Richard**. 'Reference Correlation of the Thermal Conductivity of Carbon Dioxide from the Triple Point to 1100 K and up to 200 MPa'. In: *Journal of Physical and Chemical Reference Data* 45.1 (Feb. 2016), p. 013102. ISSN: 0047-2689. DOI: `10.1063/1.4940892`.

[78] **Hulburt, Hugh M. and Katz, Stanley**. 'Some problems in particle technology: A statistical mechanical formulation'. In: *Chemical Engineering Science* 19.8 (1964), pp. 555–574. ISSN: 0009-2509. DOI: `10.1016/0009-2509(64)85047-8`.

[79] **International Association for the Properties of Water and Steam**. 'Revised Release on Surface Tension of Ordinary Water Substance'. In: (June 2014).

[80] **Invernizzi, Costante**. *Closed Power Cycles. Thermodynamic Fundamentals and Applications*. Vol. 11. Jan. 2013, p. 109. ISBN: 978-1-4471-5139-5. DOI: `10.1007/978-1-4471-5140-1`.

[81] **Jaeger, Gregg**. 'The Ehrenfest Classification of Phase Transitions: Introduction and Evolution'. In: *Archive for History of Exact Sciences* 53 (May 1998), pp. 51–81. DOI: `10.1007/s004070050021`.

[82] **Kantrowitz, Arthur**. 'Nucleation in Very Rapid Vapor Expansions'. In: *The Journal of Chemical Physics* 19.9 (Dec. 2004), pp. 1097–1100. ISSN: 0021-9606. DOI: `10.1063/1.1748482`.

[83] **Katopodes, Nikolaos D.** *Free-Surface Flow*. Butterworth-Heinemann, 2018, pp. 11–13. ISBN: 9780128154892.

[84] **Knudsen, Martin and Weber, Sophus**. 'Luftwiderstand gegen die langsame Bewegung kleiner Kugeln'. In: *Annalen der Physik* 341.15 (1911), pp. 981–994. DOI: `10.1002/andp.19113411506`.

[85] **Kouremenos, Dimitrios A. and Kakatsios, Xenofon K.** 'The three isentropic exponents of dry steam'. In: *Forschung im Ingenieurwesen A* 51 (1985), pp. 117–122. DOI: `10.1007/BF02558416`.

[86] **Laesecke, Arno and Muzny, Chris**. 'Reference Correlation for the Viscosity of Carbon Dioxide'. In: *Journal of Physical and Chemical Reference Data* 46 (Mar. 2017), p. 013107. DOI: `10.1063/1.4977429`.

[87] **Lax, Peter D.** 'Weak solutions of nonlinear hyperbolic equations and their numerical computation'. In: *Communications on Pure and Applied Mathematics* 7.1 (1954), pp. 159–193. DOI: `10.1002/cpa.3160070112`.

[88] **Leer, Bram van**. 'Flux-Vector Splitting for the Euler Equation'. In: vol. 170. Jan. 1982. ISBN: 978-3-540-11948-7. DOI: `10.1007/3-540-11948-5_66`.

[89] **Leer, Bram van**. 'Towards the ultimate conservative difference scheme. II. Monotonicity and conservation combined in a second-order scheme'. In: *Journal of Computational Physics* 14.4 (1974), pp. 361–370. ISSN: 0021-9991. DOI: `10.1016/0021-9991(74)90019-9`.

[90] **Leer, Bram van, Thomas, James, Roe, Philip L., and Newsome, Richard**. 'A Comparison of Numerical Flux Formulas for the Euler and Navier-Stokes Equations'. In: June 1987. DOI: `10.2514/6.1987-1104`.

[91] **Lemmon, Eric W., Bell, Ian, Huber, Marcia, and McLinden, Mark O.** 'NIST Standard Reference Database 23: Reference Fluid Thermodynamic and Transport Properties-REFPROP, Version 10.0, National Institute of Standards and Technology'. 2018. DOI: `10.18434/T4/1502528`.

[92] **Liou, Meng-Sing**. 'A generalized procedure for constructing an upwind-based TVD scheme'. In: *25th AIAA Aerospace Sciences Meeting* (Jan. 1987). DOI: `10.2514/6.1987-355`.

[93] **Liou, Meng-Sing, Leer, Bram Van, and Shuen, Jian-Shun**. 'Splitting of inviscid fluxes for real gases'. In: *Journal of Computational Physics* 87.1 (1990), pp. 1–24. ISSN: 0021-9991. DOI: `10.1016/0021-9991(90)90222-M`.

[94] **Maqueo Martínez, Manuel Ernesto, Schippling, Stefan, Schatz, Markus, and Vogt, Damian M.** 'New Supersonic Nozzle Test Rig Used to Generate Condensing Flow Test Data According to Barschdorff'. In: *International Journal of Turbomachinery, Propulsion and Power* 8.4 (2023). ISSN: 2504-186X. DOI: `10.3390/ijtpp8040040`.

[95] **Marchionni, Matteo, Bianchi, Giuseppe, and Tassou, Savvas**. 'Review of supercritical carbon dioxide (sCO2) technologies for high-grade waste heat to power conversion'. In: *SN Applied Sciences* 2 (Mar. 2020). DOI: `10.1007/s42452-020-2116-6`.

[96] **Maxwell, James Clerk**. *Theory of heat*. Longmans, Green, and Co., London, 1872, pp. 163–171.

[97] **McGraw, Robert**. 'Description of Aerosol Dynamics by the Quadrature Method of Moments'. In: *Aerosol Science and Technology* 27.2 (1997), pp. 255–265. DOI: `10.1080/02786829708965471`.

[98] **Mei, Yi and Guha, Abhijit**. 'Modification of the upwind schemes for the computation of condensing two-phase flows'. In: *Proceedings of The Institution of Mechanical Engineers Part A-journal of Power and Energy - PROC INST MECH ENG A-J POWER* 220 (Nov. 2006). DOI: `10.1243/09576509JPE146`.

[99] **Menter, Florian, Kuntz, Martin, and Langtry, Robin. B.** 'Ten years of industrial experience with the SST turbulence model'. In: *Turbulence, Heat and Mass Transfer* 4 (Jan. 2003), pp. 625–632.

[100] **Miyagawa, Kazuyoshi and Hill, Philip G.** 'A Tabular Taylor Series Expansion Method for Fast Calculation of Steam Properties'. In: *Journal of Engineering for Gas Turbines and Power* 119.2 (Apr. 1997), pp. 485–491. ISSN: 0742-4795. DOI: `10.1115/1.2815600`.

[101] **Moore, Michael J., Walters, Paul T., Crane, Robert I., and Davidson, Bernhard J.** 'Predicting the Fog-Drop Size in Wet-Steam Turbines'. In: *Proceedings of the IMechE Conference on Heat and Fluid Flow in Steam and Gas Turbine Plant* (Apr. 1973), pp. 101–109.

[102] **Moses, Clifford A. and Stein, Gilbert D.** 'On the Growth of Steam Droplets Formed in a Laval Nozzle Using Both Static Pressure and Light Scattering Measurements'. In: *Journal of Fluids Engineering* 100.3 (Sept. 1978), pp. 311–322. ISSN: 0098-2202. DOI: `10.1115/1.3448672`.

[103] **Mottura, Lorenzo, Vigevano, Luigi, and Zaccanti, Marco**. 'An Evaluation of Roe's Scheme Generalizations for Equilibrium Real Gas Flows'. In: *Journal of Computational Physics* 138.2 (1997), pp. 354–399. ISSN: 0021-9991. DOI: `10.1006/jcph.1997.5838`.

[104] **Mulero, Angel and Cachadina, Isidro**. 'Recommended Correlations for the Surface Tension of Several Fluids Included in the REFPROP Program'. In: *Journal of Physical and Chemical Reference Data* 43.2 (June 2014), p. 023104. ISSN: 0047-2689. DOI: `10.1063/1.4878755`.

[105] **Mulero, Angel, Cachadina, Isidro, and Parra, Maria**. 'Recommended Correlations for the Surface Tension of Common Fluids'. In: *Journal of Physical and Chemical Reference Data* 41 (Dec. 2012). DOI: `10.1063/1.4768782`.

[106] **Nannan, Nawin R., Guardone, Alberto, and Colonna, Piero**. 'On the fundamental derivative of gas dynamics in the vapor–liquid critical region of single-component typical fluids'. In: *Fluid Phase Equilibria* 337 (2013), pp. 259–273. ISSN: 0378-3812. DOI: `10.1016/j.fluid.2012.09.017`.

[107] **Ndjinga, Michaël, Kumbaro, Anela, De Vuyst, Florian, and Laurent-Gengoux, Pascal**. 'Numerical simulation of hyperbolic two-phase flow models using a Roe-type solver'. In: *Nuclear Engineering and Design* 238.8 (2008). ICONE-14 - 14th International Conference on Nuclear Energy, pp. 2075–2083. ISSN: 0029-5493. DOI: `10.1016/j.nucengdes.2007.11.014`.

[108] **Neises, Ty W. and Turchi, Craig S.** 'A Comparison of Supercritical Carbon Dioxide Power Cycle Configurations with an Emphasis on CSP Applications'. In: *Energy Procedia* 49 (2014). Proceedings of the SolarPACES 2013 International Conference, pp. 1187–1196. ISSN: 1876-6102. DOI: `10.1016/j.egypro.2014.03.128`.

[109] **Nishikawa, Keiko and Tanaka, Ibuki**. 'Correlation lengths and density fluctuations in supercritical states of carbon dioxide'. In: *Chemical Physics Letters* 244.1 (1995), pp. 149–152. ISSN: 0009-2614. DOI: `10.1016/0009-2614(95)00818-O`.

[110] **Osher, Stanley**. 'Numerical Solution of Singular Perturbation Problems and Hyperbolic Systems of Conservation Laws'. In: *Analytical and Numerical Approaches to Asymptotic Problems in Analysis*. Ed. by O. Axelsson, L.S. Frank, and A. Van Der Sluis. Vol. 47. North-Holland Mathematics Studies. North-Holland, 1981, pp. 179–204. DOI: `10.1016/S0304-0208(08)71109-5`.

[111] **Otero-Rodriguez, Gustavo J., Patel, Ashish, Diez S., Rafael, and Pečnik, René**. 'Turbulence modelling for flows with strong variations in thermo-physical properties'. In: *International Journal of Heat and Fluid Flow* 73 (2018), pp. 114–123. ISSN: 0142-727X. DOI: `10.1016/j.ijheatfluidflow.2018.07.005`.

[112] **Peery, Kelton M. and Imlay, Scott T.** 'Blunt-body flow simulations'. In: *24th Joint Propulsion Conference*. 1988. DOI: `10.2514/6.1988-2904`.

[113] **Petr, Vita**. 'Wave propagation in wet steam'. In: *Proceedings of the Institution of Mechanical Engineers, Part C: Journal of Mechanical Engineering Science* 218.8 (2004), pp. 871–882. DOI: `10.1243/0954406041474237`.

[114] **Petruccelli, Giuseppe, Grönman, Aki, and Turunen-Saaresti, Teemu**. 'A novel numerical approach for simulating low-pressure and high-pressure non-equilibrium condensation in real gases'. In: *International Journal of Multiphase Flow* 171 (2024), p. 104700. ISSN: 0301-9322. DOI: `10.1016/j.ijmultiphaseflow.2023.104700`.

[115] **Pečnik, René, Ren, Jie, and Otero-Rodriguez, Gustavo J.** 'Characterizing and modelling turbulence in supercritical fluids'. In: *4th European sCO2 Conference for Energy Systems: March 23-24, 2021, Online Conference* (Mar. 2021), pp. 301–306. ISSN: 2510-7852. DOI: `10.17185/duepublico/73942`.

[116] **Pečnik, René, Rinaldi, Enrico, and Colonna, Piero**. 'Computational Fluid Dynamics of a Radial Compressor Operating With Supercritical CO2'. In: *Journal of Engineering for Gas Turbines and Power* 134 (June 2012), p. 122301. DOI: `10.1115/GT2012-69640`.

[117] **Pipich, Vitaliy and Schwahn, Dietmar**. 'Densification of Supercritical Carbon Dioxide Accompanied by Droplet Formation When Passing the Widom Line'. In: *Physical Review Letters* 120 (Apr. 2018). DOI: `10.1103/PhysRevLett.120.145701`.

[118] **Pollak, Rolf**. 'Die thermodynamischen Eigenschaften von Wasser - dargestellt durch eine kanonische Zustandsgleichung für die fluiden homogenen und heterogenen Zustände bis 1200 Kelvin und 3000 bar'. Doctoral Thesis. Ruhr-Universität Bochum, 1974.

[119] **Prando, Dario, Renzi, Massimiliano, Gasparella, Andrea, and Baratieri, Marco**. 'Monitoring of the energy performance of a district heating CHP plant based on biomass boiler and ORC generator'. In: *Applied Thermal Engineering* 79 (2015), pp. 98–107. ISSN: 1359-4311. DOI: `10.1016/j.applthermaleng.2014.12.063`.

[120] **Radovskii, Isaak S.** 'Speed of sound in two-phase vapor-liquid systems'. In: *Journal of Applied Mechanics and Technical Physics* 11 (1970), pp. 778–784.

[121] **Richardson, Lewis F.** *Weather prediction by numerical process*. Cambridge University Press, 1922, p. 219.

[122] **Rinaldi, Enrico, Pečnik, René, and Colonna, Piero**. 'Steady State CFD Investigation of a Radial Compressor Operating With Supercritical CO2'. In: *Proceedings of the ASME Turbo Expo* 8 (June 2013). DOI: `10.1115/GT2013-94580`.

[123] **Roache, Patrick J.** 'Quantification of Uncertainity in Computational Fluid Dynamics'. In: *Annual Review of Fluid Mechanics* 29.1 (1997), pp. 123–160. DOI: `10.1146/annurev.fluid.29.1.123`.

[124] **Roe, Philip L.** 'Approximate Riemann solvers, parameter vectors, and difference schemes'. In: *Journal of Computational Physics* 43.2 (1981), pp. 357–372. ISSN: 0021-9991. DOI: `10.1016/0021-9991(81)90128-5`.

[125] **Roe, Philip L. and Pike, Jack**. 'Efficient Construction and Utilisation of Approximate Riemann Solutions'. In: June 1985, pp. 499–518.

[126] **Romei, Alessandro, Vimercati, Davide, Persico, Giacomo, and Guardone, Alberto**. 'Non-ideal compressible flows in supersonic turbine cascades'. In: *Journal of Fluid Mechanics* 882 (2020). DOI: `10.1017/jfm.2019.796`.

[127] **Ruppeiner, George, Sahay, Anurag, Sarkar, Tapobrata, and Sengupta, Gautam**. 'Thermodynamic geometry, phase transitions, and the Widom line'. In: *Physical review. E, Statistical, nonlinear, and soft matter physics* 86 (Nov. 2012), p. 052103. DOI: `10.1103/PhysRevE.86.052103`.

[128] **Rusanov, Viktor V.** 'The calculation of the interaction of non-stationary shock waves and obstacles'. In: *USSR Computational Mathematics and Mathematical Physics* 1.2 (1962), pp. 304–320. ISSN: 0041-5553. DOI: `10.1016/0041-5553(62)90062-9`.

[129] **Schames, Leon**. 'Erweiterung des Clausius-Maxwell'schen Kriteriums'. In: *Helvetica Physica Acta* 1.4 (1928), pp. 417–420.

[130] **Schatz, Markus, Eberle, Timo, Grübel, Marius, Starzmann, Jörg, Vogt, Damian, and Sürken, Norbert**. 'Two-Phase Flow Modeling and Measurements in Low-Pressure Turbines: Part 2 — Turbine Wetness Measurement and Comparison to CFD-Predictions'. In: Turbo Expo: Power for Land, Sea, and Air Volume 1B: Marine; Microturbines, Turbochargers and Small Turbomachines; Steam Turbines (June 2014), V01BT27A006. DOI: `10.1115/GT2014-25245`.

[131] **Schiller, Ludwig and Naumann, Alexander**. 'Über die grundlegenden Berechnungen bei der Schwerkraftaufbereitung'. In: *Zeitschrift des Vereins Deutscher Ingenieure* 77 (1933), pp. 318–320.

[132] **Shao, Wenyang, Yang, Jinguang, Wang, Xiaofang, and Ma, Ziyue**. 'Accuracy study and stability control of a property-table-based CFD strategy for modeling SCO2 compressors working near the critical point of the fluid'. In: *Applied Thermal Engineering* 183 (2021), p. 116222. ISSN: 1359-4311. DOI: `10.1016/j.applthermaleng.2020.116222`.

[133] **Simeoni, Giovanna G., Bryk, Taras, Gorelli, Federico A., Krisch, Michael, Ruocco, Giancarlo, Santoro, Mario, and Scopigno, Tullio**. 'The Widom line as the crossover between liquid-like and gas-like behaviour in supercritical fluids'. In: *Nature Physics* 6.7 (July 2010), pp. 503–507. DOI: `10.1038/nphys1683`.

[134] **Skripov, Vladimir P.** 'Metastable States'. In: *Journal of Non-Equilibrium Thermodynamics* 17.3 (1992), pp. 193–236. DOI: `10.1515/jnet.1992.17.3.193`.

[135] **Spalart, Philippe and Allmaras, Steven**. 'A One-Equation Turbulence Model for Aerodynamic Flows'. In: *AIAA* 439 (Jan. 1992). DOI: `10.2514/6.1992-439`.

[136] **Span, Roland and Wagner, Wolfgang**. 'A New Equation of State for Carbon Dioxide Covering the Fluid Region from the Triple-Point Temperature to 1100 K at Pressures up to 800 MPa'. In: *Journal of Physical and Chemical Reference Data* 25.6 (Nov. 1996), pp. 1509–1596. ISSN: 0047-2689. DOI: `10.1063/1.555991`.

[137] **Spinelli, Andrea, Cammi, Giorgia, Gallarini, Simone, Zocca, Marta, Cozzi, Fabio, Gaetani, Paolo, Dossena, Vincenzo, and Guardone, Alberto**. 'Experimental evidence of non-ideal compressible effects in expanding flow of a high molecular complexity vapor'. In: *Experiments in Fluids* 59 (July 2018). DOI: `10.1007/s00348-018-2578-0`.

[138] **Starzmann, Jörg et al.** 'Results of the International Wet Steam Modeling Project'. In: *Proceedings of the Institution of Mechanical Engineers, Part A: Journal of Power and Energy* 232.5 (2018), pp. 550–570. DOI: `10.1177/0957650918758779`.

[139] **Stephan, Peter, Schaber, Karlheinz, Stephan, Karl, and Mayinger, Franz**. *Thermodynamik Grundlagen und technische Anwendungen Band 1: Einstoffsysteme*. 19., ergänzte Aufl. 2013. Springer-Lehrbuch. Springer Berlin Heidelberg, 2013, pp. 8–10. ISBN: 9783642300981.

[140] **Stokes, George Gabriel**. 'On the Effect of the Internal Friction of Fluids on the Motion of Pendulums'. In: *Mathematical and Physical Papers*. Vol. 3. Cambridge Library Collection - Mathematics. Cambridge University Press, 2009, 1–10. DOI: `10.1017/CBO9780511702266.002`.

[141] **Stokes, George Gabriel**. 'On the Theories of the Internal Friction of Fluids in Motion, and of the Equilibrium and Motion of Elastic Solids'. In: *Mathematical and Physical Papers*. Vol. 1. Cambridge Library Collection - Mathematics. Cambridge University Press, 2009, 75–129. DOI: `10.1017/CBO9780511702242.005`.

[142] **Tegethoff, Katharina, Schuster, Sebastian, and Brillert, Dieter**. 'Numerical simulation of real gas one-component two-phase flow using a Roe-based scheme'. In: *Computers & Fluids* 245 (2022), p. 105560. ISSN: 0045-7930. DOI: `10.1016/j.compfluid.2022.105560`.

[143] **Tegethoff, Katharina, Almeida, Carolina Borges de, Schuster, Sebastian, and Brillert, Dieter**. 'Numerical method for investigating non-ideal flow demonstrated on a centrifugal compressor operating near the critical point of CO2'. In: Proceedings of the ASME Turbo Expo 2024: Turbo Expo: Power for Land, Sea, and Air, Volume 11: Supercritical CO_2 (June 2024). DOI: `10.1115/GT2024-124068`.

[144] **Theis, Gerhard**. 'Spontankondensation in übersättigten Dampfströmungen von Kohlendioxid und von Difluordichlormethan'. Doctoral Thesis. Karlsruhe: Fakultät für Chemieingenieurwesen, 1985, pp. 22–23,28–30,35.

[145] **Thol, Monika, Dubberke, Frithjof, Baumhögger, Elmar, Vrabec, Jadran, and Span, Roland**. 'Speed of Sound Measurements and Fundamental Equations of State for Octamethyltrisiloxane and Decamethyltetrasiloxane'. In: *Journal of Chemical & Engineering Data* 62 (July 2017). DOI: `10.1021/acs.jced.7b00092`.

[146] **Thompson, Philip A.** 'A Fundamental Derivative in Gasdynamics'. In: *The Physics of Fluids* 14.9 (Sept. 1971), pp. 1843–1849. ISSN: 0031-9171. DOI: `10.1063/1.1693693`.

[147] **Thompson, Philip A. and Lambrakis, Konstantine C.** 'Negative shock waves'. In: *Journal of Fluid Mechanics* 60.1 (1973), 187–208. DOI: `\url{10.1017/S002211207300011X}`.

[148] **Toro, Eleuterio F.** *Riemann Solvers and Numerical Methods for Fluid Dynamics: A Practical Introduction.* Springer Berlin, Heidelberg, Jan. 2009, p. 349. ISBN: 9783540252023. DOI: `10.1007/b79761`.

[149] **Toro, Eleuterio F., Spruce, Michael, and Speares, William**. 'Restoration of the contact surface in the HLL-Riemann solver'. In: *Shock Waves* 4 (1994), pp. 25–34.

[150] **Tosto, Francesco, Lettieri, Claudio, Pini, Matteo, and Colonna, Piero**. 'Dense-vapor effects in compressible internal flows'. In: *Physics of Fluids* 33.8 (Aug. 2021). ISSN: 1070-6631. DOI: `10.1063/5.0058075`.

[151] **Tosto, Francesco, Giuffré, Andrea, Colonna, Piero, and Pini, Matteo**. 'Flow deviation and critical choking in transonic turbine cascades operating with non-ideal compressible flows'. In: *Journal of the Global Power and Propulsion Society* 6 (2022), pp. 181–199. DOI: `10.33737/jgpps/151659`.

[152] **Toumi, Imad**. 'An Upwind Numerical Method for Two-Fluid Two-Phase Flow Models'. In: *Nuclear Science and Engineering* 123.2 (1996), pp. 147–168. DOI: `10.13182/NSE96-A24180`.

[153] **Tropea, Cameron, Yarin, Alexander, and Foss, John**. *Springer Handbook of Experimental Fluid Mechanics.* Jan. 2007, pp. 288–289. ISBN: 9783540251415. DOI: `10.1007/978-3-540-30299-5`.

[154] **Vimercati, Davide, Gori, Giulio, and Guardone, Alberto**. 'Non-ideal oblique shock waves'. In: *Journal of Fluid Mechanics* 847 (2018), 266–285. DOI: `10.1017/jfm.2018.328`.

[155] **Vinokur, Marcel**. 'Flux Jacobian matrices and generaled Roe average for an equilibrium real gas'. In: 1988.

[156] **Volmer, Max and Weber, Alexander**. 'Nucleus Formation in Supersaturated Systems'. In: *Zeitschrift für Physikalische Chemie* 119.1 (1926), pp. 277–301. DOI: `10.1515/zpch-1926-11927`.

[157] **Waals, Johannes Diderik van der**. *Over de continuiteit van den gas- en vloeistoftoestand.* A. W. Sijthoff, Leiden, 1873, pp. 54–56.

[158] **Wagner, Wolfgang and Kretzschmar, Hans-Joachim**. *International steam tables - Properties of water and steam based on the industrial formulation IAPWS-IF97.* Springer Berlin, Heidelberg, 2008, pp. 30–135. ISBN: 9783642431715. DOI: `10.1007/978-3-540-74234-0`.

[159] **Wagner, Wolfgang and Pruß, Andreas**. 'The IAPWS Formulation 1995 for the Thermodynamic Properties of Ordinary Water Substance for General and Scientific Use'. In: *Journal of Physical and Chemical Reference Data* 31.2 (June 2002), pp. 387–535. ISSN: 0047-2689. DOI: `10.1063/1.1461829`.

[160] **Wagner, Wolfgang et al.** 'The IAPWS Industrial Formulation 1997 for the Thermodynamic Properties of Water and Steam'. In: *Journal of Engineering for Gas Turbines and Power* 122.1 (Jan. 2000), pp. 150–184. ISSN: 0742-4795. DOI: `10.1115/1.483186`.

[161] **Wheeler, Andrew and Ong, Jonathan**. 'The Role of Dense Gas Dynamics on Organic Rankine Cycle Turbine Performance'. In: *Journal of Engineering for Gas Turbines and Power* 135 (Oct. 2013), p. 102603. DOI: `10.1115/1.4024963`.

[162] **White, Alexander J.** 'A comparison of modelling methods for polydispersed wet-steam flow'. In: *International Journal for Numerical Methods in Engineering* 57 (June 2003), pp. 819 –834. DOI: `10.1002/nme.705`.

[163] **White, Alexander J.** 'Condensation in steam turbine cascades'. Doctoral Thesis. University of Cambridge, 1992.

[164] **White, Alexander J. and Hounslow, Mike J.** 'Modelling droplet size distributions in polydispersed wet-steam flows'. In: *International Journal of Heat and Mass Transfer* 43 (June 2000), pp. 1873–1884. DOI: `10.1016/S0017-9310(99)00273-2`.

[165] **White, Alexander J., Young, John B., and Walters, Paul T.** 'Experimental validation of condensing flow theory for a stationary cascade of steam turbine blades'. In: *Philosophical Transactions of the Royal Society of London. Series A: Mathematical, Physical and Engineering Sciences* 354.1704 (1996), pp. 59–88. DOI: `10.1098/rsta.1996.0003`.

[166] **Widom, Benjamin**. 'The critical point and scaling theory'. In: *Physica* 73.1 (1974), pp. 107–118. ISSN: 0031-8914. DOI: `10.1016/0031-8914(74)90228-6`.

[167] **Wood, Albert B.** *A Textbook of Sound: Being an Account of the Physics of Vibrations with Special Reference to Recent Theoretical and Technical Developments*. G. Bell and Sons Limited, 1930.

[168] **Wright, Steven Alan, Radel, Ross F., Vernon, Milton E., Pickard, Paul S., and Rochau, Gary Eugene**. 'Operation and analysis of a supercritical CO_2 Brayton cycle.' In: 2010. DOI: `10.2172/984129`.

[169] **Wróblewski, Włodzimierz and Dykas, Sławomir**. 'Two-fluid model with droplet size distribution for condensing steam flows'. In: *Energy* 106 (2016), pp. 112–120. ISSN: 0360-5442. DOI: `10.1016/j.energy.2016.03.052`.

[170] **Wróblewski, Włodzimierz, Dykas, Sławomir, Gardzilewicz, Andrzej, and Kolovratnik, Michal**. 'Numerical and Experimental Investigations of Steam Condensation in LP Part of a Large Power Turbine'. In: *Journal of Fluids Engineering* 131.4 (Mar. 2009), p. 041301. ISSN: 0098-2202. DOI: `10.1115/1.3089544`.

[171] **Xu, Limei, Kumar, Pradeep, Buldyrev, Sergey, Chen, Sow-Hsin, Poole, Peter, Sciortino, Francesco, and Stanley, Harry E.** 'Relation Between the Widom Line and the Dynamic Crossover in Systems With a Liquid-Liquid Phase Transition'. In: *Proceedings of the National Academy of Sciences of the United States of America* 102 (Dec. 2005), pp. 16558–62. DOI: `10.1073/pnas.0507870102`.

[172] **Young, John B.** *Spontaneous Condensation of Steam in Supersonic Nozzles*. Technical report (University of Cambridge. Department of Engineering).: A-Turbo. Cambridge University Engineering Department, 1980, p. 23.

[173] **Zeldovich, Yakov B.** 'On the theory of new phase formation: cavitation'. In: *Acta Physicochem., USSR* 18 (1943), p. 1.

[174] **Zemansky, Mark W., Dittman, Richard H., and Scott, Hugh L.** *Heat and Thermodynamics, 7th ed.* McGraw Hill, New York, 1997, pp. 226–227. ISBN: 0-07-01759-2.

[175] **Zhu, Xiaofeng, Lin, Zhirong, Yuan, Xin, Tomohiro, Tejima, Niizeki, Yoshiki, and Shibukawa, Naoki**. 'Non-equilibrium Condensing Flow Modeling in Nozzle and Turbine Cascade'. In: *International Journal of Gas Turbine, Propulsion and Power Systems* 4.3 (Oct. 2012).

[176] **Šafarík, Pavel, Nový, Adam, Jícha, David, and Hajšman, Miroslav**. 'On the speed of sound in steam'. In: *Acta Polytechnica* 55.6 (2015), 422–426. DOI: `10.14311/AP.2015.55.0422`.

Curriculum Vitae

The curriculum vitae is not included in the online version for data protection reasons.